UNIVERSITAT
POLITÈCNICA
DE VALÈNCIA

**Doctoral Thesis**

# Estimation of Atrial Electrical Complexity during Atrial Fibrillation by Solving the Inverse Problem of Electrocardiography

**PhD in Technologies for Health and Well-Being**

**Author: Rubén Molero Alabau**

**Supervisor: María de la Salud Guillem Sánchez**

**September 2023**

A straight line may be the shortest distance between two points,

but it is by no means the most interesting.

*The Doctor. Doctor Who.*

# Agradecimientos

Durante la realización de esta tesis doctoral, muchas personas han tenido un papel fundamental para que esto salga adelante, bien en lo laboral o en lo personal.

Primeramente, quiero agradecer a todos mis compañeros de ITACA COR que han hecho este proceso mucho más llevadero, han mantenido mi cordura y me han permitido desarrollar la cormedia. En especial:

A Ana y Carlos que estuvieron conmigo al empezar sacando esto hacia adelante.

A Clara, Isma, Marta, María, Raúl, Andrea, Inés, entre otros, por ser unos genios y permitirme hacer de mi lugar de trabajo un lugar donde aprender de vosotros y hacerlo un espacio seguro donde dejarme ser.

A Arantxa, por ser la mejor compañera y mi mejor público. Nos queda un año para llenar el Wizink Center, he actualizado el trello.

A María y Andreu, por guiarme en este camino. Aprender de personas tan excelentes a quien admiro es una gran suerte. Gracias por la paciencia y dedicación de estos años. Espero un día poder contribuir a esta ciencia y a la sociedad una mínima parte de lo que lo habéis hecho vosotros.

A mis compañeros de Corify, en especial a David, ver y formar parte de las primeras etapas y el proceso de crecimiento de Corify ha sido un privilegio. Estoy seguro de que millones de personas se van a beneficiar de vuestro duro trabajo y esfuerzo para revolucionar la cordiología.

A Zaida, con quien compartí los meses de estancia predoctoral en Maastricht y fue la primera persona con quien supe que no estaba solo en el camino del doctorado.

To Pietro, for welcoming me to Maastricht with open arms, someone I admire both in scientific matters and in their work ethic.

To all the colleagues in the field of Electrocardiographic Imaging, being part of the ECGI community is such an honor. I feel very fortunate to witness the growth of this field of knowledge, collaborating alongside so many excellent researchers from around the world.

A mamá, papá y Noe, porque aunque no sepáis qué he estado haciendo durante esta tesis más allá de algo con un chaleco, vuestro apoyo y confianza siempre ha estado ahí. Espero que estéis tan orgullosos de mí como yo de agradecido de teneros como familia.

A mis abuelos, en especial a mi iaia Ruse. Gràcies pel suport incondicional a tot el que faig.

A Yolanda, porque siempre desde bien pequeño me decía lo lejos que iba a llegar sin ningún tipo de duda. No estaría escribiendo esta tesis sin tu apoyo.

A Alex, a quien conocí cuando empecé esto, tu apoyo y paciencia han sido fundamentales.

A teika.

En definitiva, a todos los que habéis confiado en mí mucho más de lo que yo lo he hecho.

Gracias.

# Index

# List of Figures

# Acronyms

AAD: Antiarrhythmic Drugs

AFL: Atrial Flutter

AF: Atrial Fibrillation

AP: Action Potential

AUC: Area Under the Curve

AV: Atrioventricular

BSPM: Body Surface Potential Mapping

CC: Correlation Coefficient

CFAE: Complex Fractionated Electrogram

DF: Dominant Frequency

DTI: Diffusion Tensor Imaging

ECG: Electrocardiography

ECGI: Electrocardiographic Imaging

EGM: Electrogram

HDF: Highest Dominant Frequency

IVC: Inferior Vena Cava

$\lambda$: Regularization Parameter

LA: Left Atrium

LAA: Left Atrial Appendage

LGE-MRI: Late Gadolinium Enhancement Magnetic Resonance Imaging

LIPV: Left Inferior Pulmonary Vein

LV: Left Ventricle

LTR: Long-term Recurrence

MRI: Magnetic Resonance Imaging

NB HDF: Narrow Band filter at Highest Dominant Frequency

NOAC: Non-vitamin K Antagonist Oral Anticoagulant

$|P_1|$: Short-term recurrence at half AF cycle

$P_2$: Short-term recurrence at full AF cycle

PDE: Partial Differential Equation

PPVV: Pulmonary Veins

PVI: Pulmonary Vein Isolation

RA: Right Atrium

RAPP: Right Atrial Appendage

RDMS/RDM*: Relative Difference Measurement Star

ROC: Receiver Operating Characteristic Curve

RS: Reproducibility Score

RHE: Relative Harmonic Energy

RIPV: Right Inferior Pulmonary Vein

RS: Reproducibility Score

RSPV: Right Superior Pulmonary Vein

RV: Right Ventricle

SA: Sinoatrial

SAE: Sample Entropy

SP/PS: Singularity Point/ Phase Singularity

SRC: Sinusoidal Recomposition

SVC: Superior Vena Cava

VKA: Vitamin K Antagonist

VS: Variability Score

# Abstract

Atrial fibrillation (AF) is the most prevalent arrhythmia in the world and is associated with significant morbidity, mortality, and healthcare costs. Despite advancements in pharmaceutical treatment alternatives and ablation therapy, AF management remains suboptimal. Electrocardiographic Imaging (ECGI) has emerged as a promising non-invasive method for assessing cardiac electrophysiology and guiding therapeutic decisions in atrial fibrillation. However, ECGI faces challenges in dealing with accurately resolving the ill-posed inverse problem of electrocardiography and optimizing the quality of ECGI reconstructions. Additionally, the integration of ECGI into clinical workflows is still a challenge that is hindered by the associated costs arising from the need for cardiac imaging.

For this purpose, the main objectives of this PhD thesis are to advance ECGI technology by determining the minimal technical requirements and refining existing methodologies for acquiring accurate ECGI signals. In addition, we aim to assess the capacity of ECGI for non-invasively quantifying AF complexity. To fulfill these objectives, several studies were developed throughout the thesis, advancing from ECGI enhancement to AF evaluation using ECGI.

Firstly, geometric and signal requirements of the inverse problem were addressed by studying the effects of torso mesh density and electrode distribution on ECGI accuracy, leading to the identification of the minimal number of nodes and their distribution on the torso mesh. Besides, we identified that the correct location of the electrodes on the reconstructed torso mesh is critical for the accurate ECGI signal obtention. Additionally, a new methodology of imageless ECGI was defined and assessed by comparing ECGI-derived drivers computed with the original heart geometry of the patients to the drivers measured in different heart geometries. Our results showed the ability of imageless ECGI to the correct quantification and location of atrial fibrillation drivers, validating the use of ECGI without the need for cardiac imaging. Also, the current state-

of-the-art zero-order Tikhonov regularization and L-curve optimization for computing ECGI signals were improved by investigating the impact of electrical noise and geometrical uncertainties on the regularization. We proposed a new criterion that enhances the accuracy and reliability of ECGI solutions in situations with uncertainty from unfavorable signal conditions.

Secondly, in this PhD thesis, several analyses, signal processing methodologies, and ECGI-derived metrics were investigated to better characterize the cardiac substrate and reentrant activity in ECGI signals from AF patients. With the objective of obtaining a deeper understanding of the electrophysiological mechanisms underlying AF, we established the optimal filtering strategy to extract patient-specific reentrant patterns and derived metrics in ECGI signals. Furthermore, we investigated the reproducibility of the obtained ECGI-reentrant maps and linked them to the success of PVI ablation. Our results showed that higher reproducibility on AF drivers detected with ECGI is linked with the success of PVI, creating a proof-of-concept mechanism for stratifying AF patients prior to ablation procedures.

In conclusion, this PhD thesis makes a significant contribution to the development of a more rigorous and practical framework for the use of ECGI in clinical practice, particularly in the domain of atrial fibrillation. This thesis' findings have the potential to enhance patient stratification, individualized therapy planning, and patient outcomes in the management of AF. This study provides a strong basis for future improvements by resolving the limitations associated with ECGI technology and validating its application in assessing AF complexity.

# Resumen

La fibrilación auricular (FA) es la arritmia más prevalente en el mundo y está asociada con una elevada morbilidad, mortalidad y costes sanitarios. A pesar de los avances en opciones de tratamiento farmacológico y terapia de ablación, el manejo de la FA todavía tiene margen de mejora. La imagen electrocardiográfica (ECGI) se ha destacado como un prometedor método no invasivo para evaluar la electrofisiología cardíaca y guiar las decisiones terapéuticas en casos de fibrilación auricular. No obstante, el ECGI se enfrenta a desafíos como la necesidad de resolver de manera precisa el denominado problema inverso de la electrocardiografía y de optimizar la calidad de las reconstrucciones de ECGI. Además, la integración del ECGI en los procesos clínicos rutinarios sigue siendo un reto, en gran medida debido a los costos que supone la necesidad de imágenes cardíacas.

Por ello, los objetivos principales de esta tesis doctoral son impulsar la tecnología ECGI mediante la determinación de sus requisitos técnicos mínimos y la mejora de las metodologías existentes para obtener señales de ECGI precisas. Asimismo, buscamos evaluar la capacidad de ECGI para cuantificar de forma no invasiva la complejidad de la FA. Para lograr estos objetivos, se han llevado a cabo diversos estudios a lo largo de la tesis, desde el perfeccionamiento del ECGI hasta la evaluación de la FA utilizando esta tecnología.

En primer lugar, se han estudiado los requisitos geométricos y de señal del problema inverso mediante el estudio de los efectos de la densidad de la malla del torso y la distribución de electrodos en la precisión del ECGI, lo que ha conducido a la identificación del número mínimo de nodos y su distribución en la malla del torso. Además, hemos identificado que para obtener señales de ECGI de alta calidad, es crucial la correcta disposición de los electrodos en la malla del torso reconstruido. Asimismo, se ha definido y evaluado una nueva metodología de ECGI sin

necesidad de usar técnicas de imagen cardiaca. Para ello, hemos comparado métricas derivadas del ECGI calculadas con la geometría original del corazón de los pacientes con las métricas medidas en diferentes geometrías cardíacas. Nuestros resultados han mostrado que el ECGI sin necesidad de imágenes cardíacas es efectivo para la correcta cuantificación y localización de los patrones y zonas que mantienen la FA. En paralelo, hemos optimizado la regularización de Tikhonov de orden cero actual y la optimización de la curva L para el cálculo de las señales ECGI, investigando cómo el ruido eléctrico y las incertidumbres geométricas influyen en la regularización. A partir de ello, propusimos un nuevo criterio que realza la precisión de las soluciones de ECGI en escenarios con incertidumbre debido a condiciones de señal no ideales.

En segundo lugar, en esta tesis doctoral, se han llevado a cabo múltiples análisis relativos a diferentes metodologías de procesado de señales y obtención métricas derivadas del ECGI con el fin de caracterizar mejor el sustrato cardíaco y la actividad reentrante en las señales de ECGI de pacientes con FA. Con el objetivo de obtener una comprensión más profunda de los mecanismos electrofisiológicos subyacentes a la FA, hemos establecido la estrategia de filtrado óptima para extraer patrones reentrantes específicos del paciente y métricas derivadas de señales ECGI. Además, hemos investigado la reproducibilidad de los mapas de reentradas derivados de las señales de ECGI y hemos encontrado su relación con el éxito de la ablación de venas pulmonares (PVI). Nuestros resultados han mostrado que una mayor reproducibilidad en los patrones reentrantes de FA detectados con ECGI está relacionada con el éxito de la PVI, creando una metodología para estratificar a los pacientes con FA antes de los procedimientos de ablación.

En conclusión, esta tesis doctoral hace una contribución significativa al desarrollo de un marco más riguroso y práctico para el uso de ECGI en la práctica clínica, en particular en el ámbito de la fibrilación auricular. Los hallazgos de esta tesis tienen el potencial de mejorar la estratificación de pacientes, la planificación de terapia individualizada y mejorar los resultados de los tratamientos actuales la FA. Esta tesis sienta las bases sólidas para futuros desarrollos, enfocándose en superar las limitaciones inherentes a la tecnología ECGI y validando su utilidad para evaluar la complejidad de la FA.

# Resum

La fibril·lació auricular (FA) és l'arrítmia més prevalent al món i està associada amb una elevada morbiditat, mortalitat i costos sanitaris. Malgrat els avanços en opcions de tractament farmacològic i teràpies d'ablació, el maneig de la FA encara té marge de millora. La imatge electrocardiogràfica (ECGI) s'ha destacat com un prometedor mètode no invasiu per a avaluar l'electrofisiologia cardíaca i guiar les decisions terapèutiques en casos de fibril·lació auricular. No obstant això, l'ECGI s'enfronta a desafiaments com la necessitat de resoldre de manera precisa el denominat problema invers de la electrocardiografia i d'optimitzar la qualitat de les reconstruccions de ECGI. A més, la integració del ECGI en els processos clínics rutinaris continua sent un repte, en gran manera a causa dels costos que suposa la necessitat d'imatges cardíaques.

Per això, els objectius principals d'aquesta tesi doctoral són impulsar la tecnologia de l'ECGI mitjançant la determinació dels seus requisits tècnics mínims i la millora de les metodologies existents per obtenir senyals d'ECGI precises. A més, busquem avaluar la capacitat de l'ECGI per quantificar de forma no invasiva la complexitat de la FA. Per a aconseguir aquests objectius, s'han dut a terme diversos estudis al llarg de la tesi, des del perfeccionament de l'ECGI fins a l'avaluació de la FA utilitzant aquesta tecnologia.

En primer lloc, hem estudiat els requisits geomètrics i de senyal del problema invers mitjançant l'estudi dels efectes de la densitat de la malla del tors i la distribució d'elèctrodes en la precisió de l'ECGI, el que ha conduït a la identificació del nombre mínim de nodes i la seva distribució en la malla del tors. A més, hem identificat que per obtindre senyals d'ECGI d'alta qualitat, és crucial la correcta disposició dels elèctrodes en la malla del tors reconstruïda. També s'ha definit i avaluat una nova metodologia d'ECGI sense necessitat d'utilitzar tècniques d'imatge cardíaca. Per a això, hem comparat mètriques derivades de l'ECGI calculades amb la geometria original del cor dels pacients amb les mètriques mesurades en diferents geometries cardíaques. Els nostres resultats han mostrat que l'ECGI sense necessitat d'imatges cardíaques és efectiu per a la correcta

quantificació i localització dels patrons i zones que mantenen la FA. Paral·lelament, hem optimitzat la regularització de Tikhonov d'ordre zero actual i l'optimització de la corba L per al càlcul de les senyals d'ECGI, investigant com el soroll elèctric i les incerteses geomètriques influeixen en la regularització. Addicionalment, vam proposar un nou criteri que reforça la precisió de les solucions d'ECGI en escenaris amb incertesa degut a condicions de senyal no ideals.

En segon lloc, en aquesta tesi doctoral, s'han dut a terme múltiples anàlisis relatius a diferents metodologies de processament de senyals i obtenció de mètriques derivades de l'ECGI amb l'objectiu de caracteritzar millor el substrat cardíac i l'activitat reentrant en les senyals d'ECGI de pacients amb FA. Amb l'objectiu d'obtindre una comprensió més profunda dels mecanismes electrofisiològics subjacents a la FA, hem establert l'estratègia de filtrat òptima per extreure patrons reentrants específics del pacient i mètriques derivades de senyals ECGI. A més, hem investigat la reproductibilitat dels mapes de reentrades derivats de les senyals d'ECGI i hem trobat la seva relació amb l'èxit de l'ablació de venes pulmonars (PVI). Els nostres resultats han mostrat que una major reproductibilitat en els patrons reentrants de FA detectats amb ECGI està relacionada amb l'èxit de la PVI, creant una metodologia per estratificar els pacients amb FA abans dels procediments d'ablació.

En conclusió, aquesta tesi doctoral fa una contribució significativa al desenvolupament d'un marc més rigorós i pràctic per a l'ús de l'ECGI en la pràctica clínica, en particular en l'àmbit de la fibril·lació auricular. Els resultats d'aquesta tesi tenen el potencial de millorar l'estratificació dels pacients, la planificació d'una teràpia individualitzada i millorar els resultats dels tractaments actuals de la FA. Aquesta tesi assenta les bases sòlides per a futurs desenvolupaments, centrant-se en superar les limitacions inherents a la tecnologia ECGI i validant la seva utilitat per avaluar la complexitat de la FA.

# Chapter 1

## 1.1. Introduction and motivation

Biomedical engineering has revolutionized contemporary medicine by seamlessly merging engineering ideas with medical practice. This multidisciplinary approach has resulted in extraordinary advances in medical technology, allowing for better diagnosis, treatment, and management of a wide range of medical conditions. In particular, one revolutionary development is the Electrocardiogram (ECG), a non-invasive diagnostic tool that has changed how clinicians monitor and evaluate cardiac electrophysiology since its invention (Einthoven W., 1906). The invention of the electrocardiogram (ECG) and the following advances in cardiac activity measurement and monitoring, such as Body Surface Potential Mapping (BSPM) and Electrocardiographic Imaging (ECGI), have offered invaluable insights into the complex dynamics of cardiac activity.

Atrial fibrillation (AF) is the most common cardiac arrhythmia, affecting millions of people worldwide (Hindricks et al., 2021). The irregular and rapid electrical activity in the atria impairs the heart's ability to pump blood efficiently, leading to increased risks of stroke, heart failure, and other cardiovascular complications. Despite the multiple advances in treatment options, the success rate of pulmonary vein isolation (PVI) ablation, a common intervention for AF, remains suboptimal. This highlights the need for improved patient stratification, personalized treatment planning, and a deeper understanding of the underlying electrophysiological mechanisms of AF to enhance ablation outcomes.

In this respect, Electrocardiographic Imaging is a promising non-invasive technology for assessing cardiac electrophysiology and informing treatment decision-making as it permits a detailed reconstruction of cardiac activity on the cardiac surface. However, ECGI technology still faces several challenges, including accurately resolving the ill-posed inverse problem of electrocardiography and ensuring its clinical implementation (Salinet et al., 2021). Thus, one primary motivation for this PhD thesis is to advance ECGI technology by addressing the geometric and signal requirements for obtaining accurate ECGI-derived maps of cardiac activity. Furthermore, in this thesis we aim to optimize the quality of ECGI reconstructions and investigate the impact of electrical noise and geometrical uncertainties on the resolution of the inverse problem of electrocardiography. This research aims to enhance the accuracy and reliability of ECGI, transforming it into a more powerful tool for clinical applications, especially in the context of atrial fibrillation.

Additionally, the simplification of the ECGI workflow, which is currently hindered by the time-consuming need for cardiac imaging, is one of the main challenges to its integration into clinical workflows. To address this issue, this thesis focuses on the development of a new methodology for imageless ECGI that does not rely on CT or MRI scans. This innovation has the potential to facilitate the introduction of ECGI into daily clinical practice by reducing procedural time and economic costs.

Another driving force behind this research is the improvement of AF complexity quantification in order to improve the sub-optimal outcomes of pulmonary vein isolation. In order to achieve better patient selection for ablation procedures, we will validate the applicability of ECGI in quantifying AF complexity and guiding clinical decision-making. By investigating the optimal signal processing methodologies, and patient ECGI-derived metrics, this thesis aims to better characterize the cardiac substrate and reentrant activity in ECGI signals, which could inform towards the stratification of AF patients. Understanding the reproducibility of these metrics in relation to the success of PVI ablation may offer valuable insights for clinical decision-making and contribute to improved ablation outcomes.

In summary, the motivation for this PhD thesis is to address the demanding needs in the field of AF management by advancing ECGI technology, simplifying its workflow, and demonstrating its potential for quantifying AF complexity. Through these advancements, this research offers a solid foundation for improved patient stratification, personalized treatment planning, and, ultimately, better patient outcomes in the management of AF.

## 1.2. Objectives

This thesis has two main objectives that have been responded to in the articles developed and grouped in the two main sections of this manuscript: to improve the current state-of-the-art methodology of ECGI and to validate its applicability in the quantification of AF complexity.

**Objective 1:** To assess the geometric and signal requirements of the inverse problem of electrocardiography and to quantify the limitations and potential advancements in this technology for the evaluation of atrial fibrillation complexity. This objective is divided into the following points, which will be addressed in the following chapters:

- To determine the impact of torso mesh density and electrode placement in the torso mesh used on the inverse problem resolution in atrial fibrillation signals.
- To assess the robustness of ECGI and derived metrics in atrial fibrillation signals under the displacement of atrial geometry from its correct position.
- To determine the effect of the accuracy of the atrial geometry estimation on the inverse problem of electrocardiography in atrial fibrillation signals.
- To guide the selection of the optimal regularization parameter using the zero-order Tikhonov regularization and L-curve optimization method and to propose an alternative for identifying the optimal regularization parameter when the L-curve corner detection fails.

**Objective 2:** To evaluate the ability of ECGI to quantify atrial fibrillation complexity. This goal is divided into the following objectives, which will be addressed in the subsequent chapters:

- To establish the most appropriate signal processing methodology for evaluating reentrant activity in ECGI signals for the stratification of atrial fibrillation patients.
- To determine the reproducibility of ECGI-derived metrics in atrial fibrillation and its relationship with the success of pulmonary vein ablation.
- To assess the electrical complexity of atrial fibrillation signals in BSPM and its relationship with atrial substrate reentrant analysis using ECGI.

## 1.3. Structure of the thesis

This thesis comprises a collection of articles that address the technical requirements for obtaining high-quality Electrocardiographic Imaging signals and maps for the analysis of atrial fibrillation complexity. In Chapter 1, we introduce the motivation and objectives that underpin this thesis. Chapter 2 presents the state of the art related to the articles compiled in the thesis, providing essential background information and context. Chapters 3 to 5 focus on the improvement of ECGI, outlining the requirements for torso mesh, validating imageless ECGI, and enhancing the most commonly used mathematical methodology for computing ECGI signals. Chapters 6 to 8 present studies that employ ECGI to analyze AF complexity, reproducibility, and patient stratification prior to pulmonary vein isolation. Lastly, Chapters 9 and 10 provide a general conclusion of the studies presented and enumerate all the contributions and academic achievements accomplished during this PhD thesis.

**Chapter 2:** State of the art. This chapter summarizes the key concepts discussed in this thesis. Atrial electrophysiology will be introduced, along with a detailed discussion of atrial fibrillation and pharmacological and ablation treatments. Electrocardiography, body surface potential mapping, and electrocardiographic imaging will be described as non-invasive diagnostic procedures for AF diagnosis. Finally, cardiac mathematical models utilized for AF study will be introduced, ranging from cell to whole body models.

**Chapter 3:** In this chapter, the effects of torso mesh density and electrode distribution on ECGI accuracy are presented. This chapter corresponds to the following publication:

Molero, R., González-Ascaso, A., Hernández-Romero, I., Lundback-Mompó, D., Climent, A. M., and Guillem, M. S. (2022). Effects of torso mesh density and electrode distribution on the accuracy of electrocardiographic imaging during atrial fibrillation. Front. Physiol. 13. doi:10.3389/fphys.2022.908364.

In **Chapter 4,** we examine the robustness of imageless ECGI in the face of uncertainty in atrial morphology and location inside the torso geometry, establishing a new framework for ECGI use without the need for cardiac imaging. This chapter refers to the publication listed below:

Molero, R., González-Ascaso, A., Climent, A. M., and Guillem, M. S. (2023). Robustness of imageless electrocardiographic imaging against uncertainty in atrial morphology and location. J. Electrocardiol. 77, 58–61. doi:10.1016/j.jelectrocard.2022.12.007.

In **Chapter 5,** we present an improved alternative to the obtention of ECGI signals based on a more accurate regularization parameter selection in front of different uncertainties while solving the inverse problem of electrocardiography. This chapter corresponds to the submitted paper:

Molero R. Martínez-Pérez M., Herrero-Martín C., Reventós-Presmanes J., Roca-Luque I. Mont L., Climent A.M., Guillem M.S. Improving electrocardiographic imaging solutions: a comprehensive study on regularization parameter selection with noise considerations in l-curve optimization.

In **Chapter 6,** different post-processing alternatives for ECGI signals for reentrant activity detection are studied in order to improve atrial fibrillation patients' stratification corresponding to the following publication:

Molero, R., Hernández-Romero, I., Climent, A. M., and Guillem, M. S. (2023). Filtering strategies of electrocardiographic imaging signals for stratification of atrial fibrillation patients. Biomed. Signal Process. Control 81, 104438. doi:10.1016/j.bspc.2022.104438.

In **Chapter 7,** we analyze the reproducibility of atrial fibrillation drivers measured on electrocardiographic imaging signals and investigate its relationship with the outcome of pulmonary vein isolation for improving patient stratification. This chapter corresponds to the publication mentioned below:

Molero, R., Soler Torro, J. M., Martínez Alzamora, N., M. Climent, A., and Guillem, M. S. (2021). Higher reproducibility of phase-derived metrics from electrocardiographic imaging during atrial fibrillation in patients remaining in sinus rhythm after pulmonary vein isolation. Comput. Biol. Med. 139, 104934. doi:10.1016/j.compbiomed.2021.104934.

In **Chapter 8,** we present a study of the complexity of AF measured on body surface potentials and analyze its relationship with the epicardial drivers detected on ECGI signals. This chapter is a result of a collaboration with Maastricht University on a research stay conducted during this thesis. This chapter corresponds to the following submitted paper:

Molero R., Meste O., Peeters R., Karel J., Bonizzi P., Guillem M. S., Complexity and recurrence of body surface electrocardiograms correlates with estimated reentrant atrial activity with electrocardiographic imaging in atrial fibrillation patients.

**Chapter 9: General discussion and conclusions.** In this chapter, the overall results of the thesis are discussed and compared with the existing literature. The achieved objectives and findings obtained in this thesis are presented, along with potential future lines of research opened up by this work.

**Chapter 10: Contributions.** This final chapter lists the scientific contributions related to this thesis and obtained from the current dissertation. The scientific framework in which this thesis has been involved, including research stays and projects, are also listed.

# Chapter 2

# State of the art

In this chapter the basis for understanding the context and significance of the research articles compiled in this thesis is presented. It provides an overview of the essential aspects of cardiac electrophysiology, with a specific focus on atrial fibrillation, its diagnosis, evaluation, and treatment options. Additionally, this chapter delves into the crucial techniques used for studying cardiac electrical activity in this research, such as body surface potential mapping and electrocardiographic imaging, and mathematical modelling of cardiac activity. By outlining the current knowledge and advancements in these areas, we aim to establish a solid basis for the subsequent chapters and findings of the thesis.

## 2.1. Introduction to the heart

The heart is a muscular organ located within the thoracic cavity that acts as the core component of the circulatory system. Its primary function is to maintain the efficient distribution of oxygen and essential nutrients through the blood all over the body while also facilitating the elimination of waste products, such as carbon dioxide. The heart's behavior and function are defined by a complex interplay of electrical and mechanical processes, ensuring the rhythmic contractions that result in the adequate circulation of blood. Cardiac contractions are responsible for pumping blood through the four cavities of the heart in a specific sequence: from the body, blood enters the right atrium (RA), then, through the tricuspid valve, it moves to the right ventricle (RV), which pumps it to the lungs for oxygenation. Oxygen-rich blood returns to the left atrium (LA), and flows into the left ventricle (LV) through the mitral valve. Finally, the LV pumps the blood to the rest of the body, delivering oxygen and nutrients.

The complicated link between cardiac contraction, electrical activity, and blood pumping is essential to the heart's function. Pacemaker cells, which have the unique capacity to create and propagate electrical signals independently, are responsible for the electrical activity of the heart.

These impulses cause the heart muscle to contract in a controlled manner, resulting in the mechanical pumping of blood through the circulatory system. Synchronized electrical and mechanical activities are required to maintain a steady and appropriate blood flow to fulfill the metabolic demands of the body.

In a healthy heart, the activation sequence (Figure 2.1.) commences with the sinoatrial (SA) node, commonly referred to as the natural pacemaker. The SA node, which is located in the right atrium, generates electrical impulses that go across the atrial myocardium. The electrical impulse propagation causes the atria to contract, causing the ventricles to fill with blood at the same time. The electrical signal is subsequently sent to the atrioventricular (AV) node, which acts as a vital link between the atria and ventricles. The AV node, which is positioned at the atrioventricular junction, briefly pauses the electrical signal, ensuring that atrial contraction is finished before ventricular contraction begins. The introduced delay by the AV node is critical for optimal ventricular filling and effective cardiac output. Following the AV node, the electrical impulse travels through the bundle of His into the Purkinje fiber system, ensuring synchronized and forceful ventricular contractions for optimal blood flow.

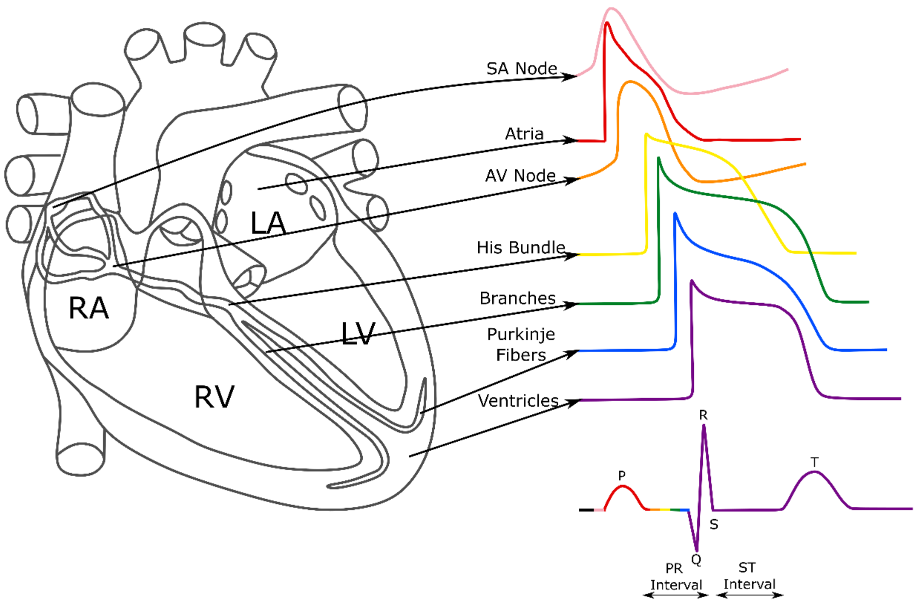

Figure 2.1. Cardiac conduction system and action potential morphology of each of the cells involved in the cardiac cycle and the resulting electrocardiogram. Image adapted from (Cervera, 2012). The cardiac activation sequence starts at the SA followed by the P-wave that corresponds to the activation of the atria, the QRS complex corresponds to the depolarization of the ventricles, and the T-wave that corresponds to the repolarization of the ventricles.

## 2.1.1. Cardiac Action Potential

At the cellular level, cardiac electrical activity is governed by a series of rapid changes in the membrane potential, known as action potentials (AP). Action potentials are the consequence of the interaction between numerous ion channels, transporters, and pumps that keep ions balanced across the cell membrane. The cardiac AP may be split into the following phases, illustrated in Figure 2.2.:

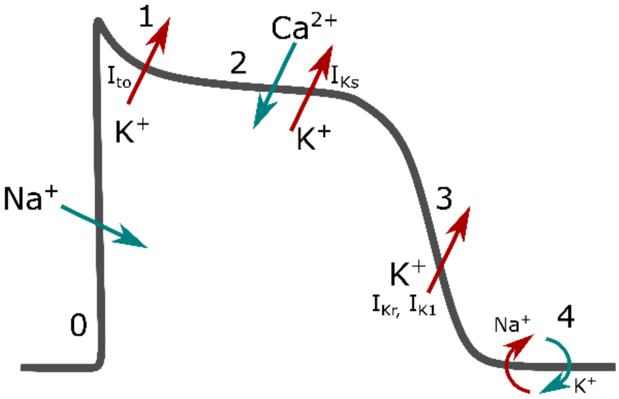

Figure 2.2. Cardiac action potential and the main phases and ionic changes between the intra- and extracellular medium.

- Before the initiation of the action potential, the cardiac cell membrane is at its resting potential. The resting state is characterized by a relatively stable membrane potential that is similar to the equilibrium potential of potassium ions, approximately -85 mV. At this stage, the cell's membrane permeability to potassium ions is significantly greater than its permeability to other ions, resulting in a maintained resting potential.
- Phase 0, or the depolarization phase, is initiated when the membrane potential reaches a threshold value of -40mV, leading to the activation of voltage-gated sodium channels. The quick inflow of sodium ions into the cell creates an abrupt increase in membrane potential.
- Phase 1, a transient outward potassium current ($I_{to}$), causes a small repolarization by allowing potassium ions to exit the cell while the sodium channels become inactivated.
- Phase 2, or the plateau phase, is marked by a balance between the influx of calcium ions through voltage-dependent calcium channels and the outflow of potassium ions through the slow delayed rectifier potassium current ($I_{Ks}$). Phase 2 is critical for sustaining the length of the action potential and enabling enough time for ventricular contraction and blood ejection.

- Phase 3, or the repolarization phase, the inactivation of calcium channels and the activation of additional potassium currents, such as the rapid delayed rectifier potassium current ($I_{Kr}$) and the inward rectifier potassium current ($I_{K1}$), result in a net efflux of potassium ions, restoring the membrane potential to its resting value.
- Phase 4, is the resting membrane potential, which is primarily maintained by the action of the sodium-potassium pump, which exchanges three intracellular sodium ions for two extracellular potassium ions, creating a negative resting membrane potential.

The propagation of electrical activity from one cardiac cell to another is facilitated by specialized cell-to-cell connections called gap junctions. These junctions allow for the rapid and synchronized spread of electrical signals throughout the cardiac tissue, ensuring a well-coordinated contraction of the heart muscle.

### 2.1.2. Cardiac Electrophysiology

Cardiac electrophysiology is the study of the heart's electrical activity, which is responsible for maintaining the normal sinus rhythm. A healthy adult at rest typically presents a heart rate between 60 and 100 beats per minute (bpm). While physiological conditions or external factors may cause normal variations in heart rate, such as bradycardia (rate below 60 bpm) or tachycardia (above 100 bpm), these deviations can be natural responses to exercise, stress, or emotional stimuli.

However, arrhythmias may develop when the heart's electrical activity becomes irregular, uncoordinated, or originates from an abnormal location. Arrhythmias are categorized into two main types: supraventricular and ventricular. Supraventricular arrhythmias arise in the atria or the AV node and encompass atrial fibrillation (AF), atrial flutter (AFl), paroxysmal supraventricular tachycardia, and atrioventricular nodal reentrant tachycardia, among others (January et al., 2014). This thesis will primarily focus on atrial fibrillation and its assessment using noninvasive imaging techniques, which provide crucial information for diagnosing and treating this common supraventricular arrhythmia.

### 2.1.3. Atrial Fibrillation

Atrial fibrillation is the most common sustained cardiac arrhythmia, affecting more than 43 million individuals worldwide (Yamamoto and Trayanova, 2022). It is characterized by rapid and irregular electrical activation of the atria between 300 and 600 activations per minute, leading to a loss of coordinated atrial contraction and an increased risk of various complications, such as stroke and heart failure (Lau et al., 2017; Brugada et al., 2020). The prevalence of AF increases with age, and it is estimated that around 2-4% of the global adult population is affected by this condition, with higher rates observed in the elderly population (Staerk et al., 2017; Benjamin et al., 2019).

Atrial fibrillation can be classified into several types based on the duration and pattern of the arrhythmic episodes (Hindricks et al., 2021). The primary categories are:

- First diagnosed: AF that has never been identified before, regardless of its duration or the presence/severity of AF-related symptoms.
- Paroxysmal Atrial Fibrillation: characterized by episodes of irregular atrial electrical activity that begin suddenly and usually resolve spontaneously within 7 days. These episodes can be symptomatic or asymptomatic and may recur at irregular intervals. Paroxysmal AF is considered a precursor to more persistent forms of the arrhythmia, with some patients progressing to longer-lasting AF over time.
- Persistent Atrial Fibrillation: defined as an arrhythmic episode that lasts longer than 7 days and does not self-terminate. Typically, medical intervention is necessary to restore normal sinus rhythm in this kind of AF, either by pharmaceutical treatment or electrical cardioversion. The progression from paroxysmal to persistent AF is defined by progressive atrial structural remodeling or development of atrial cardiomyopathy (Goette et al., 2016).
- Long-standing Persistent Atrial Fibrillation: characterized by continuous and sustained AF that lasts for more than 12 months. In long-standing persistent AF, multiple attempts to restore normal sinus rhythm may be unsuccessful or only temporarily effective, and the focus of treatment often shifts to rhythm control.
- Permanent Atrial Fibrillation: when AF is considered irreversible, and both the patient and clinician have decided not to pursue further attempts to restore normal sinus rhythm, it is classified as permanent AF. In these cases, treatment is focused primarily on controlling the ventricular rate and preventing thromboembolic complications through anticoagulation therapy.

It is critical to correctly define the kind of atrial fibrillation in each patient since it guides suitable treatment choices and informs prognosis. Clinical guidelines recommend catheter ablation treatments to symptomatic paroxysmal AF patients, however, ablation treatments remain suboptimal. For this reason, the type of AF is not a sufficient criterion for treatment recommendation. A comprehensive understanding of the underlying etiology and risk factors for

AF can further aid in developing personalized therapy strategies, which in turn can help reduce the risk of progression and associated complications.

### 2.1.3.1.Initiation and maintenance of atrial fibrillation

The exact mechanisms underlying the initiation and maintenance of AF are not fully understood and remains an area of active research (Guillem et al., 2016; Schotten et al., 2021). At the cellular level, electrical and structural remodeling, ion channel dysfunction, and alterations in intracellular calcium handling are thought to contribute to the arrhythmogenic substrate. At the tissue level, the presence of fibrosis, inflammation, and heterogeneous conduction properties can lead to a complex and dynamic interplay between functional reentrant circuits and focal drivers, perpetuating the arrhythmia.

Several hypotheses have been proposed to explain the initiation and maintenance of AF (Figure 2.3), including the multiple wavelet hypothesis (Moe and Abildskov, 1959) and the rotor and focal sources hypothesis (Mandapati et al., 2000; Jalife, 2003). The multiple wavelet hypothesis suggests that AF is sustained by numerous reentrant wavelets circulating throughout the atria, with their random interactions and collisions leading to the perpetuation of the arrhythmia. The rotors and focal sources hypothesis, on the other hand, suggests that AF is driven by a smaller number of high-frequency sources, which can be either stable rotors or focal triggers, with the surrounding atrial tissue being activated by these drivers.

### 2.1.3.2.Atrial Fibrillation Diagnosis and Evaluation

Diagnosing atrial fibrillation typically involves a combination of clinical assessment, electrocardiography (ECG), and sometimes additional imaging or monitoring techniques. The ECG is the primary diagnostic tool, as it records the electrical activity of the heart and can reveal the irregular and rapid atrial activity characteristic of AF. Atrial fibrillation is typically characterized by irregular, fast atrial activity without discernible P waves and irregular RR intervals, as evidenced by the ECG (Figure 2.4). The European Society of Cardiology establishes an ECG longer than 30 seconds with no discernible P-waves and irregular RR intervals as a requirement to establish the diagnosis of AF (Hindricks et al., 2021).

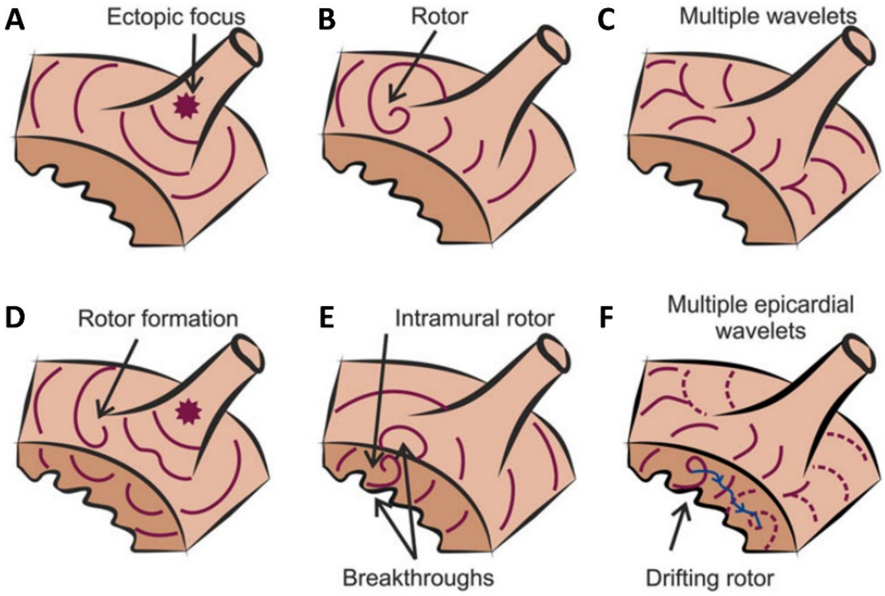

Figure 2.3. Current hypothesis for AF maintenance. From Guillem et al., 2016. (A) Ectopic focus on the pulmonary vein. (B) Example of rotor. (C) Multiple wavelets representation. (D) Rotor formation by an ectopic. (E) Breakthroughs provoked by a transmural rotor. (F) Multiple wavelets provoked by a transmural drifting rotor (blue).

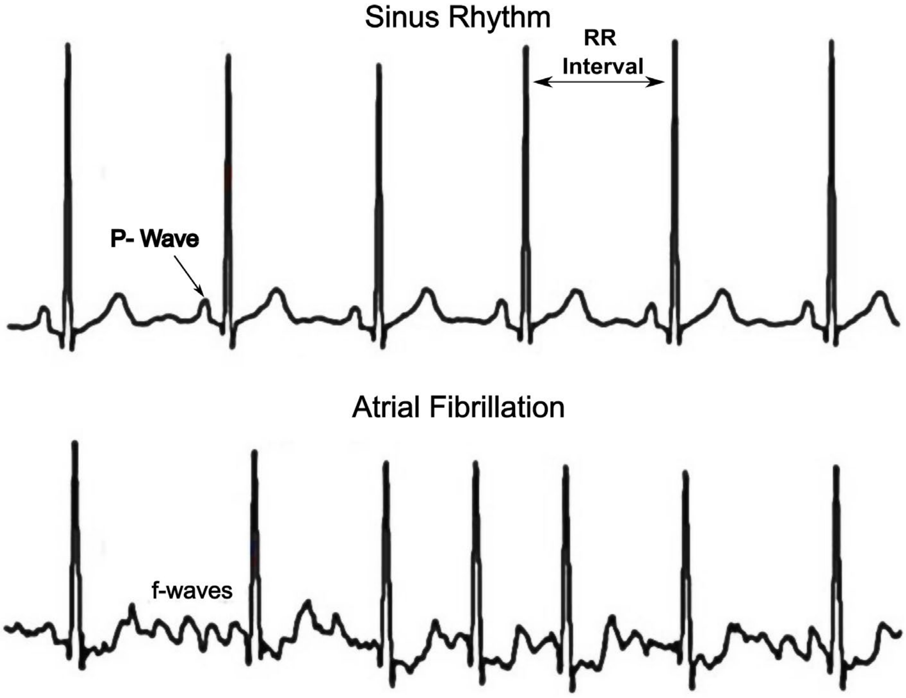

Figure 2.4. ECG of a sinus rhythm and atrial fibrillation signal. Adapted from *(Guillem, 2008)*

In addition to the traditional diagnostic tools, there exist multiple technologies available that help to AF screening before confirming a diagnosis. Wearable devices as smartwatches (Turakhia et al., 2019), smartphone photoplethysmography, wearable belts, etc., are becoming essential tools for the early diagnosis of AF and other cardiac arrhythmias (Hindricks et al., 2021).

### 2.1.3.3.Clinical Management of Atrial Fibrillation

Treatment strategies for AF typically revolve around three main objectives: anticoagulation, rate control, and rhythm control (Hindricks et al., 2021).

- Anticoagulant drugs act as a prevention barrier for stroke episodes provoked by thromboembolic complications. AF patients are evaluated based on valvulopathies and stroke risk with the $CHA_2DS_2$-VASc (Lip et al., 2010) and HAS-BLED scores (Pisters et al., 2010) before the anticoagulant prescription. There are two types of oral anticoagulants: vitamin K antagonists (VKAs), such as warfarin, and non-vitamin K antagonist oral anticoagulants (NOACs), which include dabigatran, rivaroxaban, apixaban, and edoxaban. NOACs have acquired general acceptance since their pharmacokinetics are more predictable, they have fewer pharmacological and food interactions, and they have a demonstrated reduced risk of cerebral hemorrhages (Ruff et al., 2014).
- Rate control aims to slow down the ventricular response to the rapid atrial activity, often using medications such as β-blockers, calcium channel blockers, digoxin, or combination therapy. The need for rate control in AF patients is diagnosed based on the comorbidities of the patients, the symptoms, and the failure of rhythm control (Van Gelder et al., 2016).
- Rhythm control involves the use of antiarrhythmic drugs (AADs) to restore and maintain normal sinus rhythm and improve the quality of life of symptomatic AF patients (Sethi et al., 2017). Based on their mechanism of action, AADs are divided into four major classes: class I (sodium channel blockers), class II (β-blockers), class III (potassium channel blockers), and class IV (calcium channel blockers). The type of AAD used is determined by the patient's clinical profile, the existence of structural heart disease, and the risk of adverse effects. Amiodarone, flecainide, propafenone, sotalol, and dronedarone are some of the most regularly utilized AADs for rhythm regulation in AF. In addition to pharmacological rhythm control, external cardioversion is an alternative to pharmacological cardioversion for hemodynamically unstable patients and in emergency situations.

### 2.1.3.4.Catheter ablation in atrial fibrillation

While some patients may experience a resolution of their symptomatic AF with appropriate treatment, a definitive cure for the condition remains elusive. Catheter ablation, in particular, has shown promise in achieving long-term freedom from AF in selected patients and a superior alternative to antiarrhythmic drugs (Jaïs et al., 2008). The primary goal of AF ablation is to eliminate the triggers and substrate that maintain the arrhythmia, thus restoring and maintaining normal sinus rhythm.

Catheter ablation is a minimally invasive procedure that is used to target and isolate the pulmonary veins (Fig. 2.5A) (Haïssaguerre et al., 1998). Pulmonary vein isolation (PVI) has been demonstrated to be effective in the treatment of paroxysmal AF, with success rates ranging from 60% to 80% (Calkins et al., 2012, 2017). Lower success rates (from 43% to 69%) of PVI-only ablation have been found for persistent AF patients (Clarnette et al., 2018).

The large differences between the percentages of successful PVI interventions with freedom of arrhythmia are mainly associated to the progression of AF and the subsequent cardiac remodeling. In order to improve PVI outcomes in more advanced stages of AF, additional anatomical structures and AF drivers are targeted. These include posterior wall isolation, left atrial appendage (LAA) and superior vena cava (SVC) isolation, and driver-guided ablation (Fig. 2.5B-D) among others.

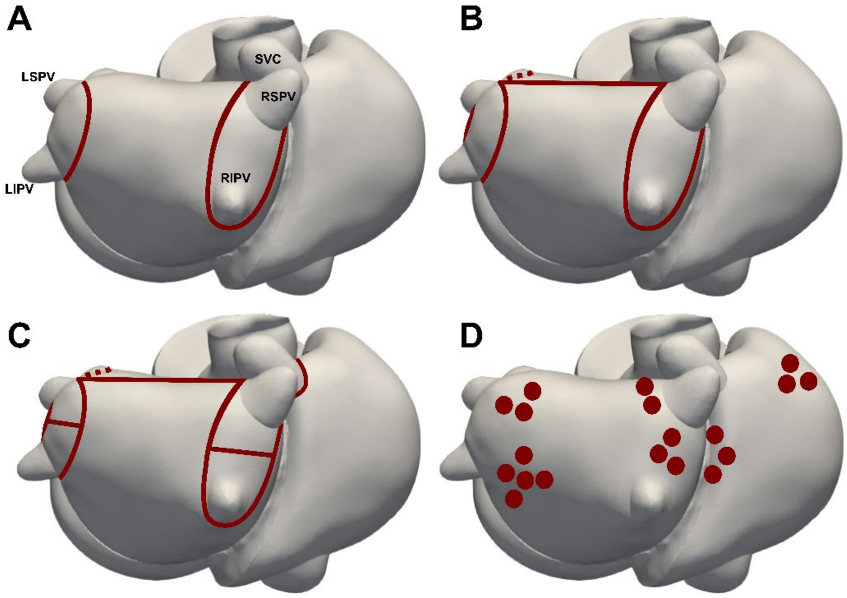

Figure 2.5. Representation of the typical lesions employed in AF ablation. A. Circumferential pulmonary vein isolation. B. Addition of roof line ablation and mitral isthmus line. C. Addition of linear ablation between pulmonary veins and superior vena cava isolation. D. Driver ablation.

In addition to PVI, posterior wall isolation is performed in nearly of 40% of repeated ablations (Calkins et al., 2017), but there is a lack of evidence that it improves ablation outcomes compared to PVI only due to inconsistent results (Kim et al., 2015). Several studies discussed the benefits of LAA isolation (Parameswaran et al., 2021), with randomized clinical trials as the BELIEF study (Di Biase et al., 2016) showing a 20% of outcome improvements compared to PVI only. Isolation of other anatomical structures as SVC has not been demonstrated to improve ablation outcomes, as analysed by systematic reviews (Sharma et al., 2017).

Dominant frequency ablation has also tried to improve the clinical outcomes of PVI. In first studies of Atienza et al. (2009), they ablated regions of high dominant frequencies (HDF) with radiofrequency catheters (Fig. 2.6A). In this study, the authors predicted sinus rhythm maintenance based on the observed elimination of DF gradients during the ablation procedure. Despite it has been demonstrated the acute AF termination after ablating HDF sites (Sanders et al., 2005), later randomized trials showed comparable results to PVI only, with no additional benefits (Atienza et al., 2014).

The existence of high-frequency rotors observed in the isolated heart (Jalife, 2003) has led to including rotor ablation as a strategy for AF termination. Narayan et al. (2013) led the trials on focal impulse rotor modulation (FIRM) using a 64-lead basket catheter that mapped the atrial surface and detected and ablated stable rotors in both atria with increasing the outcome compared to PVI-only (Fig. 2.6B). Nevertheless, there is still controversy on rotor ablation due to no incremental benefit demonstrated in clinical trials (Terricabras et al., 2020). The existence of new noninvasive mapping technologies as electrocardiographic imaging, has lead into multiple studies of rotor ablation as the AFACART study (Knecht et al., 2017) with improvement on the number of persistent AF patients free from AF up to 76.8% 12 months after the ablation.

Further approaches as the ablation of complex fractionated atrial electrogram (CFAE) ablation (Fig. 2.6.C) target areas with complex and disorganized electrical activity and low voltage areas (Nademanee et al., 2004). CFAE ablation has been implemented rapidly by multiple centers in clinical practice but with no additional benefit demonstrated (Vogler et al., 2015). Moreover, it has been stated that CFAE ablation has proarrhythmic consequences due to the extension of the ablated tissue that may affect the final clinical outcomes on the ablation (Parameswaran et al., 2021).

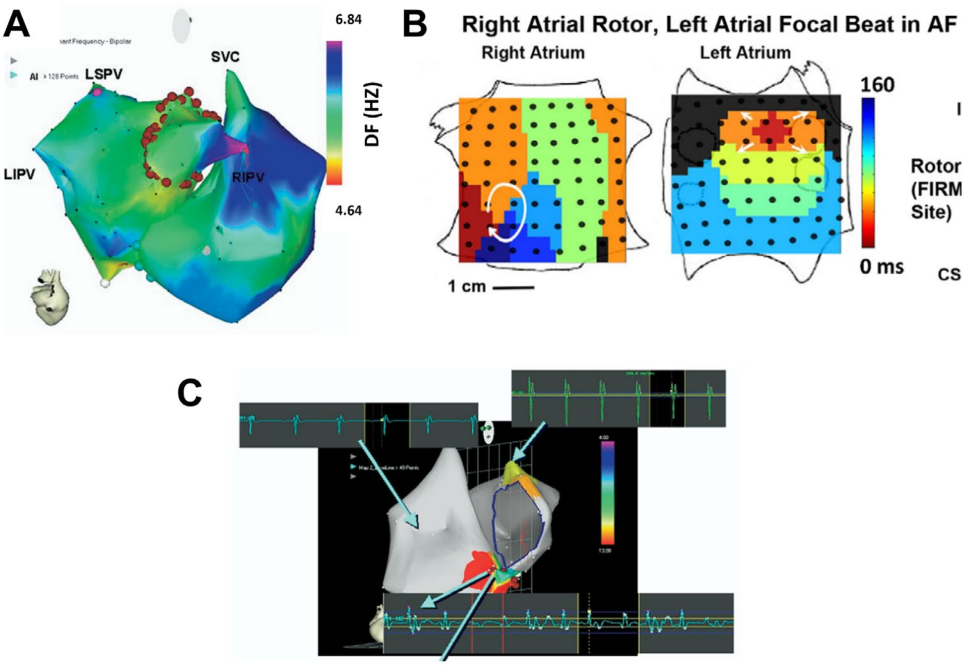

Figure 2.6. A. Intracardiac dominant frequency map from (Atienza et al., 2009) of a paroxysmal AF patient with a detection of a HDF on the right superior pulmonary vein. B. FIRM map from (Narayan et al., 2013) of a rotor detected on the right atrium and a focal source detected on the left atrium C. Biatrial CFAE map from (Nademanee et al., 2006): red color representing the areas that have the most persistent CFAEs, whereas the gray areas represent part of the atrium that have no CFAEs.

Fibrosis identification by late gadolinium enhancement MRI (LGE-MRI) permits the inclusion of this information in the ablation procedures providing more information about the atrial substrate. Nevertheless, randomized trials such as the DECAAF-II (Marrouche et al., 2022) or ALICIA (Bisbal et al., 2020) trials with fibrosis-guided ablation did not improve ablation outcomes compared to PVI-only ablation. The main limitation of fibrosis ablation is that it is strongly dependent of the threshold used in the imaging segmentation of the scar quantification (Harrison et al., 2014).

It is essential to note that AF ablation carries some risks, such as vascular access complications, cardiac tamponade, and pulmonary vein stenosis, among others. Furthermore, the attempts of improving PVI-only outcomes by isolating additional atrial structures and ablating AF drivers are still controversial methods with contradictory indications in the literature. Therefore, a careful patient selection and a thorough pre-procedural evaluation are critical factors in achieving favorable ablation outcomes and minimizing complications.

## 2.2. The electrocardiogram

The electrocardiogram (ECG) is a widely used, noninvasive diagnostic tool for assessing cardiac electrical activity. It was first introduced by Willem Einthoven in the early 20th century (Einthoven, 1906) and has become an essential tool in the diagnosis and management of various cardiac conditions, including arrhythmias, myocardial ischemia, and infarction.

The ECG consists of a set of electrodes used to record the electrical signals generated by the heart as they propagate through the body. ECG signals are detected by electrodes placed on the patient's skin in specific locations. The limb electrodes are placed on the right and left arms and left leg, while the precordial leads (V1-V6) are placed on the patient's chest in a specific location depicted in Fig. 2.7.

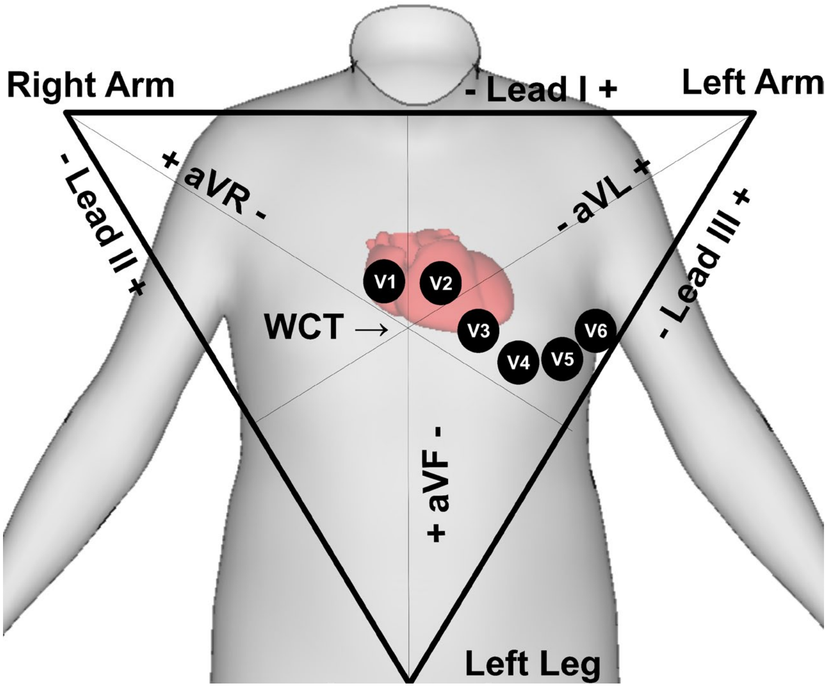

Figure 2.7. Representation of the 12-Lead ECG and Einthoven's triangle. Leads I, II, and III are located on the three edges of the triangle, while the augmented leads (aVR, aVL, and aVF) are positioned between the vertex and midpoint of each side. The potential difference between every precordial recording site and the Wilson Central Terminal (WCT), which represents the average potential of the vertices in the Einthoven triangle, is utilized to establish the precordial leads (V1-V6).

Limb leads (I, II, and III) define a triangle with the heart in the center named Einthoven's triangle. By subtracting the electrical activity recorded on the limbs, the 3 first ECG leads are defined. Additionally, the augmented leads (aVR, aVL, and aVF) show the augmented electrical activity of lead I to III by measuring the difference in electrical potential between one limb electrode and a reference point, known as Wilson's central terminal. The Wilson's central terminal is a calculated reference point derived from the average of the potentials measured by the three limb electrodes. Finally, the precordial leads (V1 to V6) are used to register the electrical potential between each precordial electrode and the Wilson's central terminal, they allow a better assessment of the anterior and lateral regions of the heart.

Each lead of the 12-lead ECG gives a distinct perspective on the electrical activity of the heart, allowing for the diagnosis of various abnormalities in various areas of the heart. It is an essential tool for clinicians that can identify arrhythmias, ischemia, infarction, and other heart disorders by studying ECG waveforms.

## 2.3. Body Surface Potential Mapping

The conventional 12-lead ECG is a valuable tool in clinical practice for arrhythmia diagnosis, yet it may not be sufficient for characterizing complex arrhythmias. The characterization of arrythmias with more complex electrical patterns requires a major number of leads distributed across the torso for its proper quantification because the multiple wavefronts present cannot always be observed in the 12-lead ECG, and require a more comprehensive coverage for an accurate assessment (Taccardi, 1963). Furthermore, the increased surface covered by BSPM electrodes increases the surface with a preferential projection from the atria, since the 12-lead ECG preferentially shows the ventricular activation.

Body Surface Potential Mapping (BSPM) is a noninvasive electrocardiographic technique that involves the use of multiple electrodes distributed across the patient's torso to record cardiac electrical activity. The minimal number of electrodes for the correct quantification of arrhythmias using BSPM has been set between 23 and 30 leads (Lux et al., 1978; de la Guillem et al., 2009). Nevertheless, the usual number of electrodes used with this technology ranges between 32 and 256 electrodes. An example of BSPM representation of the electrical propagation registered through the torso at a time instant is presented in Figure 2.8.:

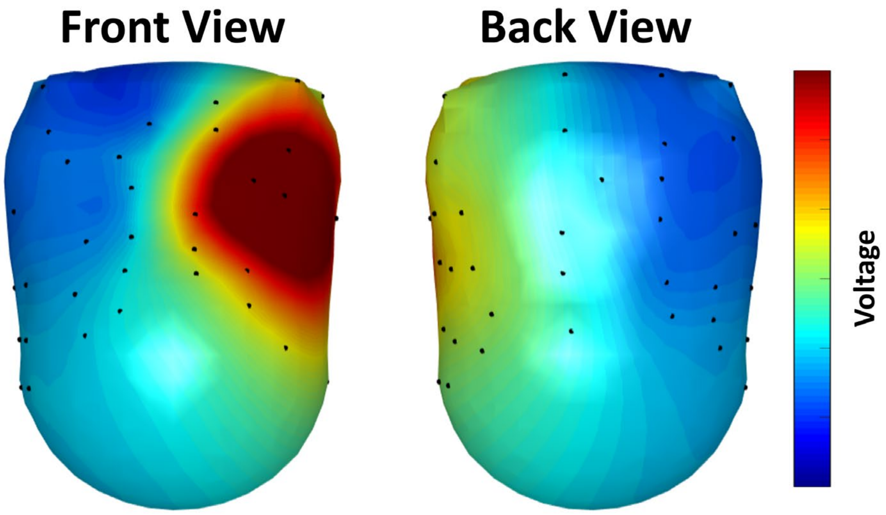

Figure 2.8. Representation of 64-lead BSPM potentials in a time instant on a patient's torso reconstructed with photogrammetry. Black dots represent the electrode location.

### 2.3.1. Body Surface Potential Mapping in atrial fibrillation

Several studies have demonstrated the utility of BSPM in identifying the sources of atrial fibrillation. In 2009, Guillem et al. showed that atrial propagation patterns can be identified in the BSPM maps. Later, Guillem et al. (2013) demonstrated that it is possible to characterize AF with BSPM recordings and identify the atrium with the highest frequency (Fig. 2.9A). Besides, the DFs identified by BSPM were comparable to the DFs obtained with intracardiac recordings with a correlation higher than 0.92. In addition, in 2014, Rodrigo et al. showed the ability of BSPM for the identification of AF reentrant drivers after band-pass filtering the signals at the HDF (Fig. 2.9B). These studies demonstrated that it is possible to find AF drivers non-invasively with more regional information than the standard 12-lead ECG.

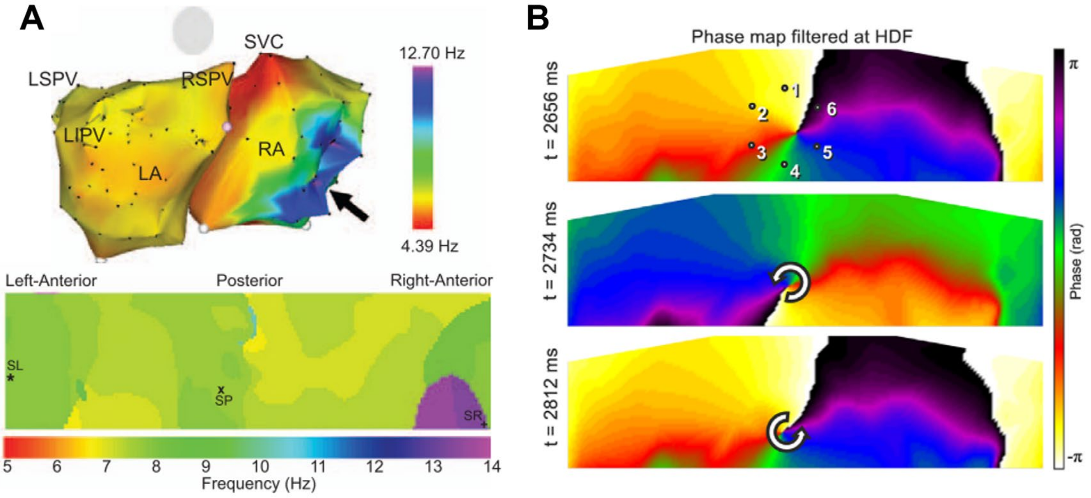

Figure 2.9. A. Intracardiac dominant frequency map and equivalent BSPM showing the highest DF at the right atrium adapted from *(Guillem et al., 2013)*. B. Identification of atrial fibrillation rotors on BSPM, adapted from *(Rodrigo et al., 2014)* .

Additionally, several studies have used BSPM for a wider evaluation of atrial substrate during AF, analyzing the complexity of AF signals and linking them to the AF progression, demonstrating its power to discriminate between short- and long-term AF (Bonizzi et al., 2014). Furthermore, BSPM has been used for patient stratification for ablation treatments, showing its power for AF ablation outcome prediction (AUC = 0.7) (Meo et al., 2018). The latest BSPM studies address the analysis of the signals in order to detect the repetitiveness of the AF dynamics, with the aim of better characterizing and understanding AF and its electrical propagation , while establishing a correlation with the AF substrate and electro-structural remodeling (Bonizzi et al., 2020).

## 2.4. Electrocardiographic Imaging

Electrocardiographic Imaging (ECGI) is a noninvasive cardiac imaging technique that combines body surface potential mapping with imaging data of the heart and torso to reconstruct the electrical activity on the heart's surface (Fig. 2.10), providing more cardiac regional information compared to BSPM. For computing ECGI, a realistic torso geometry from the patient can be obtained through segmentation of MRI or CT scan images, or by using more contemporary techniques such as photogrammetry (Remondino, 2004). Similarly, cardiac geometry can be derived from the segmentation of MRI or CT scan images.

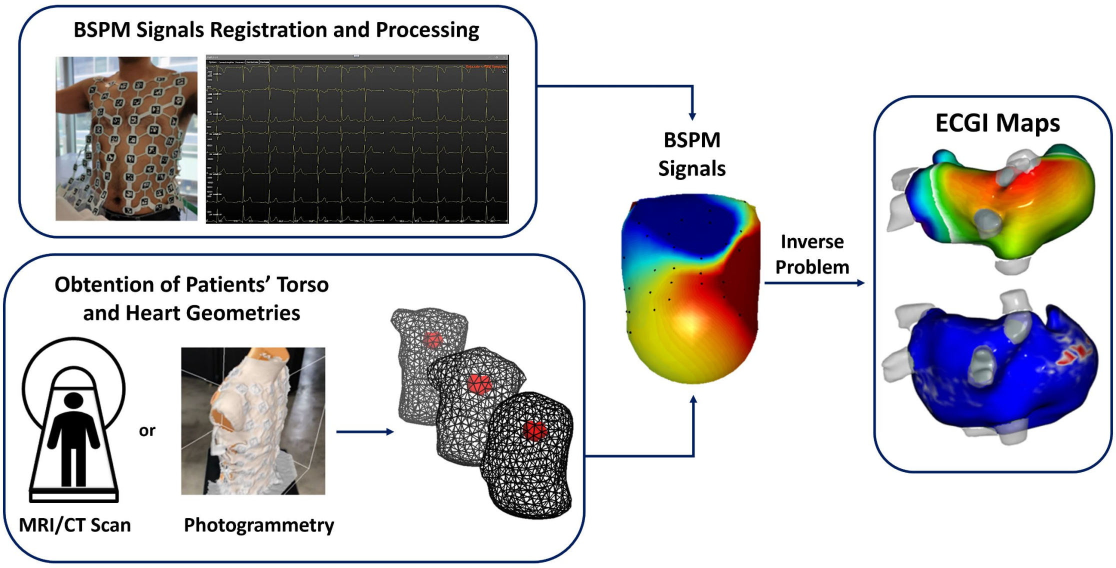

Figure 2.10. Scheme with the steps for the acquisition of ECGI signals. Acquisition of BSPM signals with the obtention of the patient's torso and heart geometries used to obtain ECGI maps that represent the epicardial atrial activity.

ECGI has shown promising results in the diagnosis, evaluation, and treatment of various cardiac arrhythmias, including atrial fibrillation. ECGI offers increased spatial resolution compared to invasive mapping, enabling a better understanding of the underlying mechanisms of arrhythmias, and facilitating the development of targeted treatment strategies. In the following subsections the forward and inverse problems are described in order to understand the mathematical workflow necessary to obtain ECGI signals.

## 2.4.1. Forward Problem of electrocardiography

The forward problem in ECGI involves modeling the relationship between the cardiac electrical activity on the heart's surface and the potential distribution on the body's surface (MacLeod and Buist, 2010). In order to adequately tackle this problem, a description of the heart and body surfaces, accounting for the distinct conductivities of the anatomical structures between the heart and torso surface, as well as the tissue conductivities of each of these regions, is necessary (Horáček and Clements, 1997). The relationship between the heart (X) and torso potentials (Y) can be defined by a transfer matrix (A) (Barr and Spach, 1977) as in Equation 1. The matrix A is not dependent on the electrical activity, and it is typically considered to be time-invariant and is not generally squared, hence it is not invertible (Pullan et al., 2014).

$$\mathrm{Y} = \mathrm{AX} \tag{1}$$

In this context, the matrix A can be computed using different methodologies as the finite element method (FEM) (Wang et al., 2010), the boundary element method (BEM) (MacLeod and Buist, 2010), and the method of fundamental solutions (MFS) (Wang and Rudy, 2006).

BEM and FEM approaches need topological links between nodes to transform Laplace's equation into a surface integral form using Green's theorem. Because BEM is based on surface integrals, boundary potentials are discretized and considered to be built as linear combinations of fundamental functions (Barr and Spach, 1977; Fischer et al., 1999). The comparison between BEM and FEM to ECG problems has shown that with equal degrees of discretization, BEM produces fewer mistakes and uses less computing time than FEM, and for this reason is more widely used (Hernández-Romero et al., 2023). In the context of this thesis, BEM was utilized for the computation of both the forward and inverse problems. Matrix A was computed as described in the following equation:

$$A = [D_{TT} - G_{TH} G_{HH}^{-1} D_{HT}]^{-1} \cdot [G_{TH} G_{HH} D_{HH} - D_{TH}] \tag{2}$$

where D is the coefficient matrix that represents the contribution of the potential of a bounding surface to another, G is the coefficient matrix representing the contribution of the voltage gradient between two surfaces, the subindex T refers to the surface of the torso, and H the surface of the heart (Pedrón Torrecilla et al., 2015).

## 2.4.2. Inverse Problem of electrocardiography

The inverse problem of electrocardiography refers to the process of the reconstruction of electrical activity on the heart's surface using recorded body surface potentials. This is a mathematically ill-posed problem, which means that minor inaccuracies in the input data can lead to considerable errors in the reconstructed solution. To address this issue, many regularization approaches, such as Tikhonov regularization and L-curve optimization, have been developed to stabilize the inverse solution (Tikhonov and Arsenin, 1977). Tikhonov regularization has been widely used for the obtention of ECGI signals, especially for atrial fibrillation (Salinet et al., 2021; Hernández-Romero et al., 2023) and consists in minimizing Equation 3:

$$\hat{X} = \mathrm{argmin}[||AX - Y||_2^2 + \lambda|LX||_2^2] \tag{3}$$

Where $\hat{X}$ are the estimated epicardial potentials, X are the epicardial potentials, A is the transfer matrix that relates the epicardial potentials and the BSPM signals, Y are the surface potentials, λ is a regularization parameter, and L is a squared matrix which can take different formulations and defines the order of Tikhonov regularization. For zero-order Tikhonov, L equals the identity matrix and imposes a limit on the magnitude of the solution. For first-order Tikhonov, L equals the gradient operator, and for second-order of Tikhonov equals the Laplacian surface operator, providing a less smooth inverse solution (Pullan et al., 2014).

Multiple approaches have been applied for computing ECGI signals, like the Generalized Minimal Residual method (Calvetti et al., 2002), singular value decomposition (Figuera et al., 2016), iterative approaches (Van Oosterom and Van Dam, 2005; Borràs and Chamorro-Servent, 2021), and hybrid combinations between Tikhonov-GMRes methods (Ramanathan et al., 2003). However, Zero-order Tikhonov regularization has been used and compared with other regularization alternatives, but the vast majority of the studies using atrial signals use this regularization approach (Salinet et al., 2021).

The λ value can be chosen by multiple approaches. One of the most common approaches is L-curve optimization (Hansen, 1992), which consists in selecting the value that reflects a trade-off in the minimization of the two terms in equation 3 or, practically by selecting the corner of the curve resulting from displaying term $||AX - Y||_2^2$ vs. term $||LX||_2^2$ (Pullan et al., 2014). The larger the regularization parameter, the more aggressive smoothing of the estimated potentials, which results in a better rejection of noise at the expense of reduced temporal and spatial resolution (Fig. 2.11).

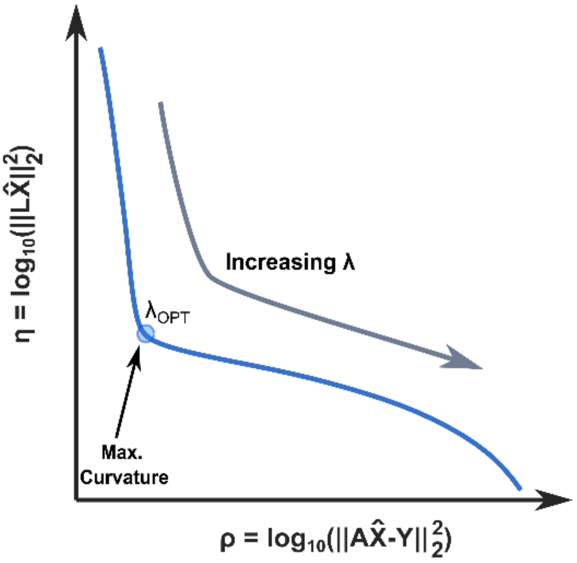

Figure 2.11. Illustration of the L-curve optimization. For each regularization parameter, the logarithmic values of the observed errors from the solution (horizontal) and the residual errors (vertical) are shown (Hansen and O’Leary, 1993). The best regularization parameter value is in the corner (point of maximum curvature) of the L-curve.

### 2.4.3. ECGI for atrial fibrillation

Electrocardiographic imaging has emerged as a valuable tool for identifying atrial fibrillation drivers and guiding clinical therapy. ECGI enables non-invasive acquisition of electrical propagation maps, which are highly valuable for detecting AF drivers. Given the rapid and unstable nature of atrial activity in this arrhythmia, ECGI holds a clear advantage over intracardiac mapping. ECGI can capture higher spatial resolution maps in a shorter time frame, eliminating the need for progressive catheter mapping, which has lower resolution and requires more time to generate a map, thereby prolonging the ablation procedure.

Frequency analysis of ECGI signals provides information of the activation rate of the atrial tissue, which is valuable for understanding AF mechanisms helping the noninvasive identification of atrial regions that sustain AF. The ability of ECGI to detect HDF regions has been demonstrated in mathematical simulations and in real data (Pedrón-Torrecilla et al., 2016). Despite some limitations in the obtention of the DFs relative to false harmonic detection as the real DF, ECGI has been demonstrated as a reliable tool for DF detection with good correlation with intracavitary data (Fig. 2.12A) (Rodrigo et al., 2021).

In addition to spectral analysis, phase mapping is a widely used technique in ECGI for identifying reentries (Zlochiver et al., 2008; Rodrigo et al., 2017a). By encoding different cardiac cycle stages with phase values between -π and π, it provides a description of the electrical state during activation cycles. Phase mapping and reentrant activity detection, as well as the DF analysis, has been validated with intracardiac data (Fig. 2.12B) with good correlation in the location of the reentries on the atrial surface (Rodrigo et al., 2020).

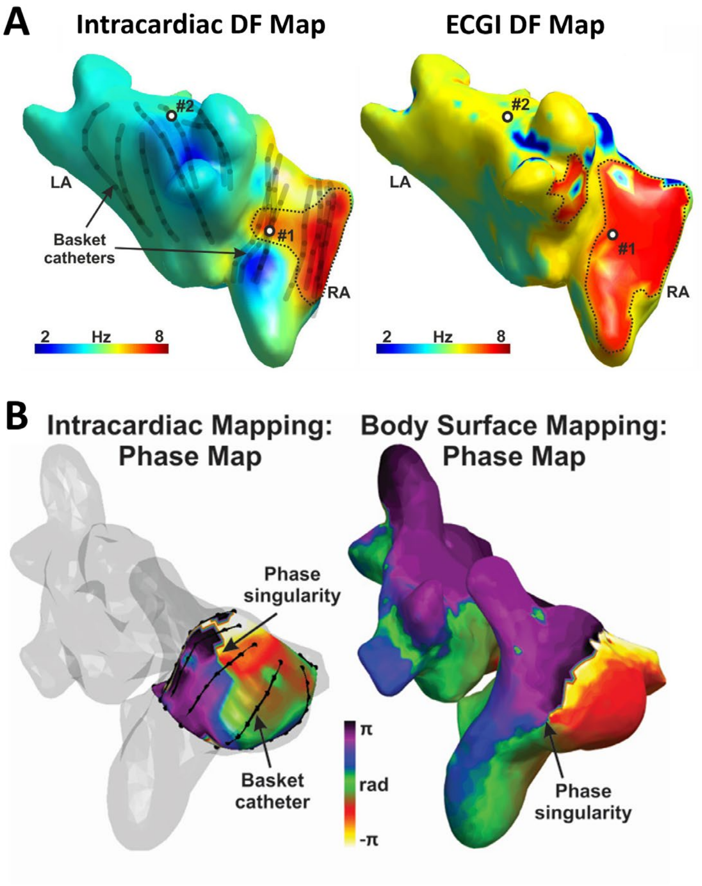

Figure 2.12. A. Dominant frequency of intracardiac and ECGI maps adapted from *(Rodrigo et al., 2021)* B. Phase singularity of intracardiac and ECGI phase maps, adapted from (Rodrigo et al., 2020)

Several investigations have found ECGI to be a reliable method for detecting and localizing reentrant activity in the atria in order to guide AF ablations (Cuculich et al., 2010; Haissaguerre et al., 2013, 2014), see Fig. 2.13. ECGI has also been used for patient stratification, revealing differences in driver locations between patients with acute termination and those with unsuccessful termination outcomes (Gao et al., 2019). More recent studies have explored the potential of preoperative noninvasive mapping for the characterization of AF in combination with other ablation procedures to personalize interventions in combined cardiac surgeries (Ehrlich et al., 2019; Osorio- Jaramillo et al., 2020). The most recent studies confirm the ability of ECGI to improve ablation outcomes of AF patients by guiding the ablation of extra-pulmonary sources (Honarbakhsh et al., 2022).

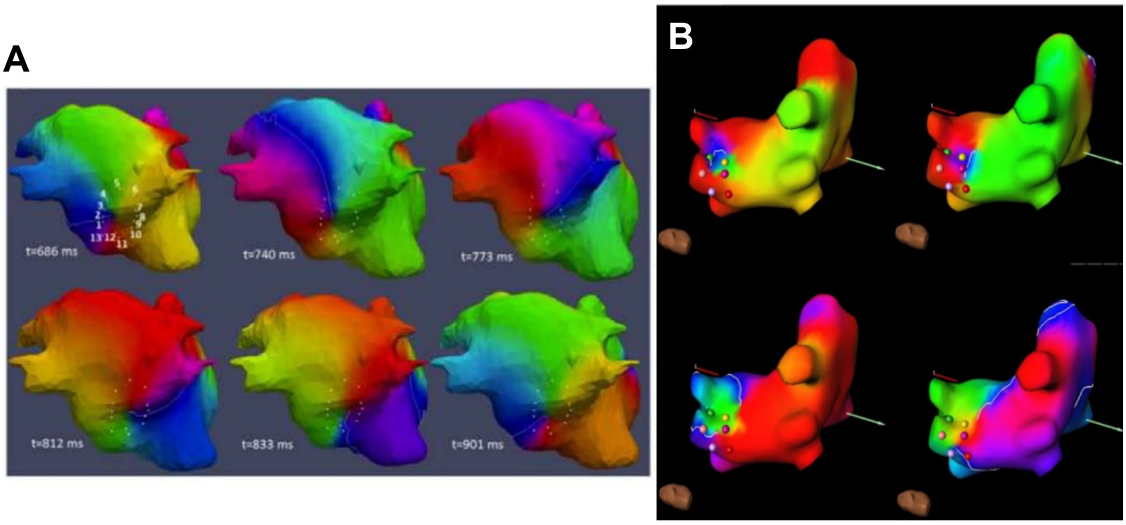

Figure 2.13. A. ECGI phase maps showing a clockwise rotor in the posterior left atrial wall (Haissaguerre et al., 2014). B. Sequential views of a rotational potential driver originating from the left superior pulmonary vein as shown on the ECGI prior PVI, (Dhillon et al., 2022).

In addition to ECGI, its application combined with structural information, such as fibrosis data collected from late gadolinium MRI images, has shown potential in finding reentrant activity surrounding fibrotic regions (Roney et al., 2016; Cochet et al., 2018). Moreover, modeling patient fibrosis and combining it with ECGI has shown better results in AF characterization (Boyle et al., 2018), which could improve therapy guidance.

Despite the demonstrated usefulness of ECGI in identifying relevant AF drivers and its potential in guiding ablation therapy, ECGI is not typically used for guiding ablation procedures due to challenges such as the need for collecting and analyzing BSPM signals, additional time and cost, trained personnel, the AF irregularity, and the use of ionizing radiation in CT scans or compatible equipment in MRI cases for the obtention of heart geometry. Nevertheless, ECGI has proven to be valuable in identifying AF drivers and has the potential to become a standard tool in ablation procedures.

## 2.5. Cardiac Modelling

Cardiac mathematical modeling is a powerful tool in the study and understanding of atrial fibrillation and other cardiac arrhythmias. By employing mathematical models and computer simulations, we can investigate the underlying mechanisms of AF, develop new diagnostic and therapeutic strategies, predict patient-specific outcomes and evaluate and develop new algorithms for the development noninvasive techniques as ECGI.

### 2.5.1. Cellular level modelling

At the cellular level, mathematical models of cardiac cells can help elucidate the electrophysiological processes responsible for the initiation and maintenance of AF. In 1952, Hodgkin and Huxley, presented the first mathematical model that describes the electrical activity of a cell (Fig. 2.14). Their work laid the foundation for understanding the ionic mechanisms underlying the generation and propagation of action potentials in excitable cells, including cardiac cells.

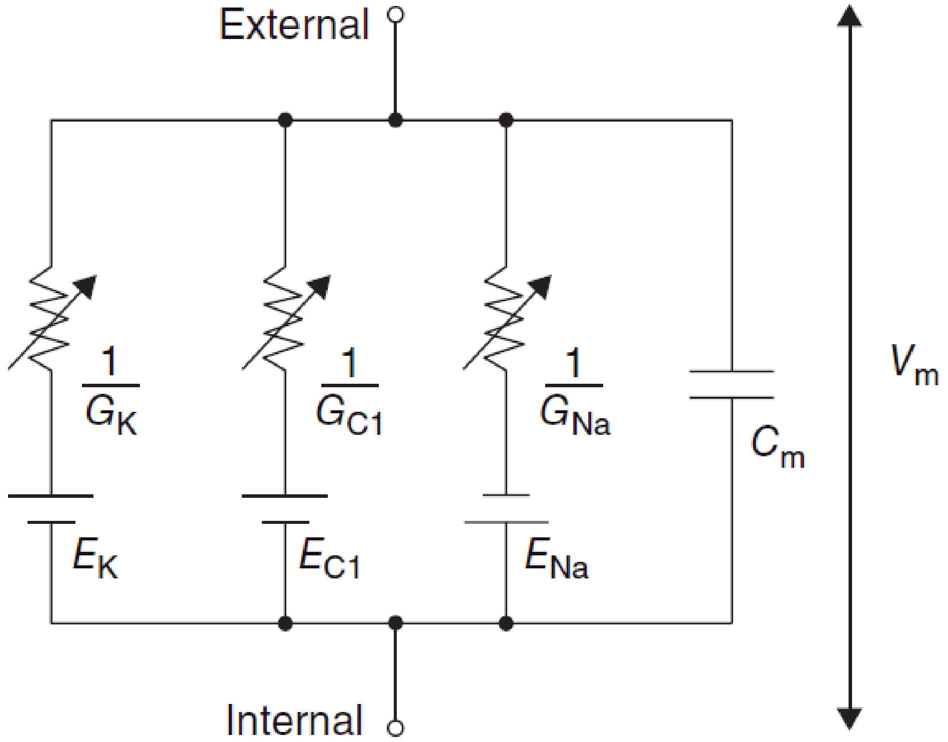

Figure 2.14. Cell model from Hodgkin and Huxley, extracted from (Jalife et al. 2009). Membrane voltage (Vm) is determined by the charge of the membrane capacitor (Cm), which is controlled by the ionic channels (represented as variable resistors or conductances) that represent the various ionic currents.

Since then, numerous mathematical models have been developed to represent various types of cardiac cells, such as atrial, ventricular, and pacemaker cells. In 1962, Noble adapted the Hodgkin and Huxley model to cardiac Purkinje and pacemaker cells. Noble's adaptation has been posteriorly improved due to the characterization in multiple patch-clamp studies of the ionic currents of the channels involved in the development of the action potential of cardiac cells. With the experimental characterization, the models started to incorporate more detailed equations that describe the activity of the ion channels, pumps, and exchangers responsible for the flow of ions across the cell membrane.

### 2.5.2. Atrial cell mathematical models

Over the last decades, multiple models of atrial cell electrophysiology have been developed to better understand the action potential dynamics (Dössel et al., 2012). The two primary models from Courtemanche et al. (1998) and Nygren et al. (1998) are used to reconstruct the action potential using differential equations based on experimental data from non-human mammals. Maleckar et al. (2008), re-implemented the Nygren model improving the description of ion currents relative to repolarization. Later, Koivumäki et al., (2011) presented a model that accounted for the atrial spatiotemporal characteristic of the sarcoplasmic reticulum, extending the Nygren and Maleckar's models. The same year, Grandi et al., (2011) presented a model that incorporated experimental data that describes intracellular calcium ions and introduced β-adrenergic and cholinergic regulation of cellular function to the regime of human atrial cell models. A comparison of these models was done by Wilhelms et al., (2013), describing and assessing the singularities of each of them (Fig. 2.15).

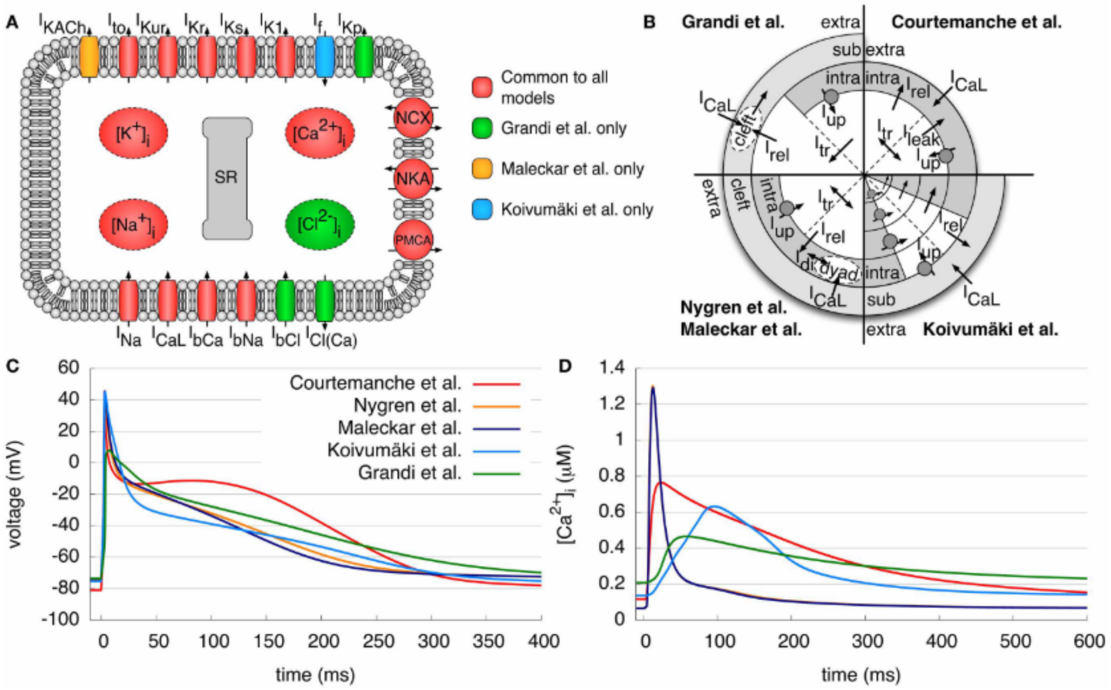

Figure 2.15. Models of human atrial electrophysiology, (Wilhelms et al., 2013). (A) Cell membrane schematic with various predicted ionic currents and intracellular ion concentrations. (B) Diagram of calcium management with several compartments and model currents. (C) APs and intracellular calcium concentrations (D) after 50 seconds of pacing with a BCL of 1 second.

### 2.5.3. Tissue level modelling

In recent years, multiscale modeling approaches have emerged, integrating cellular models with tissue and whole-heart models to provide a comprehensive understanding of AF dynamics. These approaches enable the investigation of the interplay between cellular processes and macroscopic phenomena, such as wave propagation and reentrant activity, which are critical in sustaining AF.

The behavior of electrical propagation through the tissue can be modeled using reaction-diffusion models, which allow the computation of the current received by each atrial cardiomyocyte from the connected neighboring simulated cells. A critical aspect of tissue-level modeling in atrial fibrillation is accounting for the anisotropy of the cardiac tissue.

Two common approaches for modeling electrical propagation in cardiac tissue are the monodomain and bidomain models. The monodomain model is represented by a single partial differential equation (PDE) that describes the electrical propagation in the tissue with equal anisotropy ratios:

$$\nabla \cdot (\sigma \nabla \mathrm{V_m}) = \beta \left(\mathrm{C_m} \frac{\mathrm{dV}_m}{dt} + \mathrm{I_{ion}}\right) \tag{5}$$

where σ is the conductivity tensor, $C_m$ is the membrane capacitor, $V_m$ is the transmembrane potential, β is the membrane surface-to-volume ratio, and $I_{ion}$ represents the sum of the ionic current (Dössel et al., 2012).

On the other hand, the bidomain model is more complex and takes into account the separate intra- and extracellular domains within the cardiac tissue. The bidomain model consists of two coupled PDEs:

$$\nabla \cdot (\sigma_i \nabla \mathrm{V}_i) = \beta (\mathrm{I}_m - \mathrm{I}_{se}) \tag{6}$$

$$\nabla \cdot (\sigma_e \nabla \mathrm{V}_e) = -\beta (\mathrm{I}_m - \mathrm{I}_{si}) \tag{7}$$

where $\sigma_i$ and $\sigma_e$ are the intracellular and extracellular conductivity tensors, respectively, $V_i$ and $V_e$ are the intracellular and extracellular potentials, $I_m$ the transmembrane current and $I_{se}$ and $I_{si}$ the extra- and intracellular externally applied current sources (Dössel et al., 2012).

Both models consider the electrical current ions of neighboring cells, but the monodomain model is easier to solve and consequently faster (Colli Franzone et al., 2005). On the contrary, bidomain simulations must be used to study more complex situations as electrical cardioversion (Trayanova, 2006).

In addition to understand better the behavior of atrial tissue and the use of the mathematical models for pharmacological research between others, tissue-level models are essential for the development of ECGI research. Multiple studies have used atrial-level models in other to validate regularization algorithms (Figuera et al., 2016; Cámara-Vázquez et al., 2021) and develop and validate post-processing methodologies for noninvasive driver detection (Pedrón-Torrecilla et al., 2016; Rodrigo et al., 2017b; Boyle et al., 2018). In this thesis, we utilized atrial mathematical simulations using Kouvimäki's model for atrial electrophysiology and the monodomain approach to model the electrical propagation through the cardiac tissue, as it offers a balance between computational efficiency and the level of detail necessary to accurately simulate the behavior of the atrial tissue during arrhythmias.

## 2.5.4. Geometrical models

Modeling the whole atria in 3D involves creating a geometric representation of the atrial anatomy and defining the spatial distribution of the electrophysiological properties, such as cell types, fiber orientation, and regional heterogeneities (Fig. 2.16). This information can be obtained from medical imaging techniques, such as MRI (Krueger et al., 2014; Boyle et al., 2018) or CT scans (Hwang et al., 2014).

Compared to the ventricles, the atrial wall thickness permits the use of both simplified monolayer (Jacquemet et al., 2006) or bilayer models (Qu et al., 2016) and more complex volumetric meshes with nodes along the atrial wall (Gonzales et al., 2013). Furthermore, geometric models of the atria can be further enhanced by incorporating information on fiber orientation, which significantly influences the electrical propagation in the tissue. Techniques like diffusion tensor imaging (DTI) can provide valuable data on fiber orientation and can be integrated into the atrial models to improve their accuracy (Krueger et al., 2011). Additionally, the inclusion of fibrosis data in the models can provide valuable insights into the role of structural remodeling in AF to better represent the heterogeneity of the atrial tissue (Boyle et al., 2019).

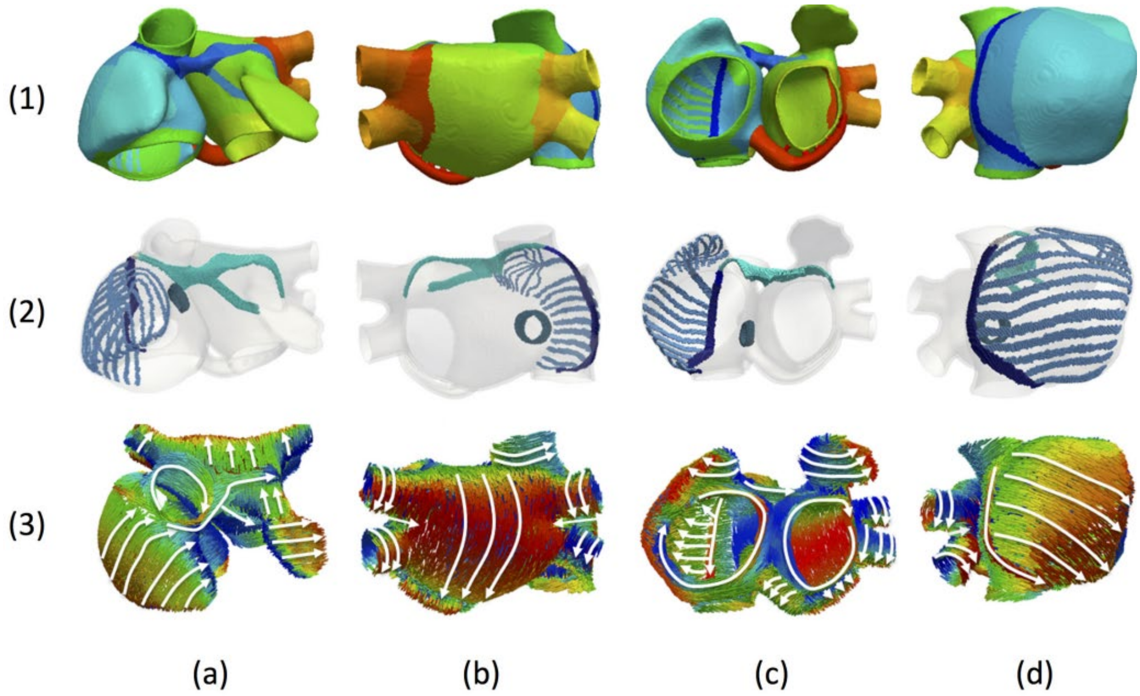

Figure 2.16. Example of a detailed 3D human atrial model from *(Ferrer et al., 2015)*. (1) 21 atrial regions divided in colors. (2) Preferential conduction bundles. (3) Principal fiber direction.

Besides, geometrical models serve a crucial role in testing the efficacy of ablation therapies (Aslanidi et al., 2011). The significance of the pulmonary veins in AF has led to further exploration of simulated ablations in studies focused on the left atrium (Verma et al., 2020; Roney et al., 2022a, 2022b). The use of detailed patient-specific geometrical models is focused on optimizing treatment strategies tailored to individual patients (Aronis et al., 2019). Although personalized models offer great utility in creating patient-specific simulations, shape uncertainty can impact the prediction of reentries, emphasizing the importance of anatomical accuracy for accurate simulations (Corrado et al., 2023). Conversely, large-scale in-silico studies may benefit from a greater number of less detailed geometries provided by shape models, enabling a broader investigation of atrial arrhythmias (Nagel et al., 2021).

# Compendium of articles

# Chapter 3

## Effects of Torso Mesh Density and Electrode Distribution on the Accuracy of Electrocardiographic Imaging During Atrial Fibrillation

Rubén Molero[1]*, Ana González-Ascaso[1], Ismael Hernández-Romero[1], David Lundback-Mompó[2], Andreu M. Climent[1], María S. Guillem[1]

## Abstract

**Introduction:** Electrocardiographic Imaging (ECGI) allows computing the electrical activity in the heart non-invasively using geometrical information of the patient and multiple body surface signals. In the present study we investigate the influence of the number of nodes of geometrical meshes and recording ECG electrodes distribution to compute ECGI during atrial fibrillation (AF).

**Methods:** Torso meshes from 100 to 2000 nodes heterogeneously and homogeneously distributed were compared. Signals from nine AF realistic mathematical simulations were used for computing the ECGI. Results for each torso mesh were compared with the ECGI computed with a 4000 nodes reference torso. In addition, real AF recordings from 25 AF patients were used to compute ECGI in torso meshes from 100 to 1000 nodes. Results were compared with a reference torso of 2000 nodes. Torsos were remeshed either by reducing the number of nodes while maximizing the overall shape preservation and then assigning the location of the electrodes as the closest node in the new mesh or by forcing the remesher to place a node at each electrode location. Correlation coefficients, relative difference measurements and relative difference of dominant frequencies were computed to evaluate the impact on signal morphology of each torso mesh.

**Results:** For remeshed torsos where electrodes match with a geometrical node in the mesh, all mesh densities presented similar results. On the other hand, in torsos with electrodes assigned to closest nodes in remeshed geometries performance metrics were dependent on mesh densities, with correlation coefficients ranging from 0.53 ± 0.06 to 0.92 ± 0.04 in simulations or from 0.42 ± 0.38 to 0.89 ± 0.2 in patients. Dominant frequency relative errors showed the same trend with values from 1.14 ± 0.26 to 0.55 ± 0.21 Hz in simulations and from 0.91 ± 0.56 to 0.45 ± 0.41 Hz in patients.

**Conclusion:** The effect of mesh density in ECGI is minimal when the location of the electrode is preserved as a node in the mesh. Torso meshes constructed without imposing electrodes to constitute nodes in the torso geometry should contain at least 400 nodes homogeneously distributed so that a distance between nodes is below 4cm.

---

R. Molero, A. González-Ascaso, I. Hernández-Romero, D. Lundback-Mompó, A. M. Climent, and M. S. Guillem, “Effects of torso mesh density and electrode distribution on the accuracy of electrocardiographic imaging during atrial fibrillation,” *Front. Physiol.*, vol. 13, 2022.

[1] ITACA Institute, Universitat Politècnica de València, València, Spain

[2] Corify Care SL, Madrid, Spain

## 3.1. Introduction

Electrocardiographic imaging (ECGI) is a non-invasive technique that can be used to estimate the electrical activity of the heart from surface electrocardiographic signals. ECGI offers multiple clinical applications, such as ablation guidance in atrial fibrillation (AF) patients. ECGI requires to use torso and heart geometries together with electrical recordings from the patient. Firstly, surface electrodes placed over the torso are used to record electrical signals. Additionally, the heart geometry is usually obtained from medical images (magnetic resonance imaging or axial computerized tomography) (Salinet et al., 2021), and the torso geometry can be derived from photogrammetry (Rodrigo et al., 2018), with latter reconstruction creating triangular or polygonal meshes (van der Graaf et al., 2016). Once these elements are acquired, the inverse problem can be solved and epicardial potentials are estimated, which can be used to compute dominant frequencies or rotor-related metrics (Rodrigo et al., 2017a).

The properties of the 3D torso geometry have been proven to affect the calculation of the ECGI. Accurate reconstructions (Messinger-Rapport and Rudy, 1990) of the anatomy of the patient's body and the use of real dimensions in the torso model (Jamison et al., 2011) show more precise results. Incorporation of inner organs into the geometry of the problem has not shown a major impact on the shape of ECGI potentials (Ramanathan and Rudy, 2001). However, additional geometrical effects should be carefully considered in order to achieve a sufficient resolution.

The objective of this study is to evaluate the repercussion of the number of nodes of the torso geometry mesh and their distribution on the resolution of the ECGI using both AF simulations and real recordings from AF patients. We hypothesized that there is an effect on the ECGI reconstruction quality related to the number of nodes on the torso mesh used independently of the number of ECG electrodes that record the signal. A careful analysis will allow us to establish a threshold to ensure good performance while keeping the computing time as low as possible. We studied two different remeshing situations based on the positioning of body surface electrodes. The first was maintaining the electrodes in the original position while remeshing the rest of the torso to quantify the effect of mesh density and distribution on the morphology of ECGI signals, and our second remeshing alternative was to remesh the whole torso surface to maximize resemblance between original and remeshed volumes, and then we reassign the electrode nodes as those with the smallest Euclidean distance between the original and remeshed torso geometries, in order to quantify the effect of electrode displacement as a consequence of remeshing. We compared the electrocardiographic signals (ECGI) using time metrics: the Pearson's correlation coefficient (CC), the relative difference measurement (RDM*) and errors in dominant frequency estimation. To obtain the ECGI potentials, we used real torso geometries from AF patients with different geometrical resolutions, 9 electrophysiological AF simulations, and 25 ECGI recordings from AF patients.

## 3.2. Materials and methods

To analyze the effect related with node variations of torso geometry on the ECGI, we first created the torso models with different numbers and distribution of nodes, then computed the respective inverse electrograms, and finally compared the results using time metrics (CC and RDM*) and dominant frequencies related maps and metrics.

### 3.2.1. Study population - Data acquisition

#### 3.2.1.1.Simulation data

Cardiac electrophysiological simulations lasting for 10 seconds included in this study were created using the same cardiac geometry and different AF episodes. A realistic 3D model of the atrial anatomy composed of 284,578 nodes and 1,353,783 tetrahedrons was used for creating the simulations (Rodrigo et al., 2017b). Variation of ionic current parameters was introduced in Ik,ACH, IK1, INa and ICaL to simulate electrical remodeling and allow the maintenance of atrial fibrillation. Fibrotic tissue was modeled by disconnecting a percentage of nodes between 20% and 60% and scar tissue by disconnecting 100% of nodes in the scar region. The system of differential equations was solved by using Runge–Kutta integration on a graphic processors unit (NVIDIA Tesla C2075 6G), (Rodrigo et al., 2017b). AF was induced by implementing an S1 S2 protocol, with the S2 stimulus applied at different locations in the atria, thus producing different AF patterns.

#### 3.2.1.2.Patient data

The electrical recordings from 25 atrial fibrillation patients from Hospital Gregorio Marañón, Madrid, Spain (Ethics Committee Approval 475/14) described elsewhere (Rodrigo et al., 2020), (Molero et al., 2021) were used. To record the signals 57 electrodes distributed on the torso of the patients were employed. The atrial geometries were also obtained from the same patients using Magnetic Resonance Imaging, and the 3D models were segmented through ITK-Snap (Yushkevich et al., 2006) and Autodesk Meshmixer (Schmidt and Singh, 2010). Furthermore, the torso models were obtained from photogrammetry, and 3D geometries consisting of triangular meshes were constructed (Remondino, 2004) and refined with Autodesk Meshmixer.

## 3.2.2. Data processing

### 3.2.2.1.Torso remeshing

In order to evaluate the effect of torso mesh density on the morphology of the electrograms after resolution of the inverse problem of electrocardiography, we constructed torso meshes with a reduced number of nodes departing from the finest torso meshes available. We used as reference the torso meshes constructed for each patient, constituted of at least 2000 nodes. The epicardial potentials computed for each of the electrophysiological models were placed in the same position as the original heart inside the thorax. In order to calculate body surface potentials for the computer model simulations, we chose 10 different patient meshes of 4000 nodes. An inhomogeneous remeshing of torso geometries down to 100, 200, 400, 500, and 1000 nodes for patients (plus a 2000 nodes mesh for cardiac simulations), maximizing shape preservation was performed with MATLAB built-in functions (see Figure 3.1A). In order to quantify the impact on ECGI resolution of the homogeneity of the distance of the nodes in the mesh, we also constructed meshes with a homogeneous distribution of nodes based on an iterative approach (Manu, 2022) (see Figure 3.1B). Properties of the different torso meshes used with simulations and patients are displayed in Figure 3.2 and 3.3, respectively.

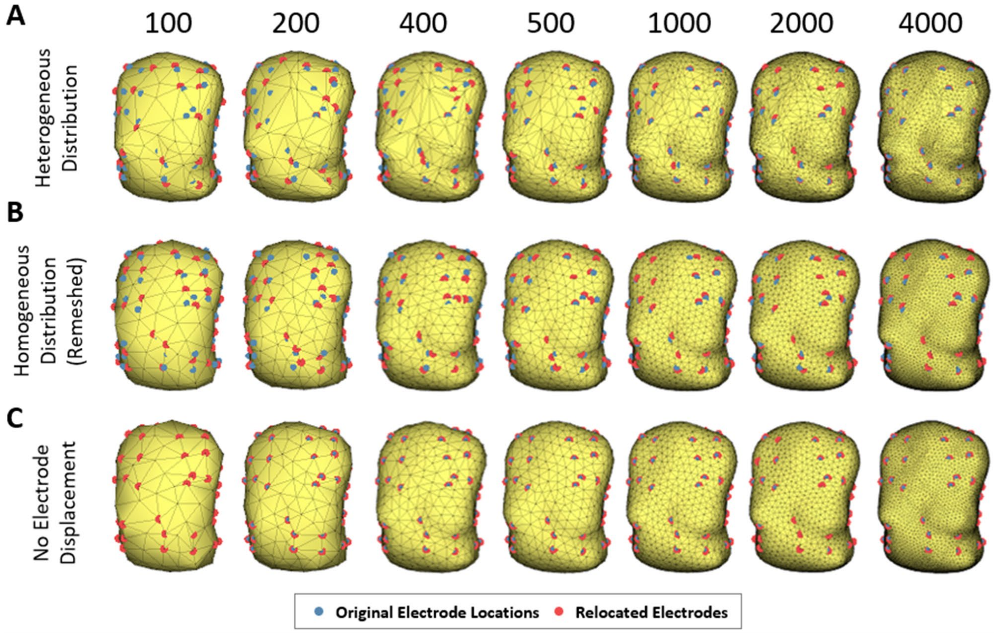

Figure 3.1. Example of torso models with different number of nodes and node distribution. The electrodes relocated appear in blue and the original locations in red. Panel A illustrates torsos with irregular mesh distribution, B with homogeneous distribution and C torsos maintaining the electrodes in the original position.

For solving the inverse problem of electrocardiography, electrodes have to be located in the torso mesh. We chose the node with the smallest Euclidean distance from each electrode to relocate electrodes on the mesh. In order to evaluate separately the effect of mesh density and electrode relocation, we also constructed downsampled meshes without electrode relocation. For imposing the electrode position in all the meshes, the closest face of the geometry to each electrode was triangulated again, and three new triangles were included joined by the original electrode position (see Figure 3.1C).

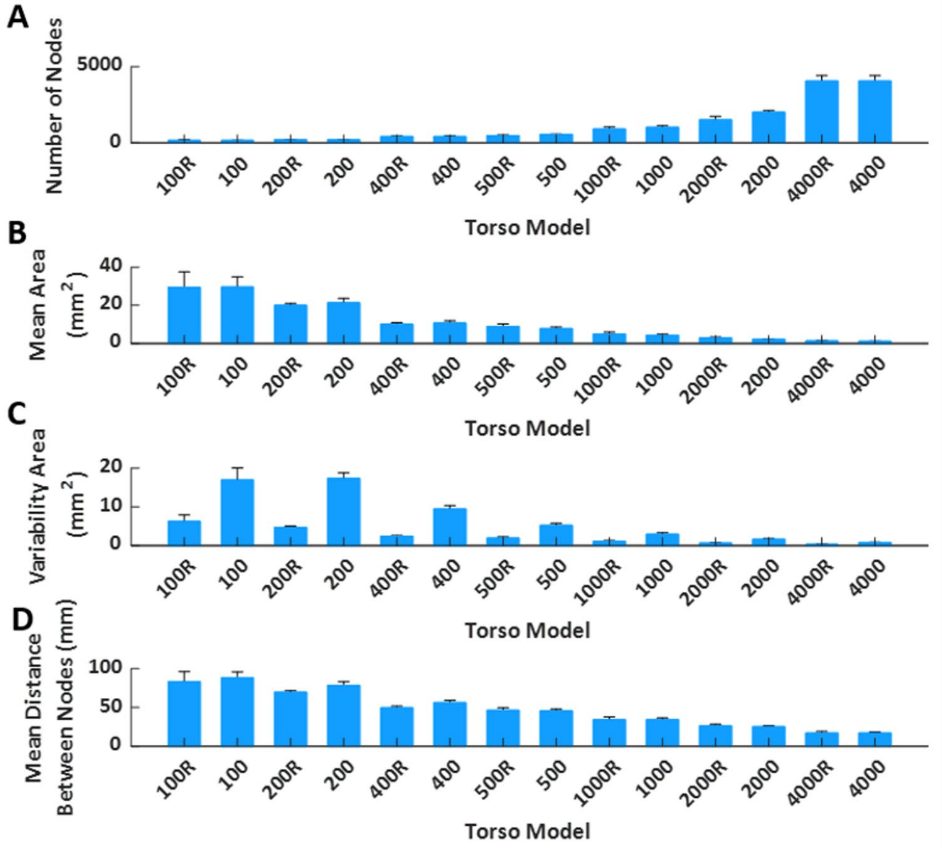

Figure 3.2. Mean value and standard deviation of torso model properties of the geometries used in the simulation study represented. A. Mean number of nodes depending on the model. B. Mean area of the faces. C. Variability of the area of the faces. D. Mean distance between nodes of the same triangle.

#### 3.2.2.2. Processing of Surface Potentials and ECGI calculation

In mathematical models, the forward problem of the simulated electrograms was calculated using the boundary element method (BEM) (Pedrón-Torrecilla et al., 2016). Noise was added to the computed surface potentials to obtain a 20dB signal to noise ratio emulating the noise present in real recordings. The baseline was subtracted, and a low pass filter of 40Hz was applied. The electrical information related to the nodes representing the 57 electrodes was selected, and the inverse problem was calculated through the BEM, using zero-order Tikhonov regularization and L-curve optimization (Pedrón-Torrecilla et al., 2016).

Body surface signals obtained from each patient with surface electrodes were pre-processed by selecting 5 seconds and removing the baseline. A 10th order Butterworth was used to band-pass filter between 2 and 45 Hz to eliminate the noise. The Principal Component Analysis (PCA) approach was performed electrode by electrode to cancel the ventricular activity (QRST segment), (Castells et al., 2005).

Once the recorded or simulated body surface signals were processed, the inverse computed electrograms were calculated through BEM using zero-order Tikhonov regularization and L-curve optimization (Pedrón-Torrecilla et al., 2016).

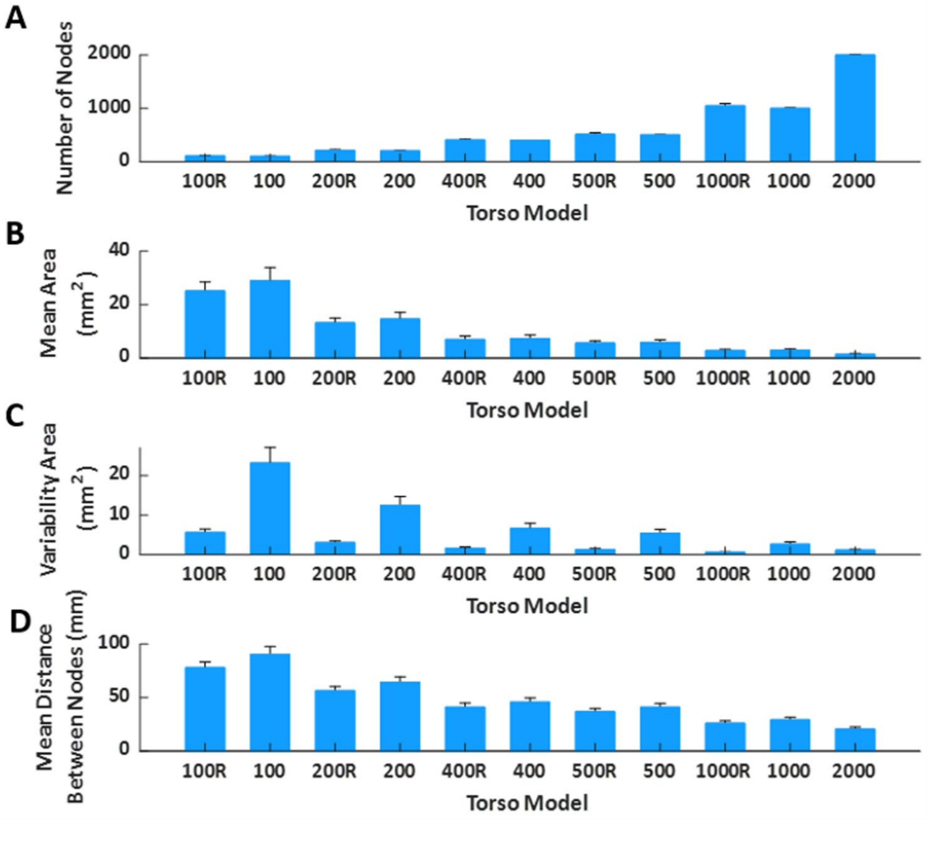

Figure 3.3. Mean value and standard deviation of torso model properties of the geometries used in the real patient’s study. A. Mean number of nodes depending on the model. B. Mean area of the faces. C. Variability of the area of the faces. D. Mean distance between nodes of the same triangle.

### 3.2.3. Quality of mesh evaluation metrics

To evaluate the effect of the mesh in the reconstruction of ECGI potentials, the similarity between ECGI signals obtained with finest and sparser torso meshes was evaluated.

Specifically, we used Pearson's correlation coefficient (CC) and the relative difference measurement (RDM*) (Meijs et al., 1989, Figuera et al., 2016). For both metrics, the temporal version was used (for each node, the CC and RDM* were computed using all the time instants, and the mean and standard deviation across nodes are then calculated).

$$\mathrm{RDM}^{*} = \sqrt{\sum_{k} \left( \frac{x_k}{\|x^2\|} - \frac{\hat{x}_k}{\|\hat{x}^2\|} \right)^2}$$

### 3.2.4. Frequency metrics

The dominant frequency (DF) of each node of the cardiac geometry was estimated after the calculation of ECGI using Welch periodogram (2-second Hamming window with a 25% overlap) (Rodrigo et al., 2017a). The absolute difference in DF for each atrial node between the reference and the other models was calculated for both AF simulations and AF patient studies (Figuera et al., 2016).

## 3.3. Results

### 3.3.1. Impact of mesh density on ECGI reconstruction

Mesh density alone -without electrode relocation- had a limited impact on ECGI signals. In Figure 3.4A, reconstructed signals with different mesh densities for a sample epicardial node show only subtle differences. Average correlation coefficients remain above 0.96 even for torso meshes with just 100 nodes, and relative errors are below 0.3%, with the lowest CC values of 0.93, Fig. 3.4.B-C. The effect of the torso's node density in the dominant frequencies is depicted in Figure 3.4.D. The observed absolute error decreases with the number of nodes of the mesh, and errors are stabilized below 0.2 Hz with torso meshes with at least 400 nodes.

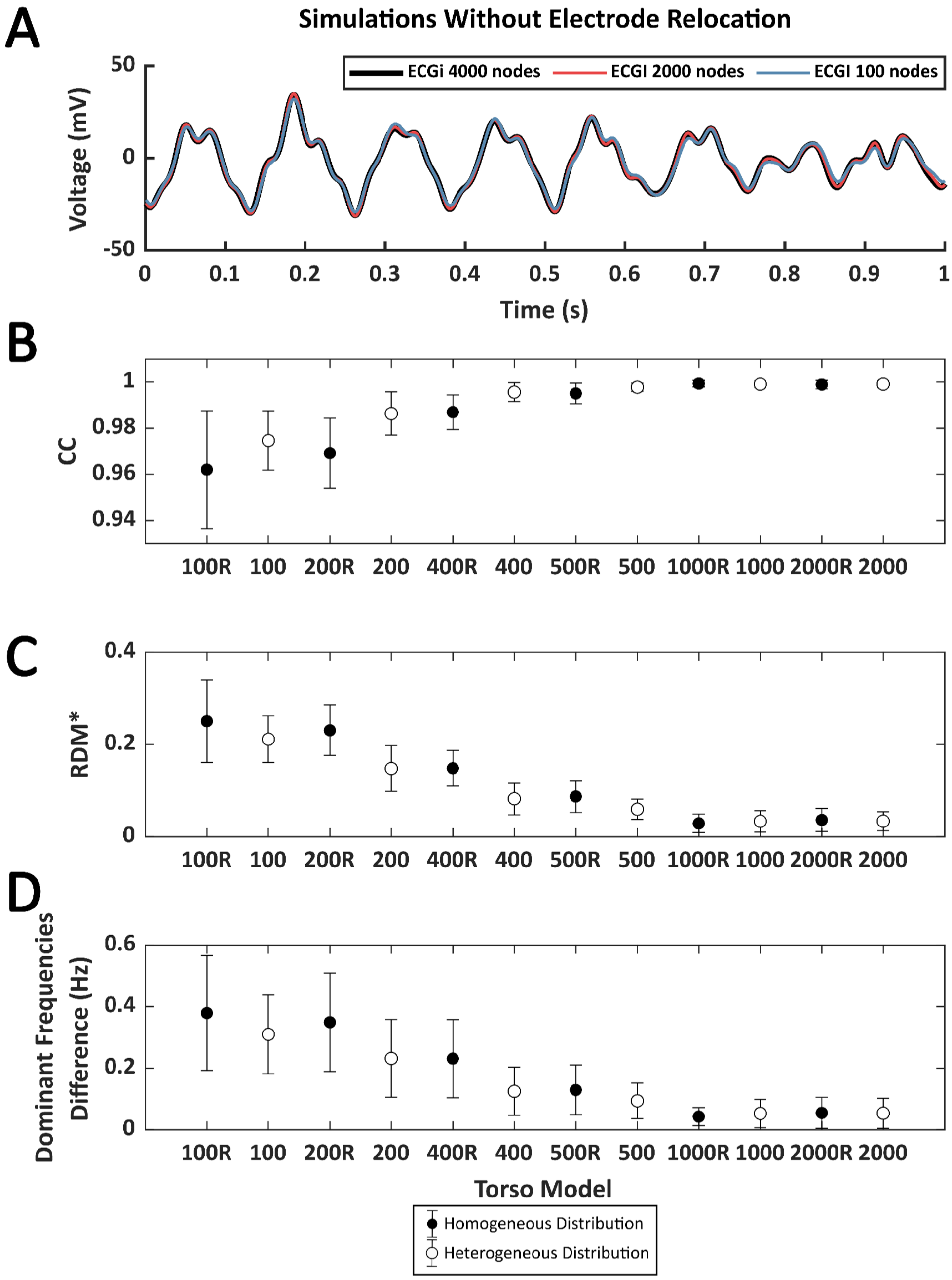

Figure 3.4. A. Example of 1 second of inverse computed electrograms obtained with different torso models and the same simulation signals for torsos without electrode relocation. Signal in black was obtained with the reference 4000-node torso, red and blue signals correspond to the ones obtained with torsos of 2000 and 100 nodes respectively. B. Pearson's correlation coefficient (CC), C. relative measurement (RDM*) and D. mean absolute difference between the reference dominant frequencies (DF) between torso models and from 100 to 2000 nodes. Points in black represent the mean value of the metrics torsos in which the distribution of the nodes is homogeneous and white points represent the torso with nodes heterogeneously placed. Whiskers represent the standard deviation.

The same analysis on real AF patient data is shown in Fig 3.5. Again, CCs were above 0.99 even for meshes with 100 nodes, relative errors were below 0.1 and errors in DF were below 0.2 Hz. CC values for low-density meshes presented very high values, even higher than those obtained for the simulated data. This was because when solving the inverse problem in patients, the optimal regularization parameter was higher than in the simulated cases (~10-5 vs. ~10-8), likely because of the presence of spatial uncertainties in ECGI reconstruction and the presence of different sources of noise on the recorded signals. These larger values of regularization parameters in patients result in smoother ECGI solutions that make the ECGI signal estimation less dependent on mesh resolution.

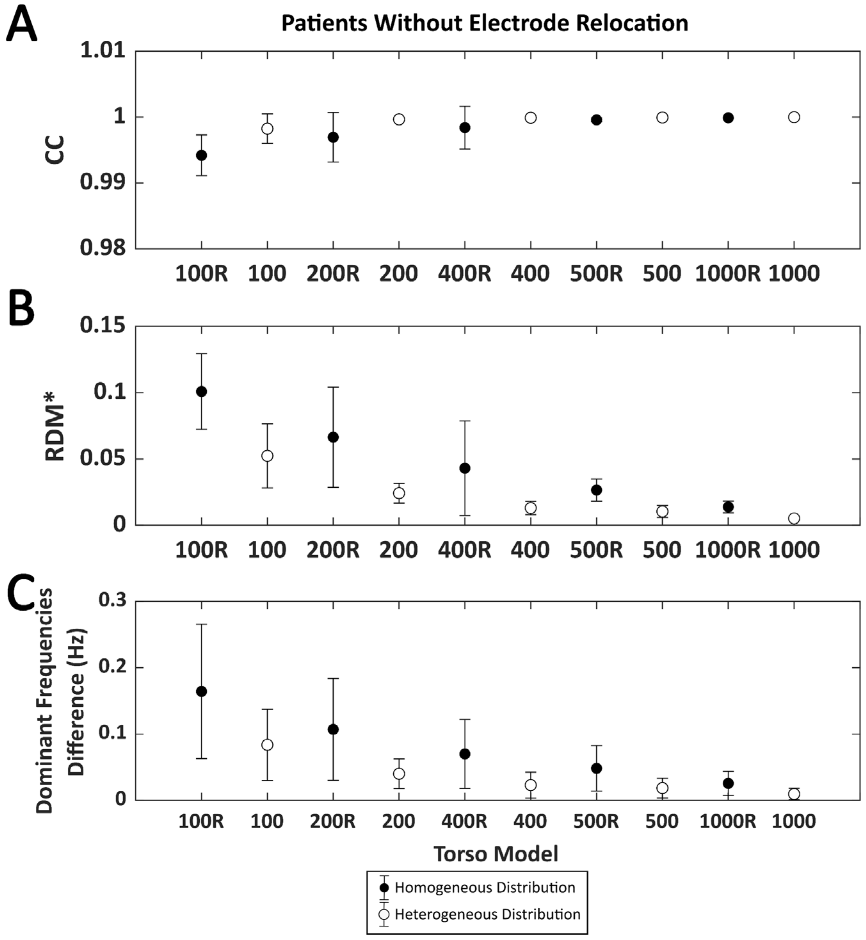

Figure 3.5. Time metrics obtained comparing the inverse computed electrograms 25 atrial fibrillation patients of the reference and the signals obtained with different torso models without electrode relocation. Points in black represent the torsos in which the distribution of the nodes is homogeneous and white points represent the torso with nodes heterogeneously placed. A. Pearson's correlation coefficient (CC) and B. Relative difference measurement (RDM*). C. Mean absolute difference between the reference dominant frequencies (DF) between torso models and from 100 to 1000 nodes.

In addition to the effect of the number of nodes, the type of remeshing affected the quality of the ECGI signal. Results showed that homogenous meshes present lower values of CC and higher values of RDM* and DF errors compared to the heterogeneous distribution of the mesh, which could be attributed to a poorer shape preservation in the homogeneous meshes.

### 3.3.2. Impact of electrode relocation in low-density torso meshes on ECGI reconstruction

ECGI signals obtained from cardiac electrophysiological simulations and using different torso meshes where the electrode position was relocated to match a mesh node after remeshing present noticeable differences with the reference ECGI signals with the finest torso meshes without electrode relocation (Figure 3.6). First, an example of simulated ECGI signals of the reference torso with coarser meshes is presented in panel Figure 3.6A. Although the overall shape of the inversely computed electrograms is preserved for lower mesh densities, some impact of shape morphology can be observed, especially for the sparser meshes (blue line). A global comparison between the signals measured through time-metrics is represented in Figure 3.6B-C for all the models. The CC and the RDM* show a strong dependency on torso mesh density. A progressive increase is shown for the CC as the number of nodes increases, from 0.53 ± 0.06 for the 100 mesh to 0.92 ± 0.04 for the 2000 node mesh. Besides, the RDM* decreases when the torso is composed with a higher number of vertices from 0.96 ± 0.07 for the 100 mesh down to 0.38 ± 0.09 for the 2000 node mesh. Regular meshes do show better correlation coefficients and RDM* values than irregular meshes with a similar number of nodes, especially for the meshes with a lower number of nodes. For the finer meshes and, therefore, smaller areas of the geometrical faces, slightly better results are observed for the irregular meshes.

Figure 3.6D shows the differences in DF between the ECGI signals calculated with the torso meshes with 4000 nodes homogeneously distributed and the remaining models. The largest difference can be observed for the torso with 100 nodes (1.14 ± 0.26 Hz), and it decreases as the number of nodes increases. Differences in the frequencies show higher values when a homogeneous distribution of the electrodes is presented for models with fewer than than 1000 nodes. However, when the number of nodes was 1000 or higher, these differences were higher in the case of the homogeneous models.

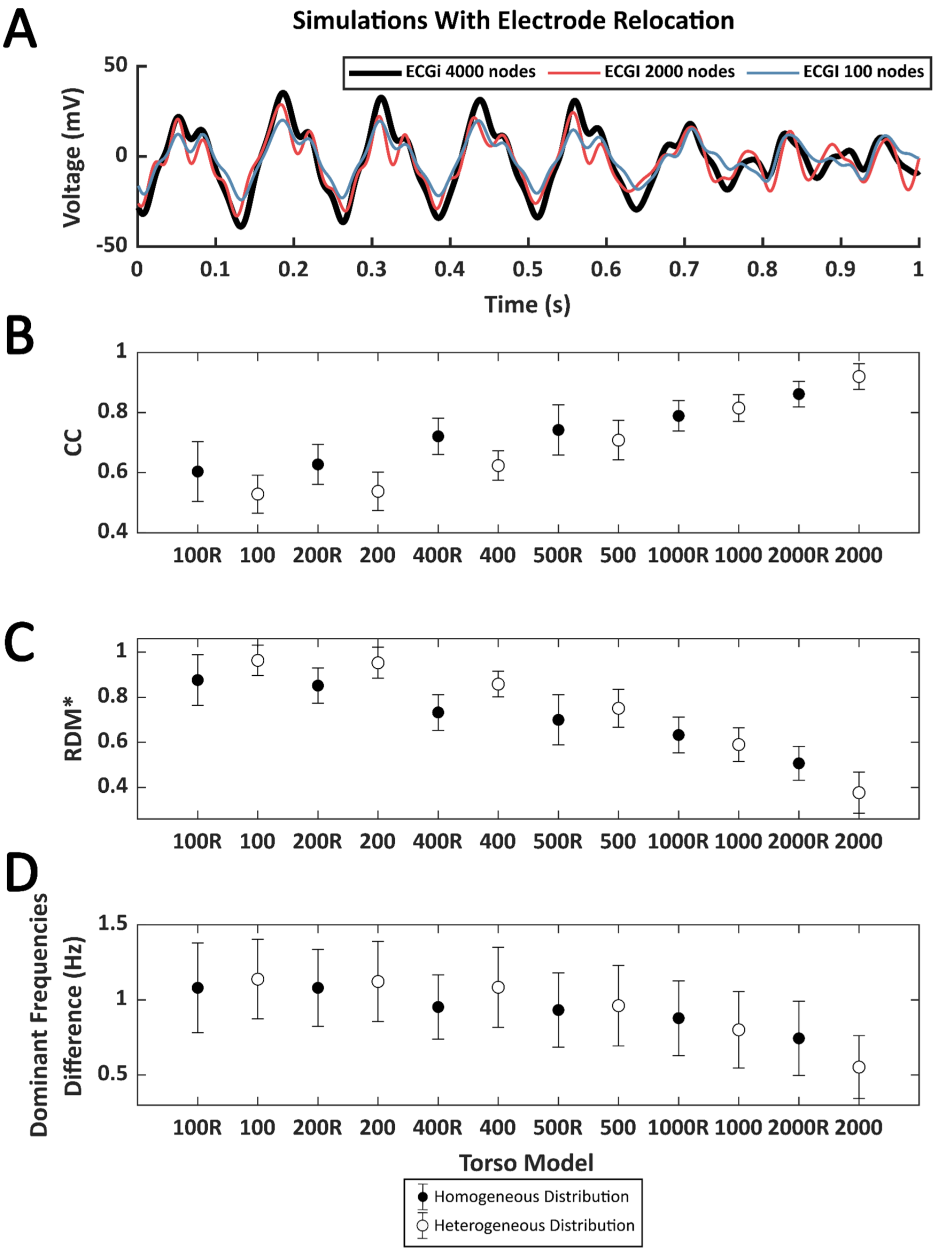

Figure 3.6. A. Example of 1 second of inverse computed electrograms obtained with different torso models and the same simulation signals for torsos with the node of the electrode displaced by the remeshing. Signal in black was obtained with the reference 4000-node torso, red and blue signals correspond to the ones obtained with torsos of 2000 and 100 nodes respectively. B. Pearson's correlation coefficient (CC), C. relative measurement (RDM*) and D. mean absolute difference between the reference dominant frequencies (DF) between torso models and from 100 to 2000 nodes. Points in black represent the mean value of the metrics torsos in which the distribution of the nodes is homogeneous and white points represent the torso with nodes heterogeneously placed. Whiskers represent the standard deviation.

The results of the CC and RDM* of the ECGI computed with each torso mesh from real AF patient data are presented in Figure 3.7. As observed with the computer simulations, the CC values increased, and the RDM* decreased with the number of nodes. Even though the trend is the same as presented in Figure 3.6, differences are more prominent using real AF signals from patients as compared to simulation data. The correlation coefficient ranged from 0.42 ± 0.38 using the 100 nodes torso and up to 0.87 ± 0.2 with the 1000 mesh. The RDM* decreases from 0.98 ± 0.45 (100 nodes) to 0.40 ± 0.33 (1000R). Although the results show a more marked effect of the remeshing in real AF signals, both CCs and RDM* values showed a stabilization for torsos above 400 nodes, as in Figure 3.6.

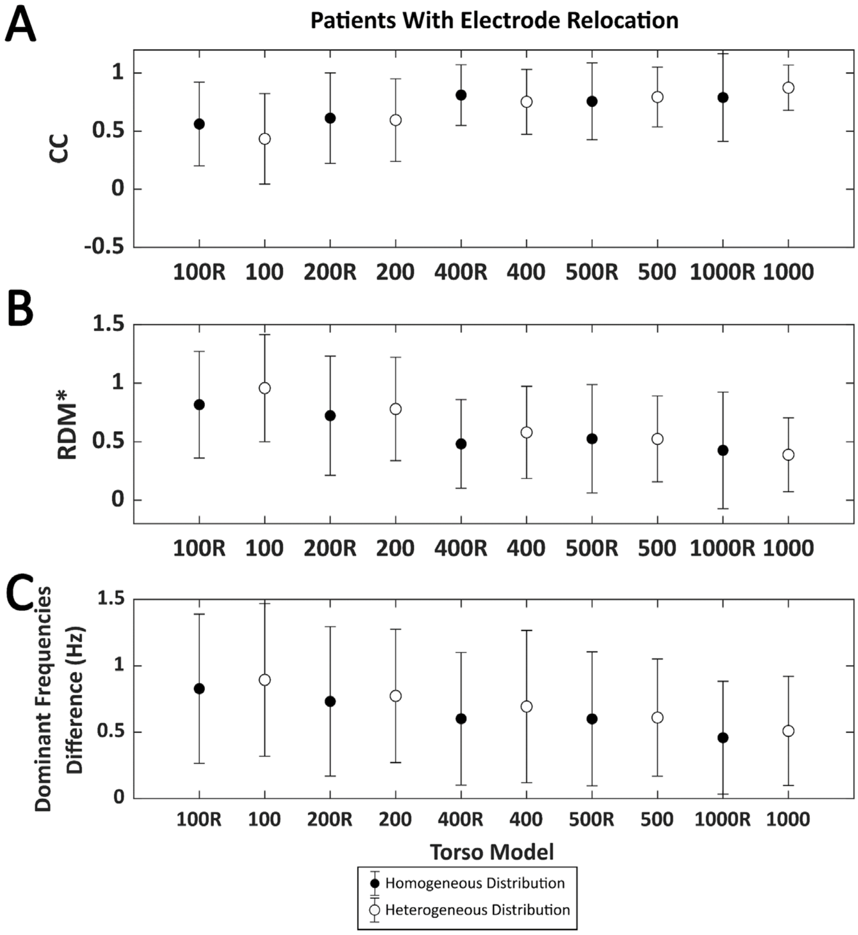

Figure 3.7. Time metrics obtained comparing the inverse computed electrograms 25 atrial fibrillation patients of the reference and the signals obtained with different torso models with the node of the electrode displaced by the remeshing. Points in black represent the torsos in which the distribution of the nodes is homogeneous and white points represent the torso with nodes heterogeneously placed. A. Pearson's correlation coefficient (CC) and B. Relative difference measurement (RDM*). C. Mean absolute difference between the reference dominant frequencies (DF) between torso models and from 100 to 1000 nodes.

The calculation of differences in dominant frequencies is shown in Figure 3.7C. The results presented the same trend as the findings for simulations, and the difference in DF decreases with increasing number of nodes. The largest difference is found for the torso with 100 nodes (0.91 ± 0.56 Hz), while the lowest difference is obtained using the 1000-node torso (0.45 ± 0.41 Hz). In this case we could observe that differences in DFs were lower for the homogeneous torso meshes than their inhomogenous counterparts. DF maps for a sample patient are shown in Figure 3.8. As the number of vertices increased, the maps looked more similar to the one obtained with the reference torso mesh (2000 nodes). Torso meshes constituted by 400 nodes or less didn't allow to determine the site with the highest DF, present in the right atrium. In addition, in torso meshes with nodes from 400 to 1000, the location and extension of the highest dominant frequency area are more similar to the reference ECGI 2000-nodes torso.

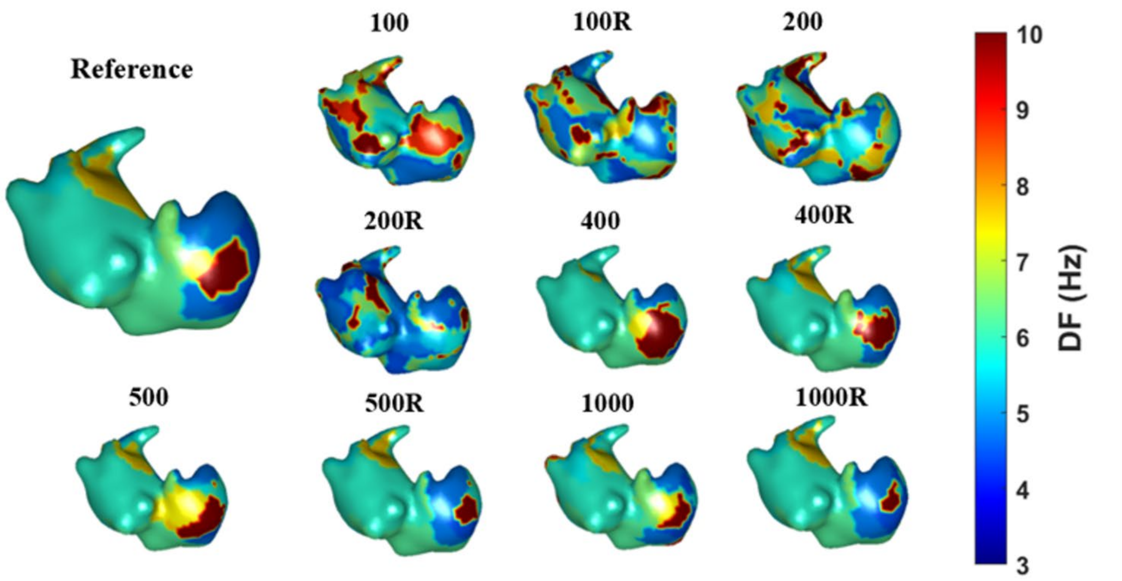

Figure 3.8. Dominant frequency maps obtained with different torso models for one real patient case.

## 3.4. Discussion

In this study, we explored the effect of torso mesh density and homogeneity on ECGI signals for atrial fibrillation simulations and real signals. Firstly, we studied the effect of the number of nodes on torso meshes with imposed nodes matching with the location of the electrodes so that they don't need to be relocated. For both simulations and real signals, the number of nodes had little effect in the ECGI solution, especially for torsos with more of 400 nodes, where the trend in the studied metrics was stabilized. This suggests that torso meshes built upon the restriction of including the electrodes as nodes in the torso mesh are reliable even for very low densities. Furthermore, we observed that irregular meshes presented better results in terms of metrics compared to regular meshes for finer geometries, likely because of a better shape preservation.

Additionally, we explored the effect of node distribution and density, considering that the remeshing affects the position of the nodes that corresponded to electrodes. This analysis is relevant in the context of building first a torso mesh and later assigning the nodes corresponding to recording electrodes in a second step. Under these constraints, the effect of torso density is no longer negligible, and CC can decrease down to 0.5 for meshes with 100 nodes in simulations when there are no further spatial uncertainties and noise is limited to 20 dB SNR. The impact of mesh density on real patient data, when different sources of uncertainty are present, is less relevant because correlations are lower than in the computer simulations even for torso meshes with 1000 nodes. In either case, correlation coefficients are affected, and decrease from 0.87 ± 0.2 for 1000 node meshes down to 0.42 ± 0.38.

The effect of the node density of the meshes of the torsos has not been widely studied. Nevertheless, an accurate torso geometry has been reported as necessary to obtain precise inverse electrograms (Messinger-Rapport and Rudy, 1990). Our study uses torso models obtained with photogrammetry, which presented realistic results but not as precise as those obtained with medical imaging techniques, which were reported to be very important for correct inverse results (Svehlikova et al., 2012). Previous studies addressed that as long as geometrical parameters are captured with local details, the significant impact on the inverse electrogram is minimal (Wang et al., 2010), which is in accordance with the presented results, especially with a larger number of nodes. Likewise, torso reshaping and remeshing with a different number of nodes affected the quality of the signals, with 400 nodes being the minimum necessary to obtain a reliable result. Torso reshaping and smoothing the geometry have been reported to produce less accurate results when computed inverse electrograms (Lenkova et al., 2012) were compared to real ones. Nevertheless, we demonstrated that a homogeneous distribution of the nodes improved the inverse solution for meshes of less than 1000 nodes independently of the type of signal used (real or simulated) when the remeshing forced a relocation of the electrodes. Heterogenous distribution of the nodes improved the results compared to the homogeneous one for geometries of more than 1000 nodes and torsos with the electrodes matching a node position. However, when number of nodes increased, the differences between the distribution of the nodes decrease, and we cannot ensure that homogeneous meshes are worse for higher number of nodes, most likely because electrode relocation is less relevant in homogenous torso meshes since the distance between the actual location of the electrode and its location in the relocated torso mesh is larger in heterogenous meshes than in their homogeneous counterparts.

The minimum number of electrodes for computing ECGI with AF signals needed has been studied previously, with 23 the minimum number for an accurate reconstruction, similar to a 12-lead ECG (Guillem et al., 2009). Although the number of electrodes remains critical for a proper inverse reconstruction, in this study, we used a reliable amount according to the literature. Notwithstanding, increasing the number may alleviate the misplacement effect and could be needed for a correct reconstruction of reliable torso meshes.

The position and displacement of the electrodes remain important, as shown in the results and described by van der Graaf et al., 2016. Nevertheless, some studies provided results that the optimal position for placing the electrodes is not unique, which matches the study (Lux et al., 1978). The possibility of a range of appropriate electrode positions allows the opportunity of having reliable ECGI reconstructions with different torso meshes and electrodes displacement as in the presented study. The remeshing influenced electrode location, but we could establish the maximum displacement tolerated of the electrodes as 2cm, the mean displacement of 400-nodes torsos, which is in accordance with what has been described in vivo studies previously (Cluitmans and Volders, 2017). This distance gives margin to consider as a good reconstruction of the location of the electrodes using photogrammetry. Furthermore, slightly displaced electrodes would not affect the results drastically. Despite that, results demonstrated that 400 nodes -or mean distance between nodes below 4 cm- is a good trade-off for torso geometry reconstruction; geometries with a higher number of nodes would alleviate electrode misplacement (Huiskamp and Van Oosterom, 1989).

### 3.4.1. Limitations

In this study, we compared real AF signals with ECGI reconstructed with a higher number of nodes in the mesh as a reference and with no intracardiac data. We considered a higher number of nodes models as a reference assuming that it will provide a better reconstruction. For this purpose, data from AF simulations were used, being the conclusions with simulations and real data in agreement.

For the used forward model, inner organs were not included. Our model may be simplistic, and for that reason, the observed results with relocated electrodes may be better in simulations than in patient analysis. Nevertheless, although the incorporation of inner organs has not shown a major impact on the shape of ECGI potentials (Ramanathan and Rudy, 2001), simulated body surface potentials are indeed affected by these torso inhomogeneities that we have not considered in the present study. Additionally, the lack of anisotropy of the forward model may influence our results because although it may not affect the ECGI resolution significantly, potential distributions that are more complex due to the anisotropy will complicate the resolution of the inverse model (Colli-Franzone et al., 1982, Potse et al., 2009, Hren et al., 1998). Furthermore, it should be noted that the presented results are not relevant to mesh-less solutions due to the influence of the BEM on the presented results. For simulations, the results for each torso geometry were compared with a reference ECGI of a 4000-nodes torso and not with the original electrogram due to the low similarity at the high-frequencies for the intrinsic smoothing of the ECGI. Nevertheless, this does not imply that we could define the effect of the quality of the mesh on the inverse solution. Finally, in the present study we have omitted the quantification of the impact of the epicardial mesh on the signals estimated by ECGI, which should be explored in future studies.

## 3.5. Conclusion

The present study shows that the effect of mesh density on ECGI signals has little effect when the original electrode position is respected, especially for geometries with more than 400 nodes. Nevertheless, if maintaining the original position of the electrode is not possible, a mesh of at least 400 nodes is recommended for solving the inverse problem of electrocardiography in the context of atrial fibrillation signals in order to achieve reliable results. Furthermore, a homogeneous distribution of the nodes showed to be convenient for computing the ECGI with a distance separation of nodes under 4 cm. A displacement of the nodes corresponding to the position of the electrodes higher than 2 cm should be avoided.

## 3.6. Ackowledgements

This work was supported by: Instituto de Salud Carlos III,and Ministerio de Ciencia e Innovación (supported by FEDER Fondo Europeo de Desarrollo Regional PI17/01106, PEJ2018-003617 and RYC2018-024346-I), EIT Health (Activity code 220385, EIT Health is supported by EIT, a body of the European Union), Generalitat Valenciana Conselleria d'Educació, Investigació, Cultura i Esport (ACIF/2020/265) and Spanish Agencia Estatal de Investigación (AEI), part of the Ministerio de Ciencia e Innovación, reference PID2020-119364RB-I00.

### Associated congress publication

Further examples of DF maps on simulations were presented in Computing in Cardiology congress in this publication:

R. Molero, A. González-Ascaso, I. Hernández-Romero, A. M. Climent, and M. de la Salud Guillem Sánchez, “Effect of Torso Mesh Density on Electrocardiographic Imaging Resolution from Atrial Fibrillation Simulations,” in *Computing in Cardiology*, 2022, vol. 49, pp. 1–4.

## References

Castells, F., Mora, C., Rieta, J. J., Moratal-Pérez, D., and Millet, J. (2005). Estimation of atrial fibrillatory wave from single-lead atrial fibrillation electrocardiograms using principal component analysis concepts. Med. Biol. Eng. Comput. 43, 557–560. doi:10.1007/BF02351028.

Colli-Franzone P, Guerri L, Viganotti C, Macchi E, Baruffi S, Spaggiari S, et al. (1982). Potential fields generated by oblique dipole layers modeling excitation wavefronts in the anisotropic myocardium. Comparison with potential fields elicited by paced dog hearts in a volume conductor. Circ. Res.; 51:330–46. doi:10.1161/01.RES.51.3.330.

Cluitmans, M. JM., and Volders, P. GA. (2017). Influence of body-surface geometry accuracy on noninvasive reconstruction of electrical activation and recovery in electrocardiographic imaging. Comput. Cardiol. 44, 1–4. doi:10.22489/CinC.2017.243-189.

Guillem, M.S., Bollmann, A., Climent, A. M., Husser, D., Millet-Roig, J., and Castells, F. (2009). How many leads are necessary for a reliable reconstruction of surface potentials during atrial fibrillation? IEEE Trans. Inf. Technol. Biomed. 13, 330–340. doi:10.1109/TITB.2008.2011894.

Figuera, C., Suárez-Gutiérrez, V., Hernández-Romero, I., Rodrigo, M., Liberos, A., Atienza, F., et al. (2016). Regularization techniques for ECG imaging during atrial fibrillation: A computational study. Front. Physiol. 7. doi:10.3389/fphys.2016.00466.

Hren R, Nenonen J, Horáček BM. (1998). Simulated epicardial potential maps during paced activation reflect myocardial fibrous structure. Ann. Biomed. Eng. 1998;26:1022–35. https://doi.org/10.1114/1.73.

Huiskamp, G., and Van Oosterom, A. (1989). Tailored Versus Realistic Geometry in the Inverse Problem of Electrocardiography. IEEE Trans. Biomed. Eng. 36, 827–835. doi:10.1109/10.30808.

Jamison, C., Navarro, C., Turner, C., Shannon, J., Anderson, J., and Adgey, J. (2011). The inverse problem utilizing the boundary element method for a nonstandard female torso. IEEE Trans. Biomed. Eng. 58, 876–883. doi:10.1109/TBME.2010.2093525.

Lenkova, J., Svehlikova, J., and Tysler, M. (2012). Individualized model of torso surface for the inverse problem of electrocardiology. J. Electrocardiol. 45, 231–236. doi:10.1016/j.jelectrocard.2012.01.006.

Manu (2022). Patch Remesher. Available at: https://uk.mathworks.com/matlabcentral/fileexchange/49691-patch-remesher., MATLAB Central File Exchange.

Lux;, R. L., Smith;, C. R., Wyatt;, R. F., and Abildskov;, J. A. (1978). Limited Lead Selection for Estimation of Body Surface Potential Maps in Electrocardiography. IEEE Trans. Biomed. Eng. BME-25, 270–276. doi:10.1109/TBME.1978.326332..

Meijs, J. W. H., Weier, O. W., Peters, M. J., and Van Oosterom, A. (1989). On the Numerical Accuracy of the Boundary Element Method. IEEE Trans. Biomed. Eng. 36, 1038–1049. doi:10.1109/10.40805.

Messinger-Rapport, B. J., and Rudy, Y. (1990). Noninvasive recovery of epicardial potentials in a realistic heart-torso geometry. Normal sinus rhythm. Circ. Res. 66, 1023–1039. doi:10.1161/01.RES.66.4.1023.

Molero, R., Torro, J. M. S., Alzamora, N. M., Climent, A. M., and Guillem, M. S. (2021). Higher reproducibility of phase derived metrics from electrocardiographic imaging during atrial fibrillation in patients remaining in sinus rhythm after pulmonary vein isolation. Comput. Biol. Med. 139, 104934. doi:10.1016/J.COMPBIOMED.2021.104934.

Pedrón-Torrecilla, J., Rodrigo, M., Climent, A. M., Liberos, A., Pérez-David, E., Bermejo, J., et al. (2016). Noninvasive estimation of epicardial dominant high-frequency regions during atrial fibrillation. J. Cardiovasc. Electrophysiol. 27, 435–442. doi:10.1111/jce.12931.

Potse M, Dubé B, Vinet A. (2009) Cardiac anisotropy in boundary-element models for the electrocardiogram. Med. Biol. Eng. Comput. 47,719–29. doi:10.1007/s11517-009-0472-x.Ramanathan, C., and Rudy, Y. (2001). Electrocardiographic imaging: II. Effect of torso inhomogeneities on noninvasive reconstruction of epicardial potentials, electrograms, and isochrones. J. Cardiovasc. Electrophysiol. 12, 241–252. doi:10.1046/j.1540-8167.2001.00241.x.

Remondino, F. (2004). 3-D reconstruction of static human body shape from image sequence. Comput. Vis. Image Underst. 93, 65–85. doi:10.1016/j.cviu.2003.08.006.

Rodrigo, M., Climent, A. M., Liberos, A., Fernández-Avilés, F., Berenfeld, O., Atienza, F., et al. (2017a). Highest dominant frequency and rotor positions are robust markers of driver location during noninvasive mapping of atrial fibrillation: A computational study. Hear. Rhythm 14, 1224–1233. doi:10.1016/j.hrthm.2017.04.017.

Rodrigo, M., Climent, A. M., Liberos, A., Fernández-Avilés, F., Berenfeld, O., Atienza, F., et al. (2017b). Technical considerations on phase mapping for identification of atrial reentrant activity in direct-And inverse-computed electrograms. Circ. Arrhythmia Electrophysiol. 10, e005008. doi:10.1161/CIRCEP.117.005008.

Rodrigo, M., Guillem, M. S., Climent, A. M., Liberos, A., Hernández-Romero, I., Arenal, Á., et al. (2018). Solving Inaccuracies in Anatomical Models for Electrocardiographic Inverse Problem Resolution by Maximizing Reconstruction Quality. IEEE Trans. Med. Imaging 37, 733–740. doi:10.1109/TMI.2017.2707413.

Rodrigo, M., Climent, A. M., Hernández-Romero, I., Liberos, A., Baykaner, T., Rogers, A. J., et al. (2020). Non-Invasive Assessment of Complexity of Atrial Fibrillation: Correlation with Contact Mapping and Impact of Ablation. Circ. Arrhythmia Electrophysiol. 13, CIRCEP.119.007700. doi:10.1161/CIRCEP.119.007700.

Salinet, J., Molero, R., Schlindwein, F. S., Karel, J., Rodrigo, M., Rojo-Álvarez, J. L., et al. (2021). Electrocardiographic Imaging for Atrial Fibrillation: A Perspective from Computer Models and Animal Experiments to Clinical Value. Front. Physiol. 12. doi:10.3389/fphys.2021.653013.

Schmidt, R., and Singh, K. (2010). Meshmixer: An interface for Rapid Mesh Composition. ACM SIGGRAPH 2010 Talks, SIGGRAPH '10. doi:10.1145/1837026.1837034.

Svehlikova, J., Lenkova, J., Turzova, M., Tysler, M., Kania, M., and Maniewski, R. (2012). Influence of individual torso geometry on inverse solution to 2 dipoles. J. Electrocardiol. 45, 7–12. doi:10.1016/j.jelectrocard.2011.07.012.

van der Graaf, A. W. M., Bhagirath, P., de Hooge, J., de Groot, N. M. S., and Götte, M. J. W. (2016). A priori model independent inverse potential mapping: the impact of electrode positioning. Clin. Res. Cardiol. 105, 79–88. doi:10.1007/s00392-015-0891-7.

Wang, L., Wong, K. C. L., Zhang, H., Liu, H., and Shi, P. (2010). How Much Geometrical Detail Do We Need in Cardiac Electrophysiological Imaging? A Generic Heart-Torso Representation for Fast Subject-Specific Customization. LNCS 6364, 232–241. doi:10.1007/978-3-642-15835-3_24.

Yushkevich, P. A., Zhang, H., and Gee, J. C. (2006). Continuous Medial Representation for Anatomical Structures. IEEE Trans. Med. Imaging 25, 1547–1564. doi:10.1109/TMI.2006.884634.

# Chapter 4

## Robustness of Imageless Electrocardiographic Imaging Against Uncertainty in Atrial Morphology and Location

Rubén Molero[1], Ana González-Ascaso[1], Andreu M. Climent[1*], María S. Guillem[1*]

## Abstract

**Introduction:** Electrocardiographic Imaging is a non-invasive technique that requires cardiac imaging for the reconstruction of the cardiac electrical activity. In this study, we explored imageless ECGI by quantifying the errors of using heart meshes with either an inaccurate location inside the thorax or an inaccurate geometry.

**Methods:** Multiple-lead body surface recordings of 25 atrial fibrillation (AF) patients were recorded. Cardiac atrial meshes were obtained by segmentation of medical images obtained for each patient. ECGI was computed with each patient's segmented atrial mesh and compared with the ECGI obtained under errors in the atrial mesh used for ECGI estimation. We modeled both the uncertainty in the location of the atria inside the thorax by artificially translating the atria inside the thorax and the geometry of the atrial mesh by using an atrial mesh in a reference database. ECGI signals obtained with the actual meshes and the translated or estimated meshes were compared in terms of their correlation coefficients, relative difference measurement star, and errors in the dominant frequency (DF) estimation in epicardial nodes.

**Results:** CC between ECGI signals obtained after translating the actual atrial meshes from the original position by 1cm was above 0.97. CC between ECGIs obtained with actual and estimated atrial geometries was 0.93±0.11. Mean errors in DF estimation using an estimated atrial mesh were 7.6±5.9%.

**Conclusion:** Imageless ECGI can provide a robust estimation of cardiac electrophysiological parameters such as activation rates even during complex arrhythmias. Furthermore, it can allow a more widespread use of ECGI in clinical practice.

---

R. Molero, A. González-Ascaso, A. M. Climent, and M. S. Guillem, "Robustness of imageless electrocardiographic imaging against uncertainty in atrial morphology and location," J. Electrocardiol., vol. 77, no. January, pp. 58–61, 2023.

[1] ITACA Institute, Universitat Politècnica de València, València, Spain

[*] Andreu M. Climent and María S Guillem share the last authorship of this paper

## 4.1. Introduction

The standard ECG has not changed much in the last 80 years (Goldberger, 1942). It has allowed the detection of many cardiac disorders but does not allow to infer the cardiac activation pattern in each individual as an electroanatomical navigator does. A non-invasive visualization of the cardiac electrical activity can be achieved, to a certain extent, through Electrocardiographic Imaging (ECGI) (Barr and Spach, 1977), which has been validated in humans almost 20 years ago (Ramanathan et al., 2004). ECGI consists of estimating the electrical potentials on the surface of the cardiac chambers, from sets of 50 to 256 electrodes distributed over the torso of the patient (Cluitmans et al., 2018; Salinet et al., 2020).

ECGI has been demonstrated to be useful for mapping atrial flutters, characterizing AF, identifying extrasystole origin, or providing support during resynchronization pacemaker implantation (Cluitmans et al., 2018; Salinet et al., 2020; Bear et al., 2019). During the last decade, commercial ECGI products have arrived at the market. Nevertheless, this novel non-invasive characterization tool of cardiac electrical activity has reached a moderate clinical impact. One potential reason for this limited clinical application of ECGI is the need for an accurate estimation of the torso and heart geometry from a CT scan of each patient while wearing the set of body surface electrodes. Potential complications associated with (1) a synchronization between cardiologists and radiologists and (2) irradiation into the patient for performing a CT scan to reconstruct the electrical activity are ethically justified only for a selected number of centers and patients.

The possibility of avoiding CT scans to perform ECGI maps is becoming an attractive approach to extend the advantages of a detailed non-invasive cardiac mapping to all cardiac arrhythmia patients (Salinet et al., 2020; Rodrigo et al., 2018). Imageless ECGI allows estimating the cardiac geometry and its location inside the thorax of a patient based on a combination of statistical information and electrical and thorax geometrical information (Rodrigo et al., 2018).

In this study, the robustness of our imageless ECGI is quantified. Specifically, the impact on ECGI signals of imposed geometrical distortions, modelling errors due to uncertainties in heart geometry, and location estimation is evaluated.

## 4.2. Material and Methods

We recruited 25 patients referred for AF ablation at Hospital General Universitario Gregorio Marañón (Madrid, Spain). Institutional Ethics Committee approved the protocol, and all patients gave informed consent.

Fifty-seven body surface electrodes were distributed over the torso of each patient for the recording of ECGI signals. Signals were recorded at 1kHz sampling rate with a bandpass filter between 0.05 and 500Hz for off-line analysis. Surface signals were pre-processed as described in (Molero et al., 2021). For each patient, a CT scan or MRI was acquired prior to the procedure to estimate the anatomy of the atria and the torso. In addition, a 3D photogrammetry was used to reconstruct the torso of the patient and locate all ECGI electrodes.

To quantify the errors in ECGI reconstruction with estimated versus measured atrial geometries, we used (1) different locations and (2) different morphologies of the atrial geometrical geometries together with the actual location and morphology of the atria of the patient and compared the estimated ECGI signals. The set of variations in the atrial mesh used for solving the inverse problem is summarized in Figure 4.1. A set of displacements of 1, 2 and 3 cm in each axis (X, Y and Z) was applied to all nodes of the actual atrial mesh of each patient (panel A). In addition, an estimated cardiac geometry and location was obtained based on a statistical approach fed by the shape of the thorax of each patient (panel B). As it can be observed, the shape of the estimated and actual atria was different, but the location and mean size were similar.

Epicardial electrograms were then estimated from body surface recordings by using the boundary element method formulation and zero-order Tikhonov regularization and L-Curve selection of the optimal regularization parameter (Pedrón-Torrecilla et al., 2016).

To compare electrograms estimated by solving the ECGI with the patient's actual atria versus the ECGI signals obtained with a different location or shape, we calculated Pearson's correlation coefficient (CC) and the relative difference measurement star (RDMS) (Figuera et al., 2016) on each node of the atria. For comparison between ECGI signals obtained with different atrial geometries, the signals with pairing nodes were compared. For each node in the actual atrial anatomy, a pairing node was chosen for the estimated anatomy that minimized the Euclidean distance between these pairs of nodes. Pairs of nodes with distances larger than 0.5 cm were not used for comparison.

In addition, dominant frequency (DF) maps were calculated from the ECGI signals obtained for translated and estimated atrial geometries and compared with the DF map obtained with the actual atrial geometry. DF was defined as the frequency with the largest power in the power spectral distribution obtained by applying the Welch periodogram (2-second Hamming window with a 25% overlap) (Rodrigo et al., 2017). The absolute difference in DF for each atrial node was quantified.

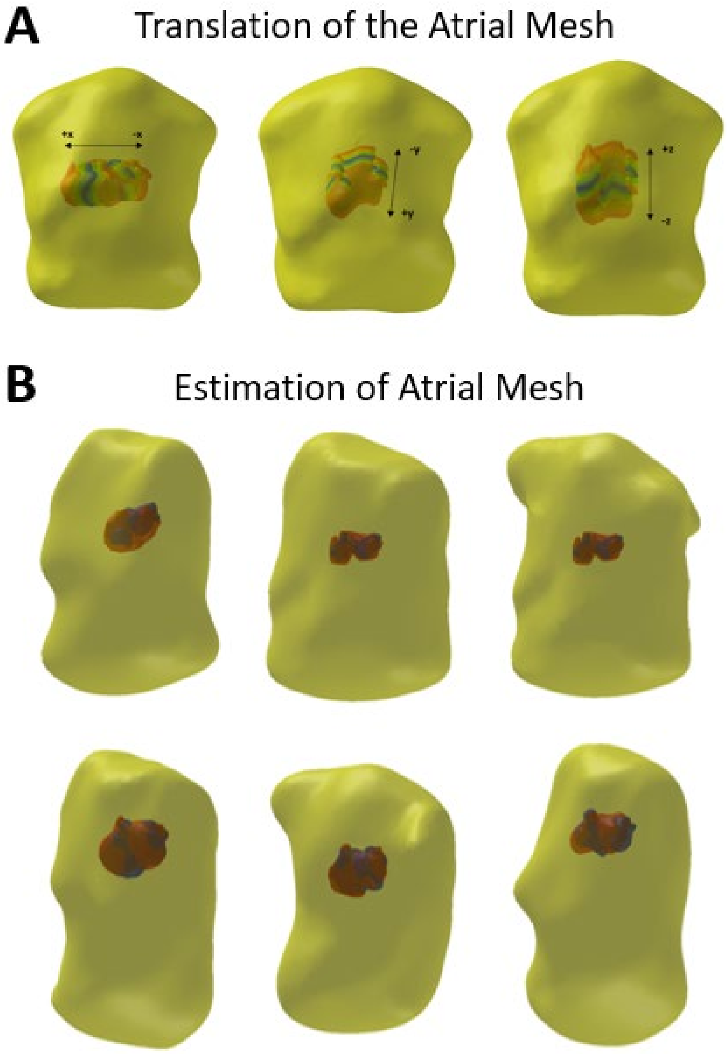

Figure 4.1. Illustration of the geometrical distortions introduced in the performed experiments. In panel A, illustration of the translation of the atria inside the thorax of the patient along the X, Y and Z axis, with maximal distances of 3cm. In panel B, comparison between actual atrial mesh obtained from a CT scan atrium (red) and the estimated atrial geometry (blue) for 6 illustrative subjects.

## 4.3. Results

Comparisons between ECGI signals are illustrated in Figure 4.2. In panel A-B, the effects of the translation of the actual atrial mesh on the X, Y, and Z axis are depicted. As it can be observed, CC decreases with increasing translation distances while RDMS values were increased. Mean CC at a ±1cm translation was 0.98±0.04 for the X axis, 0.98±0.04 for the Y axis and 0.97±0.11 for the Z axis. The lowest correlations (0.82±0.2) were found for translations of 3 cm on the Y axis.

In panel C, an example of estimated ECGI signals obtained for actual versus estimated atrial geometries in a selected node is depicted. The correlation coefficient of both ECGI signals was 0.97 and the RDMS was 0.24. In panel D, the results for the entire database are depicted. As it can be observed, by using the estimated geometry an average correlation coefficient of 0.93±0.11 and RDMS of 0.32±0.18 were obtained.

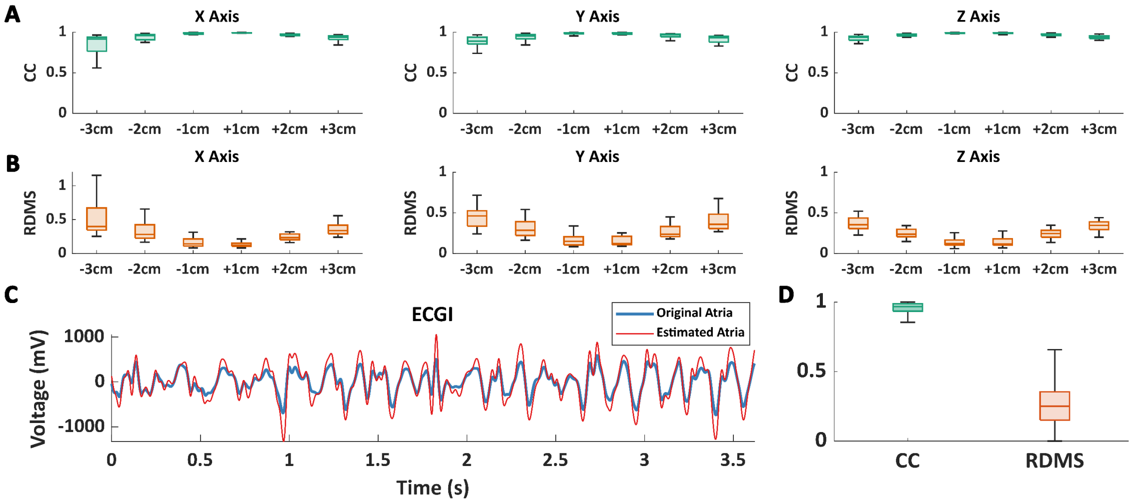

Figure 4.2. Quantification of errors in ECGI signals by geometrical distortions. Panel A-B, CC and RDMS obtained for translated atria in the X, Y and Z axis by 1, 2 or 3 centimetres. Panel C, sample ECGI electrogram estimated for the actual atrial geometry of the patient (blue) together with the estimated ECGI signal at the nearest node for the estimated atrial geometry. Panel D, quantification of the Pearson's correlation coefficient (CC) and the relative difference measurement star (RDMS) between ECGI signals in all nodes in the actual atrial mesh obtained by a CT scan and pairing nodes in the estimated atrial meshes.

DF maps obtained from ECGI signals estimated for the different atrial meshes (actual, translated and estimated) are depicted in Figure 4.3. In panel A, the DF map measured by solving the ECGI with the actual patient anatomy derived from the CT scan or MRI. In this case, the highest DF (9.37 Hz) was present in the posterior side of the right atrium (RA), while most of the atria was activated at 4.82 Hz. In panel B, DF maps obtained with the original atrial geometry translated by ±1cm in the X, Y, and Z axes are depicted. As it can be observed, DF maps were different when employing different atrial geometries, but the critical region, the site harboring the highest DF, was identifiable in all cases in the same region of the atria.

Finally, in panel C, the DF map obtained for the estimated cardiac geometry is depicted. Notice that although a few differences are noticeable between both maps, the values and distribution of DFs were correctly estimated. A systematic comparison between the DF values at all nodes and all patients obtained with the actual atrial geometry and the estimated geometry presented a mean difference of 0.47±0.35Hz.

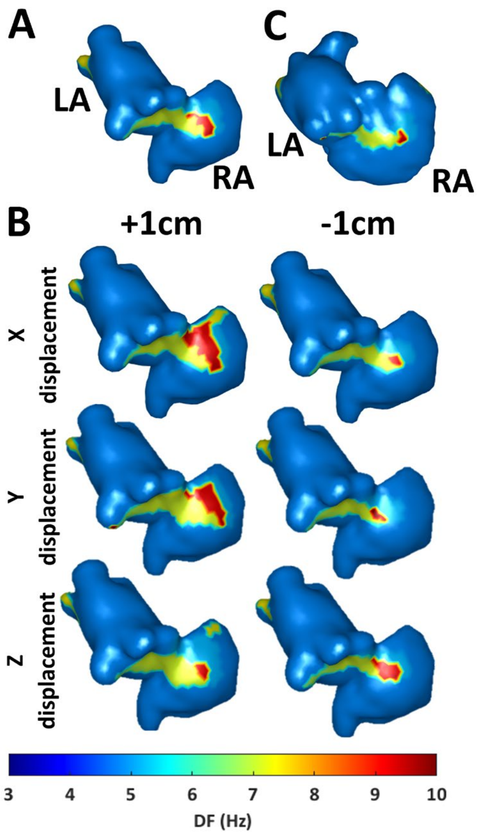

Figure 4.3. Effects of geometry and location errors on atrial fibrillation DF maps. Panel A. DF map obtained from ECGI signals estimated for the patient’s actual atrial mesh. Panel B, effects of the translation of the patient’s actual atrial mesh along the X, Y and Z axis on the DF map. Panel C. DF map obtained from ECGI signals computed for an estimated atrial mesh.

## 4.4. Discussion

In this study, we have shown that an imageless ECGI allows to extract clinically relevant information without requiring a CT scan, even during complex arrhythmias such as AF.

Current non-invasive characterization of the cardiac function is insufficient for risk stratification or a personalized identification of the mechanisms maintaining arrhythmias in each individual patient. During the last decades, significant improvements have arrived at the clinic by the hand of image and structural analysis developments thanks to systems such as echocardiography, CT scans, and MRI. However, regarding the electrophysiological function of the heart, main technological novelties have been restricted to the improvement of invasive electroanatomic mapping systems. Non-invasive characterization continues to be limited to the standard ECG used without major developments during the last century. ECGI could fill the gap between the ECG and electroanatomical mapping. However, the introduction of current ECGI technology in the clinical practice is hampered because of the extra efforts that need to be put into the acquisition of a CT scan of the patient while wearing a multielectrode vest. Primary and secondary patient care could also take advantage of imageless ECGI solutions since this non-invasive characterization could help predict the optimal treatment on an individual patient basis without requiring a CT scan or MRI in each patient. Development of imageless ECGI together with a reduction of the number of leads required (de la Guillem et al., 2009; Parreira et al., 2020) and the optimization of the regularization process to increase accuracy (Figuera et al., 2016), is the way to follow in order to extend the applicability of this technology. In addition, the combination of apriorism knowledge and mathematical electrophysiological models offers a promising line of research (van Dam, 2017; Van Oosterom, 2004)

In the present study, we have evaluated the effect of uncertainty on atrial geometry estimation during AF episodes since this could be considered a worst-case scenario with low signal-to-noise ratios and high variability in the ECG signals. In addition, although AF is the most prevalent arrhythmia, current characterization based on the standard ECG is insufficient to select the best treatment for each patient. Extension of the present results to the characterization of more regular rhythms or ventricular arrhythmias will help to validate the application of imageless ECGI. It is remarkable to notice that the estimation of cardiac chambers is based on previous knowledge and extensive databases of patients, but in case of congenital or significant heart disease that could imply dramatic changes in the cardiac morphology would continue requiring a CT scan.

## 4.5. Conclusion

Imageless ECGI can provide a robust estimation of cardiac electrophysiological parameters such as activation rates even during complex arrhythmias such as AF. Estimation of patient's cardiac geometry and its most plausible location inside the thorax opens the possibility of helping the application of non-invasive electrophysiological maps in the clinical practice.

## 4.6. Acknowledgments

This work was supported by: Instituto de Salud Carlos III, and Ministerio de Ciencia e Innovación (supported by FEDER Fondo Europeo de Desarrollo Regional DIDIMO PLEC2021-007614, ESSENCE PID2020-119364RB-I00, and RYC2018- 024346B-750), EIT Health (Activity code SAVE-COR 220385, EIT Health is supported by EIT, a body of the European Union) and Generalitat Valenciana Conselleria d'Educació, Investigació, Cultura i Esport (ACIF/2020/265). The authors want to thank the organizers of the 2022 meeting of the International Society for Computerized Electrocardiology for their invitation to the meeting.

## References

Barr, R. C., and Spach, M. S. (1977). Inverse calculation of QRS-T epicardial potentials from body surface potential distributions for normal and ectopic beats in the intact dog. Circ. Res. 42, 661–675. doi:10.1161/01.RES.42.5.661.

Bear, L. R., Bouhamama, O., Cluitmans, M., Duchateau, J., Walton, R. D., Abell, E., et al. (2019). Advantages and pitfalls of noninvasive electrocardiographic imaging. J. Electrocardiol. 57, S15–S20. doi:10.1016/j.jelectrocard.2019.08.007.

Cluitmans, M., Brooks, D. H., MacLeod, R., Dössel, O., Guillem, M. S., Van Dam, P. M., et al. (2018). Validation and opportunities of electrocardiographic imaging: From technical achievements to clinical applications. Front. Physiol. 9, 1–19. doi:10.3389/fphys.2018.01305.

Figuera, C., Suárez-Gutiérrez, V., Hernández-Romero, I., Rodrigo, M., Liberos, A., Atienza, F., et al. (2016). Regularization techniques for ECG imaging during atrial fibrillation: A computational study. Front. Physiol. 7. doi:10.3389/fphys.2016.00466.

Goldberger, E. (1942). A simple, indifferent, electrocardiographic electrode of zero potential and a technique of obtaining augmented, unipolar, extremity leads. Am. Heart J. 23, 483–492. doi:10.1016/S0002-8703(42)90293-X.

Guillem, M. S., Bollmann, A., Climent, A. M., Husser, D., Millet-Roig, J., and Castells, F. (2009). How many leads are necessary for a reliable reconstruction of surface potentials during atrial fibrillation? IEEE Trans. Inf. Technol. Biomed. 13, 330–340. doi:10.1109/TITB.2008.2011894.

Molero, R., Soler Torro, J. M., Martínez Alzamora, N., M. Climent, A., and Guillem, M. S. (2021). Higher reproducibility of phase derived metrics from electrocardiographic imaging during atrial fibrillation in patients remaining in sinus rhythm after pulmonary vein isolation. Comput. Biol. Med. 139, 104934. doi:10.1016/j.compbiomed.2021.104934.

Parreira, L., Carmo, P., Adragao, P., Nunes, S., Soares, A., Marinheiro, R., et al. (2020). Electrocardiographic imaging (ECGI): What is the minimal number of leads needed to obtain a good spatial resolution? J. Electrocardiol. 62, 86–93. doi:10.1016/j.jelectrocard.2020.07.004.

Pedrón-Torrecilla, J., Rodrigo, M., Climent, A. M., Liberos, A., Pérez-David, E., Bermejo, J., et al. (2016). Noninvasive estimation of epicardial dominant high-frequency regions during atrial fibrillation. J. Cardiovasc. Electrophysiol. 27, 435–442. doi:10.1111/jce.12931.

Ramanathan, C., Ghanem, R. N., Jia, P., Ryu, K., and Rudy, Y. (2004). Noninvasive electrocardiographic imaging for cardiac electrophysiology and arrhythmia. Nat. Med. 10, 422–428. doi:10.1038/nm1011.

Rodrigo, M., Climent, A. M., Liberos, A., Fernández-Avilés, F., Berenfeld, O., Atienza, F., et al. (2017). Highest dominant frequency and rotor positions are robust markers of driver location during noninvasive mapping of atrial fibrillation: A computational study. Hear. Rhythm 14, 1224–1233. doi:10.1016/j.hrthm.2017.04.017.

Rodrigo, M., Guillem, M. S., Climent, A. M., Liberos, A., Hernández-Romero, I., Arenal, Á., et al. (2018). Solving Inaccuracies in Anatomical Models for Electrocardiographic Inverse Problem Resolution by Maximizing Reconstruction Quality. IEEE Trans. Med. Imaging 37, 733–740. doi:10.1109/TMI.2017.2707413.

Salinet, J., Molero, R., Schlindwein, F. S., Karel, J., Rodrigo, M., Rojo-Álvarez, J. L., et al. (2021). Electrocardiographic Imaging for Atrial Fibrillation: A Perspective from Computer Models and Animal Experiments to Clinical Value. Front. Physiol. 12. doi:10.3389/fphys.2021.653013.

van Dam, P. M. (2017). A new anatomical view on the vector cardiogram: The mean temporal-spatial isochrones. J. Electrocardiol. 50, 732–738. doi:10.1016/J.JELECTROCARD.2017.08.010.

Van Oosterom, A. (2004). ECGSIM: an interactive tool for studying the genesis of QRST waveforms. Heart 90, 165–168. doi:10.1136/hrt.2003.014662.

# Chapter 5

## Improving Electrocardiographic Imaging Solutions: A Comprehensive Study on Regularization Parameter Selection in L-curve Optimization

Rubén Molero[1], Marta Martínez-Pérez[1], Clara Herrero-Martín[1], Jana Reventós-Presmanes[2], Ivo Roca-Luque[2], Lluis Mont[2], Andreu M. Climent[1], María S. Guillem[1]

## Abstract

In electrocardiographic imaging (ECGI), selecting an optimal regularization parameter (λ) is crucial for obtaining accurate inverse electrograms. This study investigates how electrical noise in body surface potential map (BSPM) signals and geometrical inaccuracies affect optimal λ selection via the L-curve optimization. We propose novel criteria for optimal λ selection, accounting for BSPM signal-to-noise ratios and potential geometrical errors. Nineteen atrial simulations (5 of regular rhythms and 14 of atrial fibrillation) were used for computing the ECGI with added white gaussian noise from 40dB to -3dB. Cardiac mesh displacements (1-3cm) were applied to simulate the uncertainty of atrial positioning and study its impact on the L-curve shape. The regularization parameter, the maximum curvature, and the most horizontal angle of the L-curve (β) were quantified. In addition, BSPM signals from real patients were used to validate our findings. L-curve maximum curvature was inversely related to both signal-to-noise ratio and errors in atrial positioning within the thorax. The β angle was found to be directly related to electrical noise and not affected by geometrical errors. Adjustment of λ based on the amount of noise in the data (or on the β angle) allows finding better ECGI solutions than a λ purely found at the corner of the L-curve. We observed that the relevant information in ECGI activation maps is preserved even under the presence of uncertainties when the regularization parameter is correctly selected. The proposed criteria for regularization parameter selection have the potential to enhance the accuracy and reliability of ECGI solutions.

---

Submitted paper

[1] ITACA Institute, Universitat Politècnica de València, València, Spain

[2] Arrhythmia Section, Cardiology Department, Hospital Clínic, Universitat de Barcelona, Barcelona

## 5.1. Introduction

The inverse problem of electrocardiography enables the estimation of the electrical activity on the surface of the heart from body surface electrocardiographic recordings. To obtain activation maps of the cardiac electrical activity, Electrocardiographic Imaging (ECGI) relies on both Body Surface Potential Mapping (BSPM) signals and an estimated geometry of the torso and the heart (Hernández-Romero et al., 2023). ECGI has shown to be consistent with intracavitary data during atrial fibrillation (AF) (Rodrigo et al., 2020, 2021) and has been used to guide ablations (Haissaguerre et al., 2014) or predict the efficacy of AF ablation (Molero et al., 2021; Fambuena-Santos et al., 2023). Nonetheless, the estimation of ECGI signals is an ill-conditioned problem (Hansen, 1992) that is strongly affected by the presence of different sources of noise, such as signal artifacts, geometrical errors and other sources of uncertainty.

Several approaches have been developed to optimize inverse resolution, with zero-order Tikhonov (Tikhonov and Arsenin, 1977) and L-curve optimization being widely adopted by the ECGI community (Salinet et al., 2020). Zero-order Tikhonov consists in minimizing both the error of the solution and the residual error, as described in (1) and it is specially well suited for situations with low signal-to-noise ratios since it allows for a strong smoothing effect that reduces the amount of noise in the solution.

$$\hat{X} = \mathrm{argmin}[||AX - Y||_2^2 + \lambda|LX||_2^2\,] \qquad (1)$$

Where $\hat{X}$ are the estimated epicardial potentials, X are the epicardial potentials, A is the transfer matrix that relates the epicardial potentials and the BSPM signals, Y are the surface potentials, λ is a regularization parameter, and L is a squared matrix that equals the identity matrix in zero-order Tikhonov regularization. The λ value can be chosen by using L-curve optimization, which consists in selecting the λ value that represents a trade-off in the minimization of the two terms in equation 1 or, practically by selecting the corner of the plot of term $||AX - Y||_2^2$ vs. term $||LX||_2^2$ (Pullan et al., 2014). A larger regularization parameter results in more aggressive smoothing of estimated potentials, improving noise rejection at the cost of reduced temporal and spatial resolution.

Whereas identification of the regularization parameter at the corner of the L-curve is a reliable method for low uncertainty situations in which the L-curve shows a sharp corner, this method becomes less reliable when the L-curve does not present a sharp corner, situation that arises under the presence of uncertainties either in the measured signals or the estimated transfer matrix. A selection of a sub-optimal regularization parameter can result in either over-smoothed or noisy estimated epicardial potentials and this, in turn, may result in inaccurate estimations of the underlying electrical activation sequence which may lead to a delivery of an inappropriate ablation therapy.

The main objective of this study is to quantify the impact of different sources of noise (electrical and geometrical) in the inverse problem resolution with zero-order Tikhonov regularization and L-curve optimization. We hypothesized that the search of the optimal regularization parameter should be affected differently by different sources of noise which, in turn, should affect differently the shape of the L-curve. To explore these variations, we used nineteen computer simulations of atrial electrical activity during regular rhythms and AF and ECGI data from two patients referred for ablation. We added different levels of noise before computing the inverse problem and introduced geometrical uncertainty in the inverse problem resolution, both on the simulations and to the patient cases. We analyzed the impact of these sources of noise in the shape of the L-curve, the optimal λ values corresponding to the corner of the L-curve and in the estimated epicardial maps. Finally, we presented a methodology for correcting the λ selection when L-curve optimization provides a sub-optimal solution.

## 5.2. Material and methods

### 5.2.1. Cardiac simulations

Nineteen cardiac simulations were generated: five simulations of regular rhythms, 2 sinus rhythm, 3 atrial flutter (AFL) of five seconds of duration, and 14 of atrial fibrillation (AF) with a duration of ten seconds. We utilized a realistic 3D model of the atrial anatomy for simulation generation. This model comprises 284,578 nodes and 1,353,783 tetrahedrons. (Rodrigo et al., 2017). To simulate electrical remodeling and maintain fibrillation in AF simulations, we varied currents in Ik,ACH, IK1, INa and ICa. We modeled fibrotic tissue by disconnecting nodes ranging from 20% to 60%, and we represented scar tissue by disconnecting all nodes (100%) in the scar region. We employed the Runge–Kutta integration method to solve the differential equation system, leveraging the computational power of a graphic processor unit (NVIDIA Tesla C2075 6G) (Rodrigo et al., 2017). To induce AFL and AF, we implemented an S1 S2 protocol, applying the S2 stimulus at different atrial locations to generate a variety of patterns (Liberos et al., 2016).

To obtain the electrical activity on the torso surface, a mesh of 771 torso nodes was used for all simulations (Aras et al., 2015). The forward problem (Macleod and Buist, 2010) was then computed with the boundary element method to obtain the body surface potentials by multiplying the transfer matrix (A) and the calculated electrograms as in equation (2) (Pullan et al., 2014).

$$\mathrm{Y} = \mathrm{AX} \tag{2}$$

where A was computed by using the boundary element method described in (3):

$$A = [D_{TT} - G_{TH}G_{HH}^{-1}D_{HT}]^{-1} \cdot [G_{TH}G_{HH}D_{HH} - D_{TH}] \tag{3}$$

where D is the coefficient matrix that represents the contribution of the potential of a bounding surface to another, and G is the coefficient matrix representing the contribution of the voltage gradient between two surfaces, the subindex T refers to the surface of the torso and H the surface of the heart (Jorge Pedrón Torrecilla, 2015). After the obtention of the torso potentials, signals from 64 nodes (24 front, 24 back, 8 on each side) were selected for matching the number of electrodes used on patients. BSPM signals were normalized in order to ease the comparison of errors in the inverse problem between different simulations with differences in amplitude.

### 5.2.2. Patient data

Four patients, two with AF, and two with AFL, respectively, admitted for ablation at Hospital Clínic de Barcelona were simultaneously co-registered using CARTO3 (Biosense Webster, Irvine CA, USA) and a 64-lead ECGI (ACORYS MAPPING SYSTEM Corify Care SL, Madrid, Spain). The protocol was approved by the Ethics Committee of the hospital and all the patients gave informed consent. A LGE-MRI was obtained prior to the procedure and segmented with ADAS (ADAS 3D SL, Barcelona, Spain). Torso geometries and lead positioning in each patient were reconstructed by photogrammetry (Molero et al., 2022). Cardiac geometries were obtained by segmentation of MRI images. The BSPM signals from both patients were pre-processed by subtracting the baseline and using a 10th-order Butterworth low-pass filter of 45 Hz.

The first AF patient of 65 y.o. arrived in sinus rhythm, AF was induced by fast pacing from coronary sinus stimulation. Before AF induction, a P-wave segment with a duration of 156ms was selected for computing the inverse problem.

From the second AF patient of 61 y.o., AF signals of 8 seconds of duration were selected and QRST complex was canceled using template subtraction computed with a Principal Component Analysis approach (Castells et al., 2005).

The first AFL patient, aged 66, exhibited a typical flutter pattern, which was revealed using electroanatomical mapping at the beginning of the procedure, eliminating the need for arrhythmia induction. From this patient's BSPM signals, we extracted an individual F-wave of 182ms duration before ablation for inverse problem computation. The second AFL patient, aged 56, presented an atypical flutter pattern. A reentry was detected in the left atrial roof after adenosine perfusion.

## 5.2.3. Modelling the influence of noise

With the objective of studying the effect of different sources of noise on the L-Curve optimization, electrical and/or geometrical noise was added to the simulations and signals from patients.

### 5.2.3.1.Addition of electrical noise.

White gaussian electrical noise was added to the BSPM signals according to (4):

$$\mathrm{Y_N} = \mathrm{Y} + \mathrm{SNR} * \mathrm{N} \tag{4}$$

where Y are the BSPM potentials, either computed after solving (2), or measured on the torso surface of patients and $\mathrm{Y_N}$ are BSPM potentials with added noise. N is a random realization of white noise with mean 0 and standard deviation of 1 at a signal to noise ratio (SNR) at either 40, 30, 20, 10, 3, 0 or -3dBs.

### 5.2.3.2.Addition of geometrical uncertainties

Geometrical noise was added by moving the atrial epicardial mesh from its original location by 1, 2, or 3 cm in the three cartesian axes, simulating physiological displacements of the cardiac anatomy inside the torso or uncertainty on its actual location (Jagsi et al., 2007). For computing the inverse problem taking into account the cardiac mesh displacement, a new transfer matrix ($\mathrm{A_d}$) was computed using (3), where the heart is translated from the location used for the forward problem calculation.

## 5.2.4. Inverse problem calculation

Before solving the inverse problem of electrocardiography after electrical noise addition, the base-line was subtracted by a second-order high-pass filter with a cut-off frequency of 0.67 Hz followed by a Butterworth 10-order low-pass filter with a cut-off frequency 45 Hz (Molero et al., 2022).

Epicardial potentials were estimated by implementing zero-order Tikhonov regularization, according to (5):

$$\hat{X} = \left(A_d^T A_d + \lambda_L L^T L\right)^{-1} A_d^T Y_N \tag{5}$$

Where $\hat{X}$ are the estimated epicardial potentials, $Y_N$ are the measured or simulated BSPM signals with added noise, $A_d$ is the forward matrix with added geometrical uncertainties and $\lambda_L$ is the regularization parameter obtained using L-curve optimization, and L the identity matrix.

### 5.2.4.1.L-curve corner-based selection of $\lambda_L$

The regularization parameter in (5) was found by using the L-curve approach, which consists in finding the corner of the L-curve (Fig. 5.1), following (6-8):

$$\rho(\lambda) = \log_{10}\left(\left|\left|A_d X \ - Y_N\right|\right|_2^2\right) \tag{6}$$

$$\eta(\lambda) = \log_{10}\left(\left|\left|LX\ \right|\right|_2^2\right) \tag{7}$$

$$curvature(\lambda_L) = \frac{\rho' \eta'' - \rho'' \eta'}{((\rho')^2 + (\eta')^2)^{3/2}} \tag{8}$$

The maximum curvature (Hansen and O'Leary, 1993) of the L-curve corresponds with its corner and is considered as the optimal solution of the inverse problem by minimizing the two norms from (6) and (7).

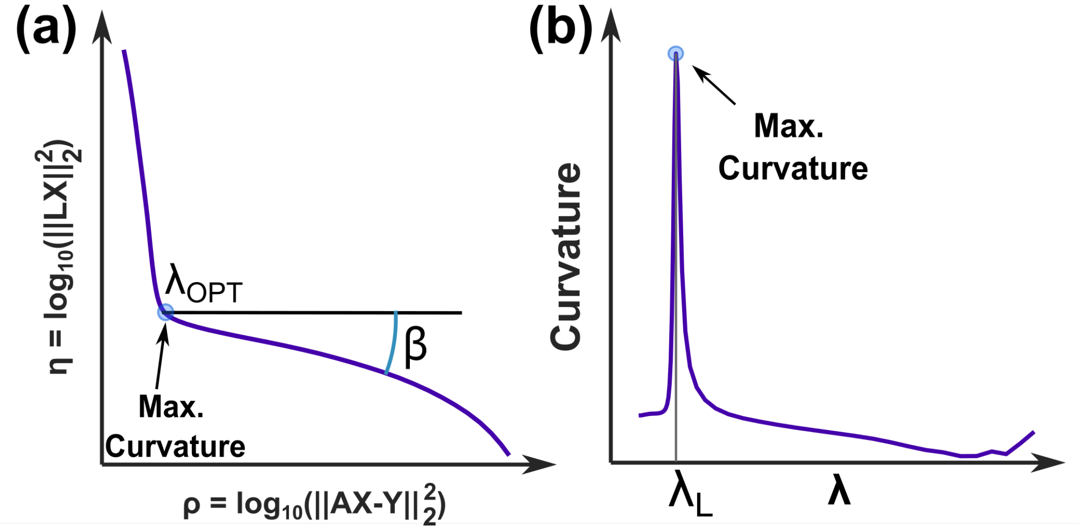

Figure 5.1 Example of an L-curve (A) and the computed geometrical parameters and the curvature (B) for all the explored λ to solve the inverse problem.

### 5.2.4.2.L-curve shape quantification and λ optimization

We defined the angle of the most horizontal component of the L-curve (β), as depicted in Fig. 5.1, as a surrogate of the shape of the L-curve, together with the L-curve curvature, defined in (8).

We proposed an alternative method for λ estimation based on the angle β. This L-curve shape-based approach has been developed as a product of our results, taking into account the influence of noise on the shape of the L-curve. First, to spot statistical differences between the curvatures the β angles obtained for ECGI signals with different SNR and introduced geometrical errors, the normality of the curvatures and β was studied using the Kolmogorov-Smirnov test followed by Student’s t-test with normal samples and Wilcoxon rank-sum test to non-normal samples. Later, to obtain the equation for determining the optimal $\lambda_\beta$, we established a mathematical relationship observed between all the β angles obtained from computing the inverse problems using the simulations of regular rhythms and AF scenarios, incorporating electrical and geometrical uncertainties and the optimal regularization parameter $\lambda_L$ obtained for each case.

### 5.2.4.3.Quantification of ECGI quality

In addition to the simulations, we introduced electrical noise and geometrical uncertainties to the BSPM signals and epicardial meshes of the selected patients. To assess the quality of electrocardiographic imaging reconstructions in these patients after incorporating noise and geometrical uncertainties, we generated local activation time (LAT) maps using ACORYS's proprietary algorithms. LAT maps were computed on both the original ECGI signals and the ECGI signals with added electrical noise and geometrical uncertainties and compared with endocardial activation time maps obtained with CARTO3.

To study the effect of the exploratory range of λ, we computed the inverse problem in an atypical flutter patient using two ranges, from $10^{-15}$ to $10^{-2}$ and from $10^{-15}$ to $10^{-7}$. LAT maps of the resulting ECGI signals were compared with endocardial maps used as a gold standard.

Lastly, on AF signals, after computing the inverse problem, phase singularities (SP) were calculated as described in (Fambuena-Santos et al., 2023). An LGE-MRI image of the fibrotic tissue of the patient was used as a reference for AF substrate burden evaluation to study the correspondence between SP and fibrotic tissue and evaluating the inverse reconstruction (Haissaguerre et al., 2016). SP maps were computed for the original ECGI maps, and the maps with the noises added.

## 5.3. Results

The impact of electrical and geometrical noise was studied separately in populations of simulations of regular and irregular rhythms. Furthermore, we assessed the effect of noise on LAT maps using an example for sinus rhythm simulation and compared it to signals from the patients experiencing atrial flutter and atrial fibrillation.

### 5.3.1. Effect of noise in the inverse problem using atrial simulations

The impact of electrical and geometrical noise on the L-curve for a single simulation and different levels of added uncertainty in inverse problem resolution is shown in Fig. 5.2. The effect of electrical noise (Fig. 5.2A) is reflected in the variation of the shape of the curve. As seen, simulations with higher SNR (warm colors) show a clear L-curve corner with low errors of the norm of the solution. As the SNR decreases, the curve transitions into a more vertical shape and, therefore, an increased value of the β angle. The shape of the L-curve is influenced by the SNR, as it is the value of maximum curvature at its corner (Fig. 5.2D). Higher values of curvature are observed for more ideal situations with low noise levels. The maximum curvature value decreases with increasing noise levels. As it can be observed in Fig. 5.2D, the optimal $\lambda_L$ (corresponding to the λ value with the maximum curvature) is strongly related to the presence of noise: it increases with higher levels of electrical noise, which, resulting in smoother inverse problem solutions.

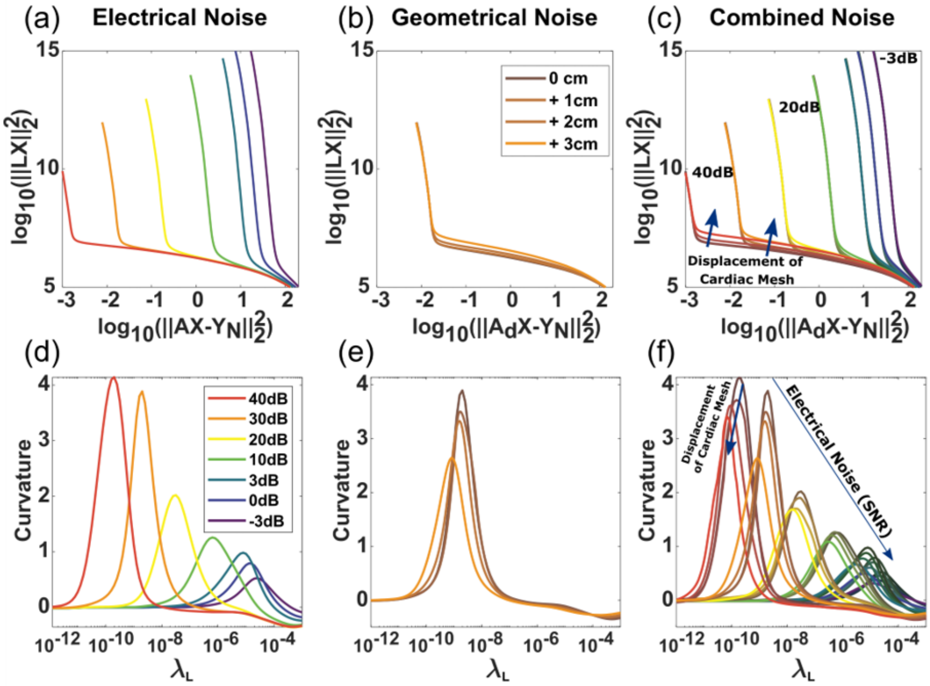

Figure 5.2. Examples of the obtained L-curves and curvatures for an atrial fibrillation simulation and different levels of uncertainty in the inverse problem resolution. In top panels L-curves and shown whereas in bottom panels the corresponding curvatures of the different L-curves are depicted. Panels A and D: different levels of added electrical noise to the simulated BSPM signals. Panels B and E: different translations of the atrial mesh before solving the inverse problem (geometrical noise). Panels C and F: combined electrical and geometrical noise.

The impact of geometrical noise on the shape of the curve is shown in Fig. 5.2B. The color saturation indicates the displacement introduced in the heart location before solving the inverse problem (1 to 3 cm). In this case, a larger geometrical error (more displacement of the atrial mesh) is translated into an increased residual error (y axis). The maximum curvature (Fig. 5.2E) decreases for increased displacements, although the obtained optimal $\lambda_L$ values are in the same range and do not change significantly. Both sources of noise combined are shown in panel C, where the general trend of curvature decay is observed for both noises combined. As seen in Fig. 5.2F., curvature and optimal $\lambda_L$ values are largely related with the level of noise. However, for low SNRs, neither curvature values nor optimal $\lambda_L$ values can be unambiguously attributed to the noise level in the presence of geometrical uncertainty.

In summary, electrical and geometrical noise impact the L-curve's shape, maximum curvature, and optimal $\lambda_L$ values, with electrical noise having a more pronounced effect, whereas low SNRs make it challenging to attribute curvature and optimal $\lambda_L$ values to noise levels in the presence of geometrical uncertainty.

### 5.3.1.1.Effects of noise in the curvature and shape of the L-curve

For all the explored SNR levels and geometrical displacements, the values of maximum curvature and the β angle are shown in Fig. 5.3. The maximum curvatures for all simulations (top row) revealed higher values in more ideal scenarios with high SNR, reaching up to 10 for sinus rhythm and AFL simulations (Fig. 5.3A) and up to 5 for atrial fibrillation (Fig. 5.3E), with some overlap between different SNR ranges (i.e., curvature for regular rhythms at 40 dBs equals 7.21 ± 1.45 vs. 5.43 ± 1.96 for 30 dBs). For low SNR values (under 10dB), the overlap in curvature values for different SNR ranges is more evident, which hinders the differentiation between noise levels based on this parameter (i.e., curvature for regular rhythms at 0 dBs equals 1.44 ± 0.34 vs. 1.14 ± 0.28 for -3 dBs). Curvature exhibits a negative correlation with the geometrical error, although this dependency appeared to be weaker than the dependency of curvature with electrical noise (i.e., curvature for 0 cm equals 4.35 ± 2.89 vs. 2.27 ± 1.63 for a 3cm displacement). For AF simulations curvature values were found to be smaller than those found for regular rhythm simulations and the dependency of curvature with geometrical uncertainties is almost neglectable (i.e., curvature for 0 cm equals 1.85 ± 1.3 vs.  to 1.57 ± 1.29 for a 3cm displacement).  Values of the angle β showed a positive relationship with added noise: smaller amounts of added noise are related with smaller β values (i.e., β for 40dB ,equals to 10.74º ± 3 vs. 59.14º ± 3.32 for -3dB for regular rhythms simulations). No overlap in β values for low SNR levels is observed, whereas some overlap in β values is observed for low added noise situations (i.e., β for 0 dBs SNR and regular rhythms equals 50.84 ± 3.01 vs. 59.14 ± 3.28 for -3 dBs SNR, $p < 0.01$). Regular rhythms showed lower values of β than those obtained for AF simulations. For this reason, we analyzed them separately. In none of the explored simulations was a clear dependency of β on geometrical noise observed.

Consequently, in the presence of varying levels of noise and geometrical displacements, maximum curvature and β angle values demonstrate a stronger dependency on electrical noise than on geometrical errors, with some overlap between SNR ranges, affecting the differentiation of noise levels based on these parameters.

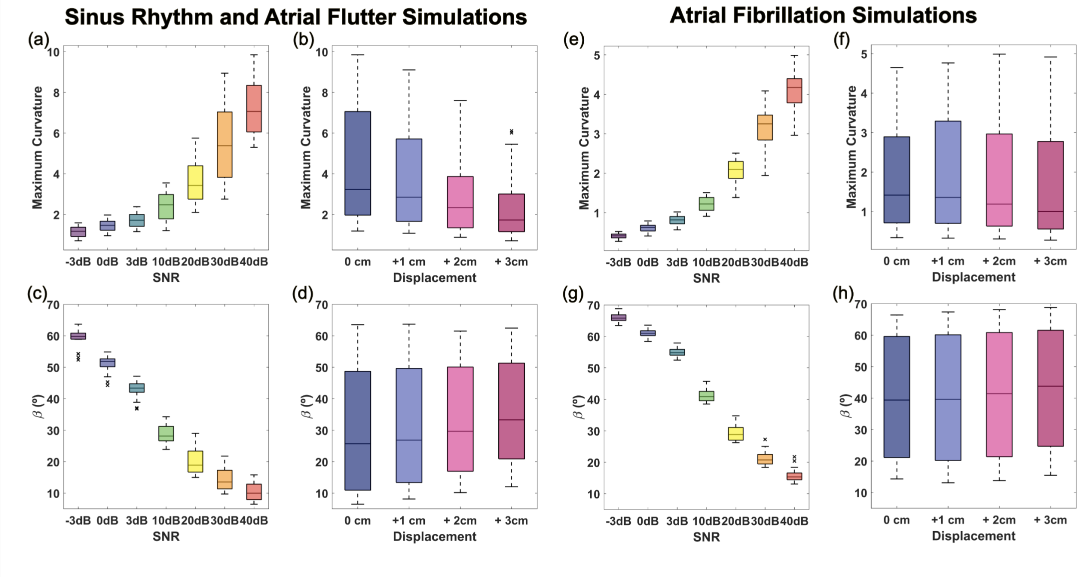

Figure 5.3. Values of maximum curvature of the L-curve and β angle for 5 regular rhythms and 14 atrial fibrillation simulations for different levels of signal-to-noise ratio and geometrical displacement of the cardiac geometry. In top panels maximum curvatures are depicted whereas in bottom panels beta values are represented. In panels A, E, C and G, curvature/beta values for all combined electrical and geometrical noise are grouped by the amount of added electrical noise. In panels B, D, F, H curvature/beta values for all combined electrical and geometrical noise are grouped by the amount of added geometrical noise.

### 5.3.1.2.Effects of noise in the optimal regularization parameter

The relationship between the optimal $\lambda_L$ according to the L-curve method and both the curvature and β is shown in Fig. 5.4. A negative correlation between the noise level, $\lambda_L$ and the curvature is observed. Higher values of $\lambda_L$ are obtained when solving the inverse problem computed with signals with more added electrical noise for both regular atrial ($R^2$=0.69) and irregular rhythms ($R^2$=0.91). Regular rhythms, when compared to AF, can be reconstructed with smaller $\lambda_L$ values, most likely because of a lower complexity of electrical patterns. It can be observed again that electrical noise is strongly related with the optimal $\lambda_L$ values selected by the L-curve method and that the optimal $\lambda_L$ values, therefore, are strongly related to the β angle, especially for AF simulations ($R^2$=0.94).

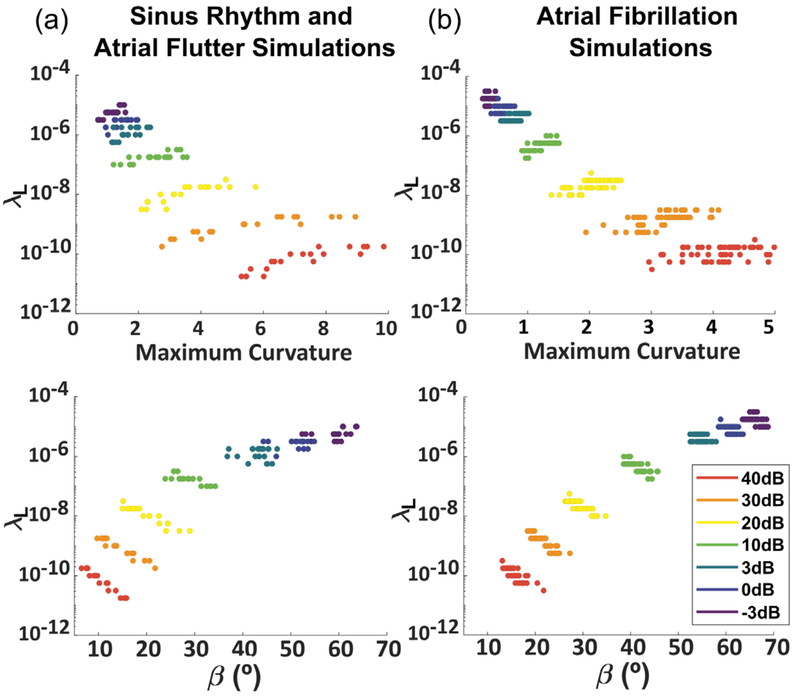

Figure 5.4. Values of maximum curvature of the L-curve and β angle for regular rhythms (A) and atrial fibrillation simulations (B) versus the optimal regularization parameter ($\lambda_L$) obtained for different levels of signal-to-noise ratio (color-coded) and displacement of the cardiac geometry (shape-coded).

Both regular rhythms and AF presented similar trends with the difference in the optimal $\lambda_L$ that resulted in smaller values for regular rhythms. We described the relationship between β and λ using the following exponential equations.

For signals from a regular rhythm:

$$\lambda_\beta = 10^{-20.86 \cdot \beta^{-0.33}} \tag{9}$$

For atrial fibrillation signals:

$$\lambda_\beta = 10^{-37 \cdot \beta^{-0.48}} \tag{10}$$

In summary, the optimal regularization parameter ($\lambda_L$) was negatively correlated with noise level and curvature, and strongly associated with the β angle, particularly for atrial fibrillation simulations, indicating that electrical noise significantly impacts the L-curve method's choice of optimal $\lambda_L$ values.

Figure 5.5 demonstrates the relationship between the optimal $\lambda_L$ and the computed LAT map, showcasing an example of a sinus rhythm simulation (A). Panel B displays LAT maps for ECGI signals with different signal-to-noise ratios and various regularization parameters for the same simulation. Panel C presents LAT maps for ECGI signals with different cardiac geometry displacements at a 20dB SNR and different regularization parameters for the same simulation. Maps computed with the optimal regularization parameter are marked with a star (*).

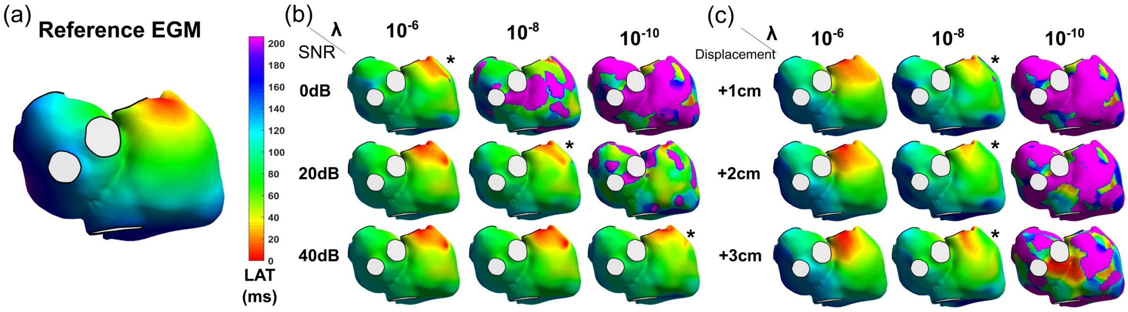

Figure 5.5. Example of local activation times (LAT) map of a sinus rhythm (SR) simulation (A). LAT maps obtained for ECGI signals obtained with different signal-to-noise ratios and different regularization parameters of the same SR simulation (B). LAT maps obtained for ECGI signals obtained with different displacements of the cardiac geometry with a 20dB SNR and different regularization parameters of the same SR simulation (C). Maps computed with the optimal regularization parameter are denoted with a star (*).

All maps obtained using the optimal $\lambda_L$ determined by the L-curve method closely resemble the reference LAT map (panel A). Again, the optimal $\lambda_L$ values were found to be more strongly related with the amount of noise of the BSPM signals than on the correct estimation of the position of the atria inside the thorax. LAT maps obtained $\lambda$ values higher than the optimal one show high similarity compared to the gold standard, although the origin of the excitation becomes more blurred. On the contrary, maps obtained with smaller $\lambda$ values showed poorer results, likely due to noise amplification caused by the smaller $\lambda$ values.

For the optimal $\lambda_L$ ($10^{-8}$) and higher values, the LAT map accurately reflected the origin of the beat at the same location as the gold standard. The displacement, although does impact on the accuracy of the estimated LAT map, was found to be unrelated to the optimal $\lambda_L$ selected in accordance with the L-curve method, as it was not modified from the value obtained without the displacement of the heart mesh.

This example illustrates how the optimal regularization parameter ($\lambda_L$) is more influenced by the noise in the signals than by the atria's position, and maps with optimal $\lambda_L$ values closely resemble the reference LAT map even with errors in the location of the cardiac geometry.

## 5.3.2. Patient examples

### 5.3.2.1. Effect of noise on ECGI maps from patients

In Fig. 5.6, LAT maps from an atrial flutter patient are shown together with its corresponding electro-anatomical LAT map. In both maps a counterclockwise reentry around the tricuspid valve can be observed. LAT maps obtained after addition of noise on the BSPM signals allow determining the same counterclockwise reentry around the tricuspid valve. As we observed in the computer simulations, the computed L-curves show an increased error in the solution with increased values of electrical noise added to the BSPM signals. The maximum curvature, as expected, decreased with lower SNR values (curvature without added noise equals 1.61 vs 0.46 for -3dBs added noise) whereas $\beta$ increased with the added noise ($\beta$ without added noise equals 55.1° vs. 73.03° for -3dBs added noise). The optimal $\lambda_L$ increased from the ECGI computed without added noise: $3.31 \cdot 10^{-6}$ vs. $7.59 \cdot 10^{-6}$ for -3dBs, which allowed filtering the noise for the more unfavorable situation, thus allowing the estimation of reliable LAT maps.

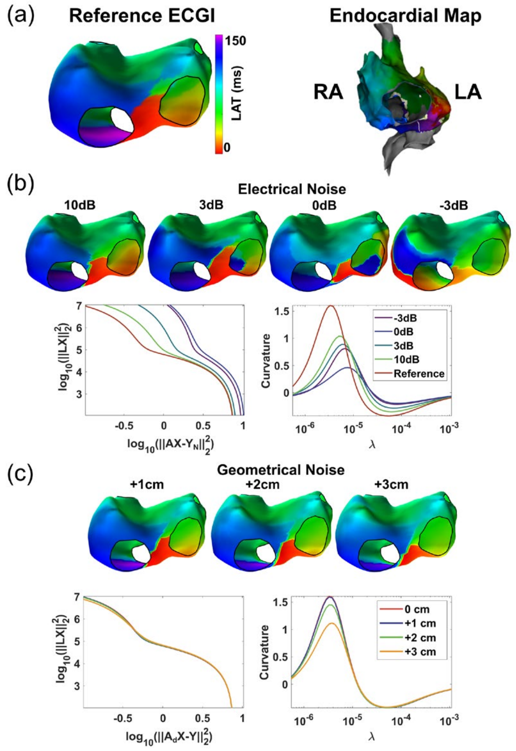

Figure 5.6. Example of local activation (LAT) maps of an atrial flutter patient obtained with ECGI and electro-anatomical mapping (A). LAT maps for adding electrical noise to body surface signals to the patient and the respective variation of the L-Curve and curvature for the explored regularization parameters (B). LAT maps obtained for displacements of the cardiac geometry and the variations of the L-curve and curvature (C).

LAT maps obtained after a displacement of the cardiac geometry whereas solving the inverse problem are also shown in Fig. 5.6. The obtained LAT maps showed a reentry at the same location in the same direction even if the atria are mislocated in up to 3 cm. The range of values for the optimal $\lambda_L$ did not change with the location error, nor the values of β, (β without translation equals 55.1º vs. 53.86º for a translation of 3 cm), whereas the maximum curvature decreased with the translation (curvature without translation equals 1.61 vs. 1.12 for a translation of 3 cm).

An additional example for an AF patient is shown in Fig. 5.7. The SP map obtained with the reference ECGI (panel A) presented SP on the posterior wall (red-colored), with a higher SP presence between the right pulmonary veins (PPVV), matching with the presence of fibrotic tissue (also in red). Independently of the SNR, the location of the SP was found at the same region of the left atrium, with less dispersed SPs in the posterior wall for lower SNR, because larger $\lambda_L$ values were chosen for decreasing SNR values and filter the inverse solution. Additionally, the obtained SP histograms computed after introducing geometrical errors showed a concentration of SP at the same location between both right PPVV. SP maps under both noisy situations did not present significant modifications with the original one.

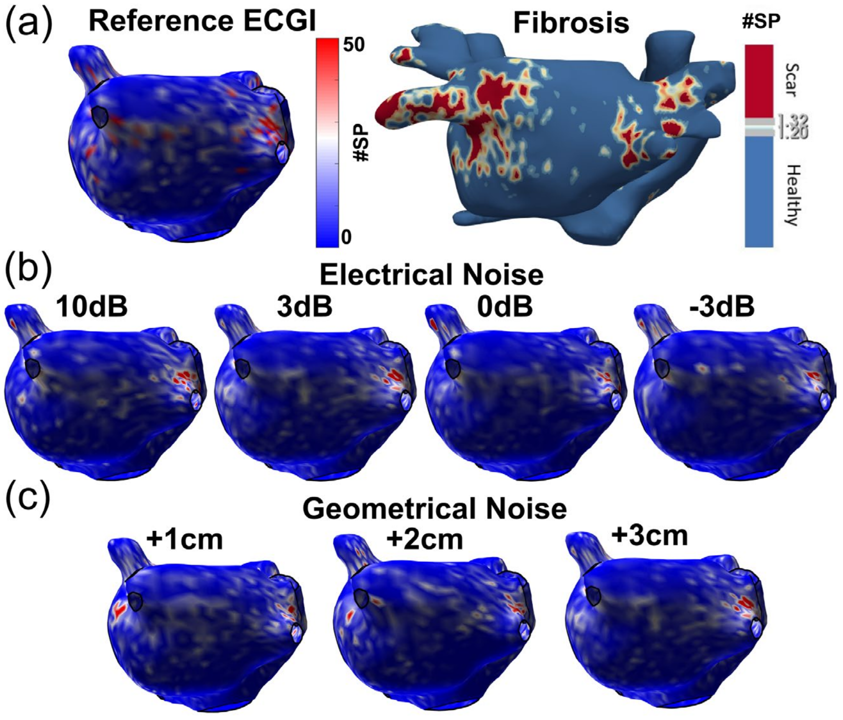

Figure 5.7. Example of singularity point (SP) histogram of an atrial fibrillation patient obtained with ECGI, and fibrosis map obtained with LGE-MRI (A). SP histograms for adding electrical noise to body surface signals to the patient (B). SP histograms obtained for displacements of the heart geometry (C).

In summary, these patient examples demonstrate that reliable LAT and SP maps can be obtained despite added noise and cardiac geometry displacement, with optimal $\lambda_L$ values adapting to filter noise effectively.

#### 5.3.2.2.Regularization optimization based on the L-curve shape

An example of the applicability of the relationship found between λ and β is shown in Fig. 5.8. LAT maps of a signal during pacing from the coronary sinus in an AF patient are displayed in panels A-B. The map obtained with a regularization parameter selected at the corner of the L-curve (A) shows a propagation consistent with coronary sinus stimulation but with an inconsistent early activation site on the right atrial appendage (RAA).

In this case, the $\lambda_L$ value obtained at the corner of the L-curve, is out of the range of values observed based on the value of β described in Fig. 4 (expected $\lambda_L$ between $10^{-5}$ and $10^{-6}$). By solving the inverse problem with a corrected $\lambda_\beta$ value increased by one order of magnitude (see (9) for details on the estimation of the λ value based on the measured β), the LAT map is more consistent with a coronary sinus stimulation and the right atrial appendage no longer appears as an earliest activation site. Selecting a regularization parameter based on the β angle is also helpful to define an exploratory range for regularization parameters, which should be chosen based on the noise present in the BSPM signals.

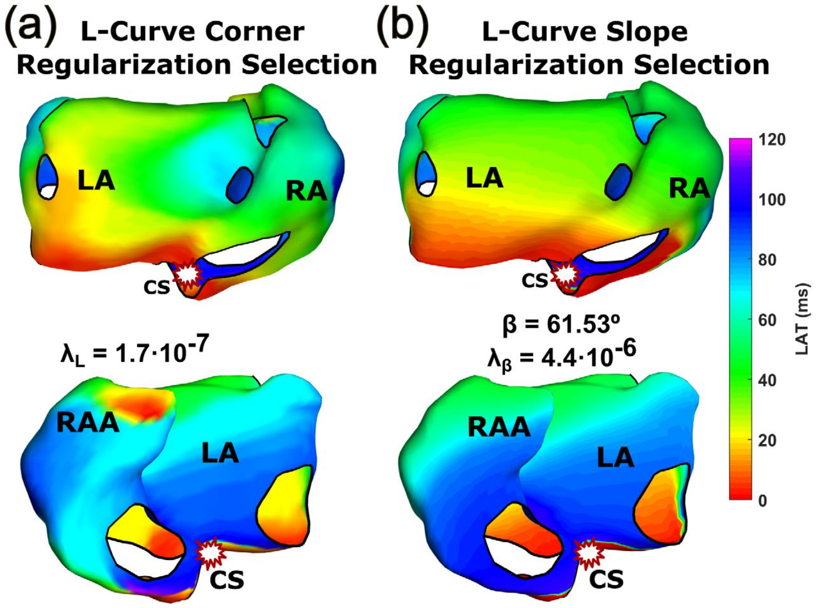

Figure 5.8. LAT maps of atria stimulated in the coronary sinus (CS). Panel A shows the LAT map with the optimal $\lambda_L$ obtained with the L-curve method and panel B shows the map obtained based on the angle β. Top row show the back part of the atrium and bottom row the front part.

In Fig. 5.9, LAT maps from an AFL patient were obtained using different exploratory ranges of $\lambda$. In panel A, the map was computed with a wide exploratory range of $\lambda_L$ between $10^{-15}$ to $10^{-2}$, observing an-L-curve with a double L shape (Fig. 5.9B) with two local maxima of the curvature. The maximum curvature value corresponds with $\lambda_L = 2.1 \cdot 10^{-5}$ and by using this regularization parameter showed the same macro-reentry found on the electroanatomical map. However, for a narrower exploratory range between $10^{-15}$ to $10^{-7}$, the $\lambda_L$ found equals $5.2 \cdot 10^{-12}$ and the resulting map (C) does not allow identifying the macroreentry due to noise amplification by a small chosen parameter. In this situation, a $\lambda$ value derived from the $\beta$ angle (following (9)) results in a $\lambda_\beta = 8.8 \cdot 10^{-6}$, and allows estimating again the macro-reentrant pattern.

In summary, the relationship between $\lambda$ and $\beta$ can be utilized to optimize regularization, resulting in more accurate LAT maps that better reflect the expected activation patterns.

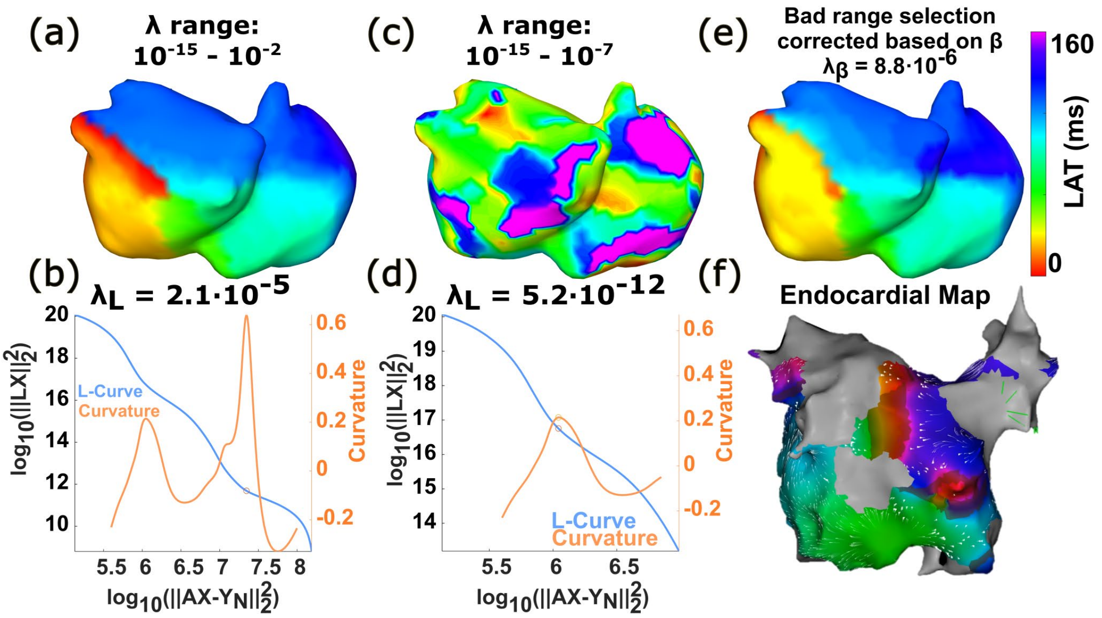

Figure 5.9. LAT map of an atrial flutter obtained with a wide range of $\lambda_L$ (A) and its L-curve and curvature (B). LAT map of an atrial flutter obtained with a sub-optimal range of $\lambda_L$ (C) and its L-curve and curvature (D). Panel E shows the LAT map corrected based on $\beta$ obtained from the L-curve of panel D. Endocardial coherence map (F).

## 5.4. Discussion

In this paper, we demonstrated the significant impact of various noise sources on the selection of optimal regularization parameter to solve the inverse problem of the electrocardiography, taking into account the signal-to-noise ratio of body surface potential map recordings and potential geometrical errors.

We evaluated the influence of electric and geometric noise sources when employing the L-curve optimization method. By introducing the β angle as a novel metric, we provided new criteria to adjust the regularization parameter when the maximum curvature of the L-curve does not offer a clear indication of the optimal value. This approach enhances our understanding of the relationship between noise sources and the L-curve method, allowing for more accurate and reliable ECGI analyses.

### 5.4.1. Effects of Noise in the L-curve

In previous studies, we have shown that a geometrical uncertainty of the estimation of the heart geometry affects to the L-curve curvature (Rodrigo et al., 2018) and this information was used to improve the location of the heart mesh inside the torso. Furthermore, other geometrical errors (Molero et al., 2022, Huiskamp et al. 1989) and uncertainties (Wang et al., 2010) have been reported as sources of errors in the inverse solution. In this study, we reveal that the maximum curvature of the L-curve is influenced by other sources of noise, such as electrical noise in the signals. Whereas the effects of electrical noise (Cheng et al., 2003) and filtering (Bear et al., 2021) on ECGI have been explored, their impact on regularization and the robustness of the analysis have not been previously reported. We propose a method to distinguish between electrical and geometrical noise based on the slope of the predominantly horizontal component of the L-curve.

We found an inverse relationship between the amount of noise in BSPM recordings and the maximum curvature of the L-curve. Although both geometric and electrical noise can decrease the maximum curvature of the L-curve, increasing $\lambda_L$ only benefits the ECGI solution in the presence of electrical noise, as this allows for noise reduction by smoothing the inverse electrograms, but does not overcome the errors introduced by geometrical noise. Our analysis of the L-curve shape revealed a direct relationship between the β value and electrical noise levels. Therefore, the proposed method can help find the optimal regularization parameter when the $\lambda_L$ values appear small for the amount of noise present in the signal, offering an alternative to identifying the corner of the L-curve when it does not exhibit an L-shape

Additionally, we demonstrated that the search space for $\lambda_L$ depends on the SNR of the BSPM signals and that this search space can be estimated based on the curvature of the β angle, tackling the problem of determining an optimal search range of this parameter. Our study describes the optimal regularization parameters that should be used in zero order Tikhonov regularization for a set of SNR levels, suggesting that small values of $\lambda_L$ can be employed in low noise situations but should be avoided when significant noise is present.

Moreover, Fig. 9 illustrates how the explored range of λ could result in sub-optimal solutions even though an L-curve is identified and the range of $\lambda_L$ is falling withing the range of the singular values of the inverse matrix (Hansen, 2001).

Lastly, we demonstrated the feasibility of estimating SNR of BSPM signals from the β angle. We observed that adding of noise above a certain SNR level (10 dBs to 20 dBs) does not affect L-curve shape, possibly indicating that the SNR level already present in our BSPM signals ranged between 20 and 10dBs.

#### 5.4.1.1.Rhythm-dependent effect of noise on the L-curve shape

Differences on the effect of noise on the L-curve shape were found between AF and regular rhythms, and consequently on the ECGI signals. During AF, the irregularity of the electrical propagation is reflected in higher residual errors than during non-fibrillatory rhythms even for the same SNR and, therefore, the shapes of the L-curve differ between rhythms. For this reason, we conducted separated analysis for fibrillating and non-fibrillating rhythms and proposed different space search for the regularization parameter for both types of rhythms.

### 5.4.2. Effects of noise in the extracted ECGI maps

As the L-curve shape changes, we anticipated finding ECGI maps that reflected the amount of noise added to the BSPM signals. We observed that, independently of the SNR and the displacement of the cardiac mesh, the relevant information of LAT maps (i.e., the center of the macroreentry of the AFL example) remains preserved even under the presence of these uncertainties when the regularization parameter is correctly selected. Additionally, equivalent results were found for singularity points histograms, where reentries were found at the same location as the original ECGI-derived histograms without electrical noise and geometrical uncertainties added. This demonstrates the robustness of the ECGI maps when the regularization parameter is accurately determined, despite the presence of noise and other geometrical uncertainties.

### 5.4.3. Limitations

In this study, we explored the effect of different sources of noise in ECGI for different atrial rhythms. Even though the difference in the L-curve variations between AF and regular rhythms was clear, more simulations of regular rhythms and more cardiac geometries should be explored in future studies.

Only two primary sources of noise were considered in this study. Other sources of uncertainty may affect the shape of the curve and the regularization, such as cardiac motion, different conductivities of the inner organs (Ramanathan and Rudy, 2001), etc. Future research might determine the impact of these additional sources of uncertainty in the ECGI resolution.

## 5.5. Conclusion

In conclusion, this study has demonstrated the significant impact of different sources of noise on the selection of the optimal regularization parameter in ECGI. For the first time, we have proposed new criteria for selecting optimal regularization parameters that take into account the signal-to-noise ratio of body surface signals and potential geometrical errors. By analyzing the L-curve shape and establishing a relationship between the β angle and the electrical noise level, we have developed a method that enables better differentiation between electrical and geometrical noise, leading to improved ECGI maps and more reliable clinical information.

The findings presented in this paper have the potential to enhance the accuracy and reliability of ECGI solutions specially during complex patterns such as AF, which could ultimately improve patient care and outcomes. As the field of ECGI continues to advance, incorporating these novel techniques will be crucial for obtaining accurate and meaningful data to guide clinical decisions and patient management.

## Ackowledgements

This work was supported by Agencia Estatal de Investigación (RYC2018-024346-I, PID2020-119364RB-I00), and Generalitat Valenciana and European Social Fund (ACIF/2020/265 and ACIF/2021/205). This research has received funding from the European Institute of Innovation and Technology (EIT) under grant agreement No 220385. This European body receives support from the Horizon 2020 research and innovation programme.

# References

Aras, K., Good, W., Tate, J., Burton, B., Brooks, D., Coll-Font, J., et al. (2015). Experimental Data and Geometric Analysis Repository - EDGAR. J. Electrocardiol. 48, 975–981. doi:10.1016/j.jelectrocard.2015.08.008.

Bear, L. R., Serinagaoglu, Y., Good, W. W., Svehlikova, J., Coll-Font, J., van Dam, E., et al. (2020). The impact of torso signal processing on noninvasive electrocardiographic imaging reconstructions. IEEE Trans. Biomed. Eng., 1–1. doi:10.1109/tbme.2020.3003465.

Castells, F., Mora, C., Rieta, J. J., Moratal-Pérez, D., and Millet, J. (2005). Estimation of atrial fibrillatory wave from single-lead atrial fibrillation electrocardiograms using principal component analysis concepts. Med. Biol. Eng. Comput. 43, 557–560. doi:10.1007/BF02351028.

Cheng, L. K., Bodley, J. M., and Pullan, A. J. (2003). Effects of experimental and modeling errors on electrocardiographic inverse formulations. IEEE Trans. Biomed. Eng. 50. doi:10.1109/TBME.2002.807325.

Fambuena-Santos, C., Hernández-Romero, I., Molero, R., Climent, A. M., and Guillem, M. S. (2023). AF driver detection in pulmonary vein area by electropcardiographic imaging : Relation with a favorable outcome of pulmonary vein isolation. 14, 1–11. doi:10.3389/fphys.2023.1057700.

Haissaguerre, M., Hocini, M., Denis, A., Shah, A. J., Komatsu, Y., Yamashita, S., et al. (2014). Driver domains in persistent atrial fibrillation. Circulation 130, 530–538. doi:10.1161/CIRCULATIONAHA.113.005421.

Haissaguerre, M., Shah, A. J., Cochet, H., Hocini, M., Dubois, R., Efimov, I., et al. (2016). Intermittent drivers anchoring to structural heterogeneities as a major pathophysiological mechanism of human persistent atrial fibrillation. J. Physiol. 594, 2387–2398. doi:10.1113/JP270617.

Hansen, C. (1992). Analysis of discrete ill-posed problems. Soc. Ind. Appl. Math. 34, 561–580. doi:https://doi.org/10.1137/1034115.

Hansen, P. C. (2002). The L-curve and its use in the numerical treatment of inverse problems. J. Biomed. Inform. 35, 51. doi:10.1016/s1532-0464(02)00008-4.

Hansen, P. C., and O'Leary, D. P. (1993). The Use of the L-Curve in the regularization of discrete ill-posed problems. SIAM J. Sci. Comput. 14, 1487–1503. doi:10.1137/0914086.

Hernández-Romero, I., Molero, R., Fambuena-Santos, C., Herrero-Martín, C., Climent, A. M., and Guillem, M. S. (2023). Electrocardiographic imaging in the atria. Med. Biol. Eng. Comput. 61, 879–896. doi:10.1007/s11517-022-02709-7.

Huiskamp, G., and Van Oosterom, A. (1989). Tailored versus realistic geometry in the inverse problem of electrocardiography. IEEE Trans. Biomed. Eng. 36, 827–835. doi:10.1109/10.30808.

Jagsi, R., Moran, J. M., Kessler, M. L., Marsh, R. B., Balter, J. M., and Pierce, L. J. (2007). Respiratory motion of the heart and positional reproducibility under active breathing control. Int. J. Radiat. Oncol. Biol. Phys. 68, 253–258. doi:10.1016/J.IJROBP.2006.12.058.

Liberos, A., Bueno-Orovio, A., Rodrigo, M., Ravens, U., Hernandez-Romero, I., Fernandez-Aviles, F., et al. (2016). Balance between sodium and calcium currents underlying chronic atrial fibrillation termination: An in silico intersubject variability study. Hear. Rhythm 13, 2358–2365. doi:10.1016/j.hrthm.2016.08.028.

MacLeod, R., and Buist, M. (2010). The Forward Problem of Electrocardiography in Comprehensive Electrocardiology, eds P. W. Macfarlane, A. V. Oosterom, O. Pahlm, P. Kligfield, M. Janse, and J. Camm (London: Springer), 247–298.

Molero, R., González-Ascaso, A., Hernández-Romero, I., Lundback-Mompó, D., Climent, A. M., and Guillem, M. S. (2022). Effects of torso mesh density and electrode distribution on the accuracy of electrocardiographic imaging during atrial fibrillation. Front. Physiol. 13. doi:10.3389/fphys.2022.908364.

Molero, R., Soler Torro, J. M., Martínez Alzamora, N., M. Climent, A., and Guillem, M. S. (2021). Higher reproducibility of phase derived metrics from electrocardiographic imaging during atrial fibrillation in patients remaining in sinus rhythm after pulmonary vein isolation. Comput. Biol. Med. 139, 104934. doi:10.1016/j.compbiomed.2021.104934.

Pedrón-Torrecilla, J., Rodrigo, M., Climent, A. M., Liberos, A., Pérez-David, E., Bermejo, J., et al. (2016). Noninvasive estimation of epicardial dominant high- frequency regions during atrial fibrillation. J. Cardiovasc. Electrophysiol. 27, 435–442. doi: 10.1111/jce.12931

Pullan, A. J., Cheng, L. K., Nash, M. P., Ghodrati, A., Macleod, R., and Brooks, D. H. The inverse problem of electrocardiology. Model. Simul. Appl 13, 175–190,. doi:10.1007/978-3-319-04801-7_6.

Ramanathan, C., and Rudy, Y. (2001). Electrocardiographic imaging: II. Effect of torso inhomogeneities on noninvasive reconstruction of epicardial potentials, electrograms, and isochrones. J. Cardiovasc. Electrophysiol. 12, 241–252. doi:10.1046/j.1540-8167.2001.00241.x.

Rodrigo, M., Climent, A. M., Hernández-Romero, I., Liberos, A., Baykaner, T., Rogers, A. J., et al. (2020). Non-invasive assessment of complexity of atrial fibrillation: correlation with contact mapping and impact of ablation. Circ. Arrhythmia Electrophysiol. 13, e007700. doi:10.1161/CIRCEP.119.007700.

Rodrigo, M., Climent, A. M., Liberos, A., Fernández-Avilés, F., Berenfeld, O., Atienza, F., et al. (2017). Technical considerations on phase mapping for identification of atrial reentrant activity in direct- and inverse-computed electrograms. Circ. Arrhythmia Electrophysiol. 10, e005008. doi:10.1161/CIRCEP.117.005008.

Rodrigo, M., Guillem, M. S., Climent, A. M., Liberos, A., Hernández-Romero, I., Arenal, Á., et al. (2018). Solving inaccuracies in anatomical models for electrocardiographic inverse problem resolution by maximizing reconstruction quality. IEEE Trans. Med. Imaging 37, 733–740. doi:10.1109/TMI.2017.2707413.

Rodrigo, M., Waddell, K., Magee, S., Rogers, A. J., Alhusseini, M., Hernandez-Romero, I., et al. (2021). Non-invasive spatial mapping of frequencies in atrial fibrillation: correlation with contact mapping. *Front. Physiol.* 11. doi:10.3389/fphys.2020.611266.

Salinet, J., Molero, R., Schlindwein, F., Karel, J., Rodrigo, M., Rojo-Alvaraez, J. L., et al. (2020). Electrocardiographic imaging for atrial fibrillation: a perspective from computer models and animal experiments to clinical value. 1–47. *Front. Physiol.* 12. doi:10.3389/fphys.2021.653013.

Tikhonov, A., and Arsenin, V. (1977). Solution of Ill-posed Problems. New York, NY: John Wiley & Sons.

Wang, L., Wong, K. C. L., Zhang, H., Liu, H., and Shi, P. (2010). How much geometrical detail do we need in cardiac electrophysiological imaging? A generic heart-torso representation for fast subject-specific customization. In: Camara, O., Pop, M., Rhode, K., Sermesant, M., Smith, N., Young, A. (eds) Statistical Atlases and Computational Models of the Heart. STACOM 2010. Lecture Notes in Computer Science, vol 6364. Springer, Berlin, Heidelberg. doi: 10.1007/978-3-642-15835-3_24

# Chapter 6

## Filtering Strategies of Electrocardiographic Imaging Signals for Stratification of Atrial Fibrillation Patients

Rubén Molero[1], Ismael Hernández-Romero[1], Andreu M Climent[1], María S Guillem[1]

### Abstract

**Background and objective:** Electrocardiographic imaging (ECGI) has been used for guiding atrial fibrillation (AF) ablation, identifying reentrant activity by phase analysis with promising results. The objective of this study is to identify the best post-processing configuration for reentrant activity detection that better differentiates AF patients with different prognoses after catheter ablation.

**Methods:** ECGI signals of 24 AF patients before pulmonary vein isolation (PVI) were recorded. Patients were classified based on recurrence 6 months after PVI. Reentrant metrics were compared using 3 types of post-processing: none, sinusoidal recomposition (SRC), and narrow band-pass filtering centered at the highest dominant frequency (NB HDF). Different thresholds for rotor duration were also compared (0.5, 1, and 1.5 turns).

**Results:** The use of raw ECGI signals with a threshold of 1 turn presented the optimal processing to identify PVI-positive responders ($p<0.05$). NB HDF showed a better ability to find statistical differences between patients than SRC.

**Conclusion:** Aggressive filtering of AF ECGI signals does not improve rotor identification to predict PVI outcome. Restrictive rotor duration thresholds diminish patient stratification. This definition of a post-processing strategy that allows patient stratification can be used for the improvement of the standard of care for finding the best candidates for PVI.

---

R. Molero, I. Hernández-Romero, A. M. Climent, and M. S. Guillem, “Filtering strategies of electrocardiographic imaging signals for stratification of atrial fibrillation patients,” Biomed. Signal Process. Control, vol. 81, p. 104438, Mar. 2023.

[1] ITACA Institute, Universitat Politècnica de València, València, Spain

## 6.1. Introduction

Atrial fibrillation (AF) is the most common cardiac arrhythmia, and maintenance can be partially attributed to drivers that cause reentrant electrical activity on the surface of the atria (Guillem et al., 2016). This arrhythmia can be terminated by invasive procedures like pulmonary vein isolation (PVI), an ablation procedure that has been shown to be effective for restoring sinus rhythm. Prior studies have shown that ablation of reentrant drivers and/or focal sites improves the results of the ablation procedures as compared to PVI only (Narayan et al., 2012; Haissaguerre et al., 2014). Identifying these reentrant patterns with current invasive mapping technologies is challenging, and for this reason, noninvasive alternatives that offer a panoramic view of both atria, i.e., electrocardiographic imaging (ECGI), can be useful for the identification of AF drivers. ECGI allows estimating the epicardial electrical activity by using body surface electrocardiograms and the information of the anatomy of the patient. Several studies have made use of ECGI to guide ablation procedures in patients with AF (Haissaguerre et al., 2013; 2014) with promising results.

With the objective of validating ECGI signals during AF, we have shown that complexity metrics of propagation patterns of intracardiac and ECGI mapping in AF patients are correlated (Rodrigo et al., 2020). However, it is still unknown the relevance of either a lack of accuracy of ECGI, poor accuracy of the intracardiac mapping technology with a limited spatial resolution and areas that cannot be mapped by basket catheters, or a poor post-processing strategy for rotor identification on the discrepancies observed between ECGI and electrogram mapping metrics during AF. Likewise, an agreed strategy of how to post-process ECGI signals is not defined to evaluate the reentrant activity of AF; thus, in this article, we compare different strategies to evaluate rotor identification.

Rotors are typically identified by phase mapping after computing the Hilbert transform of ECGI signals (Zlochiver et al., 2008; Naratan et al., 2012; Rodrigo et al., 2017). Hilbert transform allows finding an instantaneous correspondence between the time series of an ECGI signal into phases of the activation sequence. Singularity Points (SP) are sites where a propagation pattern pivots around and are found as sites where all phases converge. In previous studies using physiological computer models of AF, we have shown that connected SPs should be required to complete at least one turn to be considered as rotors in order to achieve enough specificity (Rodrigo et al., 2017b). However, this threshold has not been validated with human data, in which far field contributions still present after solving the inverse problem do result in tracking discontinuities in rotor detection. Under these uncertainties that occur in real patient data, real rotors lasting for several turns can be incorrectly detected as multiple rotors lasting less than one turn and, therefore, a too restrictive threshold may result in a lack of sensitivity.

In order to improve potential limitations of sensitivity in the detection of rotors, several post-processing filtering approaches have been proposed: none, sinusoidal recomposition filtering (Kuklik et al., 2015), and filtering the signals with a narrow band-pass filter centered at the highest dominant frequency (Rodrigo et al., 2017b). The objective of the present study is to identify which are the best post-processing techniques to identify atrial rotors, including both the filtering strategy employed for conditioning the ECGI signals and the number of turns required for SPs to be considered as rotors. We will base our selection criteria on maximizing the differences in the variability of rotor metrics of patients with a favorable and unfavorable outcome after pulmonary vein isolation (PVI), under the assumption that the underlying electrical characteristics of these two groups of patients should be different and identifiable by ECGI. Furthermore, we hypothesized that the variability of reentrant metrics should be lower in patients with good PVI outcome. A preliminary version of this work has been reported (Molero et al., 2020).

## 6.2. Methods

### 6.2.1. Patient signal and geometry acquisition

Signals from 24 AF patients (18 females and 6 males; 61.8 ± 14.3 years old) were obtained by Body Surface Potential Mapping (BSPM) with 57 electrodes placed on the torso surface prior to a wide circumferential PVI procedure (Molero et al., 2021). Patients gave informed consent, and the protocol was approved by the Ethics Committee of Hospital Gregorio Marañón, Madrid, Spain (reference 475/14). Two groups of patients were defined according to the success of PVI 6 months after the intervention: patients with sinus rhythm after 6 months (N=13), and patients with atrial arrhythmia after 6 months (recurrence of AF, atrial tachycardia, or atrial flutter, N=11).

The torso geometry of the patients and the electrode location were obtained using video recording and reconstructed by photogrammetry techniques (Remondino, 2004). MRI/CT scan images were also obtained, and both the atria and the torso were segmented using ITK-SNAP software (Yushkevich et al., 2006). Torso and atrial geometries were co-registered using the torso reference from MRI/CT images.

BSPM signals were recorded at 57 locations on the torso with 0.05 to 500Hz filtering and a sampling frequency of 1 kHz (Rodrigo et al., 2020). Two signals per patient were segmented (4 ± 0.31s) and then band-pass filtered between 2 and 45 Hz to eliminate noise, and ventricular activity (QRST segment) was canceled lead by lead by Principal Component Analysis (PCA) approach (Castells et al., 2005). Inverse computed electrograms (ECGI) of each BSPM signal were calculated by using zero-order Tikhonov regularization and L-curve optimization (Rodrigo et al., 2018).

### 6.2.2. ECGI post-processing

With the objective of adequately identifying AF drivers, 3 ECGI signal processing alternatives, Fig. 6.1, were applied before phase calculations were computed. Metrics based on raw ECGI signals (no further filtering or other post-processing) were compared with the same signal with two different filters, namely sinusoidal recomposition (SRC) and narrow band-pass filtering (NB HDF).

- Sinusoidal Recomposition (SRC) (Kuklik et al., 2015) consists of decomposing each signal into a set of sinusoidal wavelets with an amplitude proportional to the slope of the signal at a given time instant, Fig. 6.1B. The period of the wavelet is computed as the mean cycle length of each ECGI signal derived from the dominant frequency of the electrogram. Welch's periodogram was calculated to obtain the power spectral density of electrograms using a 2000ms window.

- Narrow band-pass filtering centered at the Highest Dominant Frequency (NB HDF) was applied to ECGI signals with a bandwidth of 1 Hz (HDF ± 0.5 Hz), Fig. 6.1C. HDF was calculated as the 95 percentile of the dominant frequency of all ECGI signals together. To obtain dominant frequencies, the power spectral density was computed by Welch's periodogram as in previous works (Rodrigo et al., 2014; 2017).

### 6.2.3. Reentrant activity detection

The instantaneous phase of ECGI signals was computed using Hilbert's transform (Narayan et al., 2012a). This transform allows assigning a value between $-\pi$ and $+\pi$ to each sample of the signal. The reentrant atrial activity was defined as a phase progression from $-\pi$ to $+\pi$ monotonically increasing or decreasing around a single point in the epicardium. Singularity points (SP) were required to be identified in at least two of three concentric rings (Rodrigo et al., 2017b). To consider a SP as a rotor, three different temporal thresholds were compared: 0.5, 1, and 1.5 turns. As a result of this thresholding criteria, nine alternatives: 3 filtering strategies and 3 different rotor duration thresholds, were evaluated. Furthermore, for each alternative SPs histograms were calculated to represent the cumulative SPs in each node of the atria surface.

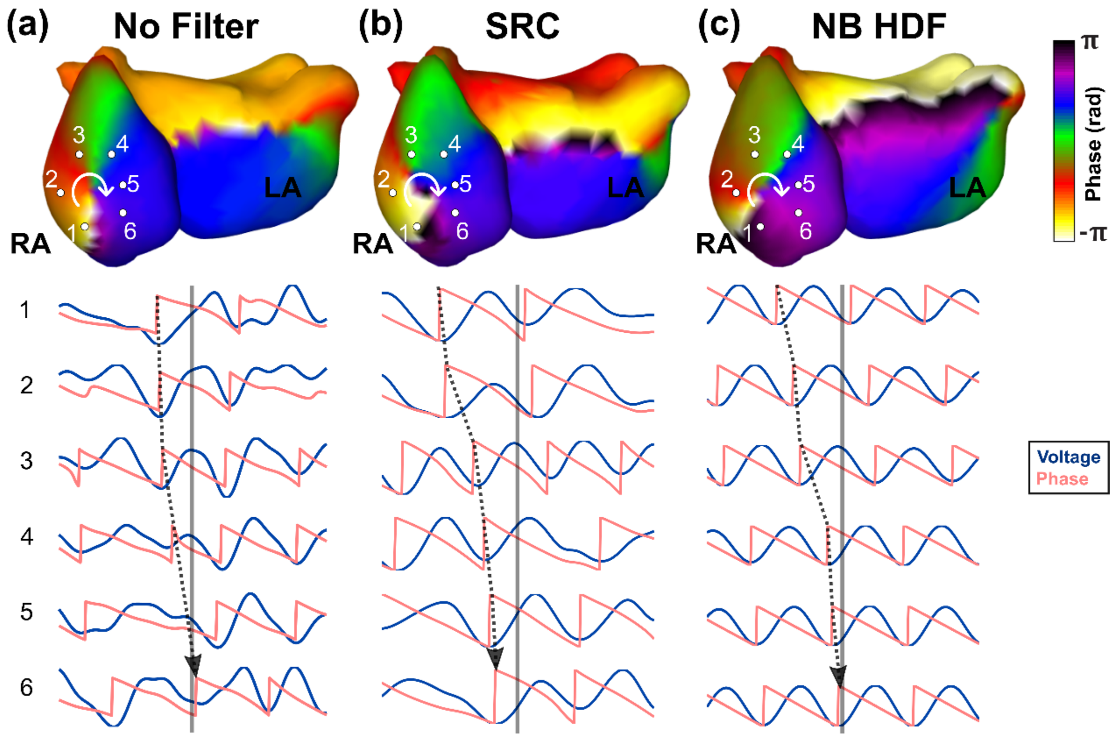

Figure 6.1. Example of consecutive ECGI signals around a phase singularity for each type of processing (no filter, sinusoidal Recomposition (SRC), and narrow band-pass filter at the highest dominant frequency (NB HDF). Blue signals represent the voltage value, and pink signals the phase obtained with Hilbert's transform. Solid line on top of the electrograms represents the time instant chosen for representation in the phase maps depicted and dotted line represents the course of the reentry, most evident in the transition of phases between -π and π.

### 6.2.4. Reentrant activity evaluation and statistical analysis

To evaluate each rotor detection alternative, different metrics were calculated. First, in order to make our SP detection independent of the sampling frequency, we quantified the amount of singularity points per time unit (SP/ms). The mean duration of rotors was also computed as the mean duration of detected rotors. Finally, the Shannon entropy of the SP histogram was calculated. The maximum displacement of each rotor was also calculated as the maximum distance between two phase singularities of the same rotor.

The mean value of metrics extracted from two segments of signals from the same patient was calculated for each post-processing alternative. To study the variability in time of the metrics, the absolute difference between metrics extracted from both signal segments was computed and calculated for the totality of the patients for each post-processing case: ΔSP/ms, ΔRduration and ΔEntropy.

To detect if there are significant differences in the variability of metrics extracted from two ECGI signals and between the two groups of patients (PVI responders or nonresponders with bad outcome), the normality of the values was studied using the Kolmogorov-Smirnov test followed by Student's t-test with normal samples and Wilcoxon rank-sum test to non-normal samples for each post-processing alternative.

For a more comprehensive evaluation of the ability to identify each patient group, a metric derived from the three presented metrics was computed, normalizing each of the metrics based on their minimum and maximum value and averaging them. Univariate logistic regression of this overall ratio was calculated for each of the post-processing techniques to quantify the ability to discriminate between patient groups. Receiver operating characteristic curves (ROC) of each case was computed as well as the resultant area under the curve (AUC). Furthermore, confusion matrices of each logistic regression were obtained using the optimal operating point of the ROC curve as a threshold.

## 6.3. Results

### 6.3.1. Reentrant activity analysis

In Fig. 6.2, an example of the effect of the different rotor detection alternatives is presented. Phase maps of the same patient at the same time instant for the 9 studied alternatives are shown. As it can be observed, the different filtering strategies do impact the phase distribution, and, therefore, rotors are identified at different locations even for the same time instant. With the less restrictive rotor duration threshold, we can observe differences between the different filtering strategies. Using raw signals, the number of short-lasting detected rotors is large because either they represent short changes in the direction of the phase that show an altered substrate or the tracking may be lost at several time frames. SRC resulted in fewer detected rotors mostly at the same locations as those detected with the raw signals, but also short-lasting. NB HDF filtering shows longer-lasting rotors and at similar locations than for the raw signals.

Restrictions on rotor duration do have an impact on the location of the detected rotors since short-living rotors or rotors that disappear transiently are not considered, which is more evident for a 1.5 turns threshold: both raw and SRC do not present rotors meeting this temporal restriction.

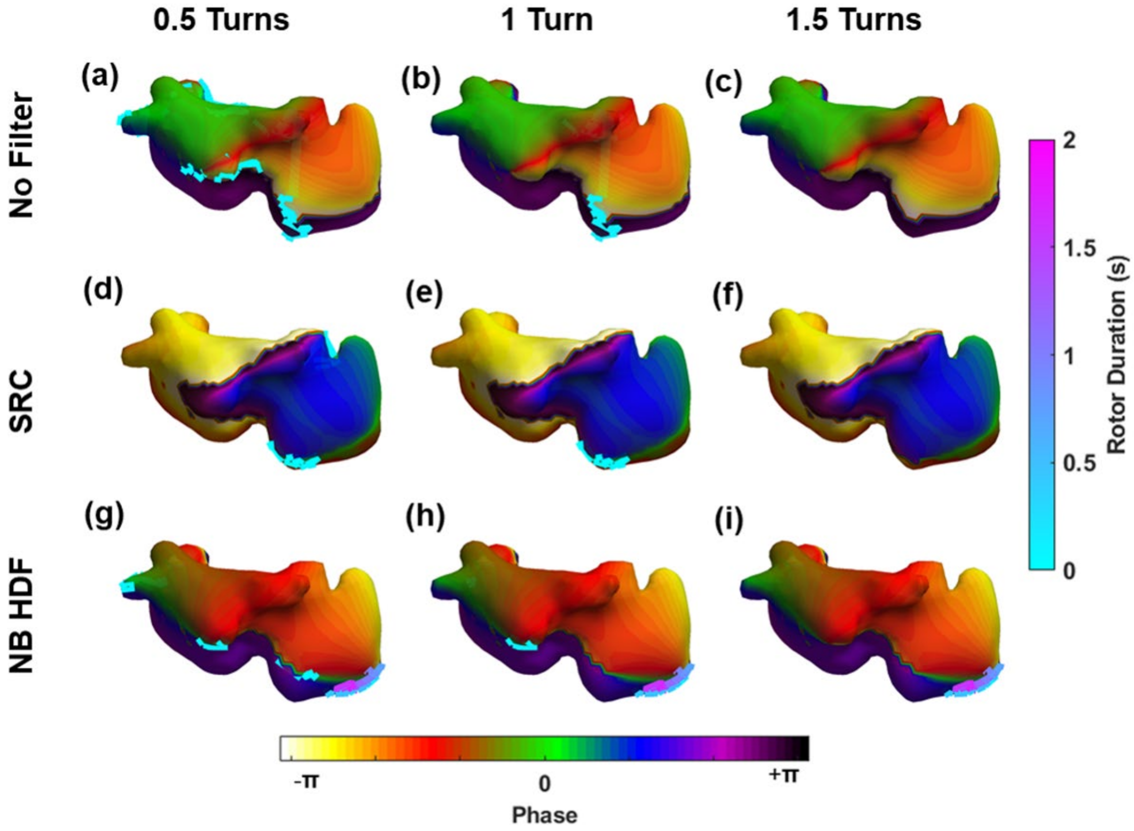

Figure 6.2. Phase maps of an ECGI signal with different types of processing (no filter, sinusoidal Recomposition (SRC), and narrow band-pass filter at the highest dominant frequency (NB HDF) using different singularity point threshold detection 0.5, 1, and 1.5 turns. Colors projected on the atrial surface represent the instantaneous phase at the sample time instant. Lines depicted on top of the maps indicate the presence of rotors at the sample time instant blue-pink color indicates the evolution in time and space of each rotor.

In Fig. 6.3, a summary of SP identification over a segment for the same patient depicted in Fig. 6.2 is illustrated. All the maps clearly show the presence of reentrant activity in the pulmonary veins and the lower part of the right atrium. Rotor histograms obtained after SRC and raw signals are very similar to each other for any rotor duration threshold. NB HDF maps show a larger amount of SPs detected compared with the other two types of processing techniques. It can be observed a decreased rotor detection when the rotor duration threshold is more restrictive (higher number of turns) for no filtered and SRC histogram maps. Despite the detection of fewer amount of rotors with a higher turn threshold, the area where the rotors anchor was preserved. On the contrary, maps with 0.5 turns as the threshold showed an increased reentrant activity that may be caused by the consideration of areas of lower changes in phase as SPs.

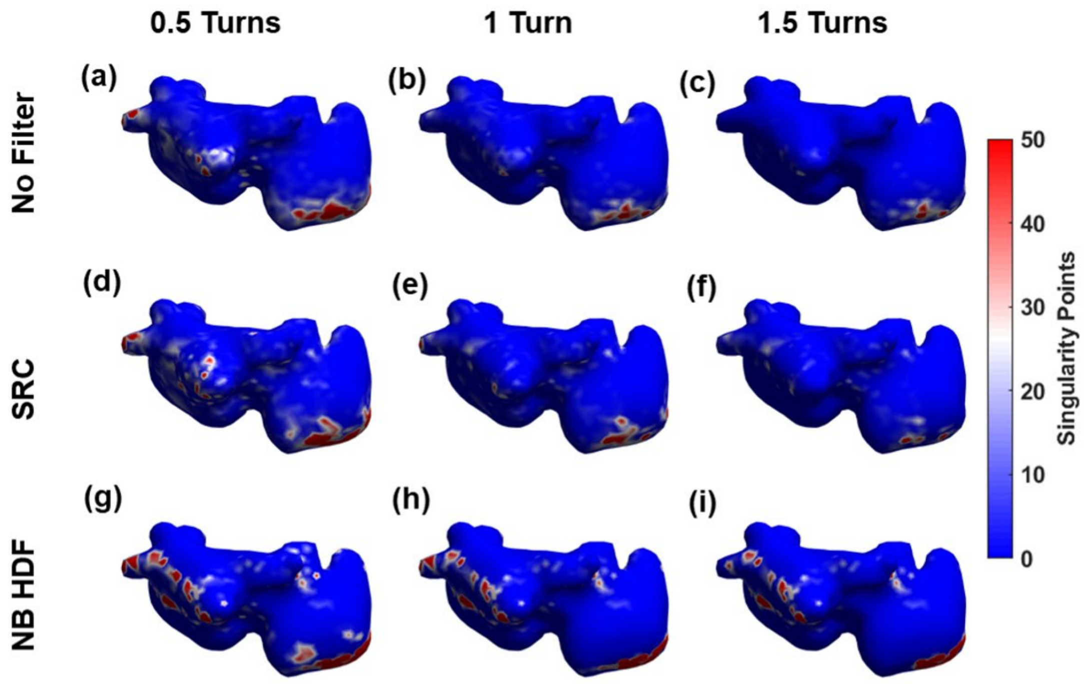

Figure 6.3. Singularity point histogram of an ECGI signal with different types of processing (no filter, sinusoidal Recomposition (SRC), and narrow band-pass filter at the highest dominant frequency (NB HDF) using different singularity point threshold detection 0.5, 1, and 1.5 turns. The color projected on the atrial surface represents the number of rotors detected at each atrial site.

Temporal evolution of rotor detection with the different strategies presented is depicted in Fig. 4, where each row in each panel represents a rotor, and the vertical axis represents time. The length of each row represents the duration of each rotor, and the color shows its displacement across the atria. Raw and SRC ECGI signals show a similar number of rotors for each turn threshold (i.e. 0.5 turns, 169 vs. 175 rotors respectively). In phase maps obtained both without filtering or with SRC, rotors last shorter and present longer trajectories than with NB HDF filtering.

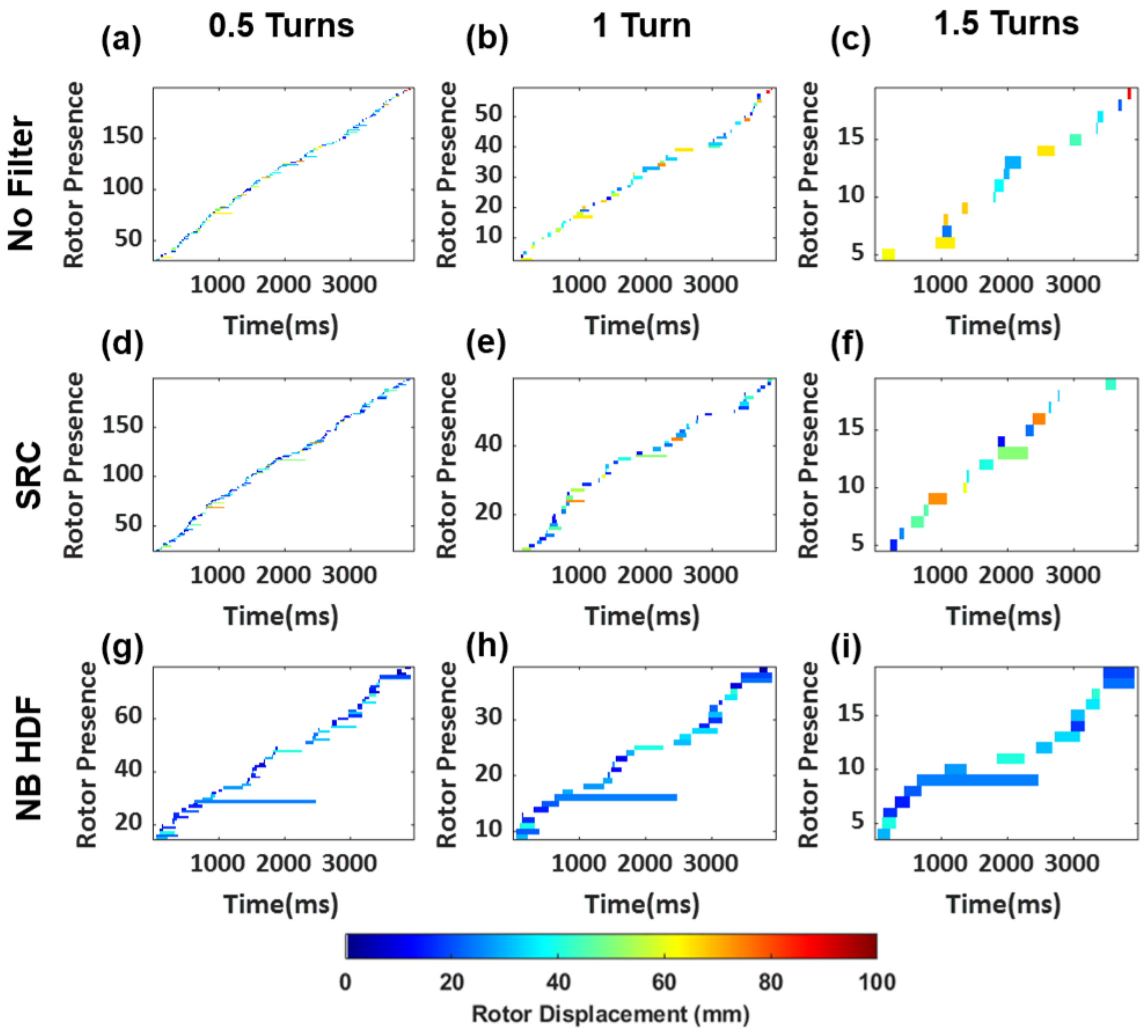

Figure 6.4. Rotor presence during a 4-seconds recording with different types of processing (no filter, sinusoidal Recomposition (SRC), and narrow band-pass filter at the highest dominant frequency (NB HDF) using different singularity point threshold detection 0.5, 1, and 1.5 turns. Each row represents a rotor detected ordered by time at which each rotor first appears. Color represents the maximum rotor displacement.

As observed in Fig. 6.2-6.4, filtering, in general, tended to stabilize rotors, making them last longer and be less fragmented in time and space. Again, NB HDF filtering resulted in more stable rotors. A clear reduction in the number of rotors is shown when the duration threshold is increased as compared with less restrictive thresholds.

These findings can be further observed in the results from the whole population of 24 patients depicted in Fig. 6.5A-C, where the mean and standard deviation values of two measurements of all metrics are presented. Raw signals presented very similar values compared to SRC filtering of SP/ms and spatial entropy. The number of SP/ms was significantly higher ($p<0.01$) for NB HDF signals than for both raw or SRC signals (11.4 ± 8.07, 9.77 ± 6.89, and 9.4 ± 6.05, respectively, for 0.5 turns). By increasing the threshold for SP detection, the number of detected SP/ms decreased for the three filtering methods, although with more intensity for raw and SRC signals and for NB HDF to a lower extent.

Rotor duration, as depicted in Fig 6.5B, presented values under 0.2s for raw signals. The duration was increased when filters were applied, especially in NB HDF filtered signals (1.5 turns SRC: 0.22 ± 0.07s, HDF filtering: 0.47 ± 0.10s). In addition, rotor duration presented increased values when thresholds were more restrictive (no filter at 0.5 turns: 0.07 ± 0.02s, 1 turn: 0.1 ± 0.03s and 1.5 turn: 0.14 ± 0.04s). Therefore, both filtering and restrictive thresholds avoid the detection of reentrant patterns of shorter duration.

Spatial entropy presented fewer differences when filters were applied compared to other metrics. In this metric, the highest values were found for raw signals, with more similar results between SRC and NB HDF signals (1 turn: 9.23 ± 0.53, 8.68 ± 0.72, and 8.46 ± 0.69, respectively). Besides, spatial entropy showed lower values at higher turn thresholds. On the contrary, NB HDF filtered signals were not significantly decreased with restrictive thresholds (0.5 turns: 8.68 ± 0.66, 1 turn: 8.46 ± 0.69, and 1.5 turns: 8.23 ± 0.73). Overall, filtering and restrictive thresholds terminate with less complex SP histograms with lower spatial entropy.

In Fig. 6.5D-F, the variability of each metric is presented for each post-processing alternative. Filtering did not reduce the temporal variability of the different metrics as it was expected, especially for NB HDF filtering. In Fig. 6.5D it can be observed that ΔSP/ms presented similar results for raw and filtered signals, being decreased for higher turn thresholds. On the contrary, ΔSP/ms for NB HDF presented higher values, less affected by the turn threshold (1 turn raw: 13.8 ± 21.5 vs. NB HDF: 25.5 ± 40.5). The ΔRduration was found to be lower in raw signals, showing low differences in the variability for the different thresholds. Nevertheless, the threshold on ΔRduration presented more drastic effects for the filtering signals, which presented rotors of more variable durations for higher turn thresholds. Finally, ΔEntropy showed higher values when the threshold increased, and higher variations between thresholds were seen for both raw (1 turn: 0.27 ±0.29, 1.5 turns: 0.43 ± 0.46), and SRC filtered signals (1 turn: 0.38 ±0.49, 1.5 turns: 0.58 ± 0.49).

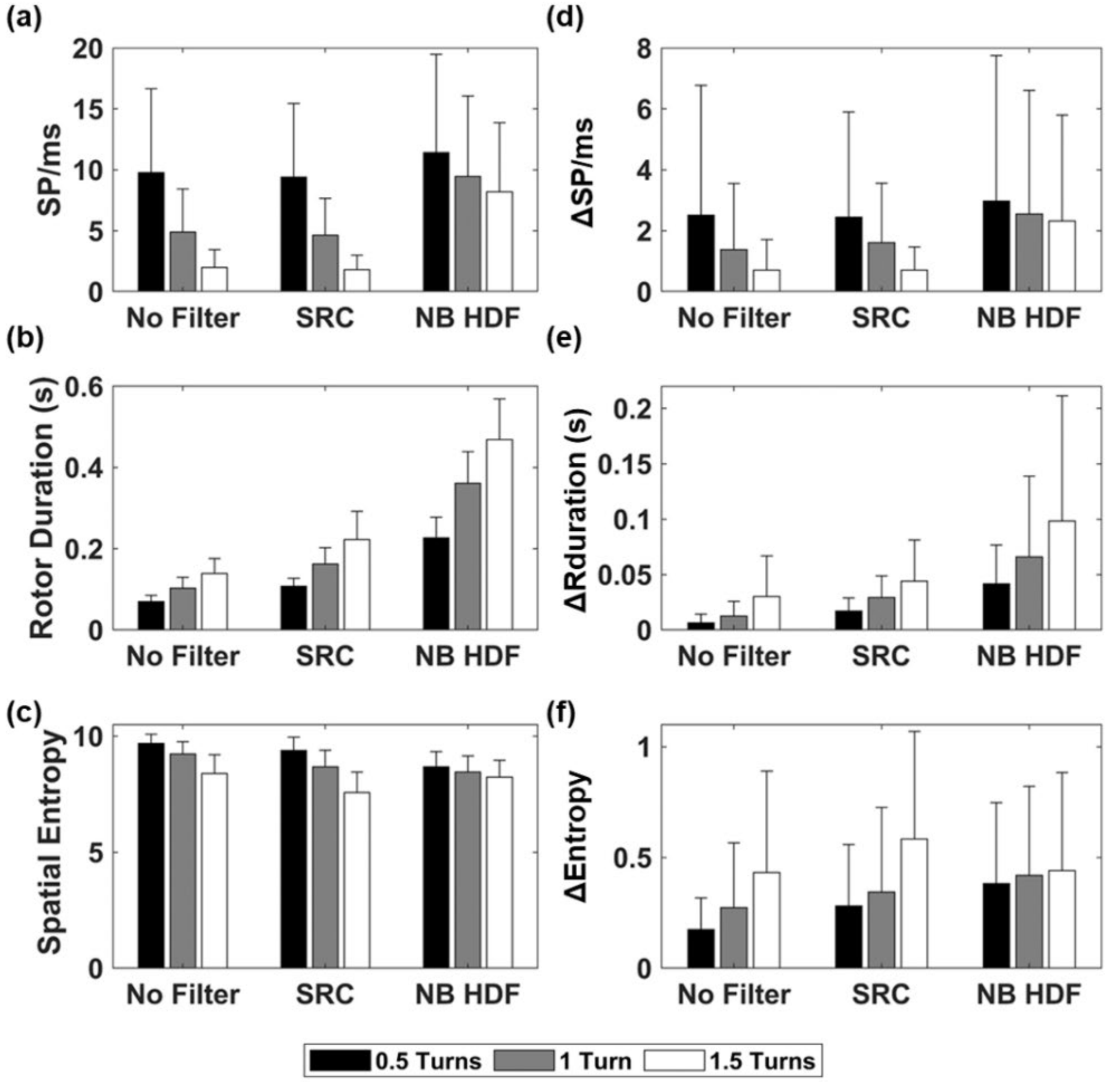

Figure 6.5. Mean and standard deviation A-C values for each metric using different post-processing methods (no filter, sinusoidal Recomposition (SRC), and narrow band-pass filter at the highest dominant frequency (NB HDF) and different singularity points detection thresholds: 0.5 (black), 1 (gray) and 1.5 turns white). Variability between metrics extracted from two segments of each patient for the named post-processings D-F.

## 6.3.2. Post-processing effects and PVI outcome

Values of the absolute difference between two metrics were compared between two groups of patients depending on their outcome 6 months after PVI. Fig. 6.6 shows boxplot diagrams of the quantified reentrant metrics for both the sinus and arrhythmia recurrence groups of patients. In general terms, patients with successful PVI at 6 months showed a lower variability of the metrics independently of the post-processing technique employed compared with patients with poor PVI outcome, although most of these differences were non-significant. The best post-processing alternative for discriminating between patients with a later successful PVI ablation was found to be raw signals and a duration threshold of 1 turn with p values for ΔRduration and ΔEntropy of 0.03 and 0.04, respectively.

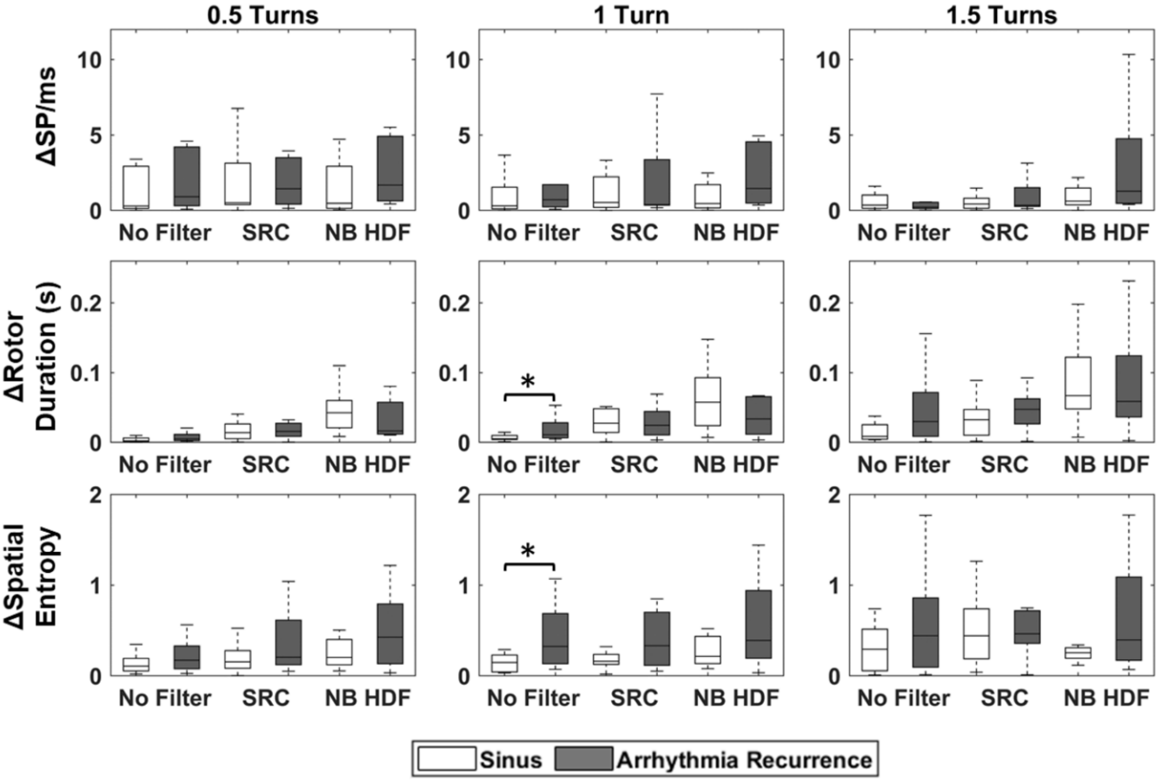

Figure 6.6. Mean absolute difference between two measurements for reentrant metrics for patients classified by PVI outcome. Each row of panels represents each metric and each column of panels the thresholds used to detect a rotor. In each panel, on the left boxplots, no filtering is applied, middle: sinusoidal recomposition (SRC) and right: narrow band-pass filter at the highest dominant frequency (NB HDF). White boxplots represent patients with good PVI outcome, gray boxplots patients with bad PVI outcome. Outliers were removed for a better visualization of the results.

Receiver operating characteristic curves were computed with the result of the univariate logistic regression of the normalized value of the combination of the variability of each alternative. In Fig. 6.7, ROC curves and area under the curve values are presented. The highest AUC value, 0.8, was found for raw signals with 1 turn threshold, which is consistent with the results displayed in Figure 5. Both SRC and NB filtering were less successful for discriminating between patients with different outcomes, with the highest AUC equal to 0.71 and 0.62, respectively. Confusion matrices show that for the best AUC, a sensitivity of 100% was obtained, with low values of specificity, that were higher in other post-processing alternatives that presented a worse general patient classification.

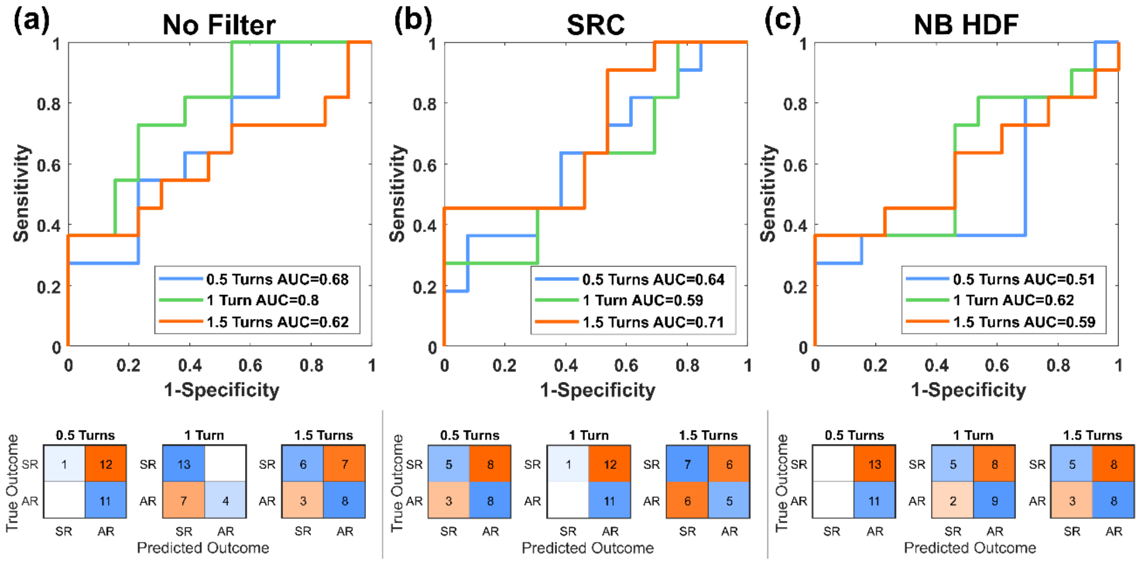

Figure 6.7. Receiver operating characteristic curves and values of area under the curve (AUC) for the logistic regression with normalized mean variability of the three metrics for patients' classification based on PVI outcome for each filtering strategy and confusion matrices obtained with the optimal operating point of the ROC curve (SR: sinus rhythm, AR: arrhythmia recurrence). ROC curves obtained with 0.5, 1, and 1.5 phase singularities thresholds are presented in blue, green, and orange, respectively.

## 6.4. Discussion

In this paper, we present a comparison of different signal post-processing methods for reentrant activity detection in ECGI maps. We have shown that the interpretation of ECGI maps is dependent on the post-processing strategies employed, although results show that rotor location is stable and comparable between the proposed alternatives. The main findings of our work are that it is possible to find statistical differences in the variability of phase metrics obtained with

ECGI recordings between patients with AF termination after PVI ablation and that those differences rely on the post-processing of ECGI signals before phase analysis.

We have shown that both sinusoidal recomposition and narrow band pass filtering centered at the HDF do stabilize phase singularities and make them easier to be tracked but reduce the differences in the variability of SP/ms, rotor duration, and the spatial entropy for different PVI outcome groups. The duration threshold for phase singularities to be considered has been shown to be of little relevance for the predictive power of phase-derived metrics.

### 6.4.1. ECGI-derived phase metrics and PVI outcome

We have found that rotor-derived metrics that best allow determining the differences between groups of patients depending on their PVI outcome are better found when no aggressive filters are applied prior to phase calculation in rotor duration and spatial entropy, especially when a traditional threshold of 1 turn was applied for the detection. Patients with a good PVI outcome presented lower variability between rotor duration and spatial entropy along time. A lower variability of the metrics can reflect a more stable atrial substrate with a better response to ablation treatments. Therefore, this may indicate that the detected rotors are related to the electrical substrate and are not just post-processing artifacts without a link to the atrial substrate of the patient. This observation of the patients with lower variability in the detected drivers is consistent with the success of therapies aiming at rotor elimination (Narayan et al., 2012; Haissaguerre et al., 2014) that have shown an improved outcome by ablating AF sources since more stable in time reentrant activity can ease the AF termination.

In the logistic regression analysis, we observed consistent results with the individual metrics comparison. The resulting ROC curves of the study are moderate specially for SRC and NB-HDF filtering, with AUC values under 0.65 and a weak power of classification of the patients based on the PVI outcome. No filtering the ECGI signal and using a 1 turn SP detection threshold presented an AUC of 0.8 and could classify properly the totality of patients with good PVI response. Nevertheless, it was observed an increased number of patients with arrhythmia recurrence classified as PVI responders.

### 6.4.2. Effects of filtering ECGI signals for rotor detection

We have shown that filtering ECGI signals before applying the phase transform do impact the number of phase singularities detected and the resultant metrics. Filtering stabilized rotors but reduced the statistical differences between patients with different outcomes, especially for SRC filtering.

In previous studies from our group, we have used NB HDF filtering prior to phase singularity detections (Rodrigo et al., 2017; 2014; 2020; Costoya-Sánchez et at., 2020). These studies show the potential of NB filtering in simulated and intracardiac electrograms of AF patients by stabilizing rotors that are unstable when using raw ECGI signals or the BSPM phase. We have also shown that HDF filtering applied to inverse computed simulated electrograms may cause artefactual rotors (Rodrigo et al., 2017), which is consistent with the decreased discriminative power between patients with different outcomes compared to no filtered signals. No previous study has shown the effect of this filter on ECGI signals from AF patients. Even though it is not possible to know in a real case scenario which of our detected rotors are real and which rotors are artefactual, it is feasible that false rotor detection is also produced in real ECGI signals when HDF filter is applied. Nonetheless, the three different filtering approaches show equivalent results, being no filtering the signals the easier approach and more optimal for patient differentiation.

We have shown that the use of sinusoidal recomposition to detect reentrant activity in ECGI signals prior to SP detection does not improve rotor metrics as compared to the use of raw signals. Kuklik et al. showed that SRC filtering robustly alleviates the effect of noise on the phase of the signal (Kuklik et al., 2015), but it is not able to find a statistical difference in the variability of metrics between patients. In the same direction, more recent studies applying SRC to epicardial atrial electrograms have shown that filtering the SPs had low specificity for identifying rotating wavefronts during human AF since lines of conduction block do result in phase singularities (Podziemski et al., 2018). This is consistent with the presented results, which showed a decreased number of SP/ms when SRC was applied prior to rotor detection. The decreased value with the lower ability to differentiate patients per PVI outcome may indicate that SRC worsens the proper quantification of the real atrial substrate.

### 6.4.3. Effects of time-space criteria for rotor detection

In previous studies, we demonstrated that using 3 concentric rings to detect singularity points increases the sensitivity of reentrant activity identification (Rodrigo et al., 2017b) whereas others recommended only 2 for a robust detection (Kuklik et al., 2017). Furthermore, SRC was applied to previous SP identification using 1 turn as threshold criteria (Kuklik et al., 2017; Dharmaprani et al., 2019). Several authors used this same threshold to consider a gradient of phase rotating a point in the atria to accept as a reentrant activity, but no consensus on this value has been established for ECGI signals of AF patients (Haissaguerre et al., 2014; Kuklik et al., 2015; Podziemski et al. 2018). Despite the lack of consensus, we showed a good correlation of noninvasive detected drivers with intracardiac mapping with a threshold of 1 turn (Rodrigo et al., 2020).

The effect of establishing a duration threshold in the detection of rotors in patient signals has affected the discriminative power of the rotor metrics. In this study, we decided to test three different thresholds to detect SP. Better performance for longer and restrictive values (1.5 turns) was expected due to the elimination of spurious rotation detections. In the present results, the threshold of 1 turn showed a better ability to differentiate relevant singularities to relate AF patients to their PVI outcome. This observation does not mean that there are no rotors that last less than one turn, but the propagation of this electrical pattern to the torso may hinder the tracking of the singularities, and more restrictive threshold values lose significant rotors. On the other hand, for thresholds lower than 1 turn, our results showed lower significance in the variability of the studied metrics.

### 6.4.4. Clinical implications

Pulmonary vein isolation has a 60% success of AF termination (Narayan et al., 2012b), with higher success in patients with paroxysmal AF. For this reason, the inclusion criteria for this intervention mainly rely on AF patients' symptoms and AF classification (Hindricks et al., 2021). Despite this, the low effectiveness of the ablation needs an improvement of the procedure and inclusion criteria of the patients. Other alternatives like rotor-driven ablation have demonstrated promising results in increasing AF termination compared to PVI only (Narayan et al., 2012; Haissaguerre et al., 2014), nonetheless presence of rotors has not been used to predict AF ablation outcome (Haissaguerre et al., 2014). The use of ECGI has been reported to be useful for rotor identification (Rodrigo et al., 2020), and our study opens the possibility of using it as a clinical decision method to personalize treatments and as inclusion criteria for PVI to better select patients more likely to benefit from PVI. We present here a benchmark study to standardize the best post-processing methods for quantifying the presence of rotors in ECGI maps from patients with AF.

### 6.4.5. Limitations and future work

We have compared two aggressive filtering strategies of ECGI signals with a wide-band ECGI filtering and shown no benefits of filtering for identifying differences in rotor metrics related to PVI outcome. We cannot exclude the possibility that other post-processing methods could enhance significant differences in rotor metrics related to PVI outcome. Furthermore, the possibility of consideration of artifacts as rotors needs to be taken into account, as well as the possibility of considering that other possible mechanisms that may maintain AF could be detected after each filtering as wavelets (Schotten et al., 2021).

It was not possible to determine the presence and location of rotors in intracardiac recordings because simultaneous intracardiac mapping with enough time-space resolution cannot be performed. For this reason, we have not been able to quantify the effect of post-processing techniques with intracavitary measurements as a gold standard, and we focused our study on finding significant differences between the variability of reentrant metrics from patients with different PVI outcomes.

## 6.5. Conclusion

Rotor metrics based on raw ECGI signals allow for differentiation of patients with different prognoses after pulmonary vein isolation. Aggressive filtering strategies of atrial ECGI signals are not necessary to identify relevant rotor features. A band-pass filtering of the signal before the inverse problem between 2 and 45Hz is sufficient for proper differentiation between patients depending on their outcome based on phase-derived metrics. Additionally, to compute reentrant metrics, the threshold of 1 turn performed as the best alternative since it presents a compromise between not missing real detected rotors and not detecting just changes in the direction of the propagating wavefront.

**Acknowledgments**

The authors wish to thank Dr. Felipe Atienza for his support of the project and clinical advice.

## Funding Sources

This work was supported in part by: Instituto de Salud Carlos III FEDER (Fondo Europeo de Desarrollo Regional PI17/01106), Agencia Estatal de Investigación (RYC2018-024346-I and PID2020-119364RB-100), Generalitat Valenciana Grants (ACIF/2020/265) and EIT Health (Activity code 19600). EIT Health is supported by EIT, a body of the European Union.

### Associated congress publication

This paper is an extensive version of the study presented in Computing in Cardiology in 2020. For this congress publication, I was a finalist of the Rosanna Degani Young Investigator Award.

R. Molero, A. M. Climent, and M. S. Guillem, "Post-Processing of Electrocardiographic Imaging Signals to Identify Atrial Fibrillation Drivers," in Computing in Cardiology, 2020, vol. 47.

## References

Castells, F., Mora, C., Rieta, J. J., Moratal-Pérez, D., and Millet, J. (2005). Estimation of atrial fibrillatory wave from single-lead atrial fibrillation electrocardiograms using principal component analysis concepts. Med. Biol. Eng. Comput. 43, 557–560. doi:10.1007/BF02351028.

Costoya-Sánchez, A., Climent, A. M., Hernández-Romero, I., Liberos, A., Fernández-Avilés, F., Narayan, S. M., et al. (2020). Automatic Quality Electrogram Assessment Improves Reentrant Activity Identification in Atrial Fibrillation. Comput. Biol. Med. 117. doi:https://doi.org/10.1016/j.compbiomed.2019.103593.

Dharmaprani, D., Schopp, M., Kuklik, P., Chapman, D., Lahiri, A., Dykes, L., et al. (2019). Renewal Theory as a Universal Quantitative Framework to Characterize Phase Singularity Regeneration in Mammalian Cardiac Fibrillation. Circ. Arrhythmia Electrophysiol. 12, 1–12. doi:10.1161/CIRCEP.119.007569.

Guillem, M. S., Climent, A. M., Rodrigo, M., Fernández-Avilés, F., Atienza, F., and Berenfeld, O. (2016). Presence and stability of rotors in atrial fibrillation: evidence and therapeutic implications. Cardiovasc. Res. 109, 480–492. doi:10.1093/cvr/cvw011.

Haissaguerre, M., Hocini, M., Denis, A., Shah, A. J., Komatsu, Y., Yamashita, S., et al. (2014). Driver domains in persistent atrial fibrillation. Circulation 130, 530–538. doi:10.1161/CIRCULATIONAHA.113.005421.

Haissaguerre, M., Hocini, M., Shah, A. J., Derval, N., Sacher, F., Jais, P., et al. (2013). Noninvasive panoramic mapping of human atrial fibrillation mechanisms: A feasibility report. J. Cardiovasc. Electrophysiol. 24, 711–717. doi:10.1111/jce.12075.

Hindricks, G., Potpara, T., Dagres, N., Bax, J. J., Boriani, G., Dan, G. A., et al. (2021). 2020 ESC Guidelines for the diagnosis and management of atrial fibrillation developed in collaboration with the European Association for Cardio-Thoracic Surgery (EACTS). Eur. Heart J. 42, 373–498. doi:10.1093/eurheartj/ehaa612.

Kuklik, P., Zeemering, S., Maesen, B., Maessen, J., Crijns, H. J., Verheule, S., et al. (2015). Reconstruction of instantaneous phase of unipolar atrial contact electrogram using a concept of sinusoidal recomposition and hilbert transform. IEEE Trans. Biomed. Eng. 62, 296–302. doi:10.1109/TBME.2014.2350029.

Kuklik, P., Zeemering, S., Van Hunnik, A., Maesen, B., Pison, L., Lau, D. H., et al. (2017). Identification of rotors during human atrial fibrillation using contact mapping and phase singularity detection: Technical considerations. IEEE Trans. Biomed. Eng. 64, 310–318. doi:10.1109/TBME.2016.2554660.

Molero, R., Climent, A. M., and Guillem, M. S. (2020). Post-Processing of Electrocardiographic Imaging Signals to Identify Atrial Fibrillation Drivers. in Computing in Cardiology (IEEE Computer Society). doi:10.22489/CinC.2020.113.

Molero, R., Torro, J. M. S., Alzamora, N. M., Climent, A. M., and Guillem, M. S. (2021). Higher reproducibility of phase derived metrics from electrocardiographic imaging during atrial fibrillation in patients remaining in sinus rhythm after pulmonary vein isolation. Comput. Biol. Med. 139, 104934. doi:10.1016/J.COMPBIOMED.2021.104934.

Narayan, S. M., Krummen, D. E., Enyeart, M. W., and Rappel, W. J. (2012a). Computational Mapping Identifies Localized Mechanisms for Ablation of Atrial Fibrillation. PLoS One 7, 1–8. doi:10.1371/journal.pone.0046034.

Narayan, S. M., Krummen, D. E., Shivkumar, K., Clopton, P., Rappel, W. J., and Miller, J. M. (2012b). Treatment of atrial fibrillation by the ablation of localized sources: CONFIRM (Conventional Ablation for Atrial Fibrillation with or Without Focal Impulse and Rotor Modulation) trial. J. Am. Coll. Cardiol. 60, 628–636. doi:10.1016/j.jacc.2012.05.022.

Podziemski, P., Zeemering, S., Kuklik, P., van Hunnik, A., Maesen, B., Maessen, J., et al. (2018). Rotors Detected by Phase Analysis of Filtered, Epicardial Atrial Fibrillation Electrograms Colocalize With Regions of Conduction Block. Circ. Arrhythm. Electrophysiol. 11, e005858. doi:10.1161/CIRCEP.117.005858.

Remondino, F. (2004). 3-D reconstruction of static human body shape from image sequence. Comput. Vis. Image Underst. 93, 65–85. doi:10.1016/j.cviu.2003.08.006.

Rodrigo, M., Climent, A. M., Hernández-Romero, I., Liberos, A., Baykaner, T., Rogers, A. J., et al. (2020). Non-Invasive Assessment of Complexity of Atrial Fibrillation: Correlation with Contact Mapping and Impact of Ablation. Circ. Arrhythmia Electrophysiol. 13, e007700. doi:10.1161/CIRCEP.119.007700.

Rodrigo, M., Climent, A. M., Liberos, A., Fernandez-Aviles, F., Berenfeld, O., Atienza, F., et al. (2017a). Highest Dominant Frequency and Rotor Sites are Robust Markers for Atrial Driver Location in Non:invasive Mapping of Atrial Fibrillation. 2016 Comput. Cardiol. Conf. 43, 3–6. doi:10.22489/cinc.2016.004-418.

Rodrigo, M., Climent, A. M., Liberos, A., Fernández-Avilés, F., Berenfeld, O., Atienza, F., et al. (2017b). Technical Considerations on Phase Mapping for Identification of Atrial Reentrant Activity in Direct- and Inverse-Computed Electrograms. Circ. Arrhythmia Electrophysiol. 10, e005008. doi:10.1161/CIRCEP.117.005008.

Rodrigo, M., Guillem, M. S., Climent, A. M., Liberos, A., Hernández-Romero, I., Arenal, Á., et al. (2018). Solving Inaccuracies in Anatomical Models for Electrocardiographic Inverse Problem Resolution by Maximizing Reconstruction Quality. IEEE Trans. Med. Imaging 37, 733–740. doi:10.1109/TMI.2017.2707413.

Rodrigo, M., Guillem, M. S., Climent, A. M., Pedrón-Torrecilla, J., Liberos, A., Millet, J., et al. (2014). Body surface localization of left and right atrial high-frequency rotors in atrial fibrillation patients: A clinical-computational study. Hear. Rhythm 11, 1584–1591. doi:10.1016/j.hrthm.2014.05.013.

Schotten, U., Lee, S., Zeemering, S., and Waldo, A. L. (2021). Paradigm shifts in electrophysiological mechanisms of atrial fibrillation. Europace 23, II9–II13. doi:10.1093/europace/euaa384.

Yushkevich, P. A., Zhang, H., and Gee, J. C. (2006). Continuous Medial Representation for Anatomical Structures. IEEE Trans. Med. Imaging 25, 1547–1564. doi:10.1109/TMI.2006.884634.

Zlochiver, S., Yamazaki, M., Kalifa, J., and Berenfeld, O. (2008). Rotor meandering contributes to irregularity in electrograms during atrial fibrillation. Hear. Rhythm 5, 846–854. doi:10.1016/j.hrthm.2008.03.010.

# Chapter 7

## Higher Reproducibility of Phase Derived Metrics from Electrocardiographic Imaging During Atrial Fibrillation in Patients Remaining in Sinus Rhythm after Pulmonary Vein Isolation

R. Molero[1], J. M. Soler Torro[2], N. Martínez Alzamora[2], A. M. Climent[1], and M. S. Guillem[1]

## Abstract

**Background:** Electrocardiographic imaging (ECGI) allows evaluating the complexity of the reentrant activity of atrial fibrillation (AF) patients. In this study, we evaluated the ability of ECGI metrics to predict the success of pulmonary vein isolation (PVI) to treat AF.

**Methods:** ECGI of 24 AF patients (6 males, 13 paroxysmal, 61.8 ± 14 years) was recorded prior to PVI. Patients were distributed into two groups based on their PVI outcome 6 months after ablation (sinus vs. arrhythmia recurrence). Metrics derived from phase analysis of ECGI signals were computed for two different temporal segments before ablation. Correlation analysis and variability over time were studied between the two recorded segments and were compared between patient groups.

**Results:** Temporal variability of both rotor duration and spatial entropy of the rotor histogram presented statistical differences between groups with different PVI outcome ($p<0.05$). The reproducibility of reentrant metrics was higher ($R2>0.8$) in patients with good outcome rather than arrhythmia recurrence patients ($R2<0.62$). Prediction of PVI success based on ECGI temporal variability metrics allows for an increased specificity over the classification into paroxysmal or persistent (0.85 vs. 0.64).

**Conclusions:** Patients with favorable PVI outcome present ECGI metrics more reproducible over time than patients with AF recurrence. These results suggest that ECGI derived metrics may allow selecting which patients would benefit from ablation therapies.

---

R. Molero, J. M. Soler Torro, N. Martínez Alzamora, A. M. Climent, and M. S. Guillem, "Higher reproducibility of phase derived metrics from electrocardiographic imaging during atrial fibrillation in patients remaining in sinus rhythm after pulmonary vein isolation," *Comput. Biol. Med.*, vol. 139, no. May, p. 104934, Dec. 2021.

[1] ITACA Institute, Universitat Politècnica de València, València, Spain

[2] Department of Applied Statistics and Operational Research and Quality, Universitat Politècnica de València, València, Spain

## 7.1. Introduction

Atrial fibrillation (AF) is the most prevalent arrhythmia in the adult population (Benjamin et al., 2019), and it causes a major burden both in the patients and in health systems (Hindricks et al., 2021). Although restoration of sinus rhythm would be desirable in the entire AF population of patients this is not always feasible. When drug therapies fail in restoring sinus rhythm or in minimizing AF-related symptoms, patients can be referred for catheter ablation (Hindricks et al., 2021). Pulmonary vein isolation (PVI) is recommended for patients with paroxysmal AF and persistent AF with low risks of AF recurrence, but despite these recommendations, the percentage of AF recurrence in ablated patients is still high and around 40% (Calkins et al., 2017). It has been reported that driver-guided catheter ablation of atrial areas with other lesions can reduce AF recurrence after the ablation (Baykaner et al., 2018; Haissaguerre et al., 2014) but the most recent guidelines for AF management still recommend further evidence before changing the current recommendations (Hindricks et al., 2021).

Electrocardiographic imaging (ECGI) is a non-invasive technique that has shown its ability to estimate the electrical activity of AF patients. ECGI has been used with success to guide ablations based on driver identification (Narayan et al., 2012; Haissaguerre et al., 2014; Rodrigo et al., 2020) and more recent studies have reported a good correlation between invasively and ECGI-derived estimation of the complexity of the electrical patterns during AF (Rodrigo et al., 2020). ECGI derived metrics of complexity have been shown to be related to the disease progression, and more complex patterns are typically present in persistent AF patients as compared to paroxysmal AF patients (Gao et al., 2019). However, these complexity metrics have not been related to a differential outcome prediction.

The objective of this study is to evaluate the potential of ECGI derived complexity metrics as an indicator of PVI success. We hypothesized that the reproducibility of ECGI complexity metrics can be related to the complexity of the arrhythmia and the outcome of PVI to a larger extent than the complexity estimated at a single temporal interval. We compared ECGI derived metrics of AF patients prior to PVI obtained at different time segments and evaluated its variability in time in patients with and without arrhythmia recurrence 6 months after PVI.

## 7.2. Methods

### 7.2.1. Study Population

A population of 24 atrial fibrillation patients (18 females and 6 males; 61.8 ± 14.3 years old) was studied prior to a wide antral circumferential pulmonary vein isolation procedure. Patients gave informed consent, and the protocol was approved by the ethics committee of Hospital Gregorio Marañón, Madrid, Spain (reference 475/14). Consecutive patients from this Clinical Trial that had two or more signal segments with AF recorded prior valvuloplasty and PVI were selected for being able to study the reproducibility of the metrics. Five patients of a totality of 29 did not present two AF signals prior the procedure with enough quality to be analyzed and were removed from the present study. Out of the 24 patients, 13 were classified as paroxysmal AF and 11 as persistent AF and 10 patients had valvular insufficiency. A percutaneous balloon mitral valvuloplasty was performed on patients with valvular diseases prior PVI. In procedure, patients in sinus rhythm, AF, it was induced by decremental pacing at the pulmonary veins. A total of 6 patients were under antiarrhythmic drugs (flecainide n=1, amiodarone n=5). Patients were followed 6 months after the ablation and then grouped into either sinus rhythm (N=13) or arrhythmia recurrence (atrial fibrillation, atrial tachycardia or atrial flutter, N=11, see Table 7.1). A 12 lead ECG and quality-of-life questionnaires were used for detecting arrhythmia recurrences 6 months after the PVI.

| | **All Patients (n=24)** | **Sinus (n=13)** | **Arrhythmia Recurrence (n=11)** |
|---|---|---|---|
| **Male (%)** | 6 (25 %) | 5 (38.46 %) | 1 (9.1 %) |
| **Age (Years)** | 61.83 ± 14.03 | 59.23 ± 14.01 | 64.91 ± 13.43 |
| **Paroxysmal AF (%)** | 13 (54.17 %) | 9 (69.23 %) | 4 (36.36 %) |
| **Valvuloplasty (%)** | 10 (41.67 %) | 7 (53.85 %) | 3 (27.27 %) |
| **Medical Therapy** | Flecainide – 1 | Flecainide – 1 | Amiodarone – 3 |
| | Amiodarone – 5 | Amiodarone – 2 | |
| **Medical Therapy after Ablation** | Amiodarone – 6 | Amiodarone – 4 | Amiodarone – 2 |
| | Flecainide -2 | Flecainide -2 | Beta-Blockers - 4 |
| | Beta-Blockers - 8 | Beta-Blockers - 4 | |
| **Patients with Previous Ablations** | 23 (95.8%) | 12 (92.3%) | 11 (100%) |
| **Previous Ablations per Patient** | 1.21 ± 0.5 | 1.15 ± 0.55 | 1.27 ± 0.44 |
| **Left Ventricular Ejection Fraction (%)** | 56.48 ± 6.92 | 59 ± 6.14 | 53.73 ± 6.91 |
| **Left Atrium Size ($cm^2$)** | 32.7 ± 7.41 | 33.35 ± 8.27 | 31.94 ± 6.54 |

Table 7.1. Clinical description of the study population

### 7.2.2. Data acquisition

We recorded surface ECG signals from the patients at 57 locations on the torso surface before pulmonary vein isolation and valvuloplasty. Signals were recorded with 0.05 to 500 Hz filtering and a sampling frequency of 1 kHz (Rodrigo et al., 2020). The geometry of the torso of the patients and the electrode location were obtained using video recording and reconstructed by photogrammetry (Remondino, 2004). Images from the video were exported and common image pixels were used for 3D-torso reconstruction. A 3D-torso mesh and the corresponding texture was used for electrode location identification. MRI/CT scan images were also obtained before the intervention and both the atria and the torso were segmented semi-automatically when geometries were well defined or manually layer by layer using ITK-SNAP when necessary (Rodrigo et al., 2020) (Yushkevich et al., 2006). Torso and atrial geometries were co-registered using the torso reference from MRI/CT images.

### 7.2.3. Data processing

To study the reproducibility among time of ECGI-extracted metrics, raw signals of two segments of each patient (4 ± 0.31s) were selected prior to PVI. The signals were preprocessed removing the baseline and were band-pass filtered between 2 and 45 Hz to eliminate noise using a 10th order Butterworth filter, and ventricular activity (QRST segment) was canceled lead by lead by using the Principal Component Analysis approach (Castells et al., 2005). Inverse computed electrograms were calculated by using zero-order Tikhonov regularization and L-curve optimization (Rodrigo et al., 2018) for each segment. We applied Hilbert’s transform to the ECGI signals to compute the instantaneous phase of each signal. Reentrant activity was defined as a phase progression from $-\pi$ to $+\pi$ around a single point in the epicardium. Singularity points (SP) were then defined as stable rotations around an atrial point for at least 1 turn in at least two out of three concentric rings of increasing radii as described elsewhere (Rodrigo et al., 2017b). The distance threshold between SP at consecutive time instants to considered SP related to form a rotor was 1 cm (Rodrigo et al., 2017). SP histograms were constructed to represent the cumulative SPs in each node of the epicardium, where a higher accumulation of SP detected represent areas with more frequent pivoting electrical activity (Rodrigo et al., 2020).

### 7.2.4. Atrial fibrillation complexity quantification

To evaluate the reentrant activity and the complexity of the arrhythmia in each patient, different metrics of the signals were computed in the two segments recorded of each patient. Total singularity points were computed as the number of phase singularities detected scaled by time (SP/ms). Mean rotor duration (Rduration) was computed as the mean duration in seconds of the detected rotors in the signal. Finally, the Shannon spatial entropy of the SP histogram was computed.

### 7.2.5. Reproducibility measurements

To study the reproducibility of each metric, the variability of AF complexity metrics in time was computed as the absolute difference between the metrics extracted from the two different temporal segments: ΔSP/ms, ΔRduration and ΔEntropy were computed as the absolute differences between SP/ms, Rduration and Entropy measured in interval 1 and 2, respectively. In addition, the Coefficient of determination ($R^2$) between the first and second metrics was computed.

An additional quantification of the reproducibility of the different metrics was computed as the ratio between the intra-patient variability and the variability between subjects: the variability score (VS), see Equation 1 (Jekova et al., 2016).

$$VS = \frac{Intrasubject\ Variability}{Intersubject\ Variability} = \frac{\frac{|(X1 - X2)|}{|(X1 + X2)|/2}}{\frac{\sigma_{X1}}{\mu_{X1}}} \tag{1}$$

Where X1 is any metric at time interval 1 (namely SP/ms, mean rotor duration, or spatial Shannon's entropy), X2 is the same metric computed for interval 2, $\sigma_{X1}$ is the standard deviation of X1 and $\mu_{X1}$ is the mean value of X1. The lower the VS values, the higher the reproducibility of the metric. Overall, a VS value lower than 1 is assumed to represent a reproducible metric.

### 7.2.6. Statistical analysis

In order to compare complexity metrics between groups (restoration of sinus rhythm vs. arrhythmia recurrence or paroxysmal vs. persistent), mean values of the metrics of the first and second interval were computed. Normality of the values of each patient's group was computed using the Kolmogorov-Smirnov test. To study differences between groups, student's t-test was computed to compare normal samples and Wilcoxon rank-sum test was computed to compare non-normal samples. A p-value<0.05 was considered statistically significant. Statistical differences in the $R^2$ between groups were computed using a tail t-test after Fisher r-to-z transform.

### 7.2.7. Outcome prediction based on ECGI reproducibility

A reproducibility score (RS) was computed as the average between ΔRduration and ΔEntropy in order to predict 6-months outcome of PVI. Univariate logistic regression of RS was performed to predict the PVI outcome. Sensitivity and specificity were also computed based on the threshold determined from the regression analysis and subsequent receiver operating characteristic curves (ROC) and area under the curve (AUC) were computed. Furthermore, univariate logistic regression was computed using AF type as a predictor of PVI outcome, to compare the proposed method with the current standards for selecting PVI candidates. Finally, univariate logistic regression was also computed for the determination of the AF type (paroxysmal vs. persistent) based on the reproducibility score to see if RS is related to AF type.

## 7.3. Results

Two sample cases and their phase maps and SP histograms are represented in Fig. 1, including one patient that maintained sinus rhythm 6 months after PVI (Fig 7.1A) and one patient in which AF recurred (Fig. 7.1B). Phase maps from the first and second time interval in a patient with an effective PVI do show reentries, mainly around the Right Inferior Pulmonary Vein (RIPV) and therefore rotor histogram maps show a larger incidence at the RIPV, together with some occurrences at other pulmonary veins. Phase maps of the patient with an ineffective PVI show a more complex pattern, with a more inhomogeneous propagation. Rotor histogram in this patient, therefore, showed more reentries in both atria, including the pulmonary veins but also the inferior vena cava (IVC) and other sites in the right atrium. Although rotor maps obtained from the same patient at different time instants do show large incidence areas at similar locations, the reproducibility is larger in the patient in which PVI was effective.

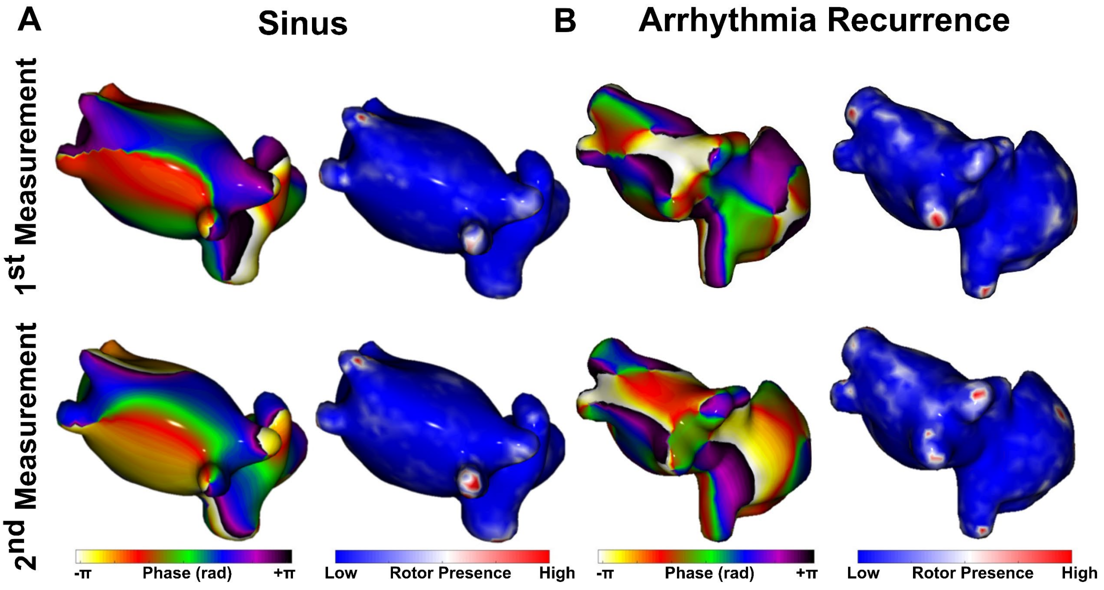

Figure 7.1. Phase map and singularity points histogram of the first and second segment of the signal of a patient that had sinus rhythm 6 months after PVI (A) and a patient with arrhythmia recurrence after ablation (B).

### 7.3.1. Reproducibility of ECGI metrics vs. patient outcome

Values for all the complexity metrics for patients with an effective and an ineffective PVI are presented in Figure 7.2. As it can be observed no statistical differences between the two groups were found in any of the parameters and, therefore, neither the amount of SP/ms found nor their duration or the entropy of the rotor histogram maps may allow anticipating in which patients PVI might be effective.

Scatter plots of the metrics in the first segment versus the second temporal segment for both groups of patients and each metric are presented in Fig. 7.3. As it can be observed, there is some reproducibility in the measurements since metrics from the first temporal segment are closely related to those in the second temporal segment and this correlation is higher for patients with a successful PVI than for patients with an unsuccessful PVI. In fact, the R2 values are higher for patients with favorable outcome and all measurements: SP/ms ($R^2$=0.87 vs. 0.36, p=0.04), spatial entropy ($R^2$=0.87 vs. 0.39, p=0.05) or mean rotor duration (0.82 vs. 0.62, p=n.s).

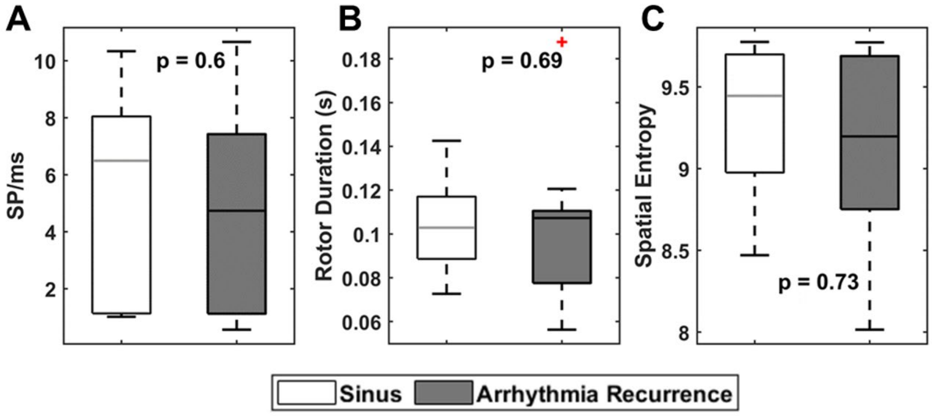

Figure 7.2. Mean values between first and second measurements for each metric for each patient group (white: good PVI outcome, black: bad PVI outcome) and p-value from the Wilkoxon rank-sum test between groups of singularity points per millisecond (A), mean rotor duration (B) and spatial entropy (C).

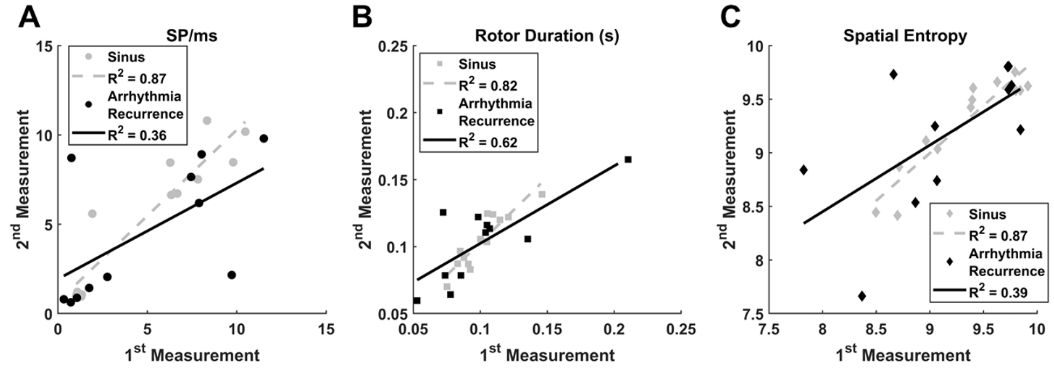

Figure 7.3. Scatter plots of the first and second measurements for each metric classified by PVI outcome (gray: good outcome), black (bad outcome): singularity points per millisecond (A), mean rotor duration (B) and spatial entropy (C).

Differences in the metrics between the first and second segment showed a similar trend than the $R^2$ values: differences were significant both of the mean rotor duration and spatial entropy (Fig. 7.4), (p=0.03 and p=0.04, respectively).

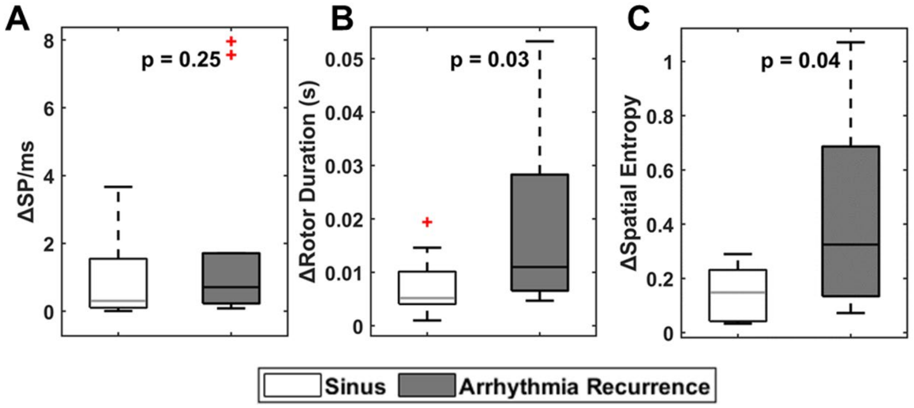

Figure 7.4. The absolute difference between the two measurements for each metric and group of patients (white: good PVI outcome, black: bad PVI outcome) is presented with the p-value from the Wilkoxon rank-sum test of singularity points per millisecond (A), mean rotor duration (B) and spatial entropy (C).

Intersubject variability against the intrasubject variability of each metric is shown in Fig. 7.5A. All the metrics presented a good reproducibility based on this criterium: variability among patients was higher than for the same patient and therefore, all pairs of values are below the identity line. Patients with a successful PVI presented both a lower intrasubject variability and intersubject variability for all metrics (white colored in Fig. 7.5A and B), showing a better reproducibility in comparison with the unsuccessful PVI. The number of SP/ms and spatial entropy presented higher differences between groups of the patients regarding intersubject variability. Mean rotor duration presented the lowest differences between groups. Variability scores, shown in Fig. 7.5B show the same tendency of the $R^2$ values: patients with good PVI outcome showed lower variability scores than patients with arrhythmia recurrence. Furthermore, differences in the value of $R^2$ and variability score between these two groups of patients are consistent, observing the highest differences in SP/ms and spatial entropy.

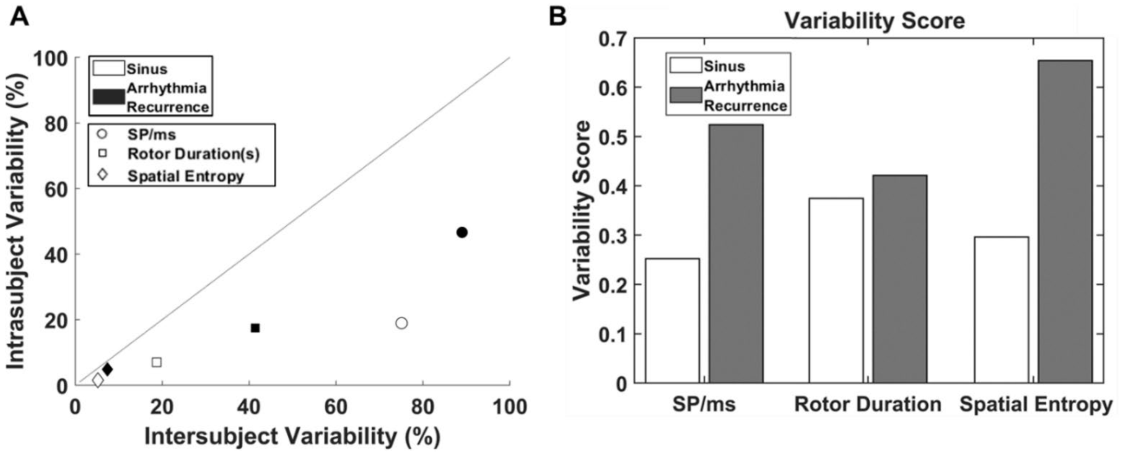

Figure 7.5. A. Intersubject variability vs intrasubject variability of the metrics calculated. Color indicates the classification of the patients and shape the metric. The area under the line shows the metrics that are in the optimal area where intersubject variability is lower than the variability between patients. B. Results for the variability score between the studied metrics and patients classified by PVI outcome.

### 7.3.2. ECGI Reproducibility vs. AF type

A comparison between metrics and their variability between groups of patients based in AF type (paroxysmal/persistent) is presented in Fig. 7.6. When patients are classified by AF type, there are no major differences in the mean value of metrics, as it happens when grouping the patients according to the PVI outcome. Differences between first and second measurements, however, were significant for the number of singularities detected, but not on the rotor duration or spatial entropy.

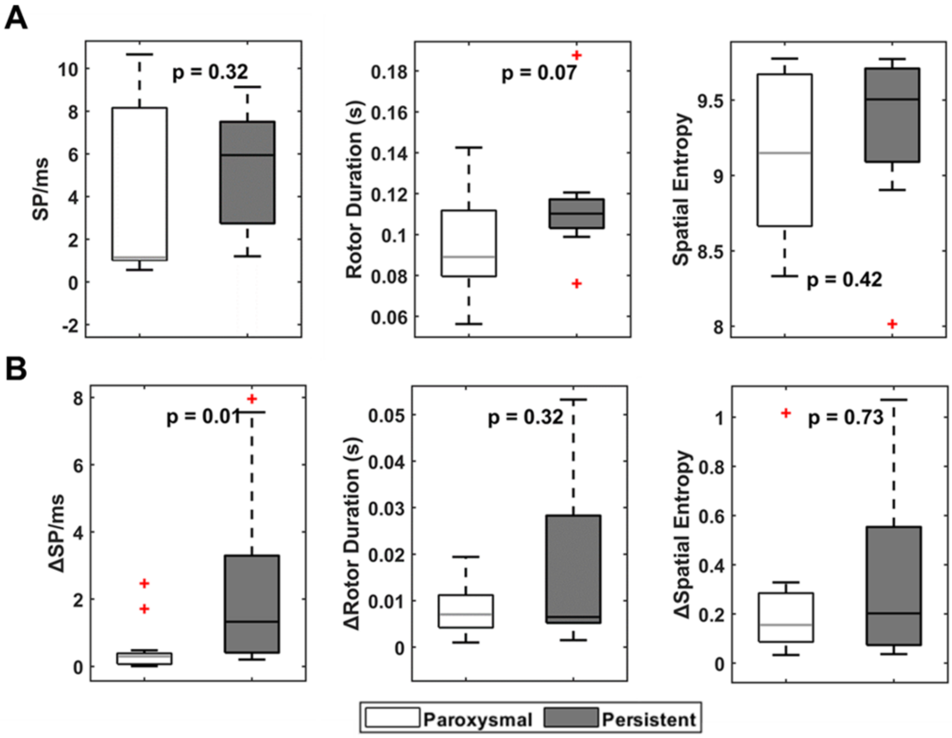

Figure 7.6. Mean values between first and second measurements for each metric are presented in A for each patient group based on AF diagnosis (white: paroxysmal AF, black: persistent AF) and p-value from the Wilkoxon rank-sum test between groups. The absolute difference between the two measurements for each metric and group of patients is presented with the p-value from the Wilkoxon rank-sum test in B.

### 7.3.3. Association of PVI success based on ECGI variability metrics

Univariate logistic regression of the proposed reproducibility score was computed with the two metrics that showed lower p-values when compared groups based on PVI outcome (ΔRduration and ΔEntropy). Results showed an area under the curve of 0.77. Area under the curve of RS for classification into paroxysmal or persistent AF was lower: 0.59, which highlights that the proposed reproducibility score based on ECGI metrics is more closely related to the PVI outcome than the AF classification.

Prediction of PVI success according to their diagnosis into paroxysmal or persistent AF, assuming that patients with paroxysmal AF will have a favorable outcome of PVI whereas patients with persistent AF will have a poor PVI outcome offered a sensitivity of 0.63 and a specificity of 0.69. Prediction based on our reproducibility score, in contrast, resulted in a sensitivity of 0.64

and a specificity of 0.85, and therefore, the use of ECGI reproducibility measurements may allow in better selecting patients that will not benefit from PVI.

## 7.4. Discussion

In this work, we have evaluated the variability of reentrant activity metrics extracted before PVI in AF patients and found a relation between this variability and PVI outcome six months after the procedure. We have found that the electrical patterns of patients with a successful PVI are more stable in time than those of patients with an unsuccessful PVI. Temporal variability of ECGI metrics during AF may allow for a better prediction of PVI outcome than the classification into paroxysmal or persistent AF.

### 7.4.1. Mechanism of AF and PVI outcome

Prior studies by Haissaguerre et al. (Haissaguerre et al., 2014), Narayan et al. (Narayan et al., 2012), and others (Baykaner et al., 2018; Choudry et al. 2020); have demonstrated that ablation of rotors and focal sites does result in a better prognosis than PVI only. In this same direction, Gao et al. reported higher reentrant activity in ECGI maps for patients with acute termination of PVI (Gao et al., 2019). These previous studies used a vest of 252 electrodes for ECGI calculation, and in the present study, 57 individual electrodes were used. Despite that a lower number of electrodes used, it was demonstrated in previous studies (Rodrigo et al., 2017; Guillem et al., 2009) that 32 electrodes are enough for a proper ECGI reconstruction. Furthermore, a good correlation of ECGI and intracardiac AF complexity evaluation with this electrode configuration has been previously shown (Rodrigo et al., 2020). Although we were anticipating that patients with successful PVI ablations would present differences in either the number of rotors or their duration as compared with patients with unsuccessful ablations we have not found significant differences in rotor metrics. Zaman et al. (Zaman et al., 2017), found that patients with paroxysmal AF recurrence after PVI had extra-PV sources, matching with our observations with more unstable reentrant activity in arrhythmia recurrence patients independently of the diagnosis. Therefore, the presence of rotors outside the pulmonary vein area in some patients may be one of the reasons behind our unobserved differences in primary rotor metrics in our patients with successful versus unsuccessful ablations. However, we believe that this observation can also be attributed to the characteristics of our cohort of patients since most of them presented a very damaged atrial substrate as a consequence of an increased atrial pressure due to the valvular impairment that may result in a low incidence of driving rotors.

### 7.4.2. Temporal reproducibility of ECGI derived metrics

We have found that patients with a good prognosis after PVI showed a more stable electrical activity in terms of the variability in time of rotational quantification metrics. This is consistent with many reports in the literature that have demonstrated a lower temporal recurrence on electrophysiological metrics in patients with persistent AF versus patients with paroxysmal AF (Zeemering et al., 2020). Lim et al (Lim et al., 2017) and others (Zeemering et al., 2020; Lim et al., 2017) found that the complexity of persistent AF drivers is higher when AF duration increases.

Our observation would also be consistent with other studies that have related an electrical temporal instability with lower rates of maintenance of sinus rhythm either after PVI (Seitz et al., 2017) or electrical cardioversion (Lankveld et al., 2016).

### 7.4.3. Clinical implications

Catheter ablation is mainly recommended for paroxysmal AF patients based on overall lower AF recurrence after ablation in this group of patients (Hindricks et al., 2021). However, there are both paroxysmal AF patients that do not benefit from PV ablation and persistent AF patients that do benefit from PVI. In our study, we have observed that temporal stability of ECGI derived rotor metrics may help to predict the success of PVI and, therefore, better select patients likely to benefit from PVI and discard the ones that will not, to tailor the treatment to AF in an individual basis with electrophysiological measurements from individual patients instead of the “one approach fits all” approach currently used today.

## 7.5. Limitations

The results of this study should be confirmed in larger datasets and compared to endocardial data. Our results may also be influenced by our study population, with a large proportion of patients with valvular disease. Although we did not find statistical differences in any of the variability of metrics when comparing valvular impaired patients with non-valvular impaired AF patients, we cannot rule out the possible effect of a substantially damaged atrial substrate that may not be representative of a more general AF population. Time separation between signals was established between 15s to 10 minutes due to the difficulties of some patients of maintaining AF during the procedure and reproducibility in time was not considered during the PVI protocol. Furthermore, it should be noted that the outcome of the studied patients could be influenced by changes in the medication, the extent and durability of transmural ablation lesions and that this could influence the results. Follow up of the patients was done 6 months after PVI and could not determine if the recurrence of the arrhythmia would be caused by PVI reconnection and not because of the atrial substrate. The fact that durable PVI can occur although the substrate of the atria may remain abnormal should be considered together with the possibility of arrhythmia recurrence after the 6 months follow up.

## 7.6. Conclusions

This study shows that ECGI derived metrics of reentrant activity in atrial fibrillation patients are reproducible over time and the degree of this reproducibility may be indicative of their electrical substrate since patients with more reproducible metrics are associated with a more favorable outcome. Therefore, variability of rotor metrics derived from ECGI may be suggestive of the ability of PVI to terminate the arrhythmia and may serve for selecting the best treatment option in AF patients.

## Acknowledgments

The authors wish to thank Dr. Felipe Atienza for his support of the project and clinical advice.

## Funding Sources

This work was supported by: Instituto de Salud Carlos III, and Ministerio de Ciencia, Innovación y Universidades (supported by FEDER Fondo Europeo de Desarrollo Regional PI17/01106 and RYC2018-024346B-750), EIT Health (Activity code 19600, EIT Health is supported by EIT, a body of the European Union) and Generalitat Valenciana Grants (ACIF/2020/265).

# References

Baykaner, T., Rogers, A. J., Meckler, G. L., Zaman, J., Navara, R., Rodrigo, M., et al. (2018). Clinical Implications of Ablation of Drivers for Atrial Fibrillation. Circ. Arrhythmia Electrophysiol. 11, e006119. doi:10.1161/CIRCEP.117.006119.

Benjamin, E. J., Muntner, P., Alonso, A., Bittencourt, M. S., Callaway, C. W., Carson, A. P., et al. (2019). Heart Disease and Stroke Statistics-2019 Update: A Report From the American Heart Association. doi:10.1161/CIR.0000000000000659.

Bonizzi, P., Zeemering, S., Karel, J. M. H., Di Marco, L. Y., Uldry, L., Van Zaen, J., et al. (2014). Systematic comparison of non-invasive measures for the assessment of atrial fibrillation complexity: A step forward towards standardization of atrial fibrillation electrogram analysis. Europace 17, 318–325. doi:10.1093/europace/euu202.

Calkins, H., Hindricks, G., Cappato, R., Kim, Y. H., Saad, E. B., Aguinaga, L., et al. (2017). 2017 HRS/EHRA/ECAS/APHRS/SOLAECE expert consensus statement on catheter and surgical ablation of atrial fibrillation: Executive summary. J. Arrhythmia 33, 369–409. doi:10.1016/j.joa.2017.08.001.

Castells, F., Mora, C., Rieta, J. J., Moratal-Pérez, D., and Millet, J. (2005). Estimation of atrial fibrillatory wave from single-lead atrial fibrillation electrocardiograms using principal component analysis concepts. Med. Biol. Eng. Comput. 43, 557–560. doi:10.1007/BF02351028.

Choudry, S., Mansour, M., Sundaram, S., Nguyen, D. T., Dukkipati, S. R., Whang, W., et al. (2020). RADAR: A multicenter food and drug administration investigational device exemption clinical trial of persistent atrial fibrillation. Circ. Arrhythmia Electrophysiol. 13, 7825. doi:10.1161/CIRCEP.119.007825.

de la Guillem, M., Bollmann, A., Climent, A. M., Husser, D., Millet-Roig, J., and Castells, F. (2009). How many leads are necessary for a reliable reconstruction of surface potentials during atrial fibrillation? IEEE Trans. Inf. Technol. Biomed. 13, 330–340. doi:10.1109/TITB.2008.2011894.

Gao, X., Lam, A. G., Bilchick, K. C., Darby, A., Mehta, N., Mason, P. K., et al. (2019). The use of non-invasive mapping in persistent AF to predict acute procedural outcome. J. Electrocardiol. 57, S21–S26. doi:10.1016/j.jelectrocard.2019.08.012.

Haissaguerre, M., Hocini, M., Denis, A., Shah, A. J., Komatsu, Y., Yamashita, S., et al. (2014). Driver domains in persistent atrial fibrillation. Circulation 130, 530–538. doi:10.1161/CIRCULATIONAHA.113.005421.

Hindricks, G., Potpara, T., Dagres, N., Bax, J. J., Boriani, G., Dan, G. A., et al. (2021). 2020 ESC Guidelines for the diagnosis and management of atrial fibrillation developed in collaboration with the European Association for Cardio-Thoracic Surgery (EACTS). Eur. Heart J. 42, 373–498. doi:10.1093/eurheartj/ehaa612.

Jekova, I., Krasteva, V., Leber, R., Schmid, R., Twerenbold, R., Müller, C., et al. (2016). Intersubject variability and intrasubject reproducibility of 12-lead ECG metrics: Implications for human verification. J. Electrocardiol. 49, 784–789. doi:10.1016/j.jelectrocard.2016.07.021.

Lankveld, T., De Vos, C. B., Limantoro, I., Zeemering, S., Dudink, E., Crijns, H. J., et al. (2016). Systematic analysis of ECG predictors of sinus rhythm maintenance after electrical cardioversion for persistent atrial fibrillation. Hear. Rhythm 13, 1020–1027. doi:10.1016/j.hrthm.2016.01.004.

Lim, H. S., Hocini, M., Dubois, R., Denis, A., Derval, N., Zellerhoff, S., et al. (2017). Complexity and Distribution of Drivers in Relation to Duration of Persistent Atrial Fibrillation. J Am Coll Cardiol doi:10.1016/j.jacc.2017.01.014.

Meo, M., Pambrun, T., Derval, N., Dumas-Pomier, C., Puyo, S., Duchâteau, J., et al. (2018). Noninvasive Assessment of Atrial Fibrillation Complexity in Relation to Ablation Characteristics and Outcome. Frontiers doi:10.3389/fphys.2018.00929.

Narayan, S. M., Krummen, D. E., Clopton, P., Shivkumar, K., and Miller, J. M. (2013). Direct or coincidental elimination of stable rotors or focal sources may explain successful atrial fibrillation ablation: On-treatment analysis of the CONFIRM trial (Conventional Ablation for AF with or Without Focal Impulse and Rotor Modulation). J. Am. Coll. Cardiol. 62, 138–147. doi:10.1016/j.jacc.2013.03.021.

Narayan, S. M., Krummen, D. E., Shivkumar, K., Clopton, P., Rappel, W. J., and Miller, J. M. (2012). Treatment of atrial fibrillation by the ablation of localized sources: CONFIRM (Conventional Ablation for Atrial Fibrillation with or Without Focal Impulse and Rotor Modulation) trial. J. Am. Coll. Cardiol. 60, 628–636. doi:10.1016/j.jacc.2012.05.022.

Remondino, F. (2004). 3-D reconstruction of static human body shape from image sequence. Comput. Vis. Image Underst. 93, 65–85. doi:10.1016/j.cviu.2003.08.006.

Rodrigo, M., Climent, A. M., Hernández-Romero, I., Liberos, A., Baykaner, T., Rogers, A. J., et al. (2020). Non-Invasive Assessment of Complexity of Atrial Fibrillation: Correlation with Contact Mapping and Impact of Ablation. Circ. Arrhythmia Electrophysiol. 13, e007700. doi:10.1161/CIRCEP.119.007700.

Rodrigo, M., Climent, A. M., Liberos, A., Fernández-Aviles, F., Atienza, F., Guillem, M. S., et al. (2017a). Minimal configuration of body surface potential mapping for discrimination of left versus right dominant frequencies during atrial fibrillation. PACE - Pacing Clin. Electrophysiol. 40, 940–946. doi:10.1111/pace.13133.

Rodrigo, M., Climent, A. M., Liberos, A., Fernández-Avilés, F., Berenfeld, O., Atienza, F., et al. (2017b). Technical Considerations on Phase Mapping for Identification of Atrial Reentrant Activity in Direct- and Inverse-Computed Electrograms. Circ. Arrhythmia Electrophysiol. 10, e005008. doi:10.1161/CIRCEP.117.005008.

Rodrigo, M., Guillem, M. S., Climent, A. M., Liberos, A., Hernández-Romero, I., Arenal, Á., et al. (2018). Solving Inaccuracies in Anatomical Models for Electrocardiographic Inverse Problem Resolution by Maximizing Reconstruction Quality. IEEE Trans. Med. Imaging 37, 733–740. doi:10.1109/TMI.2017.2707413.

Seitz, J., Bars, C., Théodore, G., Beurtheret, S., Lellouche, N., Bremondy, M., et al. (2017). AF Ablation Guided by Spatiotemporal Electrogram Dispersion Without Pulmonary Vein Isolation: A Wholly Patient-Tailored Approach. J. Am. Coll. Cardiol. 69, 303–321. doi:10.1016/j.jacc.2016.10.065.

Yushkevich, P. A., Zhang, H., and Gee, J. C. (2006). Continuous Medial Representation for Anatomical Structures. IEEE Trans. Med. Imaging 25, 1547–1564. doi:10.1109/TMI.2006.884634.

Zaman, J. A. B., Baykaner, T., Clopton, P., Swarup, V., Kowal, R. C., Daubert, J. P., et al. (2017). Recurrent Post-Ablation Paroxysmal Atrial Fibrillation Shares Substrates With Persistent Atrial Fibrillation: An 11-Center Study. JACC Clin. Electrophysiol. 3, 393–402. doi:10.1016/j.jacep.2016.10.006.

Zeemering, S., van Hunnik, A., van Rosmalen, F., Bonizzi, P., Scaf, B., Delhaas, T., et al. (2020). A Novel Tool for the Identification and Characterization of Repetitive Patterns in High-Density Contact Mapping of Atrial Fibrillation. Front. Physiol. 11, 1–12. doi:10.3389/fphys.2020.570118.

# Chapter 8

## Complexity and Recurrence of Body Surface Electrocardiograms Correlates with Estimated Reentrant Atrial Activity with Electrocardiographic Imaging in Atrial Fibrillation Patients

Rubén Molero[1], Olivier Meste[2], Ralf Peeters[3], Joël Karel[3], Pietro Bonizzi[3*], María S Guillem[1*]

# Abstract

Complexity metrics obtained from body surface potential mapping (BSPM) allow quantifying atrial fibrillation (AF) substrate complexity. This study aims to relate electrocardiographic imaging (ECGI) detected reentrant patterns with BSPM-calculated signal complexity metrics. BSPM signals were recorded from 28 AF patients (17 male, 62.69±8.09 y.o.), followed by ECGI calculation. Signal complexity and recurrence metrics were computed on BSPM and ECGI signals. Rotors per second and rotor duration were computed on ECGI signals for each atrium and the whole atrial surface. BSPM metrics and ECGI reentrant patterns were correlated for the entire atrial surface and for left (LA) and right atrium (RA). Atrial complexity and recurrence metrics strongly correlated when computed on BSPM and ECGI. Higher sample entropy and relative harmonic energy (RHE) correlated with a higher number of reentries of short duration, especially with the LA, (RHE and rotor duration, $r_{LA}$=-0.66). Higher short- and long-term recurrence of BSPM signals correlated with longer duration rotors ($r_{LA}$=0.74 vs. $r_{RA}$=0.42). Only ECGI-based reentrant parameters showed higher LA complexity compared to RA ($p<0.05$). BSPM metrics indicating a more elevated atrial electro-structural remodeling aligned with more short-duration rotors from ECGI computations. Although BSPM delivers qualitative AF reentry data, ECGI remains essential for identifying regional substrate complexity.

---

Submitted paper

[1] ITACA Institute, Universitat Politècnica de València, València, Spain
[2] Laboratoire I3S, Université Côte d'Azur, CNRS, Sophia Antipolis, France
[3] Department of Advanced Computing Sciences, Maastricht University, The Netherlands
[*] Pietro Bonizzi and María S Guillem share the last authorship of this paper

## 8.1. Introduction

Atrial fibrillation (AF) is the most prevalent cardiac arrhythmia in adults, which is linked to higher morbidity and mortality rates (Hindricks et al., 2021). The electrical complexity of the cardiac signal, commonly measured by electrocardiograms (ECGs), is used as a way to estimate morbidity and maintenance of AF (Lankveld et al., 2016b). Body surface potential mapping (BSPM) is a non-invasive method used to assess the electrical activity of the heart by means of a large number of electrodes distributed over the torso surface of a patient, which provides higher spatial resolution and more information about the arrhythmia (Bergquist et al., 2021) than the standard 12-lead ECG.

Several studies have systematically analyzed the electrical properties of BSPM signals during AF, in order to extract relevant information about AF substrate complexity and link it to disease progression and treatment outcome (Bonizzi et al., 2014; Lankveld et al., 2016a; Meo et al., 2018). Moreover, we have shown that BSPM could be used to localize non-invasively sites of the dominant frequency of the atrial activity (Guillem et al., 2013). Recently, we also investigated short- and long-term recurrent behavior of atrial activity propagation (Bonizzi et al., 2020) on BSPM signals and suggested that the variability in the recurrent behavior of the atrial activity is due mostly to an uncoordinated propagation of waveforms on the atrial surface. We also showed that the complexity of atrial fibrillation surface influences the short-term repetitive behavior of AF propagation.

At the same time, it is still unclear to what extent body surface signals can be used to characterize and localize AF propagation patterns. In this respect, electrocardiographic imaging (ECGI) has been proposed to non-invasively reconstruct epicardial potentials starting from BSPM signals and information about the geometry of the heart and the torso, and it could be used to assess the correlation between the properties of AF propagation patterns estimated on the body and on the heart surface, respectively. Although ECGI requires more information from the patient and it is consequently more burdensome to obtain ECGI maps compared to BSPM, it has been shown in the past to be helpful for the evaluation of drivers that initiate and maintain AF (Molero et al., 2021; Dhillon et al., 2022; Fambuena-Santos et al., 2023). Moreover, we proved that AF drivers detected through ECGI signals presented a good correlation with intracardiac mapping in AF patients (Rodrigo et al., 2020, 2021). ECGI has also been proven to be a reliable tool for locating and characterizing atrial rotors (Lim et al., 2017; Fambuena-Santos et al., 2023), which are one of the hypothesized mechanisms of AF generation and maintenance (Guillem et al., 2016; Bizhanov et al., 2022).

The purpose of this study is to investigate the relationship of BSPM-derived metrics that quantify AF substrate complexity and AF propagation recurrence with properties such as the number and duration of reentrant atrial patterns assessed on ECGI signals. We hypothesize that metrics computed on BSPM and ECGI should present similar trends and that the evaluation of the AF substrate complexity and AF propagation recurrence on BSPM should provide a certain level of information on the properties of atrial activity reentries and their duration as measured through ECGI. Furthermore, we evaluated reentrant metrics in each atrium separately, and we explored if metrics measured on BSPM signals would give more information about the AF substrate of a specific atrium (left or right). A graphical abstract of this study is shown below.

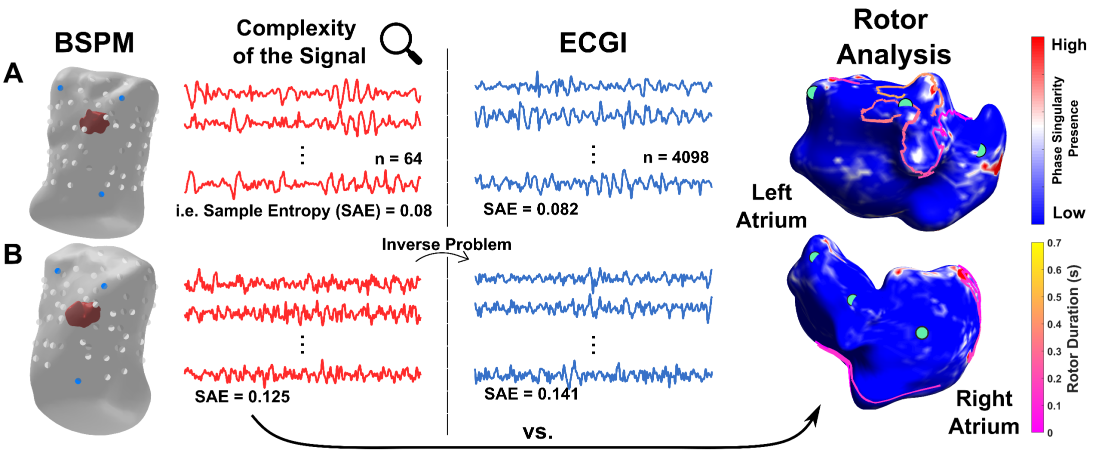

Graphical abstract. In red, atrial activity body surface potential signals (BSPM) and the value of sample entropy (SAE). In blue, electrocardiographic imaging (ECGI) atrial activity signals obtained after solving the inverse problem, and their SAE. At the right, the rotor 2D histograms (also known as density heatmaps) represented together with the detected rotors, and their duration. Panel A represents a patient with low AF substrate complexity and panel B a patient with high AF substrate complexity. This figure illustrates the methodology of this paper comparing the complexity and recurrence of the signals on BSPM with the reentrant atrial activity evaluated on ECGI.

## 8.2. Methods

### 8.2.1. Data acquisition and processing

A population of 28 AF patients (11 female, 17 male, 62.69 ± 8.09 years old) was studied prior to pulmonary vein isolation (PVI). Nine patients were diagnosed with paroxysmal AF and 19 with

Persistent AF prior to the PVI. The protocol was authorized by the Spanish Agency of Medicines and Medical Devices (AEMPS), code: FAT-ANT-2018-01 after patients provided informed consent. BSPM signals from 64 electrodes were recorded before PVI at a sampling frequency of 1kHz. The electrodes were distributed in the torso 24 on the front, 24 on the back, and 8 on each side of the torso. The geometry of each of the patient's torso and the electrode positions were obtained using photogrammetry as described in previous studies (Dhillon et al., 2022; Molero et al., 2023a). Each patient's atrial anatomy was derived from an MRI-segmented atria database based on the patient's torso similarity and placed on patient's torso reconstruction as described in (Molero et al., 2023a). Atrial geometries were segmented into regions differentiating left (LA) and right atrium (RA) using Autodesk Meshmixer (Schmidt and Singh, 2010). The BSPM signals were pre-processed by subtracting the baseline and using a 10th-order Butterworth low-pass filter of 45 Hz. Since for all patients 8 seconds of recordings are available, we decided to extract two successive signals per patient, each with a length of 4s, to increase robustness. A single-lead Principal Component Analysis technique was used to eliminate ventricular activity. (Castells et al., 2005). ECGI signals were calculated with the zero-order Tikhonov method and L-curve optimization (Hernández-Romero et al., 2023).

## 8.2.2. Assessment of AF substrate complexity and AF propagation recurrence on Body Surface Potential Mapping

### 8.2.2.1. AF substrate complexity

In the present article, the assessment of the atrial substrate complexity on BSPM is based on metrics compiled in a previous systematic analysis by Bonizzi et al. (2014). The explored metrics were computed based on the analysis of the principal components, the spatial complexity, the spectral concentration, and the organization of the signals. In the following lines, we describe in more detail the most relevant metrics in our analysis.

- Highest dominant frequency (HDF), computed as the 98th percentile of the dominant frequencies of all leads obtained from the maximum power spectral density using Welch's method (Guillem et al., 2013; Rodrigo et al., 2017). The DF is defined as the activation rate of the atrial activity, with lower values related to more organized AF.
- Sample entropy (SAE) is a statistical method used to quantify the amount of regularity or irregularity in a signal by measuring the similarity between epochs within the signal. SAE attributes a positive value to the signal, where higher values indicate greater variability.

It is expected that more organized atrial fibrillation propagation patterns are associated with lower values of SAE (Alcaraz and Rieta, 2010).

- Relative harmonic energy (RHE) is computed as the relative energy of the sub-bands from the first and second harmonics of the dominant atrial fibrillation frequency (Bonizzi et al., 2014). More organized atrial fibrillation propagation patterns are expected to be associated with lower values of RHE (Alcaraz et al., 2011).

#### 8.2.2.2. AF propagation recurrence

The analysis of AF propagation recurrence on BSPM was computed based on (Bonizzi et al., 2020). The recurrent behavior of AF was studied by looking at the short- and long-term spatial variability of the atrial activity propagation as exhibited on BSPM signals. This analysis is based on multivariate autocorrelation function of the atrial activity from body surface signals, as described in (Meste et al., 2016). The signals were resampled to 256 Hz. The multivariable autocorrelation function is defined as a square matrix R of dimensions M × M, obtained by calculating:

$$R_{i,j} = \frac{x(i)^T x(i+j-1)}{\left|\left|x(i)\right|\right|_2 \left|\left|x(i+j-1)\right|\right|_2}, \; with\, i,j = 1, \ldots, M, \tag{1}$$

Where x(i) is a vector containing the BSPM samples from all 64 electrodes at a given time instant i, and M represents the window size used for the analysis (Meste et al., 2016). Autocorrelation is therefore measured using a cosine distance, where each element in the matrix R is the cosine of the angle between two vectors (with column j including correlation at lag p = j − 1). By averaging each column (for each lag), a multivariate spatial autocorrelation function can be generated for the atrial fibrillation oscillatory patterns across lags p = 0, …, M − 1.

The following descriptive characteristics of the AF propagation recurrence were calculated for each multivariable autocorrelation function and averaged per patient based on Bonizzi et al., (2020):

- Long-term recurrence (LTR): calculated as the mean absolute value of the recurrence signals with lags between 150 and 450. LTR is defined as a metric of the patient's long-term recurrent atrial activity propagation behavior, and it is linked with the overall complexity of the AF substrate. A smaller level of electro-structural remodeling correlates with a greater LTR value.

- Short-term recurrence: computed utilizing the absolute value of the first negative peak ($|P_1|$) and the first positive peak ($P_2$) in the multivariable autocorrelation function. Higher values of $|P_1|$ and $P_2$ are associated with a lower degree of electro-structural remodeling. $|P_1|$ is correlated with half of the AF cycle length and $P_2$ with the complete AF cycle length.

### 8.2.3. Reentrant atrial activity analysis from ECGI signals

Reentrant atrial activity was estimated from the ECGI signals as described in (Fambuena-Santos et al., 2023). We computed the phase of the inverse electrograms by applying the Hilbert transform to the signals, and we defined a singularity point (SP) as a stable point where the phase rotates from $-\pi$ to $+\pi$ (Molero et al., 2021). The threshold for a candidate SP was one turn of the complete phase progression around the center of rotation of the singularity (Molero et al., 2023b). Next, we connected the SP spatiotemporally into rotors to discard transient and isolated phase singularities (Fambuena-Santos et al., 2023).

To characterize the reentrant atrial activity, we used state-of-the-art metrics for SP characterization and rotor detection (Dhillon et al., 2022; González-Ascaso et al., 2020). The number of SPs per second, rotors per second (rotors/s), the mean rotor duration, and the spatial entropy of SP histograms were computed in each patient. Furthermore, we computed the above metrics per atrium. To consider a rotor as located in one atrium (left or right), it had to be the 70% of its duration detected in that atrium. Rotors that were not detected for more than 70% of their duration in a specific atrium were discarded from the atrium specific analysis.

### 8.2.4. Statistical analysis

The metrics extracted from both 4s segments of the signal were averaged to reduce the variability. Correlation between BSPM-based and ECGI-based AF substrate complexity and AF propagation recurrence metrics was computed by using Pearson's correlation. Correlation between BSPM-based metrics and rotors properties and their duration was also investigated for each atrium. Normality of all metrics was tested by via the Kolmogorov-Smirnov test. Student's t-test was used to evaluate differences between the left and right atrium for normally distributed metrics. Alternatively, the Wilcoxon rank-sum test was used. A p-value below 0.05 was deemed statistically significant.

# 8.3. Results

## 8.3.1. BSPM-based versus ECGI-based AF substrate complexity and AF propagation recurrence

Fig. 8.1 shows the correlations between the three BSPM-based and ECGI-based AF substrate complexity metrics introduced in Section 8.2.2.1 (HDF, SAE, RHE; top row), and three BSPM-based and ECGI-based AF propagation recurrence metrics introduced in Section 8.2.2.2 ($|P_1|$, $P_2$, and LTR; bottom row). Most analyses showed high correlations between BSPM- and ECGI-based metrics, thus suggesting that the overall estimation of substrate complexity is comparable if performed on BSPM or ECGI signals. Strong correlations were also observed for LTR and short- and long-term recurrence, with $r > 0.95$. Table 1 of the supplemental material shows the correlations of the other metrics analyzed in this study.

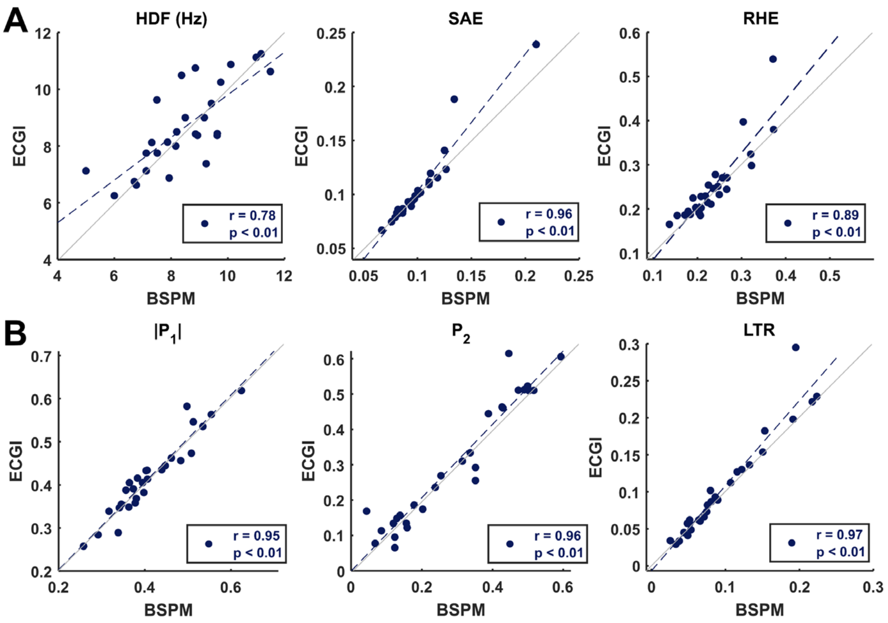

Figure 8.1. Correlations of metrics computed on the body surface electrocardiograms (BSPM) and on the ECGI solution. A. AF substrate complexity metrics: highest dominant frequency (HDF), sample entropy (SAE), and relative harmonic energy (RHE). B. AF propagation recurrence metrics: short-term ($|P_1|$ and $P_2$) and long-term (LTR) recurrence. The values of r represent the Pearson's correlation coefficient (and its p-value). In each plot, the line of best fits (dashed line) is also shown together with the line of identity.

### 8.3.2. BSPM-based AF substrate complexity and AF propagation recurrence vs ECGI-based reentrant atrial activity

To attempt a physiological interpretation of the AF complexity and recurrence as reflected on the body surface in terms of the underlying reentrant activity inside the atria, BSPM-based AF substrate complexity and AF propagation recurrence metrics were compared with ECGI-based reentrant atrial activity metrics. Fig. 8.2 illustrates the results of the comparison between the highest dominant frequency, sample entropy, and relative harmonic energy of surface electrocardiograms and rotors per second and the duration of the rotors estimated on reconstructed electrograms through ECGI. No correlation between HDF and the number of rotors/s was observed. SAE and RHE showed a positive correlation ($p<0.01$) with the number of rotors, indicating that more complex body surface atrial activity is related to a higher number of rotors on the atrial surface. Additionally, these two metrics showed an inverse correlation with the duration of rotors, indicating that more complex surface atrial activity correlates with the presence of AF reentries of shorter duration ($r = -0.73$, $p < 0.01$). This inverse relationship could be explained by a more extended electro-structural remodeling of the AF substrate that may cause both more disruptions in the propagation of atrial wavefronts (thus preventing rotors from lasting for a long period) and a greater endo-epicardial dissociation (Eckstein et al., 2011), which may hinder the reentrant activity to propagate to the surface of the atria.

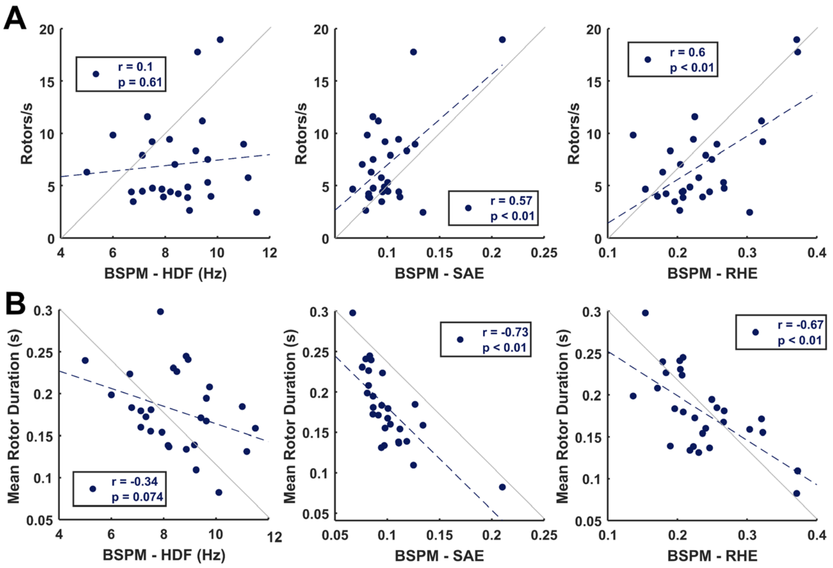

Figure 8.2. Correlations between AF substrate complexity metrics obtained on body surface (HDF, SAE, and RHE) electrocardiograms and the number of rotors per second (A) and mean rotor duration (B). The values of r represent the Pearson’s correlation coefficient (and its p-value). In each plot, the line of best fits (dashed line) is also shown together with the line of identity.

Fig. 8.3 shows the results of the comparison between the three AF propagation recurrence metrics (|$P_1$|, $P_2$, and LTR) and rotors/s and the duration of the rotors estimated on reconstructed electrograms through ECGI. Short- and long-term recurrence presented an inverse correlation with the number of rotors/s, which was significant only for the recurrent behavior at half of the AF cycle. Significant correlations ($p < 0.01$) were also found between the three metrics and the duration of rotors, showing that more repetitiveness at short- and long-term correlate with reentries of longer duration.

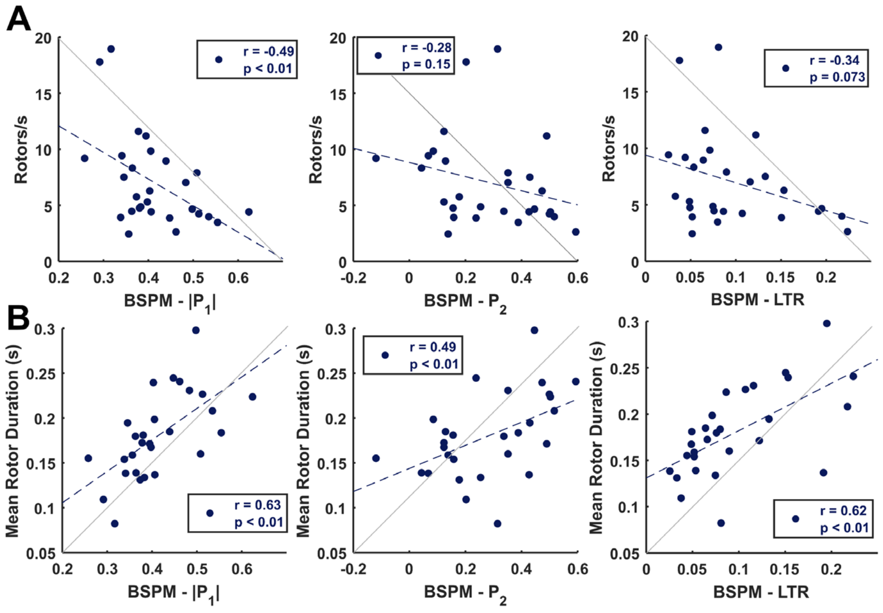

Figure 8.3. Correlations between AF propagation recurrence metrics obtained on the body surface (short (|$P_1$|, $P_2$) and long-term (LTR) recurrence) and the number of rotors per second (A) and mean rotor duration (B). The values of r represent the Pearson's correlation coefficient (and its p-value). In each plot, the line of best fits (dashed line) is also shown together with the line of identity.

### 8.3.3. Assessment of left and right atrium differences

Fig. 8.4 shows violin plots of the ECGI-based AF substrate complexity and AF propagation recurrence metrics on the left (blue) and right atrium (red). None of those metrics was able to capture significant differences between the two atria. Median values of the metrics were higher on the LA but not significant ($p > 0.05$).

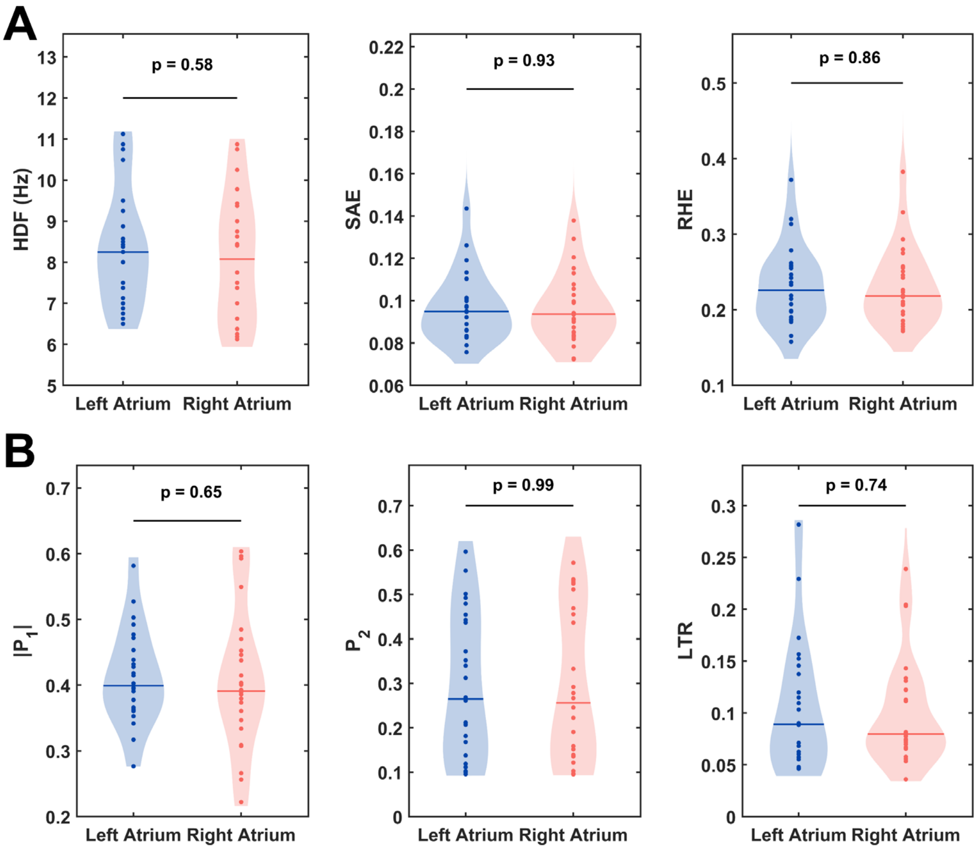

Figure 8.4. Violin plots of AF substrate complexity (A) and AF propagation recurrence metrics (B) measured in the left (blue) and the right (red) atrium. The p-value of each statistical comparison is shown on the top of each graph, the line represents the median of the metric.

In contrast, ECGI-based metrics characterizing singularity points (SP) and rotors properties were able to capture significant differences between the two atria (as illustrated in Fig. 8.5). SP per second, rotors/s, and the spatial entropy of the SP histogram were significantly higher ($p<0.01$) on the left atrium, showing a stronger reentrant activity in this atrium and possibly a more extended electro-structural remodeling of the underlying AF substrate. Mean rotor duration was not significantly different between the two atria, although rotors in the LA lasted longer on average (LA: 0.19s ± 0.07, RA: 0.15s ± 0.07, $p = 0.059$).

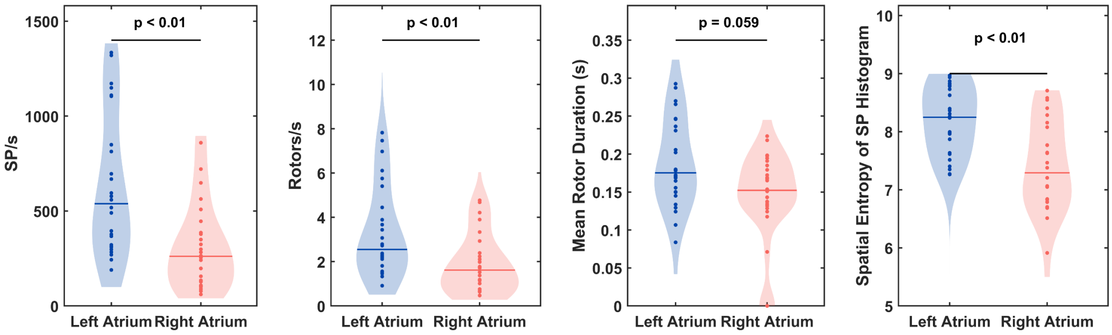

Figure 8.5. Violin plots of reentrant metrics measured at the left (blue) and right (red) atrium. The p-value of each statistical comparison is shown on the top of each graph, the line represents the median of the metric.

### 8.3.4. BSPM-based AF substrate complexity and AF propagation recurrence vs ECGI-based reentrant atrial Activity per atrium

In Fig. 8.6 we show the correlation of the rotors/s (A) and mean rotor duration (B) with HDF, SAE and RHE for the LA and the RA separately. HDF did not correlate with any of the metrics computed on each atrium. SAE presented a higher correlation with rotors/s in the LA compared to the RA (r = 0.59 vs. r = 0.12, respectively). Nevertheless, no significant differences in correlation between SAE and mean rotor duration for the different atria were observed. Additionally, RHE did not present significant differences in correlation with the rotors/s between atria, but it did with the mean rotor duration, where a higher inverse correlation of the LA compared to the RA was observed (RHE, LA: -0.66, $p<0.01$, RA: -0.47, $p<0.05$).

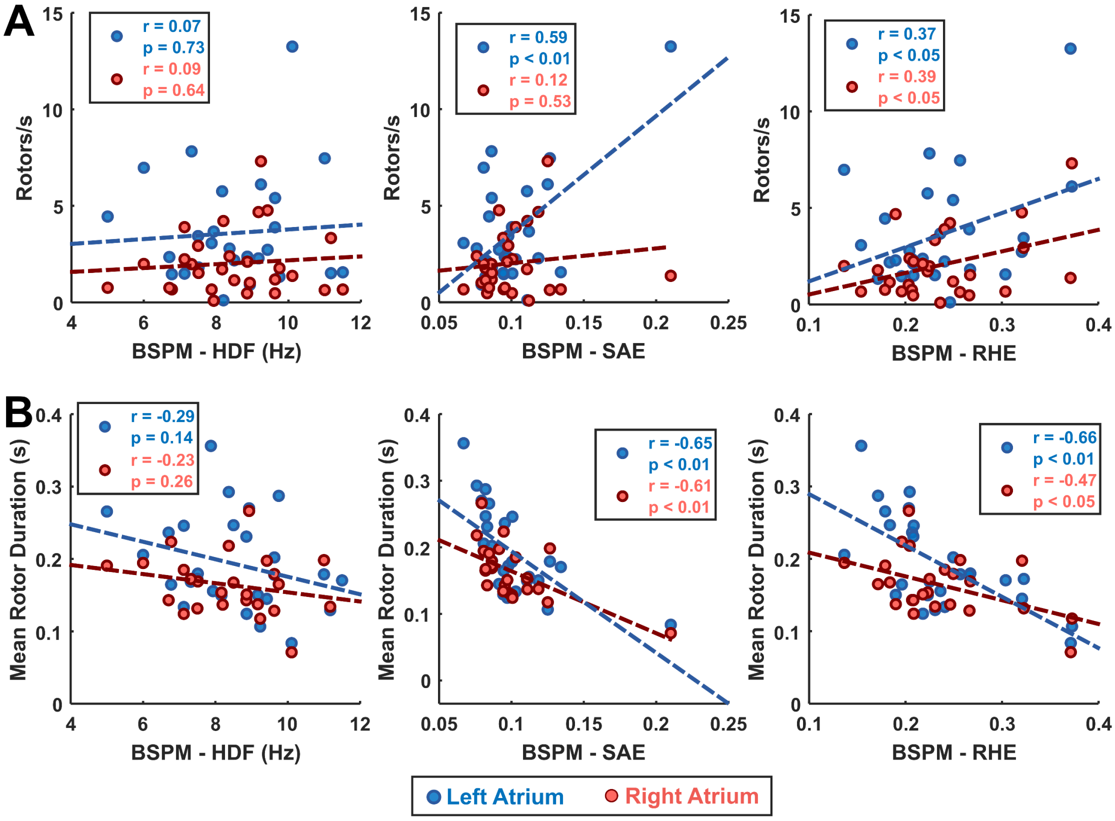

Figure 8.6. Correlation of BSPM-based AF substrate complexity metrics with the number of rotors per second (A) and mean rotor duration (B) for rotors in the left (blue dots) and in the right (red dots) atrium, respectively. The values of r represent the Pearson's correlation coefficient and its p-value of the adjusted regression lines.

Fig. 8.7 shows the correlation of the rotors/s (A) and mean rotor duration (B) with $|P_1|$, $P_2$, and LTR. Short- and long-term recurrence metrics did not show a strong correlation with rotors/s computed per atrium, although the correlation in the LA was higher for these metrics compared to the RA. Mean rotor duration showed higher correlations with these metrics in the LA compared to the RA, especially for the LTR (LA: 0.74, $p<0.01$, RA: 0.42, $p<0.05$).

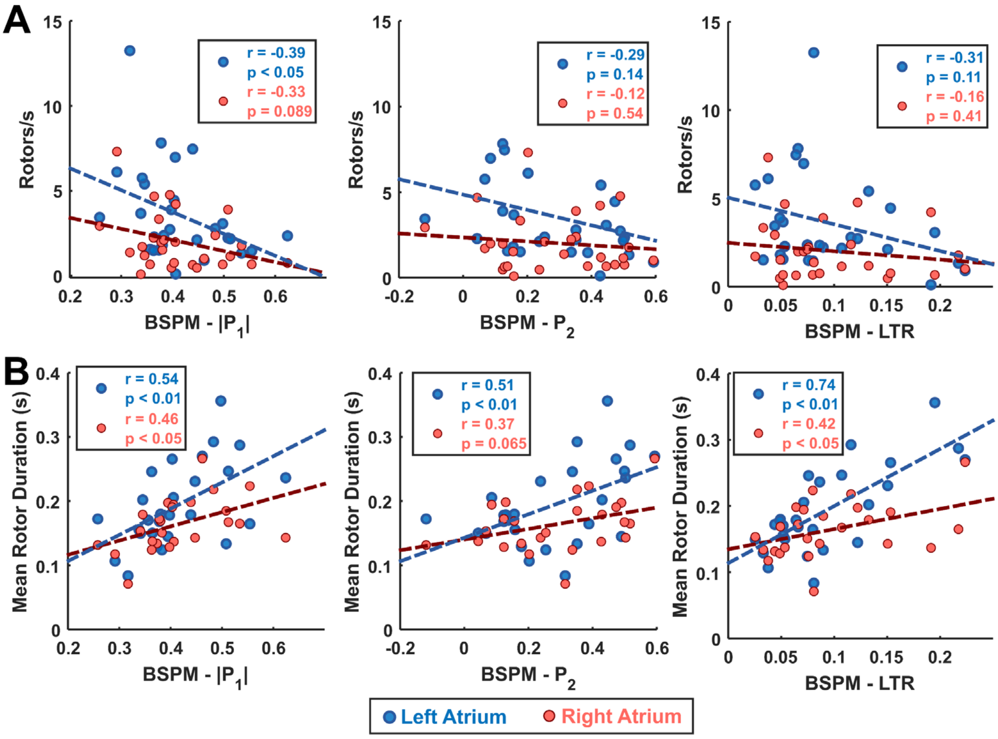

Figure 8.7. Correlation of BSPM-based AF propagation recurrence metrics with the number of rotors per second (A) and mean rotor duration (B) for rotors in the left (blue dots) and in the right (red dots) atrium, respectively. The values of r represent the Pearson's correlation coefficient and its p-value of the adjusted regression lines.

## 8.4. Discussion

In this work, we compared state-of-the-art BSPM metrics proposed to evaluate the complexity and recurrence of AF with corresponding metrics computed on epicardial signals reconstructed by means of ECGI. We did this to improve our understanding of how and to what extent surface electrocardiogram recordings relate to reentrant atrial activity on the epicardium. We showed that AF substrate complexity metrics computed on BSPM signals correlate well with the same metrics when computed on ECGI signals. Furthermore, we found that metrics that analyze the entropy and energy of the signals are good predictors of reentrant atrial activity and of its duration, both estimated from ECGI-derived maps. Short- and long-term recurrence of BSPM signals also showed high correlations with the reentrant activity from ECGI. Finally, we demonstrated that body surface metrics showed a higher correlation with reentrant activity observed in the left atrium, suggesting that atrial locations of higher complexity are reflected on BSPM recordings to a certain extent.

### 8.4.1. Relationship between reentrant activity and BSPM-based AF complexity and AF propagation recurrence

In previous studies, we have shown that BSPM signals do reflect the local activation rates (or dominant frequencies) in the atria (Guillem et al., 2013). More recently, we have evaluated the ability of BSPM signals to identify the presence and location of AF rotors using neural networks (Luongo et al., 2021), but no previous studies have reported a relationship of reentrant activity during AF and its duration and AF substrate complexity metrics derived from body surface recordings. In (Bonizzi et al., 2014), it was shown that higher SAE and RHE computed on epicardial recordings during AF were associated with a more complex and less organized AF. In this study, we found that both SAE and RHE computed on surface recordings correlated with a larger number of rotors of shorter duration as measured by ECGI. A higher number of rotors has been associated with more atrial electro-structural remodeling (Platonov et al., 2011) and fibrosis (Cochet et al., 2018), and this may be a physiological explanation of higher values of parameters as SAE and RHE, which is indicative of a greater AF substrate complexity. These results together confirm that information about AF substrate complexity and recurrence of atrial activity patterns during AF is, to a certain degree, reflected on the body surface. At the same time, although previous studies have linked the presence of rotors to AF dominant frequency measured on the body surface (Rodrigo et al., 2014), we could not find statistically significant correlations between BSPM-based HDF and the number and duration of reentries computed on ECGI, although a trend towards shorter-living rotors for higher HDFs could be observed.

In the same direction, the AF propagation recurrence computed on the BSPM signals was shown to be correlated with rotors of shorter duration as measured on ECGI signals. Especially, LTR, associated with long-term AF recurrence, presented a significant correlation with rotor duration. This suggests a link between reentrant atrial activity during AF and recurrence of BSPM-derived atrial signals, which could provide helpful information to electrophysiologists prior to ablation or other treatment without the need for estimating ECGI potentials and relying just on the BSPM data.

### 8.4.2. Left and right atrium assessment of AF substrate complexity

Estimating AF substrate complexity from a surface ECG can be challenging, especially in determining the differences in AF complexity between the atria. While the analysis of BSPM signals provides a broader view of AF progression, it may still be difficult to distinguish the different properties of the two atria without invasive intracardiac recordings. ECGI has been shown to be a valuable tool in assessing the atrial substrate, and in this study, we have shown a strong correlation between AF substrate complexity metrics measured on both BSPM and ECGI signals. However, we could not find any statistical differences in these metrics when computed on the left and right atrium through ECGI, respectively, suggesting that AF complexity and AF propagation recurrence metrics are not sufficiently accurate to capture differences in AF substrate complexity between the atria.

On the other hand, the quantification of ECGI-based atrial reentrant activity computed on the left and right atrium showed significant differences. A more complex AF substrate with more and shorter rotational activity was observed on the left than in the right atrium. This is expected in AF patients since pulmonary veins are usually the primary source of AF episodes. Our findings are consistent with other studies that also reported a greater reentrant activity in the left atrium (more SP and rotors per second, $p=10^{-3}$ and $6 \cdot 10^{-3}$ respectively) (Vijayakumar et al., 2022). This highlights the importance of utilizing ECGI and measuring reentries for a more comprehensive and specific evaluation of AF, particularly for patients undergoing ablation.

Moreover, in the studied patient population, we observed that body-surface metrics showed higher correlations with rotational activity in the left atrium. However, we could not determine whether this relationship is due to a higher complexity in the LA (as revealed by reentrant analysis), which is better captured on BSPM signals overshading the RA, or because the left atrial activity is better reflected on BSPM independently of its substrate complexity.

### 8.4.3. Limitations

This study represents an exploratory effort to interpret information about atrial reentrant activity extracted from BSPM signals. Since we only included a limited number of patients in this study, further research is needed to confirm our findings in order to assess the potential utility of BSPM-based AF substrate complexity and recurrence metrics in the clinical practice.

## 8.5. Conclusion

This study provides a physiological interpretation of BSPM-based AF substrate complexity and recurrence metrics and their relationship with AF reentrant atrial activity assessed through ECGI. BSPM metrics that reflect increased atrial electro-structural remodeling are correlated with a higher number of rotors of short duration computed on ECGI-based atrial signals, particularly in the left atrium. BSPM metrics, however, may not allow for capturing regional differences in atrial complexity (i.e. left vs right atrial electrical complexity).

## Acknowledgments

This work was supported by: Instituto de Salud Carlos III (supported by FEDER Fondo Europeo de Desarrollo Regional PI17/01106), Generalitat Valenciana and European Social Fund (ACIF/2020/265 and BEFPI/2021/062).

This article stems from a collaborative effort conducted during a predoctoral stay at Maastricht University

## Supplementary Table

| Metric | BSPM | ECGI | Correlation BSPM - ECGI | P-value |
|---|---|---|---|---|
| **$K_{095}$** | 9.07 ± 3.38 | 5.84 ± 1.44 | 0.69 | 4.37e-5 |
| **NMSE** | 0.73 ± 0.23 | 0.81 ± 0.09 | 0.40 | 0.03 |
| **C** | 18.44 ± 7.44 | 14.76 ± 6.81 | 0.82 | 1.28e-7 |
| **CV** | 3.77 ± 1.78 | 3.28 ± 2.08 | 0.78 | 8.44e-7 |
| **SC** | 0.37 ± 0.03 | 0.38 ± 0.02 | 0.77 | 1.77e-6 |
| **MOI** | 0.29 ± 0.08 | 0.47 ± 0.11 | 0.93 | 1.54e-12 |
| **MSE** | 5.73 ± 0.14 | 5.14 ± 0.25 | 0.62 | 3e-4 |
| **FWP** | 456.36 ± 63.32 | 459.96 ± 64.65 | 0.69 | 4.8e-5 |
| **FWPM** | 715.13 ± 116.55 | 718.25 ± 100.54 | 0.85 | 8.85e-9 |
| **SAE** | 0.1 ± 0.03 | 0.1 ± 0.04 | 0.96 | 1.78e-16 |
| **SAEM** | 0.05 ± 0.01 | 0.05 ± 0.01 | 0.89 | 3.40e-10 |
| **HDF** | 8.48 ± 1.54 | 8.66 ± 1.49 | 0.78 | 1.09e-6 |
| **RHE** | 0.24 ± 0.06 | 0.25 ± 0.08 | 0.89 | 2.73e-10 |
| **$\lvert P_1 \rvert$** | 0.41 ± 0.08 | 0.42 ± 0.09 | 0.95 | 4.37e-5 |
| **$P_2$** | 0.29 ± 0.16 | 0.3 ± 0.18 | 0.96 | 0.03 |
| **LTR** | 0.1 ± 0.06 | 0.1 ± 0.07 | 0.97 | 1.28e-7 |

Supplemental table 1. Mean and standard deviation values of state-of-the-art metrics of atrial fibrillation complexity computed on BSPM and ECGI signals, their correlation coefficient (r) between them and the p-value.

# References

Alcaraz, R., and Rieta, J. J. (2010). A review on sample entropy applications for the non-invasive analysis of atrial fibrillation electrocardiograms. Biomed. Signal Process. Control 5, 1–14. doi:10.1016/J.BSPC.2009.11.001.

Alcaraz, R., Sandberg, F., Sörnmo, L., and Rieta, J. J. (2011). Classification of paroxysmal and persistent atrial fibrillation in ambulatory ECG recordings. IEEE Trans. Biomed. Eng. 58, 1441–1449. doi:10.1109/TBME.2011.2112658.

Bergquist, J., Rupp, L., Zenger, B., Brundage, J., Busatto, A., and MacLeod, R. S. (2021). Body Surface Potential Mapping: Contemporary Applications and Future Perspectives. Hearts 2, 514–542. doi:10.3390/hearts2040040.

Bizhanov, K. A., Abzaliyev, K. B., Baimbetov, A. K., Sarsenbayeva, A. B., and Lyan, E. (2022). Atrial fibrillation: Epidemiology, pathophysiology, and clinical complications (literature review). J. Cardiovasc. Electrophysiol. 34, 153–165. doi:10.1111/jce.15759.

Bonizzi, P., Meste, O., Zeemering, S., Karel, J., Lankveld, T., Crijns, H., et al. (2020). A novel framework for noninvasive analysis of short-term atrial activity dynamics during persistent atrial fibrillation. Med. Biol. Eng. Comput. 58, 1933–1945. doi:10.1007/s11517-020-02190-0.

Bonizzi, P., Zeemering, S., Karel, J. M. H., Di Marco, L. Y., Uldry, L., Van Zaen, J., et al. (2014). Systematic comparison of non-invasive measures for the assessment of atrial fibrillation complexity: A step forward towards standardization of atrial fibrillation electrogram analysis. Europace 17, 318–325. doi:10.1093/europace/euu202.

Castells, F., Mora, C., Rieta, J. J., Moratal-Pérez, D., and Millet, J. (2005). Estimation of atrial fibrillatory wave from single-lead atrial fibrillation electrocardiograms using principal component analysis concepts. Med. Biol. Eng. Comput. 43, 557–560. doi:10.1007/BF02351028.

Cochet, H., Dubois, R., Yamashita, S., Al Jefairi, N., Berte, B., Sellal, J.-M., et al. (2018). Relationship Between Fibrosis Detected on Late Gadolinium-Enhanced Cardiac Magnetic Resonance and Re-Entrant Activity Assessed With Electrocardiographic Imaging in Human Persistent Atrial Fibrillation. JACC Clin. Electrophysiol. 4, 17–29. doi:10.1016/j.jacep.2017.07.019.

Dhillon, G. S., Honarbakhsh, S., Graham, A., Abbass, H., Welch, S., Daw, H., et al. (2022). ECG-I phenotyping of persistent AF based on driver burden and distribution to predict response to pulmonary vein isolation (PHENOTYPE-AF). J. Cardiovasc. Electrophysiol. 33, 2263–2273. doi:10.1111/jce.15644.

Eckstein, J., Maesen, B., Linz, D., Zeemering, S., Van Hunnik, A., Verheule, S., et al. (2011). Time course and mechanisms of endo-epicardial electrical dissociation during atrial fibrillation in the goat. Cardiovasc. Res. 89, 816–824. doi:10.1093/cvr/cvq336.

Fambuena-Santos, C., Hernández-Romero, I., Molero, R., Atienza, F., Climent, A. M., and Guillem, M. S. (2023). AF driver detection in pulmonary vein area by electropcardiographic imaging: Relation with a favorable outcome of pulmonary vein isolation. Front. Physiol. 14, 1–11. doi:10.3389/fphys.2023.1057700.

Gonzalez-Ascaso, A., Molero, R., Climent, A. M., and Guillem, M. S. (2020). ECGi Metrics in Atrial Fibrillation Dependency on Epicardium Segmentation. in Computing in Cardiology, 104438. doi:10.22489/CinC.2020.156.

Guillem, M. S., Climent, A. M., Millet, J., Arenal, Á., Fernández-Avilés, F., Jalife, J., et al. (2013). Noninvasive Localization of Maximal Frequency Sites of Atrial Fibrillation by Body Surface Potential Mapping. Circ. Arrhythmia Electrophysiol. 6, 294–301. doi:10.1161/CIRCEP.112.000167.

Guillem, M. S., Climent, A. M., Rodrigo, M., Fernández-Avilés, F., Atienza, F., and Berenfeld, O. (2016). Presence and stability of rotors in atrial fibrillation: evidence and therapeutic implications. Cardiovasc. Res. 109, 480–492. doi:10.1093/cvr/cvw011.

Hernández-Romero, I., Molero, R., Fambuena-Santos, C., Herrero-Martín, C., Climent, A. M., and Guillem, M. S. (2023). Electrocardiographic imaging in the atria. Med. Biol. Eng. Comput. 61, 879–896. doi:10.1007/s11517-022-02709-7.

Hindricks, G., Potpara, T., Dagres, N., Bax, J. J., Boriani, G., Dan, G. A., et al. (2021). 2020 ESC Guidelines for the diagnosis and management of atrial fibrillation developed in collaboration with the European Association for Cardio-Thoracic Surgery (EACTS). Eur. Heart J. 42, 373–498. doi:10.1093/eurheartj/ehaa612.

Lankveld, T., De Vos, C. B., Limantoro, I., Zeemering, S., Dudink, E., Crijns, H. J., et al. (2016a). Systematic analysis of ECG predictors of sinus rhythm maintenance after electrical cardioversion for persistent atrial fibrillation. Hear. Rhythm 13, 1020–1027. doi:10.1016/J.HRTHM.2016.01.004.

Lankveld, T., Zeemering, S., Scherr, D., Kuklik, P., Hoffmann, B. A., Willems, S., et al. (2016b). Atrial Fibrillation Complexity Parameters Derived from Surface ECGs Predict Procedural Outcome and Long-Term Follow-Up of Stepwise Catheter Ablation for Atrial Fibrillation. Circ. Arrhythmia Electrophysiol. 9. doi:10.1161/CIRCEP.115.003354.

Lim, H. S., Hocini, M., Dubois, R., Denis, A., Derval, N., Zellerhoff, S., et al. (2017). Complexity and Distribution of Drivers in Relation to Duration of Persistent Atrial Fibrillation. J Am Coll Cardiol doi:10.1016/j.jacc.2017.01.014.

Luongo, G., Azzolin, L., Schuler, S., Rivolta, M. W., Almeida, T. P., Martínez, J. P., et al. (2021). Machine learning enables noninvasive prediction of atrial fibrillation driver location and acute pulmonary vein ablation success using the 12-lead ECG. Cardiovasc. Digit. Heal. J., 1–11. doi:10.1016/j.cvdhj.2021.03.002.

Meo, M., Pambrun, T., Derval, N., Dumas-Pomier, C., Puyo, S., Duchâteau, J., et al. (2018). Noninvasive Assessment of Atrial Fibrillation Complexity in Relation to Ablation Characteristics and Outcome. Front. Physiol. | www.frontiersin.org 9. doi:10.3389/fphys.2018.00929.

Meste, O., Zeemering, S., Karel, J., Lankveld, T., Schotten, U., Crijns, H., et al. (2016). Noninvasive recurrence quantification analysis predicts atrial fibrillation recurrence in persistent patients undergoing electrical cardioversion. Comput. Cardiol. (2010). 43, 677–680. doi:10.22489/cinc.2016.199-342.

Molero, R., González-Ascaso, A., Climent, A. M., and Guillem, M. S. (2023a). Robustness of imageless electrocardiographic imaging against uncertainty in atrial morphology and location. J. Electrocardiol. 77, 58–61. doi:10.1016/j.jelectrocard.2022.12.007.

Molero, R., Hernández-Romero, I., Climent, A. M., and Guillem, M. S. (2023b). Filtering strategies of electrocardiographic imaging signals for stratification of atrial fibrillation patients. Biomed. Signal Process. Control 81, 104438. doi:10.1016/j.bspc.2022.104438.

Molero, R., Soler Torro, J. M., Martínez Alzamora, N., M. Climent, A., and Guillem, M. S. (2021). Higher reproducibility of phase derived metrics from electrocardiographic imaging during atrial fibrillation in patients remaining in sinus rhythm after pulmonary vein isolation. Comput. Biol. Med. 139, 104934. doi:10.1016/j.compbiomed.2021.104934.

Platonov, P. G., Mitrofanova, L. B., Orshanskaya, V., and Ho, S. Y. (2011). Structural abnormalities in atrial walls are associated with presence and persistency of atrial fibrillation but not with age. J. Am. Coll. Cardiol. 58, 2225–2232. doi:10.1016/J.JACC.2011.05.061.

Rodrigo, M., Climent, A. M., Hernández-Romero, I., Liberos, A., Baykaner, T., Rogers, A. J., et al. (2020). Non-Invasive Assessment of Complexity of Atrial Fibrillation: Correlation with Contact Mapping and Impact of Ablation. Circ. Arrhythmia Electrophysiol. 13, e007700. doi:10.1161/CIRCEP.119.007700.

Rodrigo, M., Climent, A. M., Liberos, A., Fernández-Avilés, F., Berenfeld, O., Atienza, F., et al. (2017). Highest dominant frequency and rotor positions are robust markers of driver location during noninvasive mapping of atrial fibrillation: A computational study. Hear. Rhythm 14, 1224–1233. doi:10.1016/j.hrthm.2017.04.017.

Rodrigo, M., Guillem, M. S., Climent, A. M., Pedrón-Torrecilla, J., Liberos, A., Millet, J., et al. (2014). Body surface localization of left and right atrial high-frequency rotors in atrial fibrillation patients: A clinical-computational study. Hear. Rhythm 11, 1584–1591. doi:10.1016/j.hrthm.2014.05.013.

Rodrigo, M., Waddell, K., Magee, S., Rogers, A. J., Alhusseini, M., Hernandez-Romero, I., et al. (2021). Non-invasive Spatial Mapping of Frequencies in Atrial Fibrillation: Correlation With Contact Mapping. Front. Physiol. 11, 611266. doi:10.3389/fphys.2020.611266.

Schmidt, R., and Singh, K. (2010). Meshmixer: An interface for rapid mesh composition. in ACM SIGGRAPH 2010 Talks, SIGGRAPH ’10 doi:10.1145/1837026.1837034.

Vijayakumar, R., Faddis, M. N., Cuculich, P. S., and Rudy, Y. (2022). Mechanisms of persistent atrial fibrillation and recurrences within 12 months post-ablation: Non-invasive mapping with electrocardiographic imaging. Front. Cardiovasc. Med. 9. doi:10.3389/fcvm.2022.1052195.

# Chapter 9

# Discussion and conclusions

In this chapter, we summarize the main discoveries of the thesis and compare them to prior research. We will also address the global limitations of the studies conducted throughout the thesis. Afterwards, we will evaluate the achievement of the objectives and draw the main conclusions from the thesis. Lastly, we will provide recommendations for future work, emphasizing areas for enhancement and possible future research directions.

## 9.1. Main findings

Electrocardiographic imaging is garnering increasing interest from numerous research groups and hospitals, who are working diligently to enhance the diagnosis and treatment of atrial arrhythmias. Since its origin in 1977 (Barr and Spach, 1977), the evolution of ECGI has made significant steps, as the validation non-invasive maps and metrics of cardiac activity validated with intracardiac recordings (Rodrigo et al., 2020) (Rodrigo et al. 2021). With ongoing research and development, the potential to achieve high-quality signals and derived valuable metrics will undoubtedly lead to the integration of ECGI into standard care practices and inclusion in clinical guidelines.

In this thesis we outlined the path for the implementation and use of ECGI as an extended method for an accurate non-invasive diagnosis and evaluation of atrial fibrillation. In order to obtain ECGI signals and maps with derived metrics for AF and other types of cardiac rhythms, an accurate geometric reconstruction of both the patient's torso and heart is necessary. Firstly, we quantified and standardized the geometrical minimum requirements of the torso mesh, specifying the minimum number of mesh nodes, the tolerated electrode labeling error, and the distribution of the nodes in the mesh necessary for an accurate reconstruction of epicardial potentials, in both simulations and patients. Additionally, we showed that the precision on the atrial geometry has just a moderate importance compared to its relative position inside the torso. This allowed us to develop and validate an Imageless ECGI, eliminating the need for MRI/CT scans in the workflow to obtain non-invasive signals and maps.

Once ECGI geometrical requirements have been quantified, we have identified the need to improve the ECGI signals computation method due to its limitations in high signal-to-noise situations and uncertainty in cardiac geometry localization within the zero-order Tikhonov regularization and L-curve optimization. We proved that different sources of noise affect to the curvature of the L-curve optimization used to select the optimal regularization parameter necessary to compute ECGI signals, but only electrical noise found on BSPM signals affects the selection of the optimal regularization parameter used for computing ECGI signals. As a result, we proposed a more robust method to determine an optimal regularization parameter when the state-of-the art L-curve method fails.

We have not only defined and established the technical and mathematical framework for obtaining high-quality ECGI but also developed a methodology for the evaluation and stratification of AF patients undergoing PVI treatment. To stratify patients, we must extract clinically relevant metrics; thus, we defined the optimal filtering strategy for ECGI signals to detect reentrant activity. Furthermore, we found that metrics derived from ECGI-derived rotor analysis are reproducible in AF patients, and this reproducibility is linked to the success of ablation therapies. Consequently, we have described a method for predicting PVI outcomes, which has been further validated in a different database (Molero et al., 2022) and it is now being patented.

Lastly, we have employed ECGI as a tool for evaluating AF atrial substrate to explain BSPM signal analysis measures, such as entropy and energy. By correlating ECGI reentrant metrics with BSPM-based AF complexity metrics, we were able to elucidate the underlying causes of BSPM signal complexity. Our research highlighted the indispensable role of ECGI in non-invasively evaluating the cardiac substrate, particularly when detailed atrial regional information is required.

## 9.2. Comparison with previous studies

Since the beginning of ECGI, researchers have been concerned with the obtention of high-quality ECGI signals and the requirements needed of both the torso and heart geometries, concerns addressed on this thesis. Even though previous studies have reported that an accurate torso geometry is necessary to obtain electrocardiographic imaging signals (Messinger-Rapport and Rudy, 1990) (Colli-Franzone et al., 1985), we have demonstrated that a coarse meshing is sufficient to obtain high-quality ECGI signals. Furthermore, the number and distribution of electrodes required on the torso for ECGI has been widely studied in the past. Lux et al. determined that at least 30 electrodes needed in order to capture all relevant electrical information on the thorax during sinus rhythm, observation that was extended to AF later by our group (Guillem et al., 2009). In addition to this previous knowledge, we concluded that the correct location of the BSPM electrodes in their exact position in the torso mesh is fundamental to the obtention of the ECGI signals.

Additionally, ECGI traditionally requires of CT Scan/MRI images for the obtention of the cardiac geometry and its location inside the torso mesh. In this thesis, we investigated the effect of using an estimated cardiac geometry to solve the inverse problem and we concluded that it has just a relative relevance on the derived ECGI signals and metrics. Cardiac location is also essential for the correct functioning of Imageless ECGI and in the past, in our group we developed a methodology based on the L-curve for positioning the cardiac mesh within the torso without requiring imaging techniques (Rodrigo et al., 2018). In this thesis, we determined that the cardiac mesh can be located just based on the torso of the patient with low errors in the location and the computed ECGI signals. We established Imageless ECGI as the new framework that we hope will universalize the use of ECGI, with less costs associated with cardiac imaging.

Furthermore, ECGI regularization has been widely discussed on the field. On prior research, we demonstrated that zero-order Tikhonov regularization and L-curve optimization is the most effective regularization method for computing the inverse problem in atrial fibrillation (Figuera et al., 2016), as evidenced numerous studies utilizing this approach, that we collected in this review (Salinet et al., 2021). However, Hansen and O'Leary, had previously highlighted the limitations of using the maximum curvature value for obtaining the most optimal regularization parameter, showing the room of improvement for its selection. We identified this limitation especially in signals from patients with high electrical noise presence, consequently, we defined a new methodology in order to obtain robust ECGI signals based on the most horizontal angle of the L-curve and not the maximum curvature.

Moreover, ECGI has been explored as a technique for extracting information about the complexity of the atrial substrate. In 2014, Haissaguerre et al., revealed its potential to guide ablations, which led to reduced intervention times and increased success rates. Since then, numerous studies have been conducted in various centers using ECGI to detect AF drivers and improve ablation outcomes  (Knecht et al., 2017) (Dhillon et al., 2022)(Honarbakhsh et al., 2022). However, AF-driver guided ablation is still discussed as it did not show improvements in the outcome of the ablation in different trials (Buch et al., 2016)(Parameswaran et al., 2018). In this thesis, we propose a stratification of patients prior the PVI: we proposed a methodology for selecting patients that can benefit from PVI in order to maximize PVI outcomes. This, in turn, will boost the cost-effectiveness of pulmonary vein isolation, with a higher rate of AF-freedom, and hopefully reduce the number of redo procedures.

## 9.3. Limitations

This thesis provides valuable insights into estimating atrial electrical complexity during atrial fibrillation using electrocardiographic imaging, yet certain limitations must be acknowledged. We will outline the limitations based on the origin of the signals used in our studies.

One limitation of our in-silico analyses is the simplicity of the used anatomical models, which excluded inner organs and torso inhomogeneities. Nevertheless, previous studies demonstrated that this consideration has not a major impact on the ECGI potentials (Ramanathan and Rudy, 2001). Furthermore, the lack of anisotropy in the forward model may influence our results, but its effect on ECGI resolutions may be minimal, as previously reported (Colli-Franzone et al., 1982) (Cheng et al., 2003).

In addition to the limitations of the in-silico studies, our patient-based studies have a relatively small sample size of patients, which may limit the generalization of our findings. Future research should aim to include a larger and more diverse patient population to validate and extend the conclusions presented in this thesis. A direct comparison and validation of our findings with invasive mapping techniques, such as electroanatomic mapping or intracardiac electrograms, would strengthen the conclusions and confirm the accuracy of non-invasive ECGI-derived metrics in assessing atrial electrical complexity.

Lastly, a more comprehensive analysis of factors that may influence the estimation of atrial electrical complexity, such as age, gender, comorbidities, the use of antiarrhythmic medications, or even different signal processing and regularization methodologies could further refine the results and provide a better understanding of the factors contributing to atrial fibrillation complexity.

Despite the limitations mentioned above, the findings have significant implications for the application of non-invasive electrophysiological maps in clinical practice, particularly in guiding atrial fibrillation ablation and identifying reentrant activity.

## 9.4. Conclusions

This thesis had two main objectives that have been responded in the previous chapters of this manuscript: to improve the current state-of-the-art methodology of ECGI and to validate its applicability in the quantification of AF complexity. In the following lines, we will answer how the two main objectives have been achieved with their specific objectives.

*Objective 1: To assess the geometric and signal requirements of the inverse problem of electrocardiography, and to quantify the limitations and potential advancements in this technology for the evaluation of atrial fibrillation complexity.* We have demonstrated the potential of this technology for evaluating the complexity of atrial fibrillation and have quantified the confidence ranges in which we can rely on ECGI reconstruction with regard to electrical noise, incorrect positioning of cardiac geometry, node density in torso geometry, and electrode positioning. This objective was divided into the following points:

- *To determine the impact of torso mesh density and electrode placement in the torso mesh used on the inverse problem resolution in atrial fibrillation signals.* In Chapter 3, we demonstrated that the number of nodes in the torso mesh has little effect on the quality of ECGI reconstruction if the electrode positions of the BSPMs are respected. We concluded that at least 400 homogeneously distributed nodes are needed for high-quality inverse solutions. Moreover, we showed that electrode misplacement has a greater impact on the quality of ECGI reconstruction, and that node displacements below 2 cm do not significantly affect the quality of ECGI signals.
- *To assess the robustness of ECGI and derived metrics in atrial fibrillation signals under the displacement of atrial geometry from its correct position.* In Chapter 4, demonstrated that the effect of the cardiac displacement below 3cm is negligible on the ECGI signals and ECGI-derived drivers. We reported high correlations of the ECGI signals compared to a correct location of the mesh during ECGI calculation, showing that errors on the displacement of 3cm can be tolerated to consider an ECGI map as an accurate reconstruction of epicardial activity of an atrial fibrillation signal.

- *To determine the effect of the accuracy of the atrial geometry estimation on the inverse problem of electrocardiography in atrial fibrillation signals.* The effect of atrial geometry was reported on Chapter 4. We showed that the shape of the atrial mesh used to obtain electrocardiographic imaging signals of atrial fibrillation simulations and patients has marginal effect neither in the quality of the inverse electrograms nor in the ECGI-derived metrics as dominant frequencies. Furthermore, we introduced a new methodology for imageless ECGI and showed its robustness in front on variations on the shape of the geometry. Imageless ECGI as an alternative to image-dependent ECGI may boost the introduction of ECGI into the clinical practice on a daily hospital basis, improving the diagnostics and treatment of atrial fibrillation.
- *To guide the selection of the optimal regularization parameter using the zero-order Tikhonov regularization and L-curve optimization method and to propose an alternative for identifying the optimal regularization parameter when the L-curve corner detection fails.* In chapter 6, we demonstrated that the shape and curvature of the L-curve is proportionally affected by different sources of noise, and only the electrical noise affect in the selection of the optimal regularization parameter used to obtain the ECGI signals. Moreover, we demonstrated that selecting an optimal regularization parameter using the L-curve method is more accurate when considering the entire curve shape, rather than solely relying on its corner. While the corner of the L-curve can identify the optimal regularization parameter in the absence of geometrical uncertainties, it becomes suboptimal when multiple uncertainties are present. To address this limitation, we proposed utilizing the slope of the predominantly horizontal component of the L-curve, which is closely related to the amount of noise in the BSPM signals, for determining an optimal regularization parameter.

*Objective 2: To evaluate the ability of ECGI to quantify atrial fibrillation complexity.* We developed several analyses to evaluate AF using ECGI, the extracted conclusions of each specific objective are enumerated in the following lines.

- *To establish the most appropriate signal processing methodology for evaluating reentrant activity in ECGI signals for the stratification of atrial fibrillation patients.* This objective has been addressed in Chapter 6. Given different strategies for post-processing ECGI signals, we concluded that it is not necessary to apply aggressive filters to AF signals to characterize the cardiac substrate. In addition, we demonstrated that establishing a one-turn threshold for the detection of phase singularities is optimal for finding differences between populations of AF patients with different prognoses after receiving PVI.

- *To determine the reproducibility of ECGI-derived metrics in atrial fibrillation and its relationship with the success of pulmonary vein ablation.* We proved that atrial fibrillation, despite being an irregular arrhythmia, presents reentrant patterns that are reproducible and can be characterized by using ECGI (Chapter 7). These reentrant patterns were found to be related to the outcome of pulmonary vein isolation, with patients with a favorable outcome 6-months after the ablation presenting more reproducible reentrant metrics compared to patients that were not benefited by the ablation. This study established a proof-of-concept methodology to stratify AF patients using ECGI to evaluate the cardiac substrate.
- *To assess the electrical complexity of atrial fibrillation signals in BSPM and its relationship with atrial substrate reentrant analysis using ECGI.* We showed in Chapter 8 that higher electrical complexity and recurrence dynamics measured on BSPM signals are correlated with a higher number of reentries and with a shorter duration measured on ECGI signals. Moreover, we found that the reentries located on the left atrium exhibit higher correlations with BSPM-metrics. We demonstrated that BSPM can offer qualitative data on AF reentries, while ECGI is necessary to determine regional substrate complexity differences non-invasively.

This thesis presents novel findings on the use of electrocardiographic imaging as a method to evaluate atrial fibrillation complexity. The proper definition of the torso mesh requirements used in ECGI, the possibility of using the technique without the need for a CT/MRI scan, and a new more robust regularization methodology, represent a new theoretical framework for the correct resolution of the inverse problem of electrocardiography, ensuring the obtention of high-quality epicardial signals non-invasively. Moreover, the proposed metrics and methodology to quantify the progression of atrial fibrillation in the atrial substrate can be utilized to stratify patients before undergoing ablations which could improve the success rate of the treatment by avoiding unnecessary interventions.

## 9.5. Guidelines for future works

Moving forward, several areas for future research can be identified based on the conclusions of this thesis. One important area is the further investigation into the effect of mesh density and node distribution on cardiac geometry. In our study presented in Chapter 3, the cardiac geometries used, had node densities of over 4,000 nodes, which is a higher number than that of the torso. Despite the high node density, a quantification of the minimal required number of nodes and their distribution for computing ECGI should be explored in future studies.

Another priority is the improvement of the resolution of the inverse problem. Although we have introduced a more robust methodology to handle higher SNR on BSPM and geometrical uncertainties, there remains room for improvement in the inverse problem resolution, particularly in recovering high-frequency components. Obtaining inverse electrograms with greater accuracy that closely resemble those observed using invasive mapping techniques is necessary. This level of precision would enable clinicians to rely on ECGI for more accurate diagnoses and better decision-making regarding patient treatment, thus reducing the need for invasive procedures. Developing methods to refine the resolution of the inverse problem will play a pivotal role in advancing the practical applicability of ECGI, solidifying its position as a valuable non-invasive tool for assessing and treating cardiac arrhythmias.

Future studies should also test the proposed metrics and their predictive value for PVI treatments using larger databases and explore reproducibility among larger sets of time and subsets of signals. Incorporating additional metrics, such as dominant frequencies and AF ectopics, into future studies for AF burden quantification would be beneficial for stratifying AF patients. Moreover, reproducibility analysis and ECGI metrics should be explored as a tool for pharmacological treatment recommendations, not only for predicting ablation outcomes. Additionally, the expansion of imageless ECGI to include ventricular geometries and signals is another path for investigation. This might broaden the technique's applicability to additional cardiac arrhythmias and diseases beyond atrial fibrillation.

Finally, introducing ECGI into the clinical workflow for the diagnosis and treatment of cardiac arrhythmias is an important step towards bringing the benefits of this technology to a wider patient population. In summary, the present thesis and these guidelines for future works provide a roadmap for advancing ECGI as a tool for diagnose and treat atrial fibrillation and other cardiac arrhythmias. By addressing these research areas, the potential of ECGI to revolutionize the diagnosis and treatment of cardiac diseases can be further realized, ultimately leading to improved patient quality of life and reduced healthcare costs.

# Chapter 10

# Contributions

## 10.1. Main contributions of this thesis

### 10.1.1. Journal Papers

- **R. Molero,** J. M. Soler Torro, N. Martínez Alzamora, A. M. Climent, and M. S. Guillem, "Higher reproducibility of phase derived metrics from electrocardiographic imaging during atrial fibrillation in patients remaining in sinus rhythm after pulmonary vein isolation," *Comput. Biol. Med.*, vol. 139, no. May, p. 104934, Dec. 2021 http://dx.doi.org/10.1016/j.compbiomed.2021.104934 Q1.
- **R. Molero,** A. González-Ascaso, I. Hernández-Romero, D. Lundback-Mompó, A. M. Climent, and M. S. Guillem, "Effects of torso mesh density and electrode distribution on the accuracy of electrocardiographic imaging during atrial fibrillation," *Front. Physiol.*, vol. 13, 2022 http://dx.doi.org/10.3389/fphys.2022.908364 Q1.
- **R. Molero,** I. Hernández-Romero, A. M. Climent, and M. S. Guillem, "Filtering strategies of electrocardiographic imaging signals for stratification of atrial fibrillation patients," Biomed. Signal Process. Control, vol. 81, p. 104438, Mar. 2023 http://dx.doi.org/10.1016/j.bspc.2022.104438. Q2.
- **R. Molero,** A. González-Ascaso, A. M. Climent, and M. S. Guillem, "Robustness of imageless electrocardiographic imaging against uncertainty in atrial morphology and location," J. Electrocardiol., vol. 77, no. January, pp. 58–61, 2023. http://dx.doi.org/10.1016/j.jelectrocard.2022.12.007. Q4.
- **R. Molero**, O. Meste, J. Karel, R. Peeters, P. Bonizzi, M. S. Guillem, "Complexity and recurrence of body surface electrocardiograms correlates with estimated reentrant atrial activity with electrocardiographic imaging in atrial fibrillation patients", *Submitted.*

- **R. Molero**, M. Martínez-Pérez, C. Herrero-Martín, J. Reventós-presmanes, I. Roca, L. Mont, A. M. Climent, and M. S. Guillem, "Improving Electrocardiographic Imaging solutions: A Comprehensive Study on Regularization Parameter Selection in L-curve Optimization", *Submitted.*
- J. Salinet, **R. Molero,** F. S. Schlindwein, J. Karel, M. Rodrigo, J. L. Rojo-Álvarez, O. Berenfeld, A. M. Climent, B. Zenger, F. Vanheusden, J. G. S. Paredes, R. MacLeod, F. Atienza, M. S. Guillem, M. Cluitmans, and P. Bonizzi, "Electrocardiographic Imaging for Atrial Fibrillation: A Perspective from Computer Models and Animal Experiments to Clinical Value," *Frontiers in Physiology*, vol. 12. 2021 http://dx.doi.org/10.3389/fphys.2021.653013 Q1.
- I. Hernández-Romero, **R. Molero,** C. Fambuena-Santos, C. Herrero-Martín, A. M. Climent, and M. S. Guillem, "Electrocardiographic imaging in the atria," *Med. Biol. Eng. Comput.*, vol. 61, no. 4, pp. 879–896, Apr. 2023 http://dx.doi.org/10.1007/s11517-022-02709-7 Q2.

### 10.1.2. International Conferences

- **R. Molero**, A. M. Climent, and A. Liberos, "Effects of Geometry in Atrial Fibrillation Markers Obtained with Electrocardiographic Imaging," in *Computing in Cardiology*, 2019, Singapur, Singapur. http://dx.doi.org/10.22489/CinC.2019.308
- **R. Molero**, A. M. Climent, and M. S. Guillem, "Post-Processing of Electrocardiographic Imaging Signals to Identify Atrial Fibrillation Drivers," in *Computing in Cardiology*, 2020, Rimini, Italy. http://dx.doi.org/10.22489/CinC.2020.113.
- **R. Molero**, C. Fambuena, A. M. Climent, and M. S. Guillem, "Electrocardiographic Imaging in Atrial Fibrillation: Selection of the Optimal Tikhonov-Regularization Parameter," in *Computing in Cardiology*, 2021, Brno, Czech Republic. http://dx.doi.org/10.23919/CinC53138.2021.9662918.
- **R. Molero,** A. Climent, and M. Guillem, "Prediction of ablation success in atrial fibrillation patients based on electrocardiographic imaging," *EP Eur.*, vol. 24, no. Supplement_1, 2022, Copenhagen, Denmark. http://dx.doi.org/10.1093/europace/euac053.036.
- **R. Molero**, A. González-Ascaso, I. Hernández-Romero, A. M. Climent, and M. de la Salud Guillem Sánchez, "Effect of Torso Mesh Density on Electrocardiographic Imaging Resolution from Atrial Fibrillation Simulations," in *Computing in Cardiology*, 2022, Tampere, Finland. http://dx.doi.org/10.22489/CinC.2022.187.

- **R. Molero**, O. Meste, J. Karel, R. Peeters, P. Bonizzi, M. S. Guillem, "Analysis of Atrial Fibrillation Dynamics in Body Surface Potential Maps and Electrocardiographic Imaging," in *Computing in Cardiology*, 2022, Tampere, Finland. http://dx.doi.org/10.22489/CinC.2022.175.
- **R. Molero**, J. Reventós-presmanes, I. Roca, L. Mont, A. M. Climent, and M. S. Guillem, "Impact of Noise on Electrocardiographic Imaging Resolution with Zero Order Tikhonov Regularization and L-Curve Optimization," in *Computing in Cardiology*, 2022, Tampere, Finland. http://dx.doi.org/10.22489/CinC.2022.214.
- **R. Molero,** M. Martínez-Pérez, J. Reventós-presmanes, L. Mont, A. M. Climent, and M. S. Guillem, "Robustness of electrocardiographic imaging in the presence of electrical noise", *EP Europace*, Volume 25, Issue Supplement_1, 2023, Barcelona, Spain. http://dx.doi.org/10.1093/europace/euad122.640

## 10.2. Contributions related to this thesis

### 10.2.1. Journal Papers

- C. Fambuena-Santos, I. Hernández-Romero, **R. Molero,** A. M. Climent, and M. S. Guillem, "AF driver detection in pulmonary vein area by electropcardiographic imaging: Relation with a favorable outcome of pulmonary vein isolation," Front. Physiol. 14, 1–11. http://dx.doi.org/10.3389/fphys.2023.1057700 Q1.

### 10.2.2. International Conferences

- González-Ascaso, **R. Molero**, A. M. Climent, and M. de la Salud Guillem Sánchez, "ECGi Metrics in Atrial Fibrillation Dependency on Epicardium Segmentation," in *Computing in Cardiology*, 2020, Rimini, Italy. http://dx.doi.org/10.22489/CinC.2020.156.
- Fambuena-Santos, I. Hernández-Romero, **R. Molero**, A. M. Climent, and M. S. Guillem, "An Evaluation on the Potential Clinical Outcome Prediction of Rotor Detection in Non-Invasive Phase Maps," in *Computing in Cardiology*, 2021, Brno, Czech Republic.

### 10.2.3. National Conferences

- C. Fambuena-Santos, I. Hernández-Romero, **R. Molero,** F. Atienza, A. M. Climent, and M. S. Guillem, Detección de Actividad Reentrante en Fibrilación Auricular mediante Imagen Electrocardiográfica: Relación con el Resultado Favorable tras Aislamiento de Vena Pulmonares. Congreso Nacional de la Sociedad Española de Cardiología, Mallorca, Spain, 2022.

## 10.3. Patents

**R. Molero**, C. Fambuena-Santos, J. Milagro, A.M. Climent, M. S. Guillem, 'Method for analyzing arrhythmia'. The patent is currently in the PCT (Patent Cooperation Treaty) phase of international application. PCT/EP2022/074485.

## 10.4. Awards

- 2020 – Rosanna Degani Young Investigator Award Finalist – Computing in Cardiology Conference, Rimini, Italy. "Post-Processing of Electrocardiographic Imaging Signals to Identify Atrial Fibrillation Drivers," in *Computing in Cardiology*, 2020.
- 2021 – ITACA 2nd Award Ferran Moncholí to publications with a higher impact factor in ITACA Institute.

## 10.5. Participation in scientific international committees

Member of the Consortium of Electrocardiographic Imaging (CEI):

- Member of CEI-Atrial Arrythmias. 2020-Present
- Coordinator of CEI-Atrial Arrhythmias subgroup of Impact of ECGI resolution algorithm on AF Biomarkers from ECGI Follow Up Meeting
- Member of CEI-Modelling Working Group 2021-Present
- Member of CEI-Machine Learning Working Group: 2023-Present
- Member of Organizing Committee of CEI Satellite Symposium 2020 – Online
- Member of Organizing Committee of CEI Satellite Symposium 2021 – Brno, Czech Republic

- Main coordinator of Organizing Committee of CEI Satellite Symposium 2022 – Tampere, Finland
- Member of Local Organizing Committee of ECGI Summit 2023, Valencia, Spain

## 10.6. Diffusion of results

During my thesis, extensive efforts were made to promote the scientific findings through various channels. The results obtained were disseminated in conferences, scientific events, and through social media platforms such as Twitter and LinkedIn. Additionally, the research gained visibility through coverage in multiple press publications and even featured on television, specifically on Apunt Televisió.

## 10.7. Industrial collaboration

Throughout my thesis, a close collaboration has been produced with Corify Care SL, a leading company in the field of Electrocardiographic Imaging.

## 10.8. Teaching

- 2020-2021 – Sistemas complejos bioinspirados, Ingeniería de Tecnologías y Servicios de Telecomunicación - 2.1 ECTS
- 2021 – 2022 - Sistemas complejos bioinspirados, Ingeniería de Tecnologías y Servicios de Telecomunicación - 4.2 ECTS
- 2022– 2023 - Sistemas complejos bioinspirados, Ingeniería de Tecnologías y Servicios de Telecomunicación - 4.2 ECTS
- 2022 – 2023 - Electrónica, Grado en Tecnología Digital y Multimedia - 2.6 ECTS

### 10.8.1. Supervision of bachelor thesis

- Development of a method for estimating the location of maintaining sites of atrial fibrillation using the inverse problem of electrocardiography through phase analysis and phase and frequency modulations. Estrella del Mar Ballester Hoyo, 09/12/2020. Mark: 9.5

- Study of the temporal reproducibility of inverse electrograms in patients with atrial fibrillation. Aida Sáez Sáez, 05/07/2021. Mark: 9.2
- Development of algorithms for identifying reentrant patterns in atrial flutter through solving the inverse problem of electrocardiography. María Correas García, 14/09/2021. Mark: 9.2

### 10.8.2. Supervision of master thesis

- Development of technology for the estimation of atrial conduction velocity in sinus rhythm using inverse problem of electrocardiography. Albert Marín Bernard, 21/07/2020. Mark: 9.0

## 10.9. Research stay

During the development of this thesis a research stay has been conducted on Maastricht University, the Netherlands.

Dates: 1st of September until 30th of November 2021.

During this stay an international conference paper and Chapter 8 of this thesis have been developed.

## 10.10. Research projects and funding

This PhD thesis has been funded by Generalitat Valenciana – Conselleria de Innovación, Universidades, Ciencia y Sociedad Digital under the title of ‘Estimation of atrial electrical complexity during atrial fibrillation’ and code ACIF/2020/265, with a grant amount of 66.578.40€. Furthermore, the research stay conducted during this PhD thesis has been funded by Generalitat Valenciana with a grant amount of 4331.00€, grant number BEFPI/2021/062.

In addition, this work has been developed as part of the following projects:

- Desarrollo de una herramienta de mapeo panorámico para la evaluación de sustratos electro-estructurales para guiar la ablación de la fibrilación auricular utilizando AI (PID2020-119364RB-I00)
  - Funding Entity: Agencia Estatal de Investigación

  - Project Title: Development of a panoramic mapping tool for the evaluation of electro-structural substrates to guide atrial fibrillation ablation using AI (PID2020-119364RB-I00)
  - Main Researcher: María de la Salud Guillem Sánchez
  - Grant Amount: 179,201.00€

- Artificial intelligence drive platform for atrial fibrillation stratification
  - Funding Entity: EIT HEALTH E.V.
  - Main Researcher: María de la Salud Guillem Sánchez
  - Grant Amount: 109,812.44€

- Tecnologías de imagen electrocardiográfica para la personalización de los tratamientos para fibrilación auricular (AICO/2018/267)
  - Funding Entity: Generalitat Valenciana
  - Main Researcher: María de la Salud Guillem Sánchez
  - Grant Amount: 40,000.00€

# References

Aronis, K. N., Ali, R., and Trayanova, N. A. (2019). The role of personalized atrial modeling in understanding atrial fibrillation mechanisms and improving treatment. Int. J. Cardiol. 287, 139–147. doi:10.1016/J.IJCARD.2019.01.096.

Aslanidi, O. V., Colman, M. A., Stott, J., Dobrzynski, H., Boyett, M. R., Holden, A. V., et al. (2011). 3D virtual human atria: A computational platform for studying clinical atrial fibrillation. Prog. Biophys. Mol. Biol. 107, 156–168. doi:10.1016/j.pbiomolbio.2011.06.011.

Atienza, F., Almendral, J., Jalife, J., Zlochiver, S., Ploutz-Snyder, R., Torrecilla, E. G., et al. (2009). Real-time dominant frequency mapping and ablation of dominant frequency sites in atrial fibrillation with left-to-right frequency gradients predicts long-term maintenance of sinus rhythm. Hear. Rhythm 6, 33–40. doi:10.1016/j.hrthm.2008.10.024.

Atienza, F., Almendral, J., Ormaetxe, J. M., Moya, Á., Martínez-Alday, J. D., Hernández-Madrid, A., et al. (2014). Comparison of radiofrequency catheter ablation of drivers and circumferential pulmonary vein isolation in atrial fibrillation: A noninferiority randomized multicenter RADAR-AF trial. J. Am. Coll. Cardiol. 64, 2455–2467. doi:10.1016/j.jacc.2014.09.053.

Barr, R. C., and Spach, M. S. (1977). Inverse calculation of QRS-T epicardial potentials from body surface potential distributions for normal and ectopic beats in the intact dog. Circ. Res. 42, 661–675. doi:10.1161/01.RES.42.5.661.

Benjamin, E. J., Muntner, P., Alonso, A., Bittencourt, M. S., Callaway, C. W., Carson, A. P., et al. (2019). Heart Disease and Stroke Statistics-2019 Update: A Report From the American Heart Association. Circulation 139, e56–e528. doi:10.1161/CIR.0000000000000659/FORMAT/EPUB.

Bisbal, F., Benito, E., Teis, A., Alarcón, F., Sarrias, A., Caixal, G., et al. (2020). Magnetic Resonance Imaging-Guided Fibrosis Ablation for the Treatment of Atrial Fibrillation: The ALICIA Trial. Circ. Arrhythm. Electrophysiol. 13, e008707. doi:10.1161/CIRCEP.120.008707.

Bonizzi, P., Meste, O., Zeemering, S., Karel, J., Lankveld, T., Crijns, H., et al. (2020). A novel framework for noninvasive analysis of short-term atrial activity dynamics during persistent atrial fibrillation. Med. Biol. Eng. Comput. 58, 1933–1945. doi:10.1007/s11517-020-02190-0.

Bonizzi, P., Zeemering, S., Karel, J. M. H., Di Marco, L. Y., Uldry, L., Van Zaen, J., et al. (2014). Systematic comparison of non-invasive measures for the assessment of atrial fibrillation complexity: A step forward towards standardization of atrial fibrillation electrogram analysis. Europace 17, 318–325. doi:10.1093/europace/euu202.

References

Borràs, M., and Chamorro-Servent, J. (2021). Electrocardiographic Imaging: A Comparison of Iterative Solvers. Front. Physiol. 12, 620250. doi:10.3389/fphys.2021.620250.

Boyle, P. M., Hakim, J. B., Zahid, S., Franceschi, W. H., Murphy, M. J., Vigmond, E. J., et al. (2018). Comparing reentrant drivers predicted by image-based computational modeling and mapped by electrocardiographic imaging in persistent atrial fibrillation. Front. Physiol. 9, 1–12. doi:10.3389/fphys.2018.00414.

Boyle, P. M., Zghaib, T., Zahid, S., Ali, R. L., Deng, D., Franceschi, W. H., et al. (2019). Computationally guided personalized targeted ablation of persistent atrial fibrillation. Nat. Biomed. Eng. 3, 870–879. doi:10.1038/s41551-019-0437-9.

Brugada, J., Katritsis, D. G., Arbelo, E., Arribas, F., Bax, J. J., Blomstrom-Lundqvist, C., et al. (2020). 2019 ESC Guidelines for the management of patients with supraventricular tachycardiaThe Task Force for the management of patients with supraventricular tachycardia of the European Society of Cardiology (ESC)Developed in collaboration with the Association for European Paediatric and Congenital Cardiology (AEPC). Eur. Heart J. 41, 655–720. doi:10.1093/EURHEARTJ/EHZ467.

Buch, E., Share, M., Tung, R., Benharash, P., Sharma, P., Koneru, J., et al. (2016). Long-term clinical outcomes of focal impulse and rotor modulation for treatment of atrial fibrillation: A multicenter experience. Hear. Rhythm 13, 636–641. doi:10.1016/j.hrthm.2015.10.031.

Calkins, H., Hindricks, G., Cappato, R., Kim, Y. H., Saad, E. B., Aguinaga, L., et al. (2017). 2017 HRS/EHRA/ECAS/APHRS/SOLAECE expert consensus statement on catheter and surgical ablation of atrial fibrillation: Executive summary. J. Arrhythmia 33, 369–409. doi:10.1016/j.joa.2017.08.001.

Calkins, H., Kuck, K. H., Cappato, R., Brugada, J., Camm, A. J., Chen, S. A., et al. (2012). 2012 HRS/EHRA/ECAS Expert Consensus Statement on Catheter and Surgical Ablation of Atrial Fibrillation: Recommendations for Patient Selection, Procedural Techniques, Patient Management and Follow-up, Definitions, Endpoints, and Research Trial Design. Hear. Rhythm 9, 632-696.e21. doi:10.1016/j.hrthm.2011.12.016.

Calvetti, D., Lewis, B., and Reichel, L. (2002). GMRES, L-curves, and discrete ill-posed problems. BIT Numer. Math. 42, 44–65. doi:10.1023/A:1021918118380.

Cámara-Vázquez, M. Á., Hernández-Romero, I., Rodrigo, M., Alonso-Atienza, F., Figuera, C., Morgado-Reyes, E., et al. (2021). Electrocardiographic imaging including intracardiac information to achieve accurate global mapping during atrial fibrillation. Biomed. Signal Process. Control 64, 1–23. doi:10.1016/j.bspc.2020.102354.

Cervera, E. (2012). El registro de ECG en relación con los potenciales de acción de las diferentes estructuras cardíacas. Available at: https://commons.wikimedia.org/wiki/File:Registro_ECG.jpg.

Cheng, L. K., Bodley, J. M., and Pullan, A. J. (2003). Effects of experimental and modeling errors on electrocardiographic inverse formulations; Effects of experimental and modeling errors on electrocardiographic inverse formulations. IEEE Trans. Biomed. Eng. 50. doi:10.1109/TBME.2002.807325.

Clarnette, J. A., Brooks, A. G., Mahajan, R., Elliott, A. D., Twomey, D. J., Pathak, R. K., et al. (2018). Outcomes of persistent and long-standing persistent atrial fibrillation ablation: a systematic review and meta-analysis. Europace 20, f366–f376. doi:10.1093/europace/eux297.

Cochet, H., Dubois, R., Yamashita, S., Al Jefairi, N., Berte, B., Sellal, J.-M., et al. (2018). Relationship Between Fibrosis Detected on Late Gadolinium-Enhanced Cardiac Magnetic Resonance and Re-Entrant Activity Assessed With Electrocardiographic Imaging in Human Persistent Atrial Fibrillation. JACC Clin. Electrophysiol. 4, 17–29. doi:10.1016/j.jacep.2017.07.019.

Colli-Franzone, P. A mathematical procedure for solving the inverse potential problem of electrocardiography. analysis of the time-space accuracy from in vitro experimental data. Math. Biosci 77, 353–396,. doi:10.1016/0025-5564(85)90106-3.

Colli-Franzone, P., Guerri, L., Tentoni, S., Viganotti, C., Baruffi, S., Spaggiari, S., et al. (1985). A mathematical procedure for solving the inverse potential problem of electrocardiography. analysis of the time-space accuracy from in vitro experimental data. Math. Biosci. 77, 353–396. doi:10.1016/0025-5564(85)90106-3.

Colli Franzone, P., Pavarino, L. F., and Taccardi, B. (2005). Simulating patterns of excitation, repolarization and action potential duration with cardiac Bidomain and Monodomain models. Math. Biosci. 197, 35–66. doi:10.1016/J.MBS.2005.04.003.

Corrado, C., Roney, C. H., Razeghi, O., Lemus, J. A. S., Coveney, S., Sim, I., et al. (2023). Quantifying the impact of shape uncertainty on predicted arrhythmias. Comput. Biol. Med. 153. doi:10.1016/J.COMPBIOMED.2022.106528.

Courtemanche, M., Ramirez, R. J., and Nattel, S. (1998). Ionic mechanisms underlying human atrial action potential properties: Insights from a mathematical model. Am. J. Physiol. - Hear. Circ. Physiol. 275. doi:10.1152/ajpheart.1998.275.1.h301.

References

Cuculich, P. S., Wang, Y., Lindsay, B. D., Faddis, M. N., Schuessler, R. B., Damiano, R. J., et al. (2010). Noninvasive characterization of epicardial activation in humans with diverse atrial fibrillation patterns. Circulation 122, 1364–1372. doi:10.1161/CIRCULATIONAHA.110.945709.

Dhillon, G. S., Honarbakhsh, S., Graham, A., Abbass, H., Welch, S., Daw, H., et al. (2022). ECG-I phenotyping of persistent AF based on driver burden and distribution to predict response to pulmonary vein isolation (PHENOTYPE-AF). J. Cardiovasc. Electrophysiol. 33, 2263–2273. doi:10.1111/jce.15644.

Di Biase, L., Burkhardt, J. D., Mohanty, P., Mohanty, S., Sanchez, J. E., Trivedi, C., et al. (2016). Left Atrial Appendage Isolation in Patients With Longstanding Persistent AF Undergoing Catheter Ablation: BELIEF Trial. J. Am. Coll. Cardiol. 68, 1929–1940. doi:10.1016/j.jacc.2016.07.770.

Dössel, O., Krueger, M. W., Weber, F. M., Wilhelms, M., and Seemann, G. (2012). Computational modeling of the human atrial anatomy and electrophysiology. Med. Biol. Eng. Comput. 50, 773–799. doi:10.1007/s11517-012-0924-6.

Ehrlich, M. P., Laufer, G., Coti, I., Peter, M., Andreas, M., Stix, G., et al. (2019). Noninvasive mapping before surgical ablation for persistent, long-standing atrial fibrillation. J. Thorac. Cardiovasc. Surg. 157, 248–256. doi:10.1016/j.jtcvs.2018.07.104.

Einthoven W. (1906). Le télécardiogramme. Arch Intern Physiol 4, 132–164.

Emilio Osorio- Jaramillo1, MD , Sarah Klenk, MD, Guenther Laufer, MD, and Marek P. Ehrlich, M. (2020). Noninvasive Electrocardiographic Imaging: A Novel Tool for Understanding Atrial Fibrillation in Candidates for Cardiac Surgery?

Ferrer, A., Sebastián, R., Sánchez-Quintana, D., Rodríguez, J. F., Godoy, E. J., Martínez, L., et al. (2015). Detailed anatomical and electrophysiological models of human atria and torso for the simulation of atrial activation. PLoS One 10. doi:10.1371/journal.pone.0141573.

Figuera, C., Suárez-Gutiérrez, V., Hernández-Romero, I., Rodrigo, M., Liberos, A., Atienza, F., et al. (2016). Regularization techniques for ECG imaging during atrial fibrillation: A computational study. Front. Physiol. 7. doi:10.3389/fphys.2016.00466.

Fischer, G., Tilg, B., Wach, P., Modre, R., Leder, U., and Nowak, H. (1999). Application of high-order boundary elements to the electrocardiographic inverse problem. Comput. Methods Programs Biomed. 58, 119–131. doi:10.1016/S0169-2607(98)00076-5.

Gao, X., Lam, A. G., Bilchick, K. C., Darby, A., Mehta, N., Mason, P. K., et al. (2019). The use of non-invasive mapping in persistent AF to predict acute procedural outcome. J. Electrocardiol. 57, S21–S26. doi:10.1016/j.jelectrocard.2019.08.012.

Goette, A., Kalman, J. M., Aguinaga, L., Akar, J., Cabrera, J. A., Chen, S. A., et al. (2016). EHRA/HRS/APHRS/SOLAECE expert consensus on atrial cardiomyopathies: Definition, characterization, and clinical implication. Europace 18, 1455–1490. doi:10.1093/europace/euw161.

Gonzales, M. J., Sturgeon, G., Krishnamurthy, A., Hake, J., Jonas, R., Stark, P., et al. (2013). A three-dimensional finite element model of human atrial anatomy: New methods for cubic Hermite meshes with extraordinary vertices. Med. Image Anal. 17, 525–537. doi:10.1016/J.MEDIA.2013.03.005.

Grandi, E., Pandit, S. V., Voigt, N., Workman, A. J., Dobrev, D., Jalife, J., et al. (2011). Human atrial action potential and Ca 2+ model: Sinus rhythm and chronic atrial fibrillation. Circ. Res. 109, 1055–1066. doi:10.1161/CIRCRESAHA.111.253955.

Guillem, M. (2008). Activation patterns in atrial fibrillation: contributions of body surface potential mapping.

Guillem, M. S., Climent, A. M., Castells, F., Husser, D., Millet, J., Arya, A., et al. (2009). Noninvasive mapping of human atrial fibrillation. J. Cardiovasc. Electrophysiol. 20, 507–513. doi:10.1111/j.1540-8167.2008.01356.x.

Guillem, M., Bollmann, A., Climent, A. M., Husser, D., Millet-Roig, J., and Castells, F. (2009). How many leads are necessary for a reliable reconstruction of surface potentials during atrial fibrillation? IEEE Trans. Inf. Technol. Biomed. 13, 330–340. doi:10.1109/TITB.2008.2011894.

Guillem, M. S., Climent, A. M., Millet, J., Arenal, Á., Fernández-Avilés, F., Jalife, J., et al. (2013). Noninvasive Localization of Maximal Frequency Sites of Atrial Fibrillation by Body Surface Potential Mapping. Circ. Arrhythmia Electrophysiol. 6, 294–301. doi:10.1161/CIRCEP.112.000167.

Guillem, M. S., Climent, A. M., Rodrigo, M., Fernández-Avilés, F., Atienza, F., and Berenfeld, O. (2016). Presence and stability of rotors in atrial fibrillation: evidence and therapeutic implications. Cardiovasc. Res. 109, 480–492. doi:10.1093/cvr/cvw011.

Haissaguerre, M., Hocini, M., Denis, A., Shah, A. J., Komatsu, Y., Yamashita, S., et al. (2014). Driver domains in persistent atrial fibrillation. Circulation 130, 530–538. doi:10.1161/CIRCULATIONAHA.113.005421.

References

Haissaguerre, M., Hocini, M., Shah, A. J., Derval, N., Sacher, F., Jais, P., et al. (2013). Noninvasive panoramic mapping of human atrial fibrillation mechanisms: A feasibility report. J. Cardiovasc. Electrophysiol. 24, 711–717. doi:10.1111/jce.12075.

Haïssaguerre, M., Jaïs, P., Shah, D. C., Takahashi, A., Hocini, M., Quiniou, G., et al. (1998). Spontaneous Initiation of Atrial Fibrillation by Ectopic Beats Originating in the Pulmonary Veins. N. Engl. J. Med. 339, 659–666. doi:10.1056/nejm199809033391003.

Hansen, C. (1992). Analysis of discrete ill-posed problems. Soc. Ind. Appl. Math. 34, 561–580. doi:https://doi.org/10.1137/1034115.

Hansen, P. C., and O'Leary, D. P. (1993). The Use of the L-Curve in the Regularization of Discrete Ill-Posed Problems. SIAM J. Sci. Comput. 14, 1487–1503. doi:10.1137/0914086.

Harrison, J. L., Jensen, H. K., Peel, S. A., Chiribiri, A., Grondal, A. K., Bloch, L. O., et al. (2014). Cardiac magnetic resonance and electroanatomical mapping of acute and chronic atrial ablation injury: A histological validation study. Eur. Heart J. 35, 1486–1495. doi:10.1093/eurheartj/eht560.

Hernández-Romero, I., Molero, R., Fambuena-Santos, C., Herrero-Martín, C., Climent, A. M., and Guillem, M. S. (2023). Electrocardiographic imaging in the atria. Med. Biol. Eng. Comput. 61, 879–896. doi:10.1007/s11517-022-02709-7.

Hindricks, G., Potpara, T., Dagres, N., Bax, J. J., Boriani, G., Dan, G. A., et al. (2021). 2020 ESC Guidelines for the diagnosis and management of atrial fibrillation developed in collaboration with the European Association for Cardio-Thoracic Surgery (EACTS). Eur. Heart J. 42, 373–498. doi:10.1093/eurheartj/ehaa612.

Hodgkin, A. L., and Huxley, A. F. (1952). A quantitative description of membrane current and its application to conduction and excitation in nerve. J. Physiol. 117, 500–544. doi:10.1113/JPHYSIOL.1952.SP004764.

Honarbakhsh, S., Dhillon, G., Abbas, H., Waddingham, P. H., Dennis, A., Ahluwalia, N., et al. (2022a). Non-invasive Electrocardiographic Imaging guided targeting of drivers of persistent atrial fibrillation: the TARGET-AF1 trial. Hear. Rhythm 95, 106408. doi:10.1016/j.hrthm.2022.01.042.

Honarbakhsh, S., Dhillon, G., Abbass, H., Waddingham, P. H., Dennis, A., Ahluwalia, N., et al. (2022b). Noninvasive electrocardiographic imaging–guided targeting of drivers of persistent atrial fibrillation: The TARGET-AF1 trial. Hear. Rhythm. doi:10.1016/J.HRTHM.2022.01.042.

Horáček, B. M., and Clements, J. C. (1997). The inverse problem of electrocardiography: A solution in terms of single- end double-layer sources on the epicardial surface. Math. Biosci. 144, 119–154. doi:10.1016/S0025-5564(97)00024-2.

Hwang, M., Kwon, S. S., Wi, J., Park, M., Lee, H. S., Park, J. S., et al. (2014). Virtual ablation for atrial fibrillation in personalized in-silico three-dimensional left atrial modeling: Comparison with clinical catheter ablation. Prog. Biophys. Mol. Biol. 116, 40–47. doi:10.1016/j.pbiomolbio.2014.09.006.

Jacquemet, V., Van Oosterom, A., Vesin, J. M., and Kappenberger, L. (2006). Analysis of electrocardiograms during atrial fibrillation: A biophysical model approach. IEEE Eng. Med. Biol. Mag. 25, 79–88. doi:10.1109/EMB-M.2006.250511.

Jaïs, P., Cauchemez, B., Macle, L., Daoud, E., Khairy, P., Subbiah, R., et al. (2008). Catheter ablation versus antiarrhythmic drugs for atrial fibrillation: The A4 study. Circulation 118, 2498–2505. doi:10.1161/CIRCULATIONAHA.108.772582.

Jalife, José; Delmar, Mario; Anumonwo, Justus; Berenfeld, Omer; Kalifa, J. (2009). Basic cardiac electrophysiology for the clinician.

Jalife, J. (2003). Rotors and spiral waves in atrial fibrillation. J. Cardiovasc. Electrophysiol. 14, 776–780. doi:10.1046/j.1540-8167.2003.03136.x.

January, C. T., Wann, L. S., Alpert, J. S., Calkins, H., Cigarroa, J. E., Cleveland, J. C., et al. (2014). 2014 AHA/ACC/HRS guideline for the management of patients with atrial fibrillation: A report of the American college of Cardiology/American heart association task force on practice guidelines and the heart rhythm society. J. Am. Coll. Cardiol. 64, e1–e76. doi:10.1016/J.JACC.2014.03.022.

Jorge Pedrón Torrecilla (2015). Non-invasive Reconstruction of the Myocardial Electrical Activity from Body Surface Potential Recordings.

Kim, J. S., Shin, S. Y., Na, J. O., Choi, C. U., Kim, S. H., Kim, J. W., et al. (2015). Does isolation of the left atrial posterior wall improve clinical outcomes after radiofrequency catheter ablation for persistent atrial fibrillation?: A prospective randomized clinical trial. Int. J. Cardiol. 181, 277–283. doi:10.1016/j.ijcard.2014.12.035.

Knecht, S., Sohal, M., Deisenhofer, I., Albenque, J.-P., Arentz, T., Neumann, T., et al. (2017). Multicentre evaluation of non-invasive biatrial mapping for persistent atrial fibrillation ablation: the AFACART study Ablation for atrial fibrillation. Europace 19, 1302–1309. doi:10.1093/europace/euw168.

References

Koivumäki, J. T., Korhonen, T., and Tavi, P. (2011). Impact of sarcoplasmic reticulum calcium release on calcium dynamics and action potential morphology in human atrial myocytes: A computational study. PLoS Comput. Biol. 7. doi:10.1371/journal.pcbi.1001067.

Krueger, M. W., Rhode, K. S., O'Neill, M. D., Rinaldi, C. A., Gill, J., Razavi, R., et al. (2014). Patient-specific modeling of atrial fibrosis increases the accuracy of sinus rhythm simulations and may explain maintenance of atrial fibrillation. J. Electrocardiol. 47, 324–328. doi:10.1016/j.jelectrocard.2013.11.003.

Krueger, M. W., Schmidt, V., Tobón, C., Weber, F. M., Lorenz, C., Keller, D. U. J., et al. (2011). Modeling atrial fiber orientation in patient-specific geometries: A semi-automatic rule-based approach. Lect. Notes Comput. Sci. (including Subser. Lect. Notes Artif. Intell. Lect. Notes Bioinformatics) 6666 LNCS, 223–232. doi:10.1007/978-3-642-21028-0_28/COVER.

Lau, D. H., Nattel, S., Kalman, J. M., and Sanders, P. (2017). Modifiable Risk Factors and Atrial Fibrillation. Circulation 136, 583–596. doi:10.1161/CIRCULATIONAHA.116.023163.

Lip, G. Y. H., Nieuwlaat, R., Pisters, R., Lane, D. A., Crijns, H. J. G. M., Andresen, D., et al. (2010). Refining clinical risk stratification for predicting stroke and thromboembolism in atrial fibrillation using a novel risk factor-based approach: The Euro Heart Survey on atrial fibrillation. Chest 137, 263–272. doi:10.1378/chest.09-1584.

Lux, R. L., Smith, C. R., Wyatt, R. F., and Abildskov, J. A. (1978). Limited Lead Selection for Estimation of Body Surface Potential Maps in Electrocardiography. IEEE Trans. Biomed. Eng. BME-25, 270–276. doi:10.1109/TBME.1978.326332.

Macleod, R., and Buist, M. (2010). The Forward Problem of Electrocardiography. 247–298.

Maleckar, M. M., Greenstein, J. L., Trayanova, N. A., and Giles, W. R. (2008). Mathematical simulations of ligand-gated and cell-type specific effects on the action potential of human atrium. Prog. Biophys. Mol. Biol. 98, 161–170. doi:10.1016/j.pbiomolbio.2009.01.010.

Mandapati, R., Skanes, A., Chen, J., Berenfeld, O., and Jalife, J. (2000). Stable microreentrant sources as a mechanism of atrial fibrillation in the isolated sheep heart. Circulation 101, 194–199. doi:10.1161/01.CIR.101.2.194.

Marrouche, N. F., Wazni, O., McGann, C., Greene, T., Dean, J. M., Dagher, L., et al. (2022). Effect of MRI-Guided Fibrosis Ablation vs Conventional Catheter Ablation on Atrial Arrhythmia Recurrence in Patients With Persistent Atrial Fibrillation: The DECAAF II Randomized Clinical Trial. Jama 327, 2296–2305. doi:10.1001/jama.2022.8831.

Meo, M., Pambrun, T., Derval, N., Dumas-Pomier, C., Puyo, S., Duchâteau, J., et al. (2018). Noninvasive assessment of atrial fibrillation complexity in relation to ablation characteristics and outcome. Front. Physiol. 9, 929. doi:10.3389/fphys.2018.00929.

Messinger-Rapport, B. J., and Rudy, Y. (1990). Noninvasive recovery of epicardial potentials in a realistic heart-torso geometry. Normal sinus rhythm. Circ. Res. 66, 1023–1039. doi:10.1161/01.RES.66.4.1023.

Moe, G. K., and Abildskov, J. A. (1959). Atrial fibrillation as a self-sustaining arrhythmia independent of focal discharge. Am. Heart J. 58, 59–70. doi:10.1016/0002-8703(59)90274-1.

Nademanee, K., Mckenzie, J., Kosar, E., Schwab, M., Sunsaneewitayakul, B., Vasavakul, T., et al. (2004). A New Approach for Catheter Ablation of Atrial Fibrillation: Mapping of the Electrophysiologic Substrate. J. Am. Coll. Cardiol. 43, 2044–2053. doi:10.1016/j.jacc.2003.12.054.

Nademanee, K., Schwab, M., Porath, J., and Abbo, A. (2006). How to perform electrogram-guided atrial fibrillation ablation. Hear. Rhythm 3, 981–984. doi:10.1016/j.hrthm.2006.03.018.

Nagel, C., Schuler, S., Dössel, O., and Loewe, A. (2021). A bi-atrial statistical shape model for large-scale in silico studies of human atria: Model development and application to ECG simulations. Med. Image Anal. 74, 102210. doi:10.1016/J.MEDIA.2021.102210.

Narayan, S. M., Krummen, D. E., Clopton, P., Shivkumar, K., and Miller, J. M. (2013). Direct or coincidental elimination of stable rotors or focal sources may explain successful atrial fibrillation ablation: On-treatment analysis of the CONFIRM trial (Conventional Ablation for AF with or Without Focal Impulse and Rotor Modulation). J. Am. Coll. Cardiol. 62, 138–147. doi:10.1016/j.jacc.2013.03.021.

Noble, D. (1962). A modification of the Hodgkin—Huxley equations applicable to Purkinje fibre action and pacemaker potentials. J. Physiol. 160, 317–352. doi:10.1113/jphysiol.1962.sp006849.

Nygren, A., Fiset, C., Firek, L., Clark, J. W., Lindblad, D. S., Clark, R. B., et al. (1998). Mathematical model of an adult human atrial cell: The role of K+ currents in repolarization. Circ. Res. 82, 63–81. doi:10.1161/01.RES.82.1.63.

Parameswaran, R., Al-Kaisey, A. M., and Kalman, J. M. (2021). Catheter ablation for atrial fibrillation: current indications and evolving technologies. Nat. Rev. Cardiol. 18, 210–225. doi:10.1038/s41569-020-00451-x.

References

Parameswaran, R., Voskoboinik, A., Gorelik, A., Lee, G., Kistler, P. M., Sanders, P., et al. (2018). Clinical impact of rotor ablation in atrial fibrillation: A systematic review. Europace 20, 1099–1106. doi:10.1093/europace/eux370.

Pedrón-Torrecilla, J. Noninvasive estimation of epicardial dominant high-frequency regions during atrial fibrillation. J. Cardiovasc. Electrophysiol 27, 435–442,. doi:10.1111/jce.12931.

Pedrón-Torrecilla, J., Rodrigo, M., Climent, A. M., Liberos, A., Pérez-David, E., Bermejo, J., et al. (2016). Noninvasive estimation of epicardial dominant high-frequency regions during atrial fibrillation. J. Cardiovasc. Electrophysiol. 27, 435–442. doi:10.1111/jce.12931.

Pisters, R., Lane, D. A., Nieuwlaat, R., De Vos, C. B., Crijns, H. J. G. M., Lip, G. Y. H., et al. (2010). A novel user-friendly score (HAS-BLED) to assess 1-year risk of major bleeding in patients with atrial fibrillation: The euro heart survey. Chest 138, 1093–1100. doi:10.1378/chest.10-0134.

Pullan, A. J., Cheng, L. K., Nash, M. P., Ghodrati, A., Macleod, R., and Brooks, D. H. The inverse problem of electrocardiology. Model. Simul. Appl 13, 175–190,. doi:10.1007/978-3-319-04801-7_6.

Pullan, A. J., Cheng, L. K., Nash, M. P., Ghodrati, A., Macleod, R., and Brooks, D. H. (2014). The inverse problem of electrocardiology. Model. Simul. Appl. 13, 175–190. doi:10.1007/978-3-319-04801-7_6.

Qu, Z., Aslanidi, O., Jacquemet, V., Bayer, J. D., Roney, C. H., Pashaei, A., et al. (2016). Novel Radiofrequency Ablation Strategies for Terminating Atrial Fibrillation in the Left Atrium: A Simulation Study. Front. Physiol. | www.frontiersin.org 1, 108. doi:10.3389/fphys.2016.00108.

Ramanathan, C., Jia, P., Ghanem, R., Calvetti, D., and Rudy, Y. (2003). Noninvasive Electrocardiographic Imaging "ECGI…: Application of the Generalized Minimal Residual "GMRes… Method. doi:10.1114/1.1588655.

Ramanathan, C., and Rudy, Y. (2001). Electrocardiographic imaging: I. Effect of torso inhomogeneities on body surface electrocardiographic potentials. J. Cardiovasc. Electrophysiol. 12, 229–240. doi:10.1046/j.1540-8167.2001.00229.x.

Remondino, F. (2004). 3-D reconstruction of static human body shape from image sequence. Comput. Vis. Image Underst. 93, 65–85. doi:10.1016/j.cviu.2003.08.006.

Rodrigo, M., Climent, A. M., Hernández-Romero, I., Liberos, A., Baykaner, T., Rogers, A. J., et al. (2020). Non-Invasive Assessment of Complexity of Atrial Fibrillation: Correlation with

Contact Mapping and Impact of Ablation. Circ. Arrhythmia Electrophysiol. 13, e007700. doi:10.1161/CIRCEP.119.007700.

Rodrigo, M., Climent, A. M., Liberos, A., Fernández-Avilés, F., Berenfeld, O., Atienza, F., et al. (2017a). Highest dominant frequency and rotor positions are robust markers of driver location during noninvasive mapping of atrial fibrillation: A computational study. Hear. Rhythm 14, 1224–1233. doi:10.1016/j.hrthm.2017.04.017.

Rodrigo, M., Climent, A. M., Liberos, A., Fernández-Avilés, F., Berenfeld, O., Atienza, F., et al. (2017b). Technical Considerations on Phase Mapping for Identification of Atrial Reentrant Activity in Direct- and Inverse-Computed Electrograms. Circ. Arrhythmia Electrophysiol. 10, e005008. doi:10.1161/CIRCEP.117.005008.

Rodrigo, M., Guillem, M. S., Climent, A. M., Liberos, A., Hernández-Romero, I., Arenal, Á., et al. (2018). Solving Inaccuracies in Anatomical Models for Electrocardiographic Inverse Problem Resolution by Maximizing Reconstruction Quality. IEEE Trans. Med. Imaging 37, 733–740. doi:10.1109/TMI.2017.2707413.

Rodrigo, M., Guillem, M. S., Climent, A. M., Pedrón-Torrecilla, J., Liberos, A., Millet, J., et al. (2014). Body surface localization of left and right atrial high-frequency rotors in atrial fibrillation patients: A clinical-computational study. Hear. Rhythm 11, 1584–1591. doi:10.1016/j.hrthm.2014.05.013.

Rodrigo, M., Waddell, K., Magee, S., Rogers, A. J., Alhusseini, M., Hernandez-Romero, I., et al. (2021a). Non-invasive Spatial Mapping of Frequencies in Atrial Fibrillation: Correlation With Contact Mapping. Front. Physiol. 11, 611266. doi:10.3389/fphys.2020.611266.

Rodrigo, M., Waddell, K., Magee, S., Rogers, A. J., Alhusseini, M., Hernandez-Romero, I., et al. (2021b). Non-invasive Spatial Mapping of Frequencies in Atrial Fibrillation: Correlation With Contact Mapping. Front. Physiol. 11. doi:10.3389/fphys.2020.611266.

Roney, C. H., Bayer, J. D., Zahid, S., Meo, M., Boyle, P. M. J., Trayanova, N. A., et al. (2016). Modelling methodology of atrial fibrosis affects rotor dynamics and electrograms. Europace 18, iv146–iv155. doi:10.1093/europace/euw365.

Roney, C. H., Sim, I., Yu, J., Beach, M., Mehta, A., Alonso Solis-Lemus, J., et al. (2022a). Predicting Atrial Fibrillation Recurrence by Combining Population Data and Virtual Cohorts of Patient-Specific Left Atrial Models. Circ. Arrhythm. Electrophysiol. 15, e010253. doi:10.1161/CIRCEP.121.010253.

References

Roney, C. H., Sim, I., Yu, J., Beach, M., Mehta, A., Solis-lemus, J. A., et al. (2022b). Predicting Atrial Fibrillation Recurrence by Patient-Specific Left Atrial Models. 1–9. doi:10.1161/CIRCEP.121.010253.

Ruff, C. T., Giugliano, R. P., Braunwald, E., Hoffman, E. B., Deenadayalu, N., Ezekowitz, M. D., et al. (2014). Comparison of the efficacy and safety of new oral anticoagulants with warfarin in patients with atrial fibrillation: A meta-analysis of randomised trials. Lancet 383, 955–962. doi:10.1016/S0140-6736(13)62343-0.

Salinet, J., Molero, R., Schlindwein, F. S., Karel, J., Rodrigo, M., Rojo-Álvarez, J. L., et al. (2021a). Electrocardiographic Imaging for Atrial Fibrillation: A Perspective From Computer Models and Animal Experiments to Clinical Value. Front. Physiol. 12, 1–23. doi:10.3389/fphys.2021.653013.

Salinet, J., Molero, R., Schlindwein, F. S., Karel, J., Rodrigo, M., Rojo-Álvarez, J. L., et al. (2021b). Electrocardiographic Imaging for Atrial Fibrillation: A Perspective From Computer Models and Animal Experiments to Clinical Value. Front. Physiol. 12. doi:10.3389/fphys.2021.653013.

Sanders, P., Berenfeld, O., Hocini, M., Jaïs, P., Vaidyanathan, R., Hsu, L. F., et al. (2005). Spectral analysis identifies sites of high-frequency activity maintaining atrial fibrillation in humans. Circulation 112, 789–797. doi:10.1161/CIRCULATIONAHA.104.517011.

Schotten, U., Lee, S., Zeemering, S., and Waldo, A. L. (2021). Paradigm shifts in electrophysiological mechanisms of atrial fibrillation. Europace 23, II9–II13. doi:10.1093/europace/euaa384.

Sethi, N. J., Feinberg, J., Nielsen, E. E., Safi, S., Gluud, C., and Jakobsen, J. C. (2017). The effects of rhythm control strategies versus rate control strategies for atrial fibrillation and atrial flutter: A systematic review with meta-analysis and Trial Sequential Analysis. PLoS One 12, 1–28. doi:10.1371/journal.pone.0186856.

Sharma, S. P., Sangha, R. S., Dahal, K., and Krishnamoorthy, P. (2017). The role of empiric superior vena cava isolation in atrial fibrillation: a systematic review and meta-analysis of randomized controlled trials. J. Interv. Card. Electrophysiol. 48, 61–67. doi:10.1007/s10840-016-0198-2.

Staerk, L., Sherer, J. A., Ko, D., Benjamin, E. J., and Helm, R. H. (2017). Atrial Fibrillation: Epidemiology, Pathophysiology, Clinical Outcomes. Circ. Res. 120, 1501–1517. doi:10.1161/CIRCRESAHA.117.309732.

Taccardi, B. (1963). Distribution of heart potentials on the thoracic surface of normal human subjects. Circ. Res. 12, 341–352. doi:10.1161/01.RES.12.4.341.

Terricabras, M., Piccini, J. P., and Verma, A. (2020). Ablation of persistent atrial fibrillation: Challenges and solutions. J. Cardiovasc. Electrophysiol. 31, 1809–1821. doi:10.1111/jce.14311.

Tikhonov, A., and Arsenin, V. (1977). Solution of Ill-posed Problems. Winston, Washington, DC.

Trayanova, N. (2006). Defibrillation of the heart: Insights into mechanisms from modelling studies. Exp. Physiol. 91, 323–337. doi:10.1113/expphysiol.2005.030973.

Turakhia, M. P., Desai, M., Hedlin, H., Rajmane, A., Talati, N., Ferris, T., et al. (2019). Rationale and design of a large-scale, app-based study to identify cardiac arrhythmias using a smartwatch: The Apple Heart Study. Am. Heart J. 207, 66–75. doi:10.1016/j.ahj.2018.09.002.

Van Gelder, I. C., Rienstra, M., Crijns, H. J. G. M., and Olshansky, B. (2016). Rate control in atrial fibrillation. Lancet 388, 818–828. doi:10.1016/S0140-6736(16)31258-2.

Van Oosterom, A., and Van Dam, P. (2005). The intra-myocardial distance function used in inverse computations of the timing of depolarization and repolarization. Comput. Cardiol. 32, 567–570. doi:10.1109/CIC.2005.1588164.

Verma, A., Liu, T., Niederer, S. A., Roney, C. H., Beach, M. L., Mehta, A. M., et al. (2020). In silico Comparison of Left Atrial Ablation Techniques That Target the Anatomical, Structural, and Electrical Substrates of Atrial Fibrillation. Front. Physiol. | www.frontiersin.org 1, 572874. doi:10.3389/fphys.2020.572874.

Vogler, J., Willems, S., Sultan, A., Schreiber, D., Lüker, J., Servatius, H., et al. (2015). Pulmonary Vein Isolation Versus Defragmentation the CHASE-AF Clinical Trial. J. Am. Coll. Cardiol. 66, 2743–2752. doi:10.1016/j.jacc.2015.09.088.

Wang, D., Kirby, R. M., and Johnson, C. R. (2010). Resolution Strategies for the Finite-Element-Based Solution of the ECG Inverse Problem. IEEE Trans. Biomed. Eng. 57, 220–237. doi:10.1109/TBME.2009.2024928.

Wang, Y., and Rudy, Y. (2006). Application of the method of fundamental solutions to potential-based inverse electrocardiography. Ann. Biomed. Eng. 34, 1272–1288. doi:10.1007/s10439-006-9131-7.

Wilhelms, M., Hettmann, H., Maleckar, M. M., Koivumäki, J. T., Dössel, O., and Seemann, G. (2013). Benchmarking electrophysiological models of human atrial myocytes. Front. Physiol. 3 JAN, 1–16. doi:10.3389/fphys.2012.00487.

References

Yamamoto, C., and Trayanova, N. A. (2022). Atrial fibrillation: Insights from animal models, computational modeling, and clinical studies. eBioMedicine 85, 104310. doi:10.1016/j.ebiom.2022.104310.

Zlochiver, S., Yamazaki, M., Kalifa, J., and Berenfeld, O. (2008). Rotor meandering contributes to irregularity in electrograms during atrial fibrillation. Hear. Rhythm 5, 846–854. doi:10.1016/j.hrthm.2008.03.010.